

Cardiff University  
School of Chemistry

Aleksandar Živković

# **Computational investigations of copper oxides for solar cell applications**

This thesis is being submitted in partial fulfilment of the requirements for the degree  
of Doctor of Philosophy

Cardiff, 2019

# Computational investigations of copper oxides for solar cell applications

Aleksandar Živković

Cardiff University School of Chemistry  
Cardiff 2019

## Abstract

Photovoltaic (PV) technology which makes use of the superabundant and freely available Sun's energy to generate electricity has obvious economic, environmental and societal benefits. However, to achieve significant market penetration PV devices have to be efficient and composed of cheap and readily available material. Semiconducting copper oxide compounds are formed from comparatively inexpensive and non-toxic elements, emerge in abundant quantities, demonstrate ease of fabrication and are environmentally friendly – which makes them attractive for large-scale PV applications.

Using quantum mechanical theoretical calculations based on density functional theory (DFT), distinct copper oxide compounds were investigated to assess, quantify, revise and boost their overall PV potential. First, the search for a set of unique parameters that would describe all three oxides of copper ( $\text{Cu}_2\text{O}$ ,  $\text{Cu}_4\text{O}_3$ , and  $\text{CuO}$ ) simultaneously at a desired accuracy was undertaken. On top of that, the usual metric, upon which PV absorbers are addressed as suitable or not, was extended in order to include simulated absorption spectra as well as selection rules besides the commonly employed electronic band gap value.

Using a hybrid-DFT approach, first row transition metal extrinsic dopants were introduced substitutionally on the cation site in  $\text{Cu}_2\text{O}$ . Furthermore, additional vacancies in the proximity of the dopant site were included in order to match the experimentally observed natural presence of copper vacancies. This has led to an increase in the overall PV conversion efficiencies of  $\text{Cu}_2\text{O}$ , which is one of the key factors when a material is sought for real time applications.

The occurrence of intrinsic defects in a material was proven crucial for its long-lasting and stable performance. After validating the computational parameters used within DFT against available experimental values for the ground state of  $\text{CuO}$  and  $\text{Cu}_4\text{O}_3$ , the energetics of intrinsic defects materializing in both compounds were found and proven to be in good agreement with available experimental data.

*Mojim najmilijima*

*To my family*

## Acknowledgements

Firstly, I would like to sincerely thank my supervisor, *Prof. Nora H. de Leeuw*, for giving me the trust and opportunity to pursue a research doctorate degree. Including me into her RS-DFID project has been an invaluable experience, from which I did not only benefit immensely research-wise, but also grew as a person into a better version of myself. I am also very grateful to *Dr. Alberto Roldan*, for his guidance, support, and many fruitful discussions regarding various aspects of my work.

I had the great opportunity to make a few academic friends, amongst which I would like to thank *Dr. Leonardo Bernasconi* in particular – a superb scientific role model of research excellence. His volunteering proof-reading gave additional seriousness and depth to this work.

Where would I have been without the constant support of family and friends? There are no words that could express my thankfulness and appreciation for the support and love from my nearest - my parents, *Veljko* and *Saja*, and my sister, *Katja*. I wish to also express special gratitude to *Desanka, Cvijeta, Jela, Goran, Vera, Goran, Stefan, Danilo, Sara, Aleksandra, Biljana, Dušan, Nada, Josip*.

I was fortunate to have friends, both old and new, that kept me going and did not let me down when it was hardest. This thesis would not have seen the light of day without *Matija*, who managed to somehow never forget the true value of friendship. Not to overlook his parents, *Ljiljana* and *Antun*, who are basically my second family.

Certain people made my stay in Cardiff the best it could have ever been. Amongst those, there are a few that stick out, *Peter* and *Muhao* first. Thank you both, I was able to learn incredibly lot from you and share memories which will last until the very end. Not to forget *Andrea*, whose long lasting discussions made impact to never be forgotten. Further gratitude goes to *Vedran*, who was always there when needed, and *Maja*, who shared with me the pain and joy of an academic life from the very early stages.

I wish to thank *Barbara* – needless to say why. It takes a lot of courage to share all those memories, from academic to travel-wise. If someone knows how it is not easy

with me, it would be her.

Special thanks go to my MEdU supervisor, *Igor*, who encouraged me to pursue a PhD and introduced me to the world of computational science. Not to forget the whole Department of Physics in Osijek, who laid down the foundations of physics for me.

Last but not least, I wish to express my gratefulness to family *Klement*, namely *Domagoj*, *Hrvoje*, and *Vesna*. And with special emphasis, *Dragan Klement* – a fantastic mentor who helped me discover the curiosity for natural phenomena and brought physics back to life for me, closing all the gaps left by many others.

I would also like to thank Cardiff University School of Chemistry for a PhD studentship and the Royal Society DFiD programme for funding. I acknowledge the support of the Supercomputing Wales project, which is part-funded by the European Regional Development Fund (ERDF) via Welsh Government. Via our membership of the UK's HPC Materials Chemistry Consortium, which is funded by EPSRC (EP/L000202), this work made use of the ARCHER facility, the UK's national high-performance computing service, which is funded by the Office of Science and Technology through EPSRC's High End Computing Programme. Without all of the aforementioned facilities, work outlined in this thesis would not have been feasible – *thank you*.

# Contents

<b>Acknowledgements</b>	<b>iii</b>
<b>List of Figures</b>	<b>ix</b>
<b>List of Tables</b>	<b>xi</b>
<b>List of publications</b>	<b>xii</b>
<b>1 Introduction</b>	<b>1</b>
<b>2 Methodological aspects</b>	<b>8</b>
2.1 Many-body Schrödinger equation . . . . .	9
2.2 Density functional theory . . . . .	11
2.3 Basis sets and pseudopotentials . . . . .	16
2.3.1 The band gap and its "problem" . . . . .	21
2.4 The physics of solar cells . . . . .	26
2.4.1 The solar spectrum . . . . .	27
2.4.2 Semiconducting materials . . . . .	28
2.5 Point defects in solids . . . . .	33
2.6 First-principles modelling of point defects in solids . . . . .	42
<b>3 Ground state properties of copper oxides</b>	<b>48</b>
3.1 Brief overview of literature . . . . .	49
3.1.1 Cuprous oxide - $\text{Cu}_2\text{O}$ . . . . .	49
3.1.2 Cupric oxide - $\text{CuO}$ . . . . .	55
3.1.3 Paramelaconite - $\text{Cu}_4\text{O}_3$ . . . . .	62
3.1.4 Photovoltaic potential of copper oxides . . . . .	66

3.1.5	Concluding remarks on literature review . . . . .	67
3.2	Technical details and computational parameters . . . . .	69
3.3	Results and discussion . . . . .	72
3.4	Conclusion . . . . .	82
<b>4</b>	<b>Doping of Cu<sub>2</sub>O with first row transition metals</b>	<b>84</b>
4.1	Summary of available literature . . . . .	85
4.1.1	Concluding remarks on literature review . . . . .	92
4.2	Technical details and computational parameters . . . . .	93
4.3	Results and discussion . . . . .	96
4.3.1	Formation enthalpies of pristine Cu <sub>2</sub> O . . . . .	96
4.3.2	Single substitutional cation-doped Cu <sub>2</sub> O . . . . .	97
4.3.3	Copper vacancies in cation-doped Cu <sub>2</sub> O . . . . .	102
4.4	Conclusion . . . . .	108
<b>5</b>	<b>Altering between intrinsic <i>p</i>-type and <i>n</i>-type defects of CuO</b>	<b>109</b>
5.1	Summary of available literature . . . . .	110
5.1.1	Concluding remarks on literature review . . . . .	114
5.2	Technical details and computational parameters . . . . .	115
5.3	Results and discussion . . . . .	117
5.3.1	Intrinsic defects of CuO . . . . .	122
5.3.2	The formation of defect pairs . . . . .	139
5.3.3	Intentional passivation . . . . .	143
5.4	Conclusion . . . . .	148
<b>6</b>	<b>The role of native point defects in Cu<sub>4</sub>O<sub>3</sub></b>	<b>149</b>
6.1	Technical details and computational parameters . . . . .	150
6.2	Results and discussion . . . . .	152
6.2.1	Ground state electronic structure . . . . .	152
6.2.2	Intrinsic defects . . . . .	154
6.3	Conclusion . . . . .	164
<b>7</b>	<b>Summary and future work</b>	<b>166</b>
	<b>Bibliography</b>	<b>170</b>

## List of Figures

1.1	Primary energy consumption by source . . . . .	3
1.2	Global investment in renewable technologies . . . . .	4
1.3	Solar energy potential . . . . .	6
2.1	Pseudopotentials - Schematic illustration . . . . .	20
2.2	Energy diagram of a semiconductor . . . . .	23
2.3	Electronic energies for molecules and solids in various models . . . . .	24
2.4	Standard solar spectrum . . . . .	27
2.5	Excitation processes in metals and semiconductors . . . . .	29
2.6	Electron energy diagram for direct and indirect semiconductors . . . . .	30
2.7	Absorption coefficient of GaAs . . . . .	32
2.8	Recombination processes in semiconductors . . . . .	34
2.9	Phosphorus doped silicon lattice . . . . .	34
2.10	Boron doped silicon lattice . . . . .	35
2.11	Defects in $\text{Cu}_2\text{O}$ . . . . .	37
2.12	A $pn$ -junction and its energy band diagram . . . . .	40
3.1	Band structure diagram of $\text{Cu}_2\text{O}$ . . . . .	51
3.2	Optical absorption of $\text{Cu}_2\text{O}$ . . . . .	52
3.3	Band gap of $\text{Cu}_2\text{O}$ as a function of temperature . . . . .	55
3.4	$\text{CuO}$ band gap as a function of temperature . . . . .	57
3.5	Magnetic ordering of $\text{CuO}$ . . . . .	59
3.6	Structure of $\text{Cu}_4\text{O}_3$ . . . . .	63
3.7	Fitting the $U_{\text{eff}}$ value for $\text{CuO}$ . . . . .	70
3.8	Crystal structure of copper oxides . . . . .	73
3.9	Brillouin zone of copper oxide unit cells . . . . .	73

3.10	Band structure of $\text{Cu}_2\text{O}$ . . . . .	76
3.11	Band structure of $\text{CuO}$ . . . . .	78
3.12	Electronic band structure of $\text{Cu}_4\text{O}_3$ . . . . .	79
3.13	Dielectric function of copper oxides . . . . .	80
3.14	Absorption coefficient of copper oxides . . . . .	80
3.15	Spectroscopic efficiencies of copper oxides . . . . .	81
4.1	Unfolded band structure of $\text{Cu}_2\text{O}$ . . . . .	94
4.2	Phase stability of $\text{Cu}_2\text{O}$ . . . . .	96
4.3	Band structure of doped $\text{Cu}_2\text{O}$ . . . . .	99
4.4	DOS of doped $\text{Cu}_2\text{O}$ . . . . .	100
4.5	Spin density of doped $\text{Cu}_2\text{O}$ . . . . .	101
4.6	DOS of doped $\text{Cu}_2\text{O}$ with additional vacancies . . . . .	104
4.7	Spin density of doped $\text{Cu}_2\text{O}$ with additional vacancies . . . . .	105
4.8	Partial charges of doped $\text{Cu}_2\text{O}$ . . . . .	106
4.9	PV efficiency of doped $\text{Cu}_2\text{O}$ . . . . .	107
4.10	PV efficiency of doped $\text{Cu}_2\text{O}$ with additional vacancies . . . . .	107
5.1	Modelling cells of $\text{CuO}$ . . . . .	116
5.2	Band structure of $\text{CuO}$ in the primitive cell . . . . .	118
5.3	$\text{CuO}$ spin arrangements . . . . .	119
5.4	Band gap vs $U_{\text{eff}}$ and $\alpha$ for $\text{CuO AF}_X$ . . . . .	120
5.5	Band gap vs $U_{\text{eff}}$ and $\alpha$ for $\text{CuO AF}_Z$ . . . . .	121
5.6	$\text{CuO}$ relaxed cell geometry . . . . .	121
5.7	Phase stability of $\text{CuO}$ . . . . .	123
5.8	Lattice distortions of $\text{CuO}$ with intrinsic defects . . . . .	123
5.9	Defect formation energies of $\text{CuO}$ . . . . .	124
5.10	DOS of $\text{CuO}$ with simple vacancies and antisites . . . . .	126
5.11	Partial charges of neutral Cu vacancies in $\text{CuO}$ . . . . .	127
5.12	Partial charges of neutral O vacancies in $\text{CuO}$ . . . . .	128
5.13	Partial charges of neutral Cu antisite defects in $\text{CuO}$ . . . . .	130
5.14	Partial charges of neutral O antisite defects in $\text{CuO}$ . . . . .	131
5.15	Positions of simple interstitials in $\text{CuO}$ . . . . .	131
5.16	DOS for interstitial Cu defects in $\text{CuO}$ . . . . .	132
5.17	Partial charges for interstitial $\text{Cu}_{i-1}$ in $\text{CuO}$ . . . . .	133
5.18	Partial charges for interstitial $\text{Cu}_{i-2}$ in $\text{CuO}$ . . . . .	134
5.19	Partial charges for interstitial $\text{Cu}_{i-3}$ in $\text{CuO}$ . . . . .	135
5.20	DOS for interstitial Cu defects in $\text{CuO}$ . . . . .	137
5.21	Partial charges for interstitial O defect in $\text{CuO}$ . . . . .	138

5.22	Formation energies of pair defects in CuO . . . . .	139
5.23	DOS for pair defects in CuO . . . . .	140
5.24	Partial charges for pair defects in CuO (1) . . . . .	141
5.25	Partial charges for pair defects in CuO (2) . . . . .	142
5.26	DOS for pair defects in CuO with Hydrogen . . . . .	146
5.27	DOS for pair defects in CuO with Hydrogen . . . . .	147
6.1	Unit cell of Cu <sub>4</sub> O <sub>3</sub> . . . . .	151
6.2	Band gap dependence of Cu <sub>4</sub> O <sub>3</sub> on calculation parameters . . . . .	152
6.3	Band structure of Cu <sub>4</sub> O <sub>3</sub> . . . . .	153
6.4	Phase stability of Cu <sub>4</sub> O <sub>3</sub> . . . . .	155
6.5	Native defect formation energies of Cu <sub>4</sub> O <sub>3</sub> . . . . .	155
6.6	DOS of Cu <sub>4</sub> O <sub>3</sub> for single vacancies . . . . .	156
6.7	Partial charges of Cu <sub>4</sub> O <sub>3</sub> for single vacancies . . . . .	158
6.8	DOS of Cu <sub>4</sub> O <sub>3</sub> for single antisite defects . . . . .	159
6.9	Partial charges of Cu <sub>4</sub> O <sub>3</sub> for single antisite defects . . . . .	160
6.10	Positions of simple interstitials in Cu <sub>4</sub> O <sub>3</sub> . . . . .	161
6.11	DOS of Cu <sub>4</sub> O <sub>3</sub> for single interstitials . . . . .	162
6.12	Partial charges of Cu <sub>4</sub> O <sub>3</sub> for single interstitial Cu defects . . . . .	163
6.13	Partial charges of Cu <sub>4</sub> O <sub>3</sub> for single interstitial O defects . . . . .	164

## List of Tables

3.1	Structural and mechanical properties of $\text{Cu}_2\text{O}$ . . . . .	50
3.2	Electronic and optical properties of $\text{Cu}_2\text{O}$ . . . . .	51
3.3	Transport properties of $\text{Cu}_2\text{O}$ . . . . .	53
3.4	Summary of calculated values for $\text{Cu}_2\text{O}$ . . . . .	54
3.5	Structural and mechanical properties of $\text{CuO}$ . . . . .	56
3.6	Electronic properties of $\text{CuO}$ . . . . .	57
3.7	Transport properties of $\text{CuO}$ . . . . .	60
3.8	Summary of <i>ab-initio</i> calculated properties of $\text{CuO}$ . . . . .	61
3.9	Structural properties of $\text{Cu}_4\text{O}_3$ . . . . .	63
3.10	Electronic properties of $\text{Cu}_4\text{O}_3$ . . . . .	65
3.11	Summary of transport properties of $\text{Cu}_4\text{O}_3$ . . . . .	65
3.12	Calculated structural properties of $\text{Cu}_2\text{O}$ , $\text{Cu}_4\text{O}_3$ , and $\text{CuO}$ . . . . .	74
3.13	Elastic constants of $\text{Cu}_2\text{O}$ . . . . .	74
3.14	Elastic constants of $\text{Cu}_4\text{O}_3$ . . . . .	75
3.15	elastic constants of $\text{CuO}$ . . . . .	75
3.16	Electronic band gaps of $\text{Cu}_2\text{O}$ , $\text{Cu}_4\text{O}_3$ , and $\text{CuO}$ . . . . .	78
4.1	Defect formation energies of doped $\text{Cu}_2\text{O}$ from literature . . . . .	89
4.2	Defect formation energies of extrinsically doped $\text{Cu}_2\text{O}$ . . . . .	91
4.3	Formation enthalpies of copper oxides . . . . .	96
4.4	Structural properties of doped $\text{Cu}_2\text{O}$ . . . . .	97
4.5	Formation energies of doped $\text{Cu}_2\text{O}$ . . . . .	98
4.6	Formation energies for doped $\text{Cu}_2\text{O}$ with additional vacancies . . . . .	102
4.7	Bader charges of doped $\text{Cu}_2\text{O}$ . . . . .	103
5.1	Defect formation energies of $\text{CuO}$ in literature . . . . .	113

5.2	CuO lattice parameters . . . . .	116
5.3	Electronic band gap and magnetization of CuO . . . . .	118
5.4	Defect formation energies of passivated CuO . . . . .	144
6.1	Formation enthalpies of $\text{Cu}_4\text{O}_3$ . . . . .	154
6.2	Bader charges of $\text{Cu}_4\text{O}_3$ . . . . .	155

## List of publications

- "Density functional theory study explaining the underperformance of copper oxides as photovoltaic absorbers", A. Živkovic, A. Roldan, N. H. de Leeuw, Phys. Rev. **B 99** 035154 (2019).
- "Tuning the electronic band gap of Cu<sub>2</sub>O via transition metal doping for improved photovoltaic applications" A. Živkovic, A. Roldan, N. H. de Leeuw, Phys. Rev. Materials **3**, 115202 (2019).
- "Altering the conductivity of CuO through the formation of intrinsic defects" A. Živkovic, N. H. de Leeuw, Phys. Rev. Materials (submitted).
- "Native impurities of Cu<sub>4</sub>O<sub>3</sub>" A. Živkovic, N. H. de Leeuw, (to be submitted).
- "First-principles DFT insights into the structural, elastic, and optoelectronic properties of  $\alpha$  and  $\beta$ -ZnP<sub>2</sub>: implications for photovoltaic applications", A. Živkovic, B. Farkaš, V. Uahengo, N. H. de Leeuw, and N. Y. Dzade, J. Phys.: Condens. Matter **31** 265501 (2019).

## Introduction

*"Aristotle said a bunch of stuff that was wrong. Galileo and Newton fixed things up. Then Einstein broke everything again. Now, we've basically got it all worked out, except for small stuff, big stuff, hot stuff, cold stuff, fast stuff, heavy stuff, dark stuff, turbulence, and the concept of time."*

---

Z. Weinersmith, *Science: Abridged Beyond the Point of Usefulness*

**Energy** Humanity relies on energy. Living organisms require energy in order to stay alive, such as the one humans get from food. Our civilization requires energy to function, obtained usually from energy resources such as fossil fuels, nuclear power plants or renewable energy sources.

The term *energy*, in the formal definition, is a quantitative property that needs to be transferred onto an object in order to perform work. It may exist in various forms, such as potential, kinetic, thermal, electrical, chemical, nuclear, etc. Energy can be converted from one form to another, but cannot be created or destroyed. For example, in a car engine, chemical energy stored in the fuel is converted to motion and thermal energy or, in the microwave oven, electromagnetic energy is converted from the power source into thermal energy for cooking the food. In all these processes, the total energy remains the same and no exception has ever been found.

Besides the energy in food necessary for our body to function, 30 times more energy is used to make our lives more comfortable, on average [1]. Electrical energy is one of the most utilized forms, since it can be used for almost anything. Life on Earth is based on solar energy following the photosynthesis process performed by algae, plants, and cyanobacteria. The human counterpart to that is the production of electrical energy through photovoltaic conversion by solar cells. This enabled mankind to, for the first time in history, produce high quality energy by utilizing solar energy directly, mimicking one of nature's finest mechanisms.

**Energy production and developing energy sources** Access to energy is a key pillar for human well-being, economic development and poverty alleviation. Ensuring everyone has sufficient access is an ongoing and pressing challenge for global development. However, energy systems also have important environmental impacts. Historical and current energy systems are dominated by the use of fossil fuels (coal, oil and gas) which produce air pollution, carbon dioxide (CO<sub>2</sub>), and other greenhouse gases – the fundamental drivers of global climate change. To meet the set global climate targets and balance the role of energy in social and economic development, the world should reduce its reliance on fossil fuels and transition towards lower-carbon based energy sources.

Global energy production has gone a long way, both in terms of quantity and source. Back in the 1800s, nearly all world's energy was produced from traditional biomass, essentially burning wood and other organic matter. At that point in time, only one to two percent of coal was used worldwide. By 1900, coal consumption had increased significantly, accounting for almost half of the global energy, with the other half remaining biomass. By the middle of the 20<sup>th</sup> century, the energy mix had advanced significantly, where coal reached around 20%. By 1960 the world had moved into nuclear energy production [2]. It was not until the 1980-90s that the first renewable sources were introduced, such as biofuels, wind, hydro, and solar energy (commonly referred to as *renewables*).

In 2015, the world consumed 25 times more energy than in the 1800 (around 146 000 terawatt-hours). While there might be the impression that renewables account for a large share of global energy consumption, their total contribution is still relatively small (see Figure 1.1) [3]. Even if hydropower is included, the total contribution is less than 5%. There is a long way to go if the transition from fossil fuels dominated energy into a low-carbon one is to be a successful one. However, the positive news is that investment and the production technology allowing mankind to utilise renewables efficiency is growing.

With the exception of carbon capture and storage technologies, two main options available in order to reduce the global greenhouse gas emissions are: renewable technologies (including bioenergy, hydropower, solar, wind, geothermal, and marine energy) and nuclear energy. All of these produce very low CO<sub>2</sub> per unit of energy compared to fossil fuels. Focusing on the electricity sector, from 2005 to 2015 the share of renewables in the electricity mix has increased by approximately 5-6% – good news! However, over the same period, the nuclear production share has decreased by almost exactly the same amount (5-6%).

Overall, this means that the total portion of electricity produced by low-carbon sources is almost the same as a decade ago. Comparing the amount of low-carbon

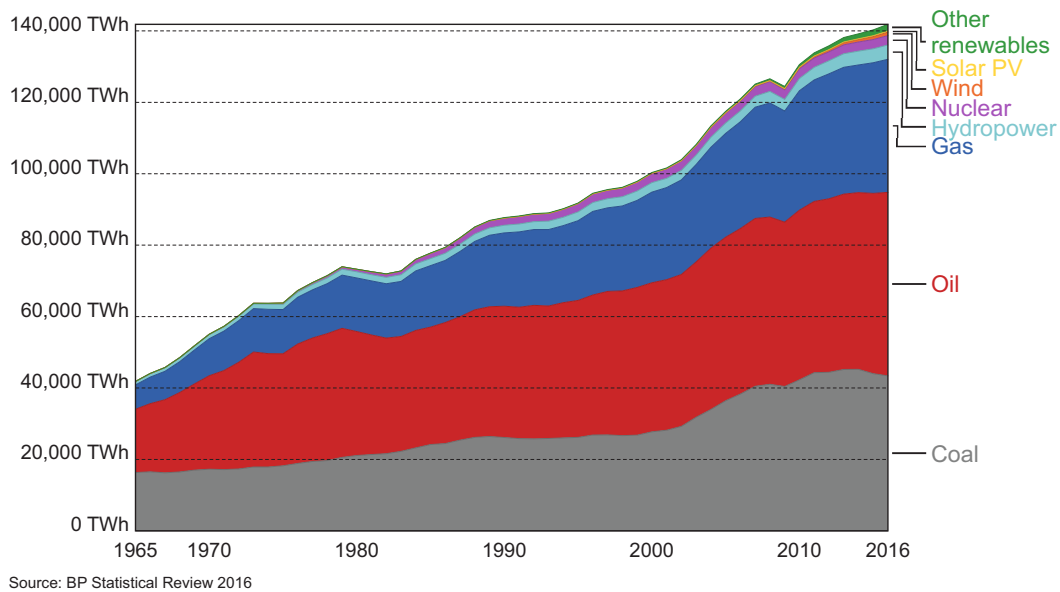


Figure 1.1: Primary energy consumption by source across the world's regions, measured in terawatt-hours (TWh). Note that this data does not include energy sourced from traditional biomass, which may form a significant component of primary energy consumption in low to middle-income countries. 'Other renewables' includes renewable sources including wind, geothermal, solar, biomass and waste.

electricity produced in 2015 to that of 1990, a drop of around 3% can be observed. Further progress in decarbonisation on electricity has been stalled in the last decade, mostly due to the growing aversion to nuclear energy.

**Investment in renewable technologies** Shifting energy systems away from fossil fuels towards renewable technologies requires significant financial investment. How much is really invested in the sector and how is this financing distributed across the world?

Figure 1.2 shows the global investments in renewable technologies for a period from 2004 to 2015. In 2004, the world invested 47 billion USD. By 2015, this rose to 286 billion USD, which is an increase of more than 600%. Investment has grown across all regions, but at significantly different rates. Growth has been greatest in China, increasing from 3 billion USD in 2004 to 103 billion USD by 2015 (an increase of 3400%). China is now the largest single investor in renewable technologies, investing approximately the same as the United States, Europe, and India combined.

In 2016, solar and wind energy both received 47% of the total investments in renewables (combining to account for 94% of global finance). These two technologies have been taking an increasing share, especially over the last five years. In 2006, bioenergy (both in the form of biomass and liquid biofuels) took a sizeable share of global investment, peaking at 36%. This has dwindled over the last decade, receiving less than four percent in 2016. These trends suggest that investors see solar and wind energy as the dominant renewable technologies of the future.

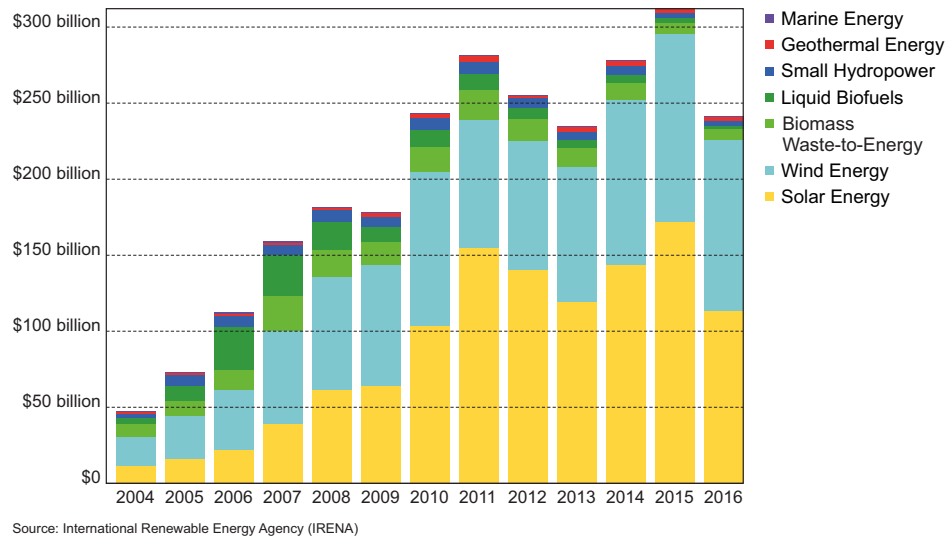


Figure 1.2: Global investment in renewable energy technologies, measured in USD per year. Note how investment figures exclude large-scale hydropower schemes.

**Solar energy** Why is solar energy predicted to be the dominant source of energy in future? The idea to convert abundant sunlight into a valuable asset such a electricity or chemical fuels can be traced back to the discovery of the photovoltaic (PV) effect by E. Becquerel in 1839. The photovoltaic effect is the creation of voltage and electric current in a material upon its exposure to light. It is both a physical and chemical phenomenon. Photovoltaic devices, solar cells, are unique in the way that they directly convert the incident solar radiation into electricity, with no noise, pollution or moving parts, making them robust, reliable and long lasting.

First practical photovoltaic devices were demonstrated in the 1950s, with a major boost following in the 1960s coming from the space industry, which required a power supply separate from the grid power for satellite applications. These space solar cells were several thousand times more expensive than they are today, but solar cells became an interesting scientific alternative to the rapidly expanding silicon transistor development with several potentially specialized markets. It took the oil crisis in the 1970s to focus world attention on the desirability of alternate energy sources for terrestrial use, which in turn promoted the investigation of photovoltaics as a means of generating terrestrial power. Although the oil crisis proved short-lived and the financial incentive to develop solar cells abated, solar cells had entered the market as a power generating technology. Their application and advantages were quickly recognized and prompted the development of the terrestrial photovoltaics industry. Small scale transportable applications (such as calculators and watches) were utilised and remote power applications began to benefit from photovoltaics.

In the 1980s research into silicon solar cells paid off and solar cells began to increase their efficiency. In 1985 silicon solar cells achieved the milestone of 20% efficiency.

Over the following decade, the photovoltaic industry experienced steady growth rates between 15 % and 20 %, largely promoted by the remote power supply market. The year 1997 saw a growth rate of 38 % and today solar cells are recognized not only as a means for providing power and increased quality of life to those who do not have grid access, but they are also a means of significantly diminishing the impact of environmental damage caused by conventional electricity generation in advanced industrial countries.

Of the different renewable energies, solar energy is by far the most abundant, accounting for more than 99 % of the total possible power from all renewable resources. The average amount of solar power striking the whole of Earth's surface (including cloud cover and night-time) is about 95 000 TW, which is more than 5000 times higher than our current energy needs (illustrated in Figure 1.3). The great challenge is to find a cost-effective method to harness efficiently just a small fraction of this vast supply of power [4].

**Challenges with solar energy** One of the main issues with solar energy is that sunlight is not very concentrated, which necessitates devices with a large area in order to capture significant amounts of power. For example, to produce the predicted 43 TW needed by 2100 with solar energy alone, devices operating at 10 % efficiency would be required with a total active area of approximately 2.3 million km<sup>2</sup>. To put things into comparison, this is six times greater than the size of Germany. However, despite being a very large number, it amounts to just a fraction of the Sahara desert ( $\approx 24$  %), and with the increased solar insolation of the Sahara versus the global average, the area required would be substantially reduced [4].

There are other suitable areas around the world where solar conversion facilities can be constructed, but this simple calculation shows that the amount of solar power available can easily meet our current and future energy needs. In order for any technology to be implemented on such a large scale, however, cheap and highly abundant materials must be used to construct the operating devices. Furthermore, the fabrication costs of the devices, including processing of the raw materials, must be kept as low as possible [5].

**The search for suitable materials** One of the turning points for renewable energy sources is the so-called grid parity, which occurs when an alternative energy source can generate power at a levelled cost of electricity that is less or equal to the price of power from the electricity grid. This also implied that an energy source becomes suitable for widespread development without the need to be subsidised or government supported. For photovoltaic systems to reach grid parity, further price reductions are required,

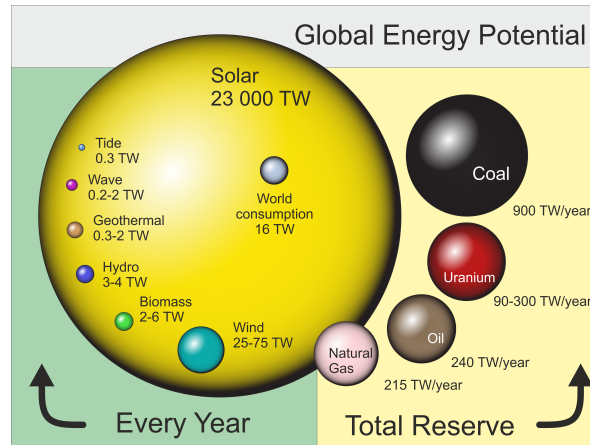


Figure 1.3: Comparison of finite and renewable energy source available on Earth.

together with the up-scaling of the production processes or novel PV concepts based on cheaper materials and low-cost deposition methods [6]. Nowadays, active research is being undertaken to find new, suitable, and efficient materials for PV applications.

Amongst the wide variety of materials, copper oxides are promising candidates for low cost solar energy conversion particularly due to their abundance, low extraction cost, simple fabrication process, and high absorption potential. Standard PV conversion efficiencies for single junction solar cells of copper oxides predict about 20% for  $\text{Cu}_2\text{O}$  and 30% for  $\text{CuO}$  [7] (based on standard Shockley-Queisser selection metric [8]). However, experimental data yields value for a whole order of magnitude lower.

The main objective of the work described in this thesis is to assess the photovoltaic potential of copper oxide semiconductors, evaluate parameters within the material's crystal structure that affect effective light capture, and explore tunability via the incorporation of intrinsic and extrinsic dopants.

**Overview** This thesis is organized as follows. In Chapter 2 the basic ideas behind density functional theory are outlined upon which the majority of calculations were performed within the scope of this work. Furthermore, the concepts underpinning the operation of solar cells are presented as well as the key quantities regarding the occurrence and modelling of defects in actual materials. Chapter 3 describes the ground state properties of three copper oxide compounds as well as their initial photovoltaic potential. The influence of transition metal dopants, substitutionally incorporated on the cation site, is discussed in Chapter 4. Towards the end of the chapter, the effect on the electronic and optical properties is being assessed as well as the improved conversion efficiencies discussed. Chapter 5 deals with a comparison of different theoretical models for  $\text{CuO}$  as well as their validity. After that, possible intrinsic defects occurring in  $\text{CuO}$  are presented and the prospect of tuning the conductivity as  $n$ -type or  $p$ -type

elucidated. A similar analysis is performed in Chapter 5, where first the ground state parameters of  $\text{Cu}_4\text{O}_3$  are analysed and the stability range assessed on top of that.

## Methodological aspects

*"Essentially, all models are wrong, but some are useful."*

---

George E. P. Box, British statistician

This chapter reviews some of the fundamental definitions, expressions, and equations valid for many-body systems of interacting electrons and their simplifications for non-interacting ones. It sets the scene to carry out practical calculations, from the perspective of materials science. Materials science is an interdisciplinary field that deals with the design and discovery of new materials, in particular solids. It incorporates elements of physics, chemistry, and engineering in order to examine and understand materials together with their structure, properties and performance. In materials science, one aims to understand materials fundamentally in order to create new materials with the desired properties, rather than using a trial-and-error approach or discovering materials by chance and exploring their properties afterwards. The basis of materials science involves connecting desired properties and relative performance of a material by characterizing its structure and exploring laws that govern its behaviour. Although characterization is often thought of being undertaken experimentally in laboratories or research centres, a great deal of information, out of which some might be inaccessible to experiments, can be obtained by employing theoretical modelling approaches. There, one creates an accurate description of the phenomena at hand and explores the laws and concepts that play a key role in the background of an operating material. The fundamental basis for understanding materials lies within the concept of electronic structure. The theory of electrons in matter still ranks amongst the greatest challenges of theoretical physics and chemistry. In other words, one relies on developing theoretical approaches and computational methods that can accurately describe the interacting system of many electrons and nuclei and how they determine the macroscopic properties of matter and materials.

## 2.1 Many-body Schrödinger equation

The property which distinguishes one material from another is the behaviour of their electrons. In other words, the electronic structure provides understanding and quantitative description of macroscopically observed phenomena. The properties of matter can be generally categorized into ground state and excited state properties. Ground state properties include equilibrium crystal structure, phase transitions, elastic constants, etc., while excited state properties involve optical properties, thermal excitations, and many more. To fully describe and understand the electronic structure of matter one needs to employ theoretical methods of quantum and statistical mechanics. The starting point for describing matter from a theoretical point of view is the Hamiltonian for a system of electrons and nuclei, which is given by:

$$\hat{H} = -\frac{\hbar^2}{2m} \sum_i \nabla_i^2 - \sum_{i,I} \frac{Z_I e^2}{|\vec{r}_i - \vec{R}_I|} + \frac{1}{2} \sum_{i \neq j} \frac{e^2}{|\vec{r}_i - \vec{r}_j|} - \sum_I \frac{\hbar^2}{2M_I} \nabla_I^2 + \frac{1}{2} \sum_{I \neq J} \frac{Z_I Z_J e^2}{|\vec{R}_I - \vec{R}_J|}, \quad (2.1)$$

where  $Z$  and  $M$  are nuclear charge and mass,  $\vec{r}$  electronic coordinates and  $\vec{R}$  nuclear coordinates,  $\hbar$  reduced Planck's constant,  $m$  electronic mass, and the differential operator nabla defined as  $\nabla = \vec{e}_x \frac{\partial}{\partial x} + \vec{e}_y \frac{\partial}{\partial y} + \vec{e}_z \frac{\partial}{\partial z}$ . Upper and lower case symbols are associated with nuclei and electrons, respectively. In the general Hamiltonian, there is one term that can be regarded as negligible, which is the inverse mass of the nuclei ( $1/M_I$ ) or in other words, the nuclear kinetic energy term. If we set the mass of the nuclei to infinity (corresponding to fixed nuclei in space), then this term can be ignored. This is the so-called Born-Oppenheimer approximation. Ignoring the nuclear kinetic energy, the fundamental Hamiltonian for a system of interacting electrons (in an external potential) can be written as:

$$\hat{H} = \hat{T} + \hat{V}_{\text{ext}} + \hat{V}_{\text{int}} + E_{II}, \quad (2.2)$$

where the kinetic energy operator for the electrons  $\hat{T}$  is defined as:

$$\hat{T} = -\frac{\hbar^2}{2m} \sum_i \nabla_i^2, \quad (2.3)$$

$\hat{V}_{\text{ext}}$  is the Coulomb attraction (potential energy) between the electrons and the nuclei,

$$\hat{V}_{\text{ext}} = \sum_{i,I} \frac{Z_I e^2}{|\vec{r}_i - \vec{R}_I|}, \quad (2.4)$$

$\hat{V}_{\text{int}}$  is the electron-electron Coulomb repulsion,

$$\hat{V}_{\text{int}} = \frac{1}{2} \sum_{i \neq j} \frac{e^2}{|\vec{r}_i - \vec{r}_j|}, \quad (2.5)$$

and the term  $E_{II}$  is the classical interaction of the nuclei with one another. The fundamental equation governing a non-relativistic quantum system is the time-independent Schrödinger eigenvalue equation:

$$E\psi(\{\vec{r}_i\}) = \hat{H}\psi(\{\vec{r}_i\}), \quad (2.6)$$

where  $\psi(\{\vec{r}_i\}) = \psi(\vec{r}_1, \dots, \vec{r}_N)$  is a  $3N$  dimensional many-body wave function for the considered electronic system and  $E$  the total energy. By solving equation 2.6 one would obtain the ground state wave function  $\psi_0$ , the state with the lowest energy, and would be able to calculate any equilibrium property of interest. This can be summarized in the following sequence:

$$\hat{V}_{\text{ext}} \xrightarrow{\text{Schr.Eq.}} \psi(\vec{r}_1, \dots, \vec{r}_N) \xrightarrow{\langle \psi | \dots | \psi \rangle} \text{observables},$$

i.e., one specifies the initial state of the system by choosing  $\hat{V}_{\text{ext}}$ , "inserts" it into the Schrödinger equation, obtains the eigenvalues and eigenvectors for that equation, and then calculates observables by taking expectation values of operators with this wave function. One amongst the mentioned observables is the electron density  $n(\vec{r})$ , which plays a central role in electronic structure theory:

$$n(\vec{r}) = N \int d^3r_2 \int d^3r_3 \dots \int d^3r_N \psi^*(\vec{r}, \vec{r}_2, \dots, \vec{r}_N) \psi(\vec{r}, \vec{r}_2, \dots, \vec{r}_N). \quad (2.7)$$

Similarly, the total energy of the system is given as the expectation value of the Hamiltonian (assuming the wave function is normalized,  $\langle \psi | \psi \rangle = 1$ ):

$$E = \langle \psi | \hat{H} | \psi \rangle \equiv \langle \hat{H} \rangle = \langle \hat{T} \rangle + \langle \hat{V}_{\text{int}} \rangle + \int d^3r V_{\text{ext}}(\vec{r}) n(\vec{r}) + E_{II}, \quad (2.8)$$

To solve equation (2.6) exactly is an extremely formidable task, due to the fact that the problem of finding the ground state scales exponentially with the number of electrons. Furthermore, the complete wave function contains more information than one might need to know about a given system. This is illustrated in a famous example by Gross *et al* [9], where the storage of the ground state of an oxygen atom is considered (excluding spin). The oxygen atom has eight electrons, hence the ground state wave function depends on 24 coordinates. Taking a grid of ten points for each coordinate yields  $10^{24}$  numbers which are required to represent that wave function. Assuming one wishes to store that wave function on DVD's, the amount of DVD's required would be sufficient

to create a tower (by stacking them on top of each other) that reaches the Moon. Instead, one is usually interested in quantities that can be extracted from the wave function, such as the probability densities or energy levels. Hence, a method that could give such quantities directly, bypassing the need to calculate the full wave function, would be highly attractive. Fortunately, such a method exists and its concepts are outlined in the following paragraphs.

## Independent-electron approximations

There are two basic independent-particle approaches that may be classified as "non-interacting" and "Hartree-Fock." Both assume that electrons are uncorrelated (do not interact with each other) except that they must obey the exclusion principle, which states that two electrons cannot occupy the same electronic state. Hartree-Fock (HF) includes the electron-electron Coulomb interaction in the energy expression itself, neglecting the correlation in the true wave function due to those interactions. On the other hand, "non-interacting" theories have some effective potential that incorporates a portion of the real interaction, but there is no explicit interaction term in the effective Hamiltonian. The latter approach is commonly referred to as "Hartree" or "Hartree-like." Concerning modern calculations, all calculations following the Kohn-Sham method involve a non-interacting Hamiltonian with an effective potential chosen to incorporate exchange and correlation effects approximately.

The HF approach is to minimize the total energy expression with respect to all degrees of freedom in the wave function with the restriction that has the form of a (antisymmetric) Slater determinant. This leads to the HF equations, which are omitted from this discussion (the reader is referred to texts like [10], [11]). In general, to solve the HF equations, one must introduce a basis, in which the energy can be written in terms of the expansion coefficients of the orbitals and the integrals involving the basis functions. This leads to the Roothan and Pople-Nesbet equations, which are widely used in quantum chemistry.

## 2.2 Density functional theory

Density functional theory (DFT), as it is widely used nowadays, originates from two famous papers, one written by P. Hohenberg and W. Kohn in 1964 [12] and the second by W. Kohn and L. J. Sham in 1965 [13]. The work of Hohenberg and Kohn (HK) is based upon two theorems. The first theorem states that the ground state particle density,  $n_0(\vec{r})$ , uniquely determines the external potential,  $V_{\text{ext}}(\vec{r})$ , for a given system of interacting particles. The external potential determines uniquely the many-body wave

function and therefore all properties of the system are fully known once the ground state density is determined. The second theorem infers that, in the ground state, the density defines uniquely the total energy. Thus, the total energy is a functional of the density (denoted with square brackets):

$$E_{\text{HK}}[n] = T[n] + E_{\text{int}}[n] + \int d\vec{r} V_{\text{ext}}(\vec{r}) n(\vec{r}). \quad (2.9)$$

The exact ground state of the system is the global minimum of this functional and the density that minimizes this functional is the ground state density. However, the major drawback with these theorems is that they do not offer a way of finding the functional or performing practical calculations. Ever since then, a number of very useful approximations have been developed.

The approach (*ansatz*) proposed by Kohn and Sham (KS) is to assume that the ground state density of the interacting many-body system is equal to that of an auxiliary system of non-interacting particles. The rewritten form of the HK expression for the ground state energy (2.9) reads:

$$E_{\text{KS}} = \underbrace{\frac{1}{2} \sum_i \int d\vec{r} |\nabla \psi_i(\vec{r})|^2}_{\text{Kinetic energy}} + \underbrace{\int d\vec{r} V_{\text{ext}}(\vec{r}) n(\vec{r})}_{\text{External potential}} + \underbrace{\frac{1}{2} \int d\vec{r} d\vec{r}' \frac{n(\vec{r})n(\vec{r}')}{|\vec{r} - \vec{r}'|}}_{\text{Hartree energy}} + \underbrace{E_{\text{XC}}[n]}_{\text{XC energy}}. \quad (2.10)$$

Here the newly introduced terms are the independent-particle kinetic energy,  $T_S$ , the exchange-correlation energy,  $E_{\text{XC}}$ , and the Hartree energy,  $E_{\text{Hartree}}$ . The Hartree energy is defined as the classical Coulomb interaction energy of the electron density interacting with itself, while the XC energy term contains all the many-body effects of exchange and correlation grouped together. Equation (2.10) simply breaks down the unknown energy functional of the ground state density into the sum of known contributions arising from the independent-particle (electron) system and an unknown term, the exchange and correlation energy. Effectively, one has collected all the unknown parts into one place, which allows easier manipulation. If we were to know this universal functional, the exact ground state energy and density of the many-body interacting electron problem could be found by solving the Kohn-Sham equations for independent-particles. Hence, the KS method provides a feasible approach of calculating the ground state properties of a many-body system, to the extent of how well the approximation of the  $E_{\text{XC}}$  describes the true exchange correlation energy.

The Kohn-Sham (Schrödinger-like) equations follow:

$$\begin{aligned}
H_{\text{KS}} \phi_i(\vec{r}) &= \varepsilon_i \phi_i(\vec{r}) \\
\left(-\frac{\hbar^2}{2m} \nabla^2 + V_{\text{KS}}(\vec{r})\right) \phi_i(\vec{r}) &= \varepsilon_i \phi_i(\vec{r}),
\end{aligned} \tag{2.11}$$

where  $\varepsilon_i$  are eigenvalues,  $\phi_i$  KS orbitals,  $H_{\text{KS}}$  the effective Hamiltonian, and  $V_{\text{KS}}$  the effective KS potential, which reads:

$$\begin{aligned}
V_{\text{KS}}(\vec{r}) &= V_{\text{ext}}(\vec{r}) + \frac{\delta E_{\text{Hartree}}}{\delta n(\vec{r})} + \frac{\delta E_{\text{XC}}}{\delta n(\vec{r})} \\
&= V_{\text{ext}}(\vec{r}) + V_{\text{Hartree}}(\vec{r}) + V_{\text{XC}}(\vec{r}).
\end{aligned} \tag{2.12}$$

where the term labelled  $V_{\text{XC}}$  is called the exchange and correlation potential. These independent-particle equations (2.11)-(2.12) need to be solved self-consistently with the resulting density. This set of equations constitutes a very powerful tool for calculating many properties of materials starting from the first principles of quantum mechanics (also known as "*ab-initio*" techniques, meaning without having to rely on empirical parameters). Within the exact  $E_{\text{XC}}$  and  $V_{\text{XC}}$  all many-body effects are in principle included and the exact ground state energy and density can be derived from the functional  $E_{\text{XC}}$ . However, this functional is not known and the problem transforms into building useful approximations for  $E_{\text{XC}}$ .

## Approximations for the exchange correlation functional

The simplest method of describing the XC energy of an electronic system is to use the local-density approximation (LDA), already postulated by Kohn and Sham in their original work [13]. In the LDA, the  $E_{\text{XC}}$  of an electronic system is constructed by assuming that it is equal to the  $E_{\text{XC}}$  per electron in a homogeneous electron gas and has the same destiny as the gas at point  $\vec{r}$ :

$$E_{\text{XC}}[n(\vec{r})] \equiv \int \varepsilon_{\text{XC}}^{\text{LDA}}(\vec{r}) n(\vec{r}) d\vec{r}, \tag{2.13}$$

with

$$\varepsilon_{\text{XC}}^{\text{LDA}}(\vec{r}) = \varepsilon_{\text{XC}}^{\text{hom}}[n(\vec{r})]. \tag{2.14}$$

The LDA assumes that the XC energy functional is purely local. Various parametrizations exist for LDA, each giving results for total energy very similar to each other. However, LDA functionals have not been used within this work, there are listed for

rather historical reasons.

The success of LDA (or LSDA as the spin dependent version) has stimulated ideas for constructing improved functionals, such as the generalized-gradient approximation (GGA). The GGA includes gradient corrections, thus making the  $E_{XC}$  a functional of the density and its gradient:

$$E_{XC}^{GGA}[n(\vec{r})] = \int d\vec{r} n(\vec{r}) F_{XC}[n(\vec{r}), \nabla n(\vec{r})] \quad (2.15)$$

where  $F_{XC}$  is a dimensionless parameter upon which different forms of the general gradient approximation can be obtained. Numerous formulations have been proposed, out of which some are listed below:

- Becke (B88)
- Perdew and Wang (PW91)
- Lee-Yang-Parr (LYP)
- Perdew, Burke, Ernzerhof (PBE)
- revised Perdew, Burke, Ernzerhof (RPBE)
- Perdew, Burke, Ernzerhof revised for solids (PBEsol).

Calculations presented in this thesis have been carried out using the PBE functional without further modifications as provided within the Vienna Ab-initio Simulation Package.

## The LDA+ $U$ method and hybrid functionals

One of the major problems with the KS approach is that no systematic way has been developed to improve the functionals for exchange and correlation. Most severe problems occur in materials where electrons tend to be localized or interact strongly. This is a particular case for transition metal oxides (e.g. NiO, CoO, CuO, etc.) and rare earth elements and compounds. Several methods have been developed over the years to incorporate some of the physical phenomena that are expected to be important in such materials. Two of those are self-interaction corrections (SIC) and "LDA+ $U$ ", attempting to circumvent the unphysical self-interaction present in many XC functionals. The self-interaction of an electron with itself present in the Hartree term is exactly cancelled when the exchange interaction is treated exactly, such as in Hartree-Fock or EXX (for more details see [14]), which is not the case for approximations to the  $E_{XC}$ .

The acronym "LDA+ $U$ " covers methods that involve LDA- or GGA-type calculations coupled with an additional orbital-dependent interaction. This interaction has a

form similar to that of the Hubbard "U" and is usually considered for highly localized atomic-like orbitals on the same site ( $d$  or  $f$  electrons mostly). The effect of this additional term is to shift the localized orbitals relative to other ones, thereby correcting errors resulting from pure LDA or GGA calculations. LDA/GGA approximations do not properly describe the energetic position of these narrow bands due to their high degree of localization, compared to more delocalized  $s$  and  $p$  bands. In LDA+ $U$ , the electrons are separated into localized ones for which the Coulomb repulsion  $U$  is taken into account via a Hubbard-like term in a model Hamiltonian, and delocalized or itinerant electrons that are assumed to be well described by the usual orbital-independent one-electron potential in LDA or GGA [15].

"LDA+ $U$ " is mostly utilized for cases where the spin states are described wrongly or the value or the energy gap is too small or vanishing. Within this work, the LDA+ $U$  approach introduced by Dudarev *et al* [16] was used, where the LDA+ $U$  functional is given by the following expression:

$$E_{\text{LSDA}+U} = E_{\text{LSDA}} + \frac{(U - J)}{2} \sum_{\sigma} (n_{m,\sigma} - n_{m,\sigma}^2), \quad (2.16)$$

where  $U$  specifies the strength of the effective on-site Coulomb interactions,  $J$  the strength of the effective on-site exchange interactions, and  $n_{m,\sigma}$  the occupation number of the  $m$ -th  $d$  state. Within the Dudarev approach,  $U$  and  $J$  do not enter the expression separately, thus only the difference ( $U - J$ ) is meaningful and often labelled as  $U_{\text{eff}}$ . Furthermore, the  $U_{\text{eff}}$  (or  $U$  and  $J$  in different approaches as the Anisimov *et al* [17] or Liechtenstein *et al* [18]) can be calculated from first principles, but more often in practice it is treated as a parameter, i.e., adjusted to reach agreement with experiment up to an extent: equilibrium volume, magnetic moment, band gap, lattice constants, etc.

Another class of functionals commonly used is called "hybrid" because they are a combination of orbital-dependent Hartree-Fock and an explicit local (LDA) or semi-local (GGA) density functional. This way a portion of the exact Hartree-Fock exchange is introduced into the system, cancelling partially the electron self-interaction present in the LDA- or GGA-type of approximation to the XC functional. Furthermore, the system is treated as a whole, compared to the LDA+ $U$  approach where individual orbitals are influenced by separate on-site potentials. Hybrid functionals achieved popularity due to the fact that they provide a simple scheme for improving the accuracy of many calculated properties, e.g. atomization energies, bond lengths, vibrational frequencies, etc. However, the main drawback is increased computational time and cost associated with those type of calculations. A few of the most popular ones and the ones used within this work are presented below.

A well known hybrid functional popular amongst the quantum chemistry community is the B3LYP functional (Becke's 3 parameter functional, combined with the non-local correlation of Lee-Yang-Parr (LYP)):

$$E_X^{\text{B3LYP}} = 0.8E_X^{\text{LDA}} + 0.2E_X + 0.72\Delta E_x^{\text{B88}} \quad (2.17)$$

$$E_C^{\text{B3LYP}} = 0.19E_C^{\text{VNM3}} + 0.81E_C^{\text{LYP}}, \quad (2.18)$$

where  $E_X^{\text{B3LYP}}$  and  $E_C^{\text{B3LYP}}$  are the B3LYP exchange and correlation energy contributions, respectively.  $E_X^{\text{B3LYP}}$  consists of 80% of LDA exchange plus 20% of non-local Fock exchange, and 72% of the gradient corrections of the Becke88 exchange functional.  $E_C^{\text{B3LYP}}$  consists of 81% LYP correlation energy, and 19% of the (local) Vosko-Wilk-Nusair (VWN) correlation functional.

Another popular hybrid functional is the PBE0 functional, which is defined as:

$$E_{\text{XC}}^{\text{PBE0}} = 0.25E_X + 0.75E_X^{\text{PBE}} + E_C^{\text{PBE}}, \quad (2.19)$$

where  $E_X^{\text{PBE}}$  and  $E_C^{\text{PBE}}$  denote the exchange and correlation part of the PBE density functional, respectively.

A wide variety of functionals are labelled as range-separated hybrid (RSH) functionals, where the amount of HF exchange included depends on the distance between electrons. A particular RSH functional used within the scope of this thesis is the HSE functional introduced by Heyd, Scuseria and Ernzerhof [19–21], which takes the following expression:

$$E_{\text{XC}}^{\text{HSE}} = 0.25E_X^{\text{SR}}(\mu) + 0.75E_X^{\text{PBE,SR}}(\mu) + E_X^{\text{PBE,LR}}(\mu) + E_C^{\text{PBE}}. \quad (2.20)$$

The separation of the electron-electron interaction into short- and long-range parts is labelled SR and LR, respectively, and is realized in the exchange interaction. Electron correlation is represented by the corresponding part of the PBE density functional. The parameter that defines the range separation is labelled  $\mu$  and was shown to be optimal for approximately  $0.2 - 0.3 \text{ \AA}^{-1}$ . Within this work, the default value  $\mu = 0.2 \text{ \AA}^{-1}$  of the HSE06 functional was kept constant.

## 2.3 Basis sets and pseudopotentials

In the preceding paragraphs it was shown how certain observables of the many-body problem can be mapped into equivalent observables in an effective one-particle problem. However, there still remains the formidable task of handling an infinite number

of non-interacting electrons moving in the potential created by an infinite number of nuclei (or ions). Two main difficulties to overcome are:

- To calculate the wave function for each electron (whose number is infinite)
- To expand each electronic wave function in an infinite basis set (since the wave function extends over the entire solid).

Both problems can be tackled efficiently by performing calculations on periodic systems and applying Bloch's theorem to the electronic wave function.

In order to introduce Bloch's theorem, it is useful to look at solids from the point of their structure and symmetry. A crystal is defined as an ordered state of matter constructed by infinite repetition of identical "building" blocks - atoms. A group of atoms (including their position and type) is called the basis and the set of mathematical points, to which the basis is attached, is called the lattice. A lattice in three dimensions can be defined by three lattice vectors  $\vec{a}_1, \vec{a}_2, \vec{a}_3$ , such that the arrangement of atoms in a crystal looks the same from points  $\vec{r}$  and  $\vec{r}'$  connected by integral multiple translations:  $\vec{r}' = \vec{r} + u_1\vec{a}_1 + u_2\vec{a}_2 + u_3\vec{a}_3$ , where  $u_1, u_2$ , and  $u_3$  are arbitrary integers. Vectors satisfying this condition (for a suitable choice of  $u$ 's) define the primitive translation vectors  $\vec{a}_i$ , often used to define crystal axes of a system.

The parallelepiped defined by primitive axes is called a primitive (unit) cell. A primitive cell has the minimum volume and fills all space by repetition of suitable crystal translation operations. The bit that defines a primitive cell further is that it always contains one lattice point per cell. Furthermore, a non-primitive cell can be defined, which contains more than one lattice point. Examples of such cells include conventional or magnetic cells, which often have a more obvious relation with some symmetry operations or define the right magnetic properties of a material.

The periodicity of a crystal leads to a translational invariance of any local physical properties under  $\vec{T} = u_1\vec{a}_1 + u_2\vec{a}_2 + u_3\vec{a}_3$ , such as the charge concentration, density of the electrons, magnetic moment density, etc. In other words, physical properties within a crystal, such as the electron density  $n(\vec{r})$ , are periodic functions of  $\vec{r}$ , with periods  $\vec{a}_i$  where  $i$  depends on the dimensions of the system:

$$n(\vec{r} + \vec{T}) = n(\vec{r}). \quad (2.21)$$

Such periodic functions can be represented by a Fourier transform in terms of Fourier components at wavevectors  $\vec{k}$  defined in reciprocal space. Points of the reciprocal lattice tell us the allowed terms in the Fourier series. Primitive vectors of the reciprocal lattice  $\vec{b}_i$  are defined through the relation:

$$b_1 = 2\pi \frac{\vec{a}_2 \times \vec{a}_3}{\vec{a}_1 \cdot \vec{a}_2 \times \vec{a}_3}; \quad b_2 = 2\pi \frac{\vec{a}_3 \times \vec{a}_1}{\vec{a}_1 \cdot \vec{a}_2 \times \vec{a}_3}; \quad b_3 = 2\pi \frac{\vec{a}_1 \times \vec{a}_2}{\vec{a}_1 \cdot \vec{a}_2 \times \vec{a}_3}, \quad (2.22)$$

together with the following condition:

$$\begin{aligned} \vec{b}_i \cdot \vec{a}_j &= 2\pi \delta_{ij}, \\ \delta_{i,j} &= \begin{cases} 1, & \text{if } i = j \\ 0, & \text{if } i \neq j, \end{cases} \end{aligned} \quad (2.23)$$

while points in the reciprocal lattice are mapped by the set of vectors:

$$\vec{G} = v_1 \vec{b}_1 + v_2 \vec{b}_2 + v_3 \vec{b}_3, \quad (2.24)$$

where  $v_i$  are integers and  $\vec{G}$  the reciprocal lattice vector.

Every crystal structure has two lattices associated with itself, the crystal lattice and the reciprocal lattice. Can the reciprocal lattice be seen? Certainly. For instance, the diffraction pattern of a crystal is a map of the reciprocal lattice of the crystal, while the very fine microscopic image would map the crystal structure in real space. Those two lattices are closely connected, thus, when we apply a transformation to the direct crystal lattice, the reciprocal lattice follows, through equation (2.22).

Having introduced some simple concepts of periodicity in crystalline solids, further properties governing the electronic states can be explored. This leads to Bloch's theorem, which states that each electronic wave function in a periodic solid can be written as a product between the cell periodic and a wave-like part:

$$\psi_i(\vec{r}) = e^{i\vec{k} \cdot \vec{r}} \cdot f_i(\vec{r}), \quad (2.25)$$

where, by imposing periodic boundary conditions, it can be shown that the wavevector  $\vec{k}$  must have the form (for a 3D system):

$$\vec{k} = \frac{m_1}{N_1} \vec{b}_1 + \frac{m_2}{N_2} \vec{b}_2 + \frac{m_3}{N_3} \vec{b}_3, \quad (2.26)$$

with  $m_i$  being integers,  $\vec{b}_i$  primitive vectors of the reciprocal space (as defined with (2.22)), and  $N_i$  the number of primitive cells in the crystal along direction  $i$ . If we now look for the solution of the Schrödinger equation for a single electron:

$$H\psi = \left( -\frac{\hbar^2}{2m} \nabla^2 + U(\vec{r}) \right) \psi = \varepsilon \psi, \quad (2.27)$$

that has the Bloch form (2.25),  $\vec{k}$  is fixed and  $f$  has the periodicity of the Bravais lattice, we find that  $f$  is determined by the eigenvalue problem:

$$H_{\vec{k}} f_{\vec{k}}(\vec{r}) = \left[ \frac{\hbar^2}{2m} \left( \frac{1}{i} \nabla + \vec{k} \right)^2 + U(\vec{r}) \right] f_{\vec{k}}(\vec{r}). \quad (2.28)$$

Because of the periodicity in  $f_{\vec{k}}(\vec{r})$  equation (2.28) can be restricted to a single primitive cell of the crystal. Moreover, due to the fixed finite volume, for each  $\vec{k}$ -point an infinite family of solutions with discretely spaced eigenvalues can be expected, labelled with the band index  $n$ . I.e., in a periodic potential (such as in a crystalline compound), each energy level varies continuously with respect to  $\vec{k}$ . This leads to a description of energy levels of an electron in a periodic potential in terms of a family of continuous functions  $\varepsilon_{n\vec{k}}$  (or  $\varepsilon_n(\vec{k})$ ), each having the periodicity of the reciprocal lattice. Information contained within these functions is referred to as the *band structure* of the solid. For each  $n$ , the set of electronic levels specified by  $\varepsilon_{n\vec{k}}$  is called an *energy band*.

Bloch's theorem changes the problem of calculating an infinite number of electronic wave functions to one of calculating a finite number of electronic wave functions at an infinite number of  $\vec{k}$  points. In theory, to compute a DFT ground state, one should integrate over all the  $\vec{k}$ -points, which would imply an infinite number of calculations to perform. However, it is possible to approximate the infinite integration by a sum over a finite number of convenient  $\vec{k}$ -points, since the wave function of  $\vec{k}$ -points that are very close together will be almost identical. Various methods have been devised for calculating the total energy of an insulator or semiconductor by calculating the electronic states at special sets of  $\vec{k}$ -points in the Brillouin zone. The method employed within the VASP software utilized in this work is the scheme by Monkhorst and Pack [22]. For metals, the situation complicates slightly, due to the requirement for a dense set of  $\vec{k}$ -point to sample the Fermi surface precisely.

## Plane waves

The basis set used within the scope of this work consists of plane waves, as implemented in the DFT code VASP. Following Bloch's theorem, the cell periodic part of the wave function can be expanded using a basis set consisting of a discrete set of plane waves whose wave vectors are reciprocal lattice vectors of the crystal:

$$f_i(\vec{r}) = \sum_{\vec{G}} c_{i,\vec{G}} e^{i\vec{G}\cdot\vec{r}}, \quad (2.29)$$

where  $\vec{G}$  is defined with (2.24). Therefore each electronic wave function can be written as a sum of plane waves:

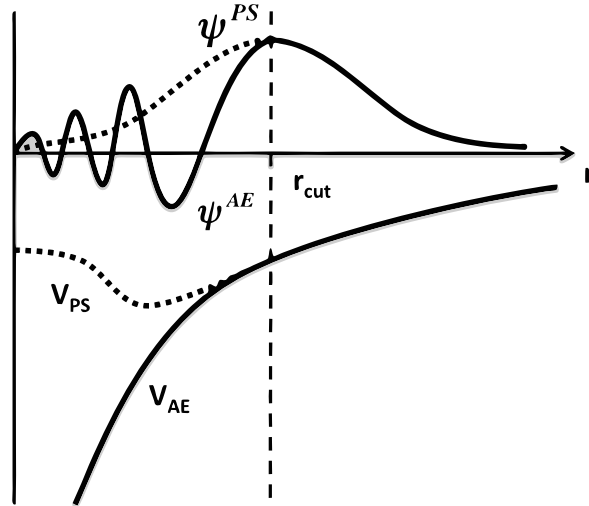


Figure 2.1: Pseudopotentials - Schematic illustration of an all-electron (solid line, labelled  $V_{AE}$ ) and pseudo-electron (dashed, labelled  $V_{PS}$ ) potential and their corresponding wave function ( $\psi^{AE}$  and  $\psi^{PS}$  for the all-electron and pseudo wave function, respectively). The point where the all electron and pseudo-electron value match is denoted with  $r_{cut}$ .

$$\psi_i(\vec{r}) = \sum_{\vec{G}} c_{i,\vec{k}+\vec{G}} e^{i(\vec{k}+\vec{G})\cdot\vec{r}}. \quad (2.30)$$

Once again, at least in principle, an infinite number of plane waves would be needed to expand the electronic wave functions in equation (2.30). However, the plane wave coefficients  $c_{i,\vec{k}+\vec{G}}$  with small kinetic energy are typically more important than those with large kinetic energy. Therefore, the plane wave basis can be truncated to include a finite number of plane waves with a kinetic energy less than a chosen cutoff. This truncation leads to an error in the computed total energy of the system, which can be reduced by increasing the cutoff energy until convergence in the energy has been reached.

## Pseudopotentials

Despite the fact that Bloch's theorem states how the electronic wave function can be expanded using a discrete set of plane waves, a plane wave basis set suffers from the problem of a very large number of plane waves that are needed to expand the core orbitals and to follow the oscillations of the wave functions of the valence electrons near the core. Using this approach, a large basis set would be required to perform a so called *all-electron* calculations, together with a great deal of computational time. The pseudopotential approximation comes here handy and allows the electronic wave function to be expanded using a much smaller plane wave basis set.

It builds on the fact that most physical properties of a solid are much more dependent on the valence rather than the core electrons. By removing the core electrons

and replacing them (and their strong ionic potential) by a weaker pseudopotential that acts on a set of pseudo wave functions rather than the true valence wave functions, one can effectively exploit these properties. This scheme is illustrated in Figure 2.1.

### Densities of state

An important quantity in materials science is the density of states (DOS) per unit of energy (and per unit of volume in extended matter), which is defined through the following expression:

$$\rho(E) = \frac{\Omega_{\text{cell}}}{(2\pi)^d} \int_{\text{BZ}} d\vec{k} \delta(\varepsilon_{n\vec{k}} - E), \quad (2.31)$$

where the integration runs over any primitive cell, while  $\Omega_{\text{cell}}$  denotes the volume of the considered unit cell and  $d$  the dimensionality of the system.

### 2.3.1 The band gap and its "problem"

The exchange-correlation potential  $V_{\text{XC}}(\vec{r})$  is the functional derivative of  $E_{\text{XC}}$ , which can be written as [14]:

$$V_{\text{XC}}(\vec{r}) = \varepsilon_{\text{XC}}([n], \vec{r}) + n(\vec{r}) \frac{\delta \varepsilon_{\text{XC}}([n], \vec{r})}{\delta n(\vec{r}, \sigma)} \quad (2.32)$$

where  $\varepsilon_{\text{XC}}([n], \vec{r})$  is defined through  $E_{\text{XC}}[n] = \int d\vec{r} n(\vec{r}) \varepsilon_{\text{XC}}([n], \vec{r})$  and is a functional of the density  $n$ . The exact  $V_{\text{XC}}(\vec{r})$  is not a potential that can be identified with interactions between particles. The second term in equation (2.32), sometimes called the "response potential", is due to the change in the exchange-correlation hole with respect to the density. In a semiconductor or insulator, this derivative is discontinuous at a band gap where the nature of the states changes discontinuously as a function of  $n$ . This leads to the so-called "derivative discontinuity" whereby the KS potential for all the electrons in a crystal shifts by a constant amount when a single electron is added. In other words, even in the exact KS theory, the difference between the highest occupied and lowest unoccupied eigenvalues should not equal the actual band gap value.

In order to examine further the intricacies of the exact Kohn–Sham theory, it is worth taking a step back to familiarize the reader with the terminology first. The energy gap between the highest occupied and lowest unoccupied electronic levels is a critical parameter determining the electronic, optical, response, transport (electrical), and many other properties of a material [23]. It comes in many "flavours", such as the band gap, HOMO–LUMO gap, fundamental gap, optical gap, transport gap – each of them having a specific meaning. Failure to understand the distinction between them causes much of the confusion with the literature, which manifests itself by use

of improper terminology. In a *molecule*, of specific interest are energies associated with the highest occupied molecular level – the **HOMO**, and the lowest unoccupied molecular orbital – the **LUMO**. However, experimentally one measures the process of excitation, which corresponds to the difference in energy between the  $N$ -electron ground state of a molecule and its  $N$ -electron excited state (no change in the total number of electrons) or ionization, which coincides with the energy difference between the  $N$ -electron ground state and its  $(N \pm 1)$ -electron ionized state. For a molecule, the **fundamental gap** is defined as the difference between the ionization potential ( $I$ ) and the electron affinity ( $A$ ):

$$E_{\text{fund}} = I - A. \quad (2.33)$$

The ionization potential (energy) is defined (following the IUPAC nomenclature [24]) as the minimum energy required to eject an electron out of a neutral atom or molecule from its ground state, while the electron affinity is the energy released when an additional electron is attached to a neutral atom or molecule (for schematic illustration see Figure 2.2). Experimentally, it is usually measured via UV photoelectron spectroscopy and electron attachment spectroscopy, while at the computational level it requires the comparison between the total energy of the  $N$ -electron ground state and the  $(N + 1)$ -electron state (to determine  $A$ ) of the  $(N - 1)$ -electron state (to determine  $I$ ). The calculated **HOMO–LUMO gap** only provides an approximation to the fundamental gap with the quality of the approximation depending on the utilized computational methodology.

The optical gap ( $E_{\text{OPT}}$ ) of a molecule is the energy of the lowest electronic transition taking place via absorption of a single photon.  $E_{\text{OPT}}$  is usually much lower than the fundamental gap, as in the excited state the electron and hole remain electrostatically bound to one another. The difference between the optical and fundamental gap is a measure of the electron–hole pair binding energy,  $E_{\text{B}}$ .

In solids, the interatomic interactions broaden the molecular energy levels into electronic bands, with the width of the band depending on the strength of the interaction between atoms. The upper occupied band is then referred to as the valence band (VB) and the lowest unoccupied band as the conduction band (CB). The **band gap** is defined as the energy difference between the top of the VB and the bottom of the CB, i.e., difference between the ionization potential and electron affinity of a material. It is also referred to as the **transport gap**, since it represents the minimum energy needed to create a positive charge carrier somewhere in the material ( $I$ ) minus the energy gained by adding a negative charge carrier elsewhere ( $A$ ). Experimentally, it is often estimated through the combination of ultraviolet photoelectron spectroscopy and inverse photoemission spectroscopy. Thus, the band gap is equivalent, at the

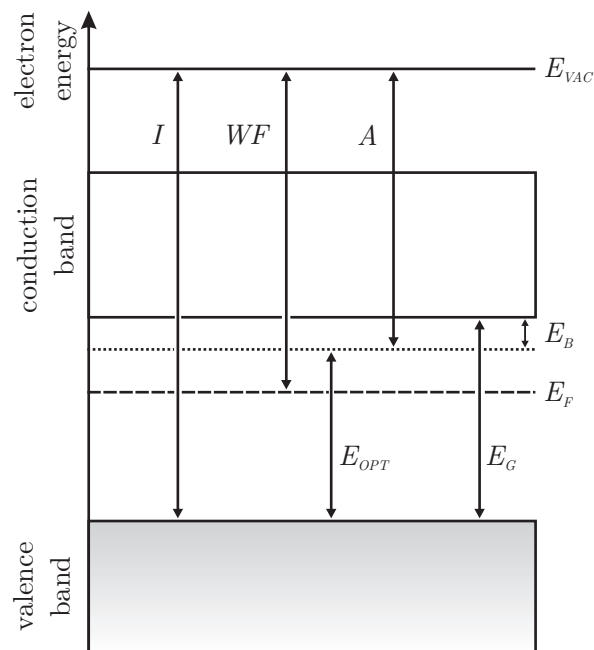


Figure 2.2: Energy diagram of a semiconductor with flat bands to the surface.  $E_{\text{opt}}$  denotes the optical gap,  $E_{\text{B}}$  the exciton binding energy,  $E_{\text{G}}$  the (transport) band gap,  $I$  the electronic ionization potential,  $A$  the electron affinity, and  $E_{\text{F}}$  the Fermi level. Two additional labels occur:  $E_{\text{VAC}}$  and  $WF$  (work function), with the first being the energy level of an electron positioned at rest within a "few nanometers" outside the solid, i.e., the zero kinetic energy with respect to the sample surface and the second being the energy needed to remove an electron from the Fermi level deep inside the material and place it at rest just outside the material.  $E_{\text{VAC}}$  also describes the energy barrier at the surface of a material that prevents electrons from escaping the material [25].

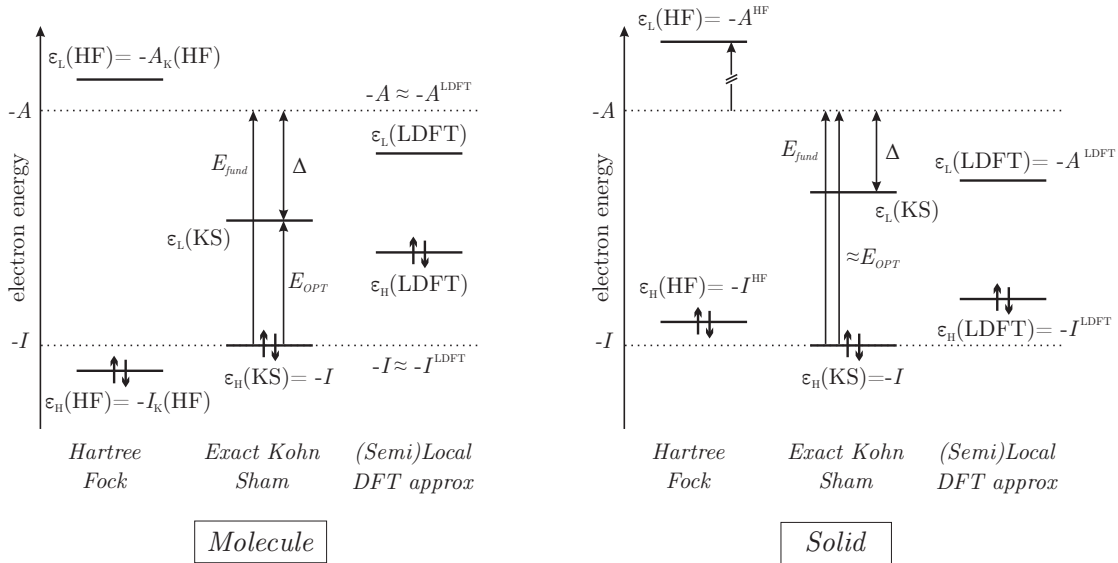


Figure 2.3: Electronic energies for molecules (left) and solids (right) calculated with various models: Hartree–Fock (HF), exact Kohn–Sham (KS), and local and semi–local density functional approximations (LDFT). For molecules (the subscript  $K$  denotes the Koopmans’ approximation): the optical gap is close to the exact KS HOMO–LUMO gap and different from the fundamental gap. LDFT orbital energies are higher compared to exact KS, but approximately for the same amount, so the HOMO–LUMO gap does not change much. The calculated  $I$  and  $A$  from the LDFT model are reasonable approximations to the exact  $I$  and  $A$ . For solids, the HS fundamental gap is much larger than the exact  $I - A$ , with the discrepancies not drawn up to scale. The optical gap is very close to the fundamental gap, while the exact KS HOMO retains the property that it describes  $I$  exactly. The LUMO is below  $A$  by an amount labelled  $\delta$ . The ionization energy and affinity of solids calculated with LDFT are not approximations to the exact  $I$  and  $A$ , compared to the molecular case.

materials level, to the molecular fundamental gap. Note how the band gap is typically smaller than the molecular fundamental gap, as a result of the polarization effects in the solid state. Upon photon absorption in solid state (crystalline) materials, the lowest optical transition defines the **optical gap**. Analogous to the molecular case, it leads to the formation of a bound electron–hole pair, termed an exciton in the context of condensed–matter physics. Again, the difference between the band (transport) gap and the optical gap determines the exciton binding energy,  $E_B$ . In semiconducting crystals,  $E_B$  is rather small (a few meV) so that at room temperature optical excitations directly lead to the formation of free charge carriers (and thus there  $E_{OPT} \approx E_{transport}$ ). Within these definitions, it was assumed that the lowest optical transition involved the transition from the ground state to the lowest excited state, i.e., a direct allowed transition. Complications arise when this transition is either symmetry forbidden or has negligible oscillator strength.

Now, what is “wrong” with the band gap and where does the controversy when reporting calculated values come from? The source of confusion is the relation between the orbital energies of the exact KS one–electron model (and local density approximations) and the  $I$  and  $A$ . This relation between orbital energies and electron attachment

and loss energies is different in different models and further varies between molecules and solids. For *molecules* in the Hartree–Fock (HF) model the HOMO energy is approximately equal to  $-I$ , while in exact KS it is equal to  $-I$ . The LUMO energies are quite different: considerably above  $-A$  in HF, but much lower than  $-A$  in exact KS. The exact KS LUMO is not an approximation to  $-A$ , neither numerically nor physically [26]. In HF, the calculated HOMO–LUMO gap is equal to the fundamental gap, under the premise of frozen ground state orbitals (Koopmans theorem, which does not allow for electronic relaxation effects). On the other hand, the exact KS HOMO–LUMO gap is much smaller than the fundamental gap but is very close to the first excitation energy. A notable difference between the two LUMOs can be deduced: while the (exact) KS LUMO represents excited electrons, the HF one represents added electrons. LDA and GGA approximations to the XC functional yield HOMO and LUMO energies that are typically  $\sim 5$  eV above the exact KS values, while hybrid functionals move the LUMO up from its initial value (close to the optical gap) towards the HF (Koopmans) fundamental gap. For *solids*, the HF model overestimates the fundamental/optical gap in solids due to a too high LUMO (CB bottom) level caused by neglecting the correlation energy. In the exact KS model, the LUMO (VB top) is considerably below  $-A$  and yields the KS band gap considerably below the fundamental gap – widely known as “*the KS band gap problem*”. The aforementioned schematics are illustrated in Figure 2.3.

On the other hand, band gap calculated with local or semi–local density functional theory approximations (LDA or GGA, which are named LDFT within this section) yield gaps similar to the exact KS one, therefore being also placed too low. But the origin of the “LDFT band gap problem” is different from the origin of the “exact KS band gap problem.” The origin of the “LDFT band gap problem” is a combination of the solid state limit (which makes the orbital energy gap equal to the total energy based fundamental gap) and the application of local approximations to delocalized ions. The latter one places the calculated energy of the ions too low, therefore yielding a low fundamental gap. The origin of the “exact KS band gap problem” lies in the fact that the exact KS potential contains the so called exchange–correlation hole potential also for unoccupied orbitals. The exchange–correlation hole describes the reduction of probability for encountering an electron at  $\vec{r}_2$ , given that there is an electron at  $\vec{r}_1$ . Describing the XC hole is out of the scope of this thesis (as one could write a whole new one about its properties). However, it should be noted that the XC hole is an important part of the exact KS potential as it exerts a stabilizing attraction on the virtual KS orbitals which is stronger than the attraction that comes from the very delocalized hole in a delocalized excitation (no excitons formed) [26]. For molecules, both the effects of the XC hole and the hole from the electron/hole pair are similar

due to small system dimensions.

How does one then compare values or make sense of those calculated from density functional theory approximations? Perhaps the most striking property of the frontier orbital energies in solids within local, semi-local, or hybrid approximations to the XC functional is that they are equal to the ionization energy and electron affinity if calculated from total energies with the same approximation. I.e., the HOMO–LUMO gap in extended systems is equal to the total energy based fundamental gap, when the same density functional approximation is used [27]:

$$\varepsilon_{\text{L}}^{\text{LDFT/h-DFT}} - \varepsilon_{\text{H}}^{\text{LDFT/h-DFT}} = I^{\text{LDFT/h-DFT}} - A^{\text{LDFT/h-DFT}}, \quad (2.34)$$

where LDFT and h-DFT are local (semi-local) and hybrid approximations to the XC functional. Hybrid functionals offer a way of exploiting the too large HF band gap and the too small (semi-)local DFT band gap by modifying the LDFT exchange and adding a percentage of the exact HF exchange. This way the band gap can be increased in order to approximate the fundamental gap. Results obtained via this hybrid approach are often very useful due to the cancellation of errors in the local approximation (within LDFT) and neglecting correlation (in HF). In practice, one needs to apply different mixing amounts to different solids in order to accurately reproduce the physics/chemistry of the system under consideration.

## 2.4 The physics of solar cells

This section deals with the basic operating principles of devices able to collect and harvest sunlight – photovoltaic (PV) solar cells. A solar cell is an electronic device which is capable of directly converting sunlight into electricity. Light that shines on the solar cell produces both a current and a voltage to generate electric power. This process requires a material in which the absorption of light excites an electron to a higher energy state and allows for the movement of this higher energy electron from the solar cell into an external circuit. Further, the electron transfers its energy to the external circuit and returns to the solar cell. A variety of materials and processes can potentially satisfy the requirements for photovoltaic energy conversion, but in practice nearly all photovoltaic energy converters use semiconductor materials in the form of a pn-junction. Thereby it is beneficial to define some of the key terminology used within the further context of this thesis, ranging from semiconducting materials, over defect induced states within the band gap, up to the working principles of solar cell operation.

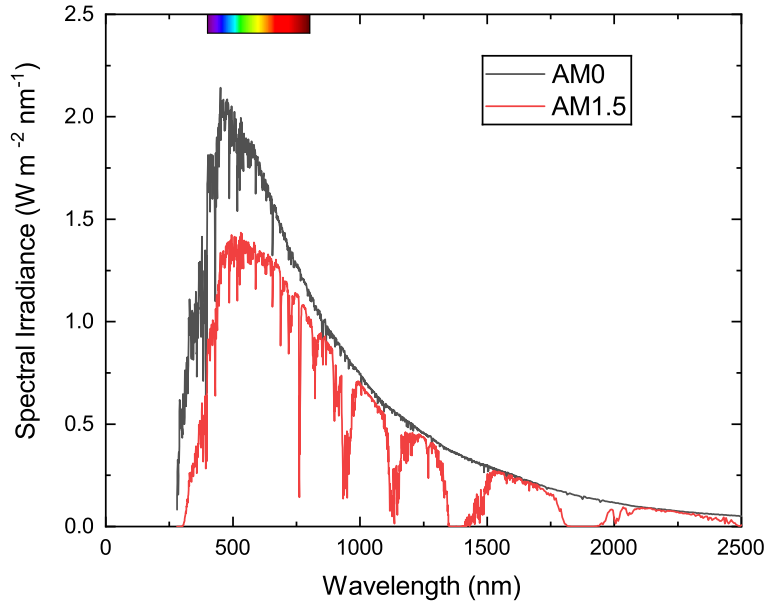


Figure 2.4: Two standard solar spectra: AM0, the spectrum outside the atmosphere, used for space application, and AM1.5, defining the standard for terrestrial measurements. The visible part of the spectrum has been indicated with the bar on top of the graph.

### 2.4.1 The solar spectrum

The Sun emits radiation as a result of its thermonuclear fusion processes of hydrogen in its core. If we assume that the Sun is a black body and take into account that it has a surface temperature of 5800 K, its emitting radiation spectrum (the energy density per photon energy) can be reproduced well from Planck's law of radiation:

$$dj_E(\hbar\omega, T) = \frac{a(\hbar\omega)d\Omega}{4\pi^3\hbar^3(c_0/n)^2} \frac{(\hbar\omega)^3}{e^{\frac{\hbar\omega}{kT}} - 1} d\hbar\omega, \quad (2.35)$$

with  $dj_E(\hbar\omega, T)$  being the energy current density (measured in  $\text{W m}^{-2}$ ),  $\hbar\omega$  photon's energy,  $a(\hbar\omega)$  absorptance,  $c_0$  the velocity of photons in vacuum,  $n$  the index of refraction,  $k$  Boltzmann constant ( $k = 8.617 \times 10^{-10} \text{ eV K}^{-1}$ ), and  $T$  temperature.

The absorptance  $a(\hbar\omega)$  is the characteristic of a body and is a function of the its geometry. It describes the fraction of the incident light that is absorbed by the body. It is related to the absorption coefficient  $\alpha(\hbar\omega)$ , which is a material property and independent of the geometry of a body. The solar spectrum has a maximum at  $E = \hbar\omega_{\max} = 2.82kT_S = 1.41 \text{ eV}$ , which lies in the infra-red part of the spectrum. This lies outside the range of visible light, which extends from 1.5 eV to 3 eV. The average energy of the solar photons is 1.35 eV. Usually, the spectrum is presented as the energy current density per wavelength as a function of the wavelength. It is often labelled as

the wavelength spectrum, while the first one is called the energy spectrum, since they are different quantities and have different units. The energy current density outside the atmosphere, i.e., the integral over each of the curves, has a value of  $1353 \text{ W m}^{-2}$ .

Solar radiation is partially absorbed during its passage through the atmosphere. The absorption is almost entirely due to low concentration gases in the infra-red region of the spectrum, such as  $\text{H}_2\text{O}$ ,  $\text{CO}_2$ ,  $\text{N}_2\text{O}$ ,  $\text{CH}_4$ , fluorinated hydrocarbons, and by ozone and oxygen in the ultraviolet region. The spectrum outside the atmosphere is labelled as the AM0 spectrum, while the one that reaches the surface of the Earth for a normal incidence as AM1. A typical spectrum for moderate climates is AM1.5, which corresponds to an incidence angle of solar radiation of  $48^\circ$  relative to the normal of the surface. Both spectra have been shown in Figure 2.4. The AM1.5 is regarded as the standard spectrum for measuring the efficiency of solar cells on the surface of the Earth and is used within the framework of this thesis. The integral over this spectrum yields a value of  $1000 \text{ W m}^{-2} \text{ a}^{-1}$ . The maximal value of energy current densities varies slightly from the tropics to the moderate zones. However, averaged over the year, the mean energy current density in Germany, for instance, is around  $115 \text{ W m}^{-2}$ , where the greatest annual amount is recorded in Saudi Arabia, with a value of  $285 \text{ W m}^{-2}$  ( $2500 \text{ W m}^{-2} \text{ a}^{-1}$ ).

## 2.4.2 Semiconducting materials

As indicated earlier, the energy of the electromagnetic spectrum is quantized and the vibrational quanta are called *photons*. On the other hand, the quantized atomic oscillations within a solid are called *phonons*. Phonon energies range from 0 eV to 0.05 eV, hence cannot be readily generated by the absorption of photons. The absorption of photons takes place through excitations of electrons into higher energy states. For this to happen over any arbitrary energy range, a continuous range of excitation energies must be available to the electrons. That is the case for metals and they would present very good absorbers, if they did not reflect most of the incoming light. On the other hand, since there is a continuous energy range, an electron that is excited through the absorption of a photon can easily lose this extra energy by generating phonons. The time order of this process is very narrow, around  $10^{-12} \text{ s}$ . Such a small time frame prevents direct utilization of metals as PV absorbers.

Semiconductors, on the other side, possess excitation energies which are separated by an energy gap (or band gap) of certain width,  $E_G$ . The energy range below the band gap is called the valence band and is almost completely occupied with electrons. The energy range above the gap is labelled as the conduction band and is nearly empty (almost fully occupied by holes). In order to excite an electron, the absorbing photon

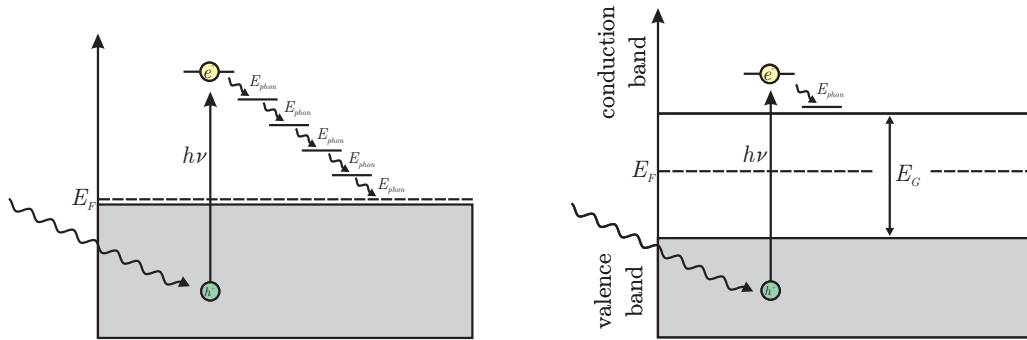


Figure 2.5: Graphical representation of the excitation process of an electron into the conduction band of a metal (left) and the excitation process of an electron from the valence into the conduction band of a semiconductor (right) by the absorption of a photon.

must have at least the energy of the band gap,  $\hbar\omega \geq E_G$ . Photons with smaller energies are not absorbed – they are either transmitted or reflected by the semiconductor. At this point we disregard the weak absorption taking place via phonons, impurities, or free charge carriers.

Once electrons are excited into the conduction band of a semiconductor, they start losing their energy just as quickly as in a metal, stepwise generating phonons, as depicted in Figure 2.5. However, once they reach the lower edge of the conduction band, there are no states left that have energy slightly lower than that of the electron. A few possibilities are still present, like the simultaneous generation of a large number of phonons at once. Alternatively, the emission process of a photon can take place. It is worth noticing how those processes are less favourable than the stepwise generation of phonons in metals. As a result, electrons can stay up to  $10^{-3}$  s in the conduction band. Compared to metals, these processes take up to multiple orders of magnitude longer in time, which is sufficient for the conversion of electron energy into electrical energy to take place.

The density of electrons follows from the Fermi–Dirac distribution function:

$$f(\varepsilon) = \frac{1}{\exp [(\varepsilon - \varepsilon_F)/k_B T] + 1} \quad (2.36)$$

where  $\varepsilon_F$  is the characteristic Fermi energy, which will be discussed later in more detail.

In isolated atoms, electrons have energy values which are distributed discretely and separated by large gaps on the energy scale. A decrease in the interatomic distance up to a few Å, as in a solid, introduces further interaction amongst the atoms and causes energy levels to split into many different values. The discrete energy levels become energy ranges where the energy values lie so close to each other that they appear as continuous. These regions of allowed electron energy values are labelled as *bands*.

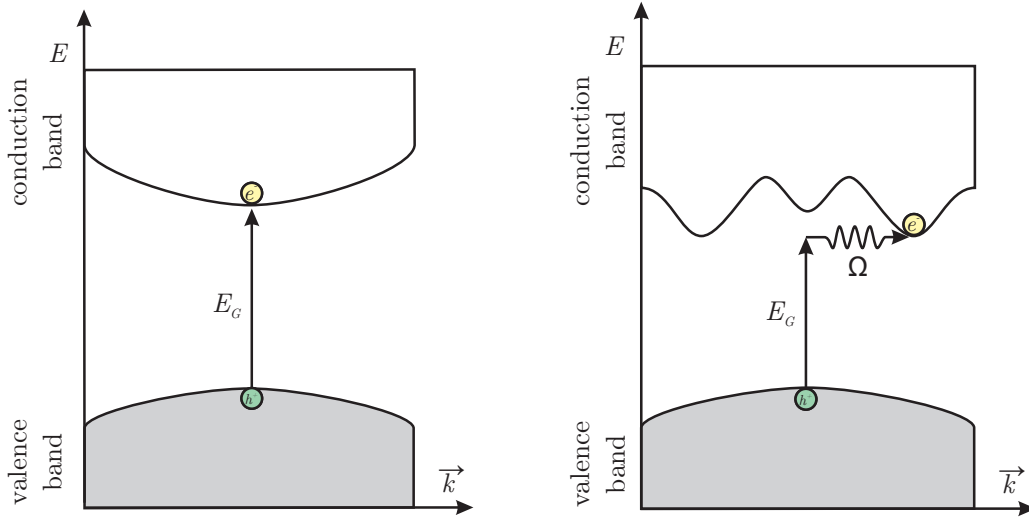


Figure 2.6: Schematic representation of the electron energy for a direct (left) and indirect (right) semiconductor as a function of their momentum. For a direct band gap semiconductor, the maximum of the valence and minimum of the conduction band occur at the same  $\vec{k}$  values. On the other hand, the indirect band gap transition involves both a photon and a phonon because the edges of the valence and conduction band are separated in  $\vec{k}$  space. Note, however, that the scheme depicts only threshold transitions, whereas transitions in general take place between all points of the bands for which the energy (and wave vector) can be conserved.

The width of the bands is proportional to the strength of the interaction amongst the electrons. This means that the core electrons show more narrow bands compared to the outer shell valence electrons which overlap entirely at high energies. Conversely, pure semiconductors and insulators are non-conductors, because the valence band is completely occupied and separated by an energy gap from the unoccupied conduction band, at least at  $T = 0$  K.

If the excitation of an electron from the VB to the CB occurs without a change in its momentum, the excitation is known as a direct transition and the semiconductor with that particular band structure a direct semiconductor. In that case, the absorption threshold frequency of the incident photon determines the energy gap,  $E_G = \hbar\omega_G$ . An example of a direct semiconductor is GaAs. On the other hand, an indirect transition between the VB and CB involves both a photon and a phonon because the band edges are widely separated in the  $\vec{k}$  space. That is, the threshold energy for the indirect process is greater than the band gap,  $\hbar\omega = E_G + \hbar\Omega$ , where  $\Omega$  denotes the frequency of an emitted phonon with the wave vector  $\vec{k}$ . Examples of indirect semiconductors include Ge and Si.

### Electrons and holes

The properties of vacant orbitals in an otherwise filled band play a specific role in semiconductor physics and solid state electronics. Those vacant orbitals in a band are commonly called holes. For the characterization of nearly empty bands, such as the

conduction band, a description in terms of occupied states is simple because the few electrons can be considered to form an ideal gas. For nearly filled bands, such as the valence band, the description in terms of electrons is vastly more complicated. Instead one can equally describe an almost full band in terms of the few unoccupied states, namely *holes*. Regarded as fictitious particles of positive charge, holes are merely the absence of electrons and vice versa, electrons can be viewed as the absence of holes. In other words, the properties of bands can be equally well described in terms of electrons or holes (occupied or unoccupied states). However, those two pictures cannot be mixed within a given band. For instance, while discussing currents, if one regards the electrons as carrying the current, then the unoccupied levels do not contribute, and vice versa, if one considers holes carrying the current then the electrons make no contribution. Nonetheless, one can regard some bands in the electron picture and others in the hole picture, merely as a matter of preference.

### Generation of electrons and holes

Solar cells generate additional electrons and holes via the process of photon absorption from solar radiation. The probability for the absorption of a photon of energy  $\hbar\omega$  is defined by the **absorption coefficient**  $\alpha(\hbar\omega)$ . The absorption coefficient is a material property, independent of its geometry, and is proportional to the density of occupied (unoccupied) states in the valence (conduction) band in which a hole (electron) can be generated. For semiconductors with a transition between the top of the VB and bottom of the CB which involves no phonons (a direct band gap semiconductor), the absorption coefficient has a square root dependence on the photon energy. An illustrative example of the absorption coefficient of GaAs is shown in Figure 2.7. Photons whose energy is lower than the band gap ( $E_G > \hbar\omega$ ) are not being absorbed and no electron-hole pairs are generated,  $\alpha(\hbar\omega) = 0$ . Those photons are either reflected or transmitted. For incident photons whose energy is larger than the band gap ( $E_G < \hbar\omega$ ),  $\alpha$  shows a steep rise and is  $\propto (\hbar\omega - E_G)^{1/2}$  for values up to  $10^4 \text{ cm}^{-1}$ . For larger values, the complexity of the band structure causes deviations from the square-root dependence. The inverse of the absorption coefficient is called the penetration depth of the photons,  $L = 1/\alpha$ . Direct semiconductors have a large absorption coefficient and, hence, small photon penetration depth. In other words, solar cells made from those materials do not have to be thicker than a few  $\mu\text{m}$  in order to absorb the part of the solar spectrum with photon energies larger than the band gap.

Contrary, in an indirect semiconductor, a transition between the VB and CB is not possible merely by the absorption of a photon, because the photon momentum is too small to satisfy the conservation of momentum. The momentum balance is held through the participation of lattice vibrations or phonons, which allow photon-

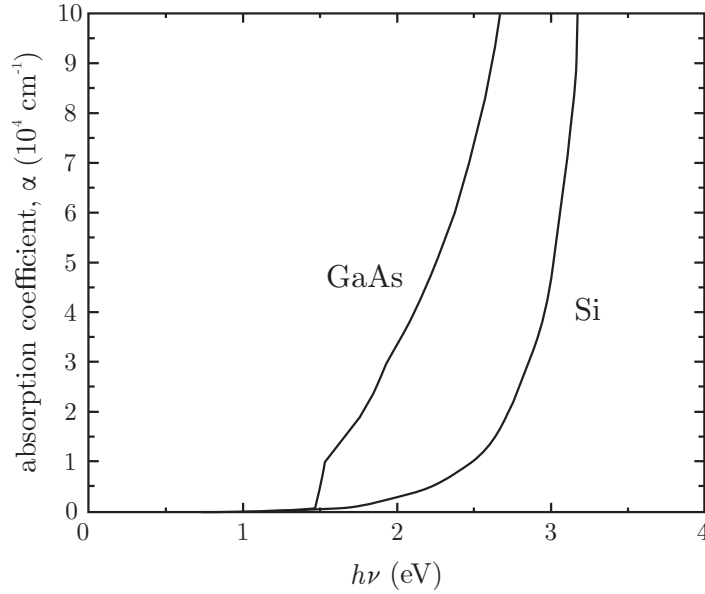


Figure 2.7: Absorption coefficient of a direct band gap semiconductor, GaAs, and an indirect band gap semiconductor, Si. Note how a steep increase is present at the absorption edge of GaAs at around 1.4 eV. This is known as the Urbach tail, which is caused by statistical fluctuations of the band gap due to lattice vibrations.

induced transitions from every state of the VB to every state of the CB that satisfy the energy balance from Figure 2.6. The expression for the absorption coefficient of indirect band gap materials yields  $\alpha(\hbar\omega) \propto (\hbar\omega - E_G \pm \hbar\Omega)^2$ . The plus and minus sign indicate photon absorption with the simultaneous phonon absorption or emission, respectively. Due to the phonon participation, the absorption coefficient of an indirect semiconductor is small. Figure 2.7 illustrates the absorption coefficient of silicon, an indirect band gap material. Note how the absorption coefficient near the band gap (around 1.1 eV for Si) is extremely small and can barely be distinguished. Furthermore, the penetration depth of photons in indirect semiconductors is large, requiring fabricated solar cells to be more than  $100 \mu\text{m}$  thick.

In addition to photon-absorbed electron-hole generation, they can be generated by thermal transitions from the valence into the conduction band via impurities. Further, in a state of equilibrium with the environment, the non-radiative generation and recombination rates must also be balanced. The inverse process of electron-hole production is called recombination, where electrons and holes are annihilated producing either photons or phonons or both simultaneously. When the system is under thermal and chemical equilibrium with its environment, the rates of production and annihilation are exactly balanced for each of the different mechanisms mentioned - which is known as the principle of detailed balance.

Recombination can be classified roughly into radiative and non-radiative recombination. **Radiative recombination** or band-to-band recombination, the reverse

of absorption, is the process in which a hole reacts with an electron and produces a photon (see Figure 2.8). This type of recombination dominates direct band gap semiconductors. Non-radiative recombination, on the other hand, is characterized by a take up of the energy created via annihilation by other particles. There are two types of non-radiative recombination:

- Auger recombination - involves a third carrier.
- Impurity recombination (a.k.a. recombination through defect levels or Shockley-Read-Hall (SRH) recombination) - includes phonons.

In **Auger recombination**, the energy set free during recombination is transferred to an electron or hole as kinetic energy that is subsequently lost due to thermal vibrations. It is significant in cases where a high carrier concentration is present, such as heavy doping or high level injection under concentrated sunlight (i.e., high light intensity). In real solar cells, however, **recombination via impurities** is the predominant recombination process. Impurities which create electronic states around the middle of the forbidden zone (band gap) play the most important role as they capture electrons and holes over a series of excited states with consecutive dissipation of energy. This way the recombination energy can be allocated to the lattice in smaller fragments through the production of phonons, making the process readily taking place. If impurity levels are close to the conduction (valence) band they are less effective, since most of the time they are not occupied by electrons (holes) and captured carriers are rather emitted back to the conduction (valence) than annihilated via recombination. In the middle of the gap, the probability of occupation by electrons and holes is equal, making the re-emission process less probable.

## 2.5 Point defects in solids

Perfect crystals (materials) exist only in theory or textbooks. In reality, they have imperfections, which can make them particularly interesting for a specific application. The deliberate addition of impurities to a semiconductor is defined as *doping*. This is done in order to vary and control the various properties of a material, e.g., electrical conductivity. The simplest case, which shall be used to illustrate important concepts, is when impurity atoms replace the atoms of the semiconductor at their lattice positions. If the impurity atom has more valence electrons than it is necessary for chemical bonding with the neighbouring atoms, it is labelled as a **donor**. That electron is bound to its atom by the Coulomb force, creating (treating the problem in a first approximation) a hydrogen-like defect state in the initial band structure. The main difference from an isolated hydrogen atom is that the electrostatic interaction is

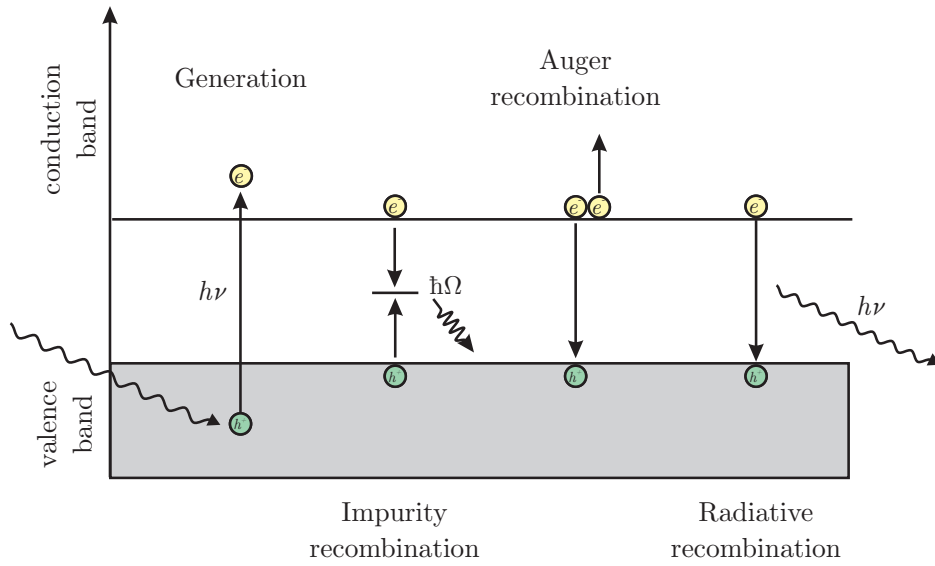


Figure 2.8: Schematic representation of possible recombination processes taking place in a semiconductor once electrons and holes are generated by the absorption of photons: impurity recombination, Auger recombination, and radiative recombination.

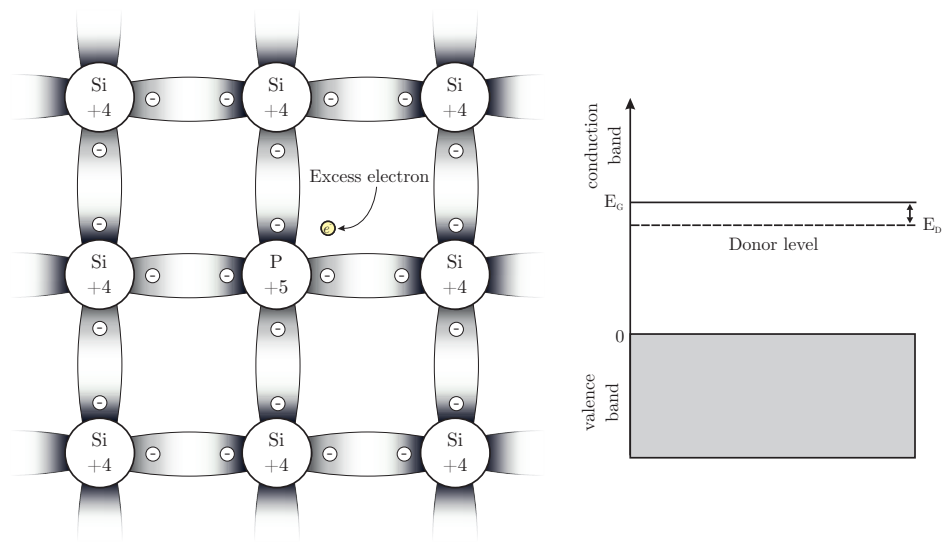


Figure 2.9: Phosphorus doped silicon lattice. Phosphorus has five while silicon has only four valence electrons. Four phosphorus electrons form tetrahedral bonds with silicon atoms and the fifth electron is available for conduction. That electron is firmly bound to the donor atom and can be ionized easily into the conduction band.

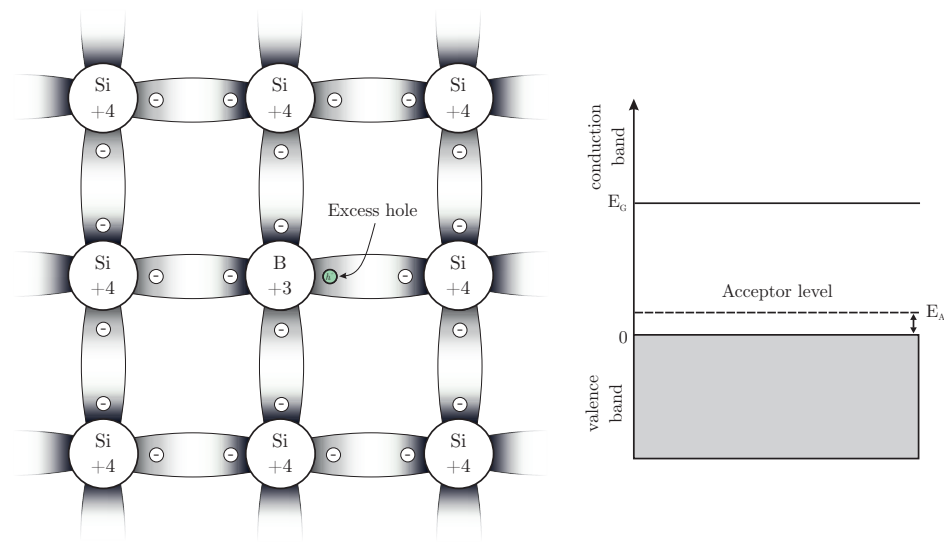


Figure 2.10: Boron doped silicon lattice. Since boron has only three valence electrons it can complete its tetrahedral bond only by taking an electron from the Si-Si bond, leaving behind a hole in the silicon valence band. That hole is weakly bound to the acceptor atom, easily ionized into the valence band.

weakened in a crystal lattice as a result of the electronic polarization of the medium (efficient electronic screening) and that the free-electron mass is replaced by the effective mass of the electrons in the conduction band. As a result of that, the electron binding energy to the donor,  $E_D$ , is only slightly smaller than the lower edge of the conduction band. Donors, therefore, donate their electrons easily to the conduction band, hence the appropriate naming. A schematic representation of a phosphorus donor in the silicon crystal lattice is depicted in Figure 2.9.

**Acceptors**, on the other hand, are impurity atoms that have one valence electron less than it is necessary for chemical bonding with its host neighbouring atoms. An electron that fills this hole in the bond, which originates from the valence band of the neighbouring lattice atoms, has no Coulomb attraction to the impurity atom. Since this bond is weak, the energy of an electron at the acceptor is only slightly greater than the upper edge of the valence band. Therefore, acceptors accept electrons from the valence band easily. In the hole picture, which is as mentioned simpler to realize for the valence band, what follows is that the holes are weakly bound to the acceptor and easily donated to the valence band (as depicted in Figure 2.10 for impurity boron in the silicon lattice).

### Classification of defects

Defects can be broadly classified by their atomic structure and symmetry as well as by the energy levels they introduce into the band gap. Intrinsic defects (or native ones) are defined as defects that only involve atoms that are present or absent in the perfect

crystal. Four types of native defects are of importance in elemental semiconductors with a fifth one applicable only to compound semiconductors (schematic representation in Figure 2.11):

- Lattice vacancies, labelled  $V_A$ , where A is the host atom.
- Interstitial atoms,  $A_i$ , also known as self-interstitials.
- Schottky defects, where a host atom leaves its position and moves to the surface, thereby creating a vacancy.
- Frenkel defects, where a host atom moves to an interstitial position, forming a vacancy-interstitial pair.
- Antisites (in compound semiconductors),  $C_A$ , where a cation (C) is found on the nominal anion site (A), or vice versa,  $A_C$ .

Extrinsic defects, on the other side, are composed of impurities - atoms that are foreign to the crystal. These can reside on various sites. A substitutional site is the one that is normally occupied by a constitutional atom in the perfect lattice. In a compound semiconductor, the substitutional site is indicated by a subscript, e.g.,  $\text{ZnP}_2:\text{Cu}_{\text{Zn}}$  denotes a copper atom substituting a zinc one in zinc diphosphide. A site that is not substitutional is called interstitial, following the same logic as for intrinsic defects. Defects can also exist as complexes, which involve a combination of two or more impurities of native defects.

The replacement of atoms in a semiconductor, in one of the aforementioned ways, can lead to the creation of electronic states inside the band gap. These states are often called energy levels, as mentioned for donors and acceptors already, and are the main reason for the increased scientific interest in semiconductors. Donor (acceptor) levels that lie close to the conduction (valence) band edge are called shallow levels. As seen in the case of silicon, phosphorus has one valence electron more than required to complete the Lewis octet when it substitutes a host silicon atom. This electron is "given up" easily to the conduction band - hence the name shallow impurity. The same reasoning applies for the boron substituting silicon, where an extra hole can be easily released to the valence band. Shallow donors (acceptors) are also called hydrogenic because they can be modelled as an electron (hole) orbiting around an ion, as in analogy to the hydrogen atom. A semiconductor can contain both donors and acceptors, where depending on the balance between them it is said how one compensates the other type of defect.

The energy difference between the conduction band minimum (valence band maximum) and the donor level is the ionization energy or donor (acceptor) binding energy.

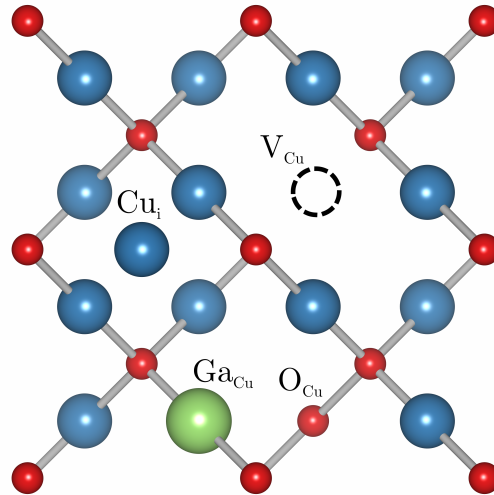


Figure 2.11: Schematic representation of defects in  $\text{Cu}_2\text{O}$ : Copper vacancy ( $V_{\text{Cu}}$ ), copper interstitial ( $\text{Cu}_i$ ), oxygen antisite ( $\text{O}_{\text{Cu}}$ ), and substitutional gallium ( $\text{Ga}_{\text{Cu}}$ ). Blue spheres represent copper atoms, red and green spheres represent oxygen and gallium atoms, respectively.

A donor (acceptor) atom is considered neutral when it has an electron (hole) bound to it and is positive (negative) when the electron (hole) is liberated. Impurities and defects can be amphoteric, meaning that they have both acceptor and donor levels. Depending on the position of the Fermi level, the impurity atom changes its charge state. Another example worth mentioning are transition metals, which can introduce a range of energy levels into the band gap that can hinder or boost effective performance, especially for solar harvesting devices. There it is often a necessity to label the impurity by its valence number or oxidation state. In the terminology within this thesis, an impurity or defect is considered "neutral" if it retains the charge state of the atom it is replacing. For example, a cobalt atom substituting copper in  $\text{CuO}$  is considered neutral if it stays in the  $\text{Co}^{2+}$  state, whereas it would have a "-" and "+" charged state for a valency of  $\text{Co}^{1+}$  and  $\text{Co}^{3+}$ , respectively.

Deep level impurities create energy levels that are far from the band gap edges. Such impurities cannot be described by the hydrogenic ground state model because the electron (hole) is bound strongly at a short distance from the impurity core.

Further examples of native defects include negative- $U$  defects (a defect centre binding two electrons under lattice relaxation),  $E$ -centres (a vacancy plus a neighbouring donor impurity), passivation (a hydrogen atom attached to a vacancy), divacancies (a pair of neighbouring vacancies), larger vacancy defects like trivacancies, tetravacancies (less known), split interstitials (two atoms sharing a single lattice site), etc. They fall out of the scope of this thesis and shall not be discussed in detail; for further information the reader is referred to [28].

## Converting sunlight into electrical energy

A generated electron-hole pair is electrically neutral. If one would remove electrons and holes pairwise, no current would be created. Therefore, it is necessary to separate the electrons and holes and drive them out of the absorber by some internal force, since they must be able to perform work in an external circuit. Electrons can "feel" the action of many forces, e.g., due to the gravitational potential acting on their mass, the electrical potential acting on their charge, the temperature gradient on their entropy, the gradient of the chemical potential acting on their quantity, etc. Gravitational forces acting on electrons are negligibly small and effects arising from temperature gradients are neglected within this work. This leaves us with two main forces governing the transport of electrons and holes through an absorber layer.

In order to generate a charge current flowing from one side to the other of the solar cell, semi-permeable membranes are required on both sides of the absorber, such that electrons can flow out on one side while the holes flow out on the other one. A membrane that is permeable for electrons, but which blocks holes effectively, would be a material with a large conductivity for electrons and small for holes. Such a material would be an *n*-type semiconductor, where the small hole conductivity arises from the small concentration of holes. A hole membrane would be, analogous to the electron membrane, a *p*-type semiconductor. The injection of holes into the electron membrane is prevented by a larger band gap, being equivalent to an energy barrier in the valence band for holes. Correspondingly, a larger band gap in the hole membrane prevents electrons from passing through by creating an energy barrier in the conduction band. Due to their larger band gaps, the membranes on each side of the absorber transmit almost all of the incoming light to the absorber.

A few requirements are set for optimal solar cell selectivity (of the conductivities) and overall performance: a difference of the quasi-Fermi energy of around 1 eV, a voltage drop not larger than 1 meV for the electron (hole) transport to the electron (hole) contact, a current of electrons and holes in the undesired direction that is smaller by a factor of 1000 than the current in the desired direction. In order to achieve this, the conductivities of the holes (electrons) in front of the electron (hole) contact must be smaller by a factor of  $10^9$  than the conductivities of the electrons (holes) in front of the electron (hole) contact. Such ratios can be achieved within different architectures, out of which the ones of most technical importance and model are listed:

*PN-Junction* - Separates the electron and hole carriers in a solar cell to create a voltage and useful work. It is the most common realization of the solar cell structure commercially available in crystalline silicon, taken as an example. The *pn*-junction is formed of two membranes and an absorber layer. In the example of silicon, a *p*-region 300  $\mu\text{m}$  thick, serving as the absorber, is "sandwiched" between a highly doped *n*-layer

on the illuminated side (electron membrane) and a highly doped  $p$ -layer on the rear side (hole membrane), both being less than  $1\ \mu\text{m}$  thick. A  $pn$ -junction in equilibrium with the environment (including the 300 K background radiation) allows no currents to flow. I.e., the electrochemical potential of the electrons and holes has the same value everywhere in the  $pn$ -junction. This is established when a spatially separated electrically neutral  $p$ -conductor and  $n$ -conductor are put in contact. Once in contact, the difference in the chemical potentials drives a diffusion current of electron from the  $n$ -conductor to the  $p$ -conductor, and vice versa. This builds up a positive charge in the  $n$ -conductor and a negative charge in the  $p$ -conductor and the diffusion current flows until an electrochemical equilibrium is established. Note that the electrochemical equilibrium is established between the electron and the holes, however, such an equilibrium between acceptors and holes does not exist. This non-equilibrium distribution is the base of a  $pn$ -junction. A schematic representation of a  $pn$ -junction is shown in Figure 2.12.

Furthermore, when the electrons and holes move to the other side of the junction, they leave behind exposed charges on fixed dopant sites in the crystal lattice. On the  $n$ -type side, positive ion cores are exposed, while on the  $p$ -type side negative ion cores are left behind. As a result of that, an electric field is formed between the positive and negative ion cores, often called the depletion region since the electric field sweeps free carriers out, thus leaving the region depleted of free carriers. This electric field represents a barrier to the flow of the forward bias (the application of voltage such that the generated electric field reduces the electric field of the depletion region). Most majority carriers that enter the depletion region move back towards their originating region, however, statistically some carriers will have enough velocity to cross the junction. Once majority carriers cross the junction, they become minority carriers. They continue to diffuse away from the junction and can travel a distance equal to the diffusion length before they recombine. The current generated by the diffusion of carriers across the junction is called the diffusion current. Minority carriers which reach the edge of the diffusion region, i.e., reach the depletion region again, get swept back again across it by the electric field. This current is called the drift current. Overall, the net current of the  $pn$ -junction is zero, due to the equilibrium between diffusion, drift, carrier generation, and carrier recombination processes taking place.

The  $pn$ -junction is able to collect carriers generated via the absorption of incident photons, preventing recombination between the electron-hole pairs. The generated carriers are separated by the action (force) of the electric field existing at the  $pn$ -junction. If the photo-induced carrier reaches the  $pn$ -junction, it swept across it and becomes a majority carrier. If the emitter and the base of the solar cell are connected (the solar cell is short-circuited), the light-generate carriers flow through the external

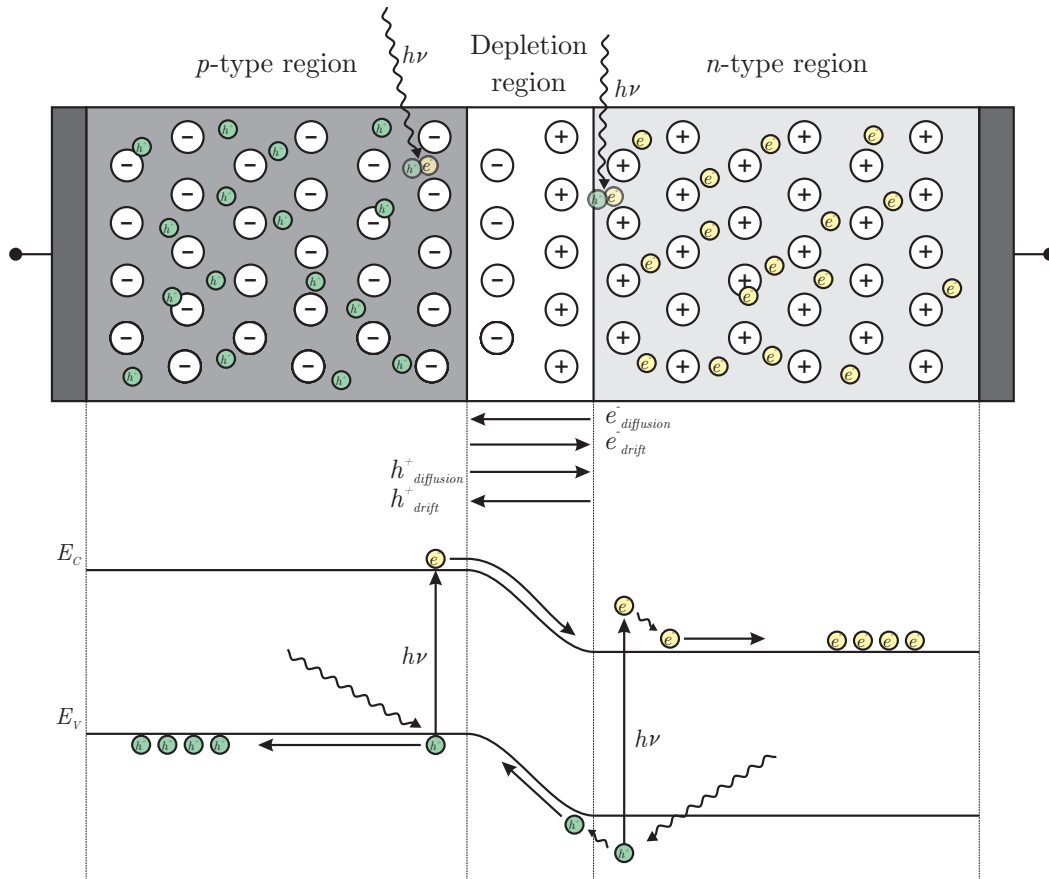


Figure 2.12: Schematic representation of a *pn*-junction (top) and its energy band diagram (bottom). The half labelled *p*-type contains acceptor atoms with extra holes and the half labelled *n*-type contains donor atoms which have extra electrons. When the two halves meet, a depletion region is created, where electron have moved towards the *p*-type region and holes towards the *n*-type region, leaving behind the exposed charge on the atom sites in the crystal lattice. Once equilibrium is reached, the net current of the *pn*-junction is zero. If an incident photon has an energy ( $h\nu$ ) that is equal or larger than the band gap, the process of absorption will take place and an electron-hole pair will be created. If the *pn*-junction collects these carriers before they recombine, they are separated across the electric field of the junction and become majority carriers. If the emitter and the base of the solar cell are connected, a light-generated current flows through the external circuit. Within this scheme, the electron is depicted with a circle coloured light-yellow with a sign " $e^-$ ", while the hole is depicted with a circle coloured green-ish with a sign " $h^+$ ".

circuit. The probability that a carrier generated by the light absorption in a certain region of the device will be collected depends on the distance that the carrier must travel relative to the diffusion length, as well as on the surface properties of the device. The collection probability is equal to unity in the depletion region and drops away from the junction. If the carriers are generated more than a diffusion length away from the junction, they are more likely to recombine before they are effectively collected.

Apart from a *pn*-junction, other commonly used architectures include:

- *Dye (Organic) Solar Cells* - The absorber layer, where the electron-hole pairs are created, is a dye layer. Due to the small mobilities of electrons and holes, the layer is very thin for charge carriers to reach the membranes within their lifetimes before they recombine. One of the major issues regarding dye solar cells is the stability over a longer period of time.
- *Heterojunctions* - Since many materials can only be prepared as either *p*-type or *n*-type, the preparation of a *pn*-junction from a single material (homojunction) is not always possible. A heterojunction is a *pn*-junction created by interfacing different materials. For such devices, it is not sufficient to bring semiconductors of suitable band gaps and electron affinities in contact, it is more important that the interfaces are as free as possible of states within the band gap in order to eliminate additional recombination effects and charge trapping.
- *Tandem (multi-junction) solar cells* - A concept that allows the reduction of thermalization losses and improved absorption efficiency by splitting the solar spectrum and using solar cells for photons within a narrow energy interval and processing the other photons by solar cells with different band gaps. Similarly to the previous cases, the difficulty with tandem solar cells lies within finding suitable materials with a specific band gap and that, once interfaced, do not possess states within the band gap.

In addition, one has to keep in mind how the situations described above refer to ideal systems for photon collection, where the effects like recombination via impurities, non-radiative recombination effects, indirect absorption via phonons, resistive effects, temperature effects of sunlight fluctuations have been mostly neglected. All of these present a great challenge for the fabrication, assessment and improvement of solar cells. However, they would require great effort of introduction and lie out of the scope of this thesis.

### Solar Cell Efficiency

The most commonly used parameter to compare the performance between different solar cells is efficiency. It is defined as the ratio of energy output from the solar cell to input energy from the Sun. In addition to reflecting the performance of the solar cell itself, the efficiency depends on the spectrum and intensity of the incident sunlight and the temperature of the solar cell. In order to compare the performance between devices, the efficiency of terrestrial solar cells is measured under the mentioned AM1.5 condition and a temperature of 25° C, while that of solar cells utilized in space conditions is measured under AM0 conditions. The efficiency of a solar cell, also known as the power conversion efficiency (PCE), is determined as the fraction of incident power which is converted to useful electricity:

$$P_{\max} = V_{OC} I_{SC} FF, \quad (2.37)$$

$$\eta = \frac{P_{\max}}{P_{\text{in}}} = \frac{V_{OC} I_{SC} FF}{P_{\text{in}}}. \quad (2.38)$$

$V_{OC}$  is the open-circuit voltage (maximum voltage from a solar cell),  $I_{SC}$  is the short-circuit current (maximum current from a solar cell), FF the fill factor, and  $\eta$  the efficiency. The fill factor is a parameter which is usually determined graphically as the area of the largest rectangle which fits the I-V curve.

## 2.6 First-principles modelling of point defects in solids

As mentioned earlier, point defects and impurities play an important role in the physical properties of materials. Experimental detection of defects is typically difficult and requires a combination of various different techniques. Calculations from first principles, on the other hand, have emerged as a powerful approach that can complement experiments and have become reliable enough to serve as a predictive tool [29]. In such calculations, one typically works in the dilute limit, in which the defect concentration is low and defect-defect interactions are negligible. Here, the basic formalism required to study the occurrence of defects in solids will be outlined.

### Phase stability

At elevated temperatures, defects will always form in semiconductors. A system in thermodynamic equilibrium, at pressure  $P$  and temperature  $T$ , minimizes the Gibbs free energy:

$$G = H - TS, \quad (2.39)$$

where  $H$  is the enthalpy and  $S$  the entropy. The enthalpy is defined as:

$$H = E + PV \quad (2.40)$$

with  $E$  being the total (also labelled as internal) energy and  $V$  the volume of the considered sample. Note that in the regime of low temperatures (in quantum mechanics one often works at zero K),  $G \equiv H$ . Within this notation, for instance, the enthalpy required to remove one atom from the interior of the crystal and place it on the surface is labelled as  $H_V$ , while  $H_I$  would label the enthalpy required to take an atom from the surface and place it into an interstitial site. Given the knowledge of the defect formation enthalpy  $H^f$ , one can calculate the defect concentration  $n$  (neglecting vibrational entropy contributions,  $S_V$ ):

$$n = N \exp \left[ - \frac{H^f}{k_B T} \right] \quad (2.41)$$

where  $N$  is the concentration of sites where the defect can reside. Also, under normal conditions of pressure,  $H^f$  is equivalent to the formation energy  $E^f$ . An important factor for compound semiconductors that influences the formation enthalpy is the chemical potential of the various molecular species. It provides information about the chemical environment in which the semiconductor dwells. An illustrative example is GaAs, in which arsenic antisites are more likely to form if the chemical potential of arsenic is high [30]. The chemical potential is defined through the Gibbs free energy:

$$G = \sum_i n_i \mu_i, \quad (2.42)$$

where  $n_i$  and  $\mu_i$  are the number of molecular species and their respective chemical potential. Chemical potentials of pure phases depend on pressure and temperature and, in the general formalism, they are often regarded as variables. However, they are subject to specific boundaries, which are set by the existence or appearance of secondary phases. For instance, considering the growth of GaN, the chemical potentials of Ga and N are linked by the stability of the GaN phase:

$$\mu_{\text{Ga}} + \mu_{\text{N}} = \mu_{\text{GaN}}. \quad (2.43)$$

Bounds on the chemical potentials are set by the formation of metallic Ga and molecular N:

$$\mu_{\text{Ga}} \leq \mu_{\text{Ga}}(\text{Ga metal}), \quad (2.44)$$

$$\mu_{\text{N}} \leq \mu_{\text{N}}(\text{N}_2, P, T). \quad (2.45)$$

Combining those equations with (2.43), the lower bounds on  $\mu_{\text{Ga}}$  and  $\mu_{\text{N}}$  transform into upper bounds for the corresponding other species:

$$\mu_{\text{GaN}} - \mu_{\text{N}}(\text{N}_2, P, T) \leq \mu_{\text{Ga}}, \quad (2.46)$$

$$\mu_{\text{GaN}} - \mu_{\text{Ga}}(\text{Ga metal}) \leq \mu_{\text{N}}. \quad (2.47)$$

When impurities are present in a material, their chemical potentials  $\mu_i$  are subject to similar bounds, imposed by the formation of stable phases with the elements of the host material, or amongst each other. Values of chemical potentials always depend on their implicit reference. In electronic-structure based calculations, they can be referenced to the total energy of the elementary phases at  $T = 0$  K. Experimental databases usually employ elementary phases referenced at standard conditions ( $T = 273.15$  K or  $298.15$  K and  $P = 100$  kPa or  $101.325$  kPa). These approaches are equally valid and the crucial thing is that a consistent choice is made for all chemical potentials and formation energies (enthalpies). It is advised to include the choice of reference directly into the equations to avoid confusion:

$$\Delta\mu_{\text{Ga}} = \mu_{\text{Ga}} - \mu_{\text{Ga}}^{\circ}, \quad (2.48)$$

$$\Delta\mu_{\text{N}} = \mu_{\text{N}} - \mu_{\text{N}}^{\circ}, \quad (2.49)$$

$$\begin{aligned} \Delta\mu_{\text{GaN}} &= \mu_{\text{GaN}} - \mu_{\text{Ga}}^{\circ} - \mu_{\text{N}}^{\circ} \\ &= \Delta_f G^{\circ}(\text{GaN}), \end{aligned} \quad (2.50)$$

where the standard Gibbs energy of formation was introduced,  $\Delta_f G^{\circ}(\text{GaN})$ , as well as the notation for elements in their standard phase,  $\mu_{\text{Ga}}^{\circ} \equiv \mu_{\text{Ga}}(\text{Ga metal})$  and  $\mu_{\text{N}}^{\circ} \equiv \mu_{\text{N}}(\text{N}_2, P, T)$ . Using these definitions, equation (2.43) becomes:

$$\Delta\mu_{\text{Ga}} + \Delta\mu_{\text{N}} = \Delta_f G^{\circ}(\text{GaN}), \quad (2.51)$$

independent of the underlying reference [29, 31]. For gas phase species it is critical to take the temperature and pressure dependence into account. For solid phases, on the other hand, these dependencies are usually negligible in first approximation. In principle, chemical potentials can be related to partial pressures using standard thermodynamic expressions. E.g., the chemical potential for hydrogen is given by [31]:

$$2\mu_{\text{H}} = E_{\text{H}_2} + kT \left[ \ln \left( \frac{pV_Q}{kT} \right) - \ln Z_{\text{rot}} - \ln Z_{\text{vib}} \right], \quad (2.52)$$

where  $E_{\text{H}_2}$  is the energy of an  $\text{H}_2$  molecule,  $k$  is the Boltzmann constant,  $T$  temperature, and  $p$  pressure.  $V_Q = (h^2/2\pi mkT)^{3/2}$  is the quantum volume and  $Z_{\text{rot}}$  and

$Z_{\text{vib}}$  are the rotational and vibrational partition functions. When using expressions for chemical potentials one should be careful to verify that equilibrium conditions apply. For instance, when a material is annealed at high temperatures under an overpressure of a certain element, it may be appropriate to relate the chemical potential of that element to the partial pressure of the gas.

### Defect energetics

The formation energy of a defect  $X$  in a charge state  $q$  is defined as [30, 31]:

$$E^f[X^q] = E_{\text{tot}}[X^q] - E_{\text{tot}}[\text{bulk}] - \sum_i n_i \mu_i + qE_F + E_{\text{corr}}. \quad (2.53)$$

$E_{\text{tot}}[X^q]$  is the total energy derives from a supercell calculation containing the defect  $X$ , and  $E_{\text{tot}}[\text{bulk}]$  is the total energy for the perfect crystal using an equivalent supercell. The integer  $n_i$  indicates the number of atoms of type  $i$  (host atoms of impurity atoms) that have been added to ( $n_i > 0$ ) or removed from ( $n_i < 0$ ) the supercell to form the defect, and  $\mu_i$  are the corresponding chemical potentials of the considered species. As already discussed, the chemical potentials represent the energy of the reservoirs with which atoms are being exchanged. Finally,  $E_{\text{corr}}$  is a correction term that account for the finite k-point sampling (in the case of shallow impurities) or for elastic and/or electrostatic interactions between supercells.

In principle, one should use the Gibbs free energy in equation (2.53) taking into account the full temperature and volume dependence of the electronic and vibrational entropy. However, explicit calculations of such entropies are very demanding and not very feasible when one wishes to address a large number of defects. These entropy effects cancel up to some extent, and in general, they are small enough not to affect qualitative conclusions [31].

### The supercell approach

This work focuses on the calculations of defects and the related quantities in a supercell geometry. Within this approach, the supercell consists of the defect surrounded by a dozen, up to a few hundred atoms of the host material and this whole structure is periodically repeated. The supercell approach has the following advantages over alternative approaches:

1. It allows for the use of mathematical techniques that are used to model periodic solids.
2. The band structure of the host crystal is well described. This contrasts cluster approaches, where the host is modelled by a finite number of atoms terminated

at a surface. Even fairly large clusters still produce sizeable quantum effects that significantly affect the band structure and interactions between the surface and the defect wave functions are hard to avoid.

3. The results are straightforward to interpret, unlike, e.g., the Green's function approach, which is challenging from a programming point of view and less transparent than the supercell technique whilst explaining physical phenomena.

Unfortunately, a periodic array of defects contains unrealistically large defect concentrations, resulting in artificial interactions between the defects that cannot be neglected. Those interactions are quantum-mechanical, elastic, magnetic, and electrostatic in nature. These artefacts can be easily circumvented as they become negligibly small when the supercell size is increased. It is therefore crucial to estimate the magnitude and decay behaviour of different defects, to employ the right computational schemes that minimize the calculation error, and correct eventual remaining effect *a posteriori* whenever possible. One has to keep in mind how supercell artefacts differ from defect to defect and that they can be avoided to the extent that the underlying mechanism is understood. There is no universal scheme that corrects for all remnants.

One of the aforementioned effects is the *dispersion of the defect band*. An isolated defect (corresponding to the limit of an infinitely large supercell) leads to a flat, dispersionless defect level in the infinitely large Brillouin zone. The overlap between the defect wave function and the neighbouring supercells turns the single-particle state from an isolated defect level into a dispersive defect band. I.e., the magnitude of the dispersion is a direct measure of the artificial interaction between the defect and its neighbouring images. For deep defects, the electronic state is largely (but not completely) contained within the supercell. Such a defect band disperses around the level of the isolated defect. For a localized state within the band gap, the defect wave function decays exponentially away from the defect centre. Hence, a sufficiently large supercell leads to a minimized dispersion. For shallow levels, the spatial extent of the wave functions significantly exceeds typical supercell sizes. Since shallow levels are hydrogenic effective masses, their dispersion follows closely the host band from which they are derived. In the case when one knows the valence and conduction band dispersions, the effects of dispersion and occupation can directly be corrected. For details of the derived formalism, the reader is referred to an excellent review by Freysoldt *et al* [29].

A further common issue affecting supercell calculations is the treatment of charged systems. Such calculations need to include a compensating background charge, since the electrostatic energy of a system with a net charge in the unit cell diverges. A further issue is the convergence with respect to supercell size of such systems, because

the electrostatic interactions between a charged defect and its periodic images scale as  $1/L$ , with  $L$  being the dimension of the supercell. Furthermore, an alignment procedure for the electrostatic potential between the supercell and the bulk is required to establish a reference level for consistent formation energy calculations.

Despite the fact that such calculations allow one to estimate charge transition levels and compare them to experimental ionization energies, they have been omitted from this work due to the mentioned complexity of correcting for errors produced within. The approach utilized within this work is to treat eventual charge imbalance effects arising from oxidation states that differ from the initial one by introducing compensating defects such as cation vacancies in order to keep the system charge neutral.

## Ground state properties and photovoltaic potential of copper oxides

*"All truth passes through three stages. First, it is ridiculed. Second, it is violently opposed. Third, it is accepted as being self-evident."*

---

Arthur Schopenhauer, *German philosopher*

Upon oxidation, copper forms three stable types of oxides:

- Copper (I) oxide, also known as *cuprous oxide*, with the structural formula  $\text{Cu}_2\text{O}$ .
- Copper (II) oxide, also known as *cupric oxide*, with the formula  $\text{CuO}$ .
- Paramelaconite, an intermediate compound between the previously mentioned cuprous and cupric oxide. It has the chemical formula  $\text{Cu}_4\text{O}_3$ .

Two other copper oxides which can be found in literature are copper peroxide ( $\text{CuO}_2$ ) and copper (III) oxide ( $\text{Cu}_2\text{O}_3$ ). Copper peroxide is unstable, decomposing into oxygen and other copper oxides, while copper (III) oxide has not been isolated as a pure solid. Copper (III) oxides are also known as constituents of cuprate superconductors [32].

Throughout history, copper oxides have been studied thoroughly, both theoretically and experimentally, especially because their unique electronic and optical properties allow their potential applicability as transparent conducting oxides (TCOs) [33]. They are *p*-type semiconducting materials with band gap values that make them suitable for photovoltaic (PV) applications [4]. In addition, copper oxides are abundant, non-toxic, and have low extraction costs [34].

$\text{Cu}_2\text{O}$  is a well-examined binary oxide of copper, especially for harvesting solar energy. Schottky junctions, homo-junctions, and hetero-junctions up to nanocomposite structures based on  $\text{Cu}_2\text{O}$ , have all been studied extensively during the last two decades. However, the largest reported solar power conversion efficiency (PCE) has

not exceeded 1 %, and solar cells based on CuO and especially Cu<sub>4</sub>O<sub>3</sub> have not achieved noticeable photovoltaic performances yet. Solar cells based on CuO thin film heterojunctions with amorphous silica have reached only 3 % PCE [35], despite their almost ideal band gap value which lies in the visible part of the electromagnetic spectrum [36]. So far, only Cu<sub>2</sub>O has reached reasonable efficiencies of 5 – 6 %, being part of multi-junction solar cell devices [37].

The main reason that copper oxides are still attracting the attention of the scientific community is the theoretical PCE of Cu<sub>2</sub>O and CuO, which are estimated using the Shockley and Queisser (SQ) [8] predictor to be  $\approx 20\%$  and  $\approx 30\%$ , respectively [7]. Although, to the best of author's knowledge, data for the PCE of Cu<sub>4</sub>O<sub>3</sub> do not exist, some authors have suggested that it could be a better absorbing material than the previously characterized copper materials [38]. Following those promising arguments, the inevitable question arises why copper oxides still fail to display good photovoltaic absorbing efficiencies.

This chapter is organized as follows: in the first section, a brief review of copper oxides properties from the literature is presented. In the subsequent section the theoretical parameters have been listed, followed by a section of results and discussion, where appropriate. In the last section, answers to the questions outlined above will be addressed and the extent of the validity of results outlined.

## 3.1 Brief overview of literature

### 3.1.1 Cuprous oxide - Cu<sub>2</sub>O

**Structural properties** Cu<sub>2</sub>O is a *p*-type semiconductor (positive-hole conductor), considered as one of the oldest semiconducting materials with a high symmetry cubic structure (space group  $Pn\bar{3}m$ , Number 224, summarized in Table 3.1) [39]. It contains six atoms in the unit cell, four Cu atoms which form a face-centered sublattice, and two O atoms which make a body-centered sublattice. In other words, copper atoms are situated on the vertices of a tetrahedron around each oxygen atom. The experimental lattice constant is 4.2696 Å, and the Cu–O bond length is 1.85 Å [40]. It is a favourable material for studying semiconductivity due to the ease with which compact specimen can be prepared by the oxidation process of metallic copper [41]. During this process, an essential step is to avoid the formation of cupric oxide (CuO) which can easily form whilst cooling the cuprous oxide formed at high temperatures. The lower temperature limit of safe Cu<sub>2</sub>O oxidation is around 1050° C. However, there is an interplay between the annealing time and the quality of the grown specimen of Cu<sub>2</sub>O because, whilst avoiding the precipitation of CuO, with increased time the concentration of copper

vacancies increases [42]. Later on, it was demonstrated that  $\text{Cu}_2\text{O}$  thin-films can be produced at room-temperature using a non-vacuum process [43].

Table 3.1: Structural and mechanical properties of  $\text{Cu}_2\text{O}$ .

Lattice Constant	$a = 4.2696 \pm 0.0010 \text{ \AA}$
Space Group	$Pn\bar{3}m$ (224)
Crystal Structure	cubic
Cu - O	1.849 $\text{\AA}$
O - O	3.698 $\text{\AA}$
Cu - Cu	3.019 $\text{\AA}$
Bulk modulus	131 GPa [44]

**Mechanical properties** High-pressure x-ray diffraction experiments show that  $\text{Cu}_2\text{O}$  is stable up to 10 GPa. After that it undergoes a phase transition from cuprite into a hexagonal structure. By further increasing pressure, it undergoes another phase transition after 18 GPa, this time to the  $\text{CdCl}_2$ -type structure. In the range of 13 – 18 GPa the hexagonal and  $\text{CdCl}_2$ -type structure show coexistence. Furthermore, no decomposition of  $\text{Cu}_2\text{O}$  into  $\text{CuO}$  and  $\text{Cu}$  has been observed up to 24 GPa [44].  $\text{Cu}_2\text{O}$  has one Raman active mode,  $F_{2g}$  [45].

**Electronic properties**  $\text{Cu}_2\text{O}$  has a direct band gap at the centre of the Brillouin zone ( $\Gamma$  point). The highest valence band consists predominantly of Cu  $3d$  states, while the lowest conduction band is being formed by Cu  $4s$  levels. The  $\Gamma_{25+}$  valence band is split by spin-orbit coupling into  $\Gamma_{7+}$  (higher in energy) and  $\Gamma_{8+}$ , while the conduction band  $\Gamma_{1+}$  is labelled as  $\Gamma_{6+}$  when spin is regarded. The fundamental band gap is parity forbidden. Its value is  $E_g(\Gamma_{7+} \rightarrow \Gamma_{6+}) = 2.1720 \text{ eV}$ . It corresponds to the yellow exciton series and has the characteristic that it is a quadrupole allowed, but dipole forbidden transition (due to same parity of the Bloch states) [46]. The first direct dipole and quadrupole allowed one is the  $\Gamma_{7+} \rightarrow \Gamma_{8-}$  transition (see Figure 3.1). The transitions are named accordingly to their corresponding wavelength positions [38].

**Optical properties** Optical properties elucidate how a certain material interacts with electro-magnetic radiation in the visible part of the spectrum.  $\text{Cu}_2\text{O}$  was one of the first materials, together with Ge, whose exciton optical absorption mechanism was successfully explained. Elliot's theory from 1957 ([52]) unravelled the main features of its absorption spectra, showing the direct forbidden nature of the energy gap. The experimental absorption spectra of  $\text{Cu}_2\text{O}$  is shown in Figure 3.2 according to data from

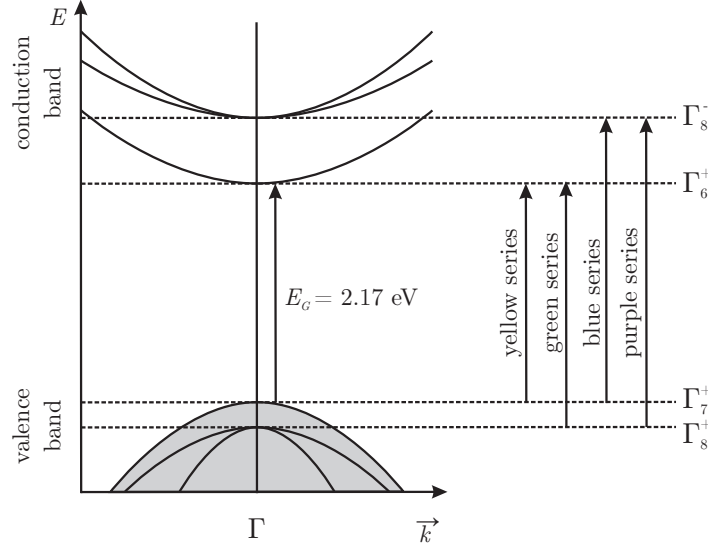


Figure 3.1: Electronic band structure diagram of  $\text{Cu}_2\text{O}$  in the proximity of the  $\Gamma$  point of the reciprocal space. On the right hand side the irreducible representation of the bands can be found together with the corresponding band transitions and their names (after Ref. [38]).

Table 3.2: Electronic and optical properties of  $\text{Cu}_2\text{O}$ .

Yellow exciton series (eV)	1.91 – 2.38 (520-650 nm) [47]
Green exciton series (eV)	2.30 – 2.58 (480-540 nm) [47]
Blue exciton series (eV)	2.53 – 2.76 (450-490 nm) [47]
	$\approx 2.6$ [48]
Violet exciton series (eV)	2.48 – 3.54 (350-500 nm) [47]
	$\approx 2.8$ [48]
Electronic band gap (eV)	2.17 [49]
	2.06 eV [50]
Optical band gap (eV)	2.38 – 2.51 [50]
Effective mass ( $m_0$ )	0.58 [51]
Optical dielectric constant	6.95 [48]

[53]. Four regions can be identified: yellow, green, blue and violet, corresponding to four excitonic series observed measuring the absorption of light at low temperatures. The yellow series is formed when an electron-hole pair is formed across the  $\Gamma_{7+}$  and  $\Gamma_{6+}$  bands. Other series can be identified in Figure 3.1 following the given colour pattern. This explains why  $\text{Cu}_2\text{O}$  actually starts to absorb light significantly only after 2.4 eV, which corresponds to the first dipole allowed band transition [54]. One additional feature of the absorption spectra is that by performing a linear fit on it, a value of the optical gap can be obtained and a phase purity check undertaken. Unfortunately, as pointed out by Malerba *et al* [55], for  $\text{Cu}_2\text{O}$  this is not the case. The most common

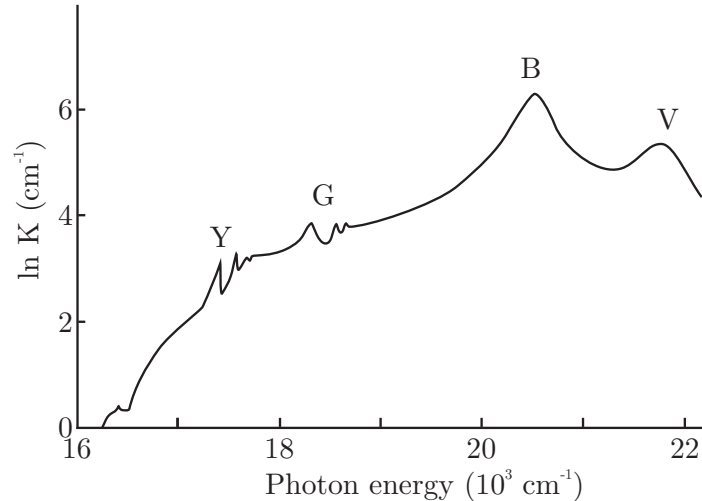


Figure 3.2: The optical absorption spectrum of Cu<sub>2</sub>O at 4.2 K, as re-plotted after Hodby *et al* [53]. Four exciton series can be identified from the spectrum's peaks: yellow (Y), green (G), blue (B), and violet (V).

expression used to fit the absorption spectrum is<sup>1</sup>:

$$\left(\hbar\nu - E_g\right)^r, \quad r = \frac{1}{2}, 2, \frac{3}{2}, \text{ and } 3,$$

where  $r$  accounts for direct allowed, indirect allowed, direct forbidden and indirect forbidden transitions, respectively. None of these is a reliable way of determining the gap of a Cu<sub>2</sub>O sample. It has been demonstrated that one can vary the optical band gap of Cu<sub>2</sub>O (thin films) by tuning the annealing temperature [50]. Increased annealing time removes copper vacancies and decreases the carrier concentration.

**Transport properties** Measurements of the electrical conductivity have been performed at the beginning of the 20<sup>th</sup> century, and have shown that it increases at any temperature with the addition of oxygen [56]. The value has been listed, together with values of mobility and scattering times, in Table 3.3. Early results suggested that the capture of photocarriers due to impurities is not effective below 100 K [42]. As in every  $p$ -type semiconductor, conduction in Cu<sub>2</sub>O arises from the presence of holes in the valence band due to doping/annealing. In contrast to other oxides, the states at top of the valence band are derived from fully occupied Cu  $3d^{10}$  orbitals, and not from O  $2p$  ones, which makes them more mobile when converted into holes [57]. The  $p$ -type conductivity remains preserved up to high temperatures, as confirmed by Hall measurements [41]. Photoconductivity and spectroscopy measurements show that the  $p$ -type conductivity arises from Cu vacancies, which give hole states 0.45 – 0.55 eV above the valence band [57]. A two-fold increase in the free hole concentration was observed for

<sup>1</sup>Also known as the Tauc expression

Cu<sub>2</sub>O with increasing oxygen flux during deposition. This was attributed to Cu<sub>2</sub>O becoming non-stoichiometric with the increasing flux, in particular the formation of intrinsic acceptor defects in the form of copper vacancies and oxygen interstitials [58].

Table 3.3: Transport properties of Cu<sub>2</sub>O as found in existing literature.

	Temperature	Value
Electrical conductivity	285 K	$2 \times 10^{-10} (\Omega \text{ cm})^{-1}$ [56]
	room temp.	$0.5 (\Omega \text{ m})^{-1}$ [58]
Hole mobility	4.2 K	$1.8 \times 10^5 \text{ cm}^2 \text{ V}^{-1} \text{ s}^{-1}$ [42]
	273 K	$130 \text{ cm}^2 \text{ V}^{-1} \text{ s}^{-1}$ [59]
Electron mobility	room temp.	$1 - 12 \text{ cm}^2 \text{ V}^{-1} \text{ s}^{-1}$ [58]
	4.2 K	$1.3 \times 10^5 \text{ cm}^2 \text{ V}^{-1} \text{ s}^{-1}$ [42]
Free hole density	room temp.	$0.084 - 2.23 \text{ cm}^2 \text{ V}^{-1} \text{ s}^{-1}$ [60]
	room temp.	$5.81 \times 10^{18} - 2.17 \times 10^{21} \text{ cm}^3$ [60]
Scattering time - holes	4.2 K	60 ps [42]
Scattering time - electrons	4.2 K	70 ps [42]
Resistivity	273 K	$3.7 \times 10^3 \Omega \text{ cm}$
Hole concentration	273 K	$1 \times 10^{17} - 5 \times 10^{18} \text{ cm}^{-3}$ [61]
	room temp.	$2 \times 10^{15} - 2 \times 10^{17} \text{ cm}^{-3}$ [58]
Seebeck coefficient	room temp.	$200 - 900 \mu\text{V K}^{-1}$ [58]
Thermal conductivity	room temp.	$5.2 \text{ W m}^{-1} \text{ K}^{-1}$ [58]

**Theoretical studies** Cuprous oxide has been extensively studied using theoretical approaches, mostly in the form of density functional theory. A comparison of selected calculated values for stoichiometric Cu<sub>2</sub>O can be found in Table 3.4. One of the first theoretical examination of cuprous oxide dates back to the work of Dahl and Switendick from 1965 [62]. They calculated one-electron energies at high-symmetry points in the Brillouin zone using the augmented plane wave method (APW), obtaining a value of 1.77 eV for the band gap. Including spin-orbit coupling effects yielded a value of 1.86 eV, being reasonably close to the experimental value of 2.17 eV. However, their calculations suffered from very narrow O 2*p* bands well below the Cu 3*d* bands. After that, more theoretical works followed rapidly, ranging from Hartree-Fock-Slater [63, 64], over tight-binding [65], full-potential APW [66] to periodic Hartree-Fock calculations [67]. Isseroff *et al* [68] used the G<sub>0</sub>W<sub>0</sub> approach to model the electronic properties

of  $\text{Cu}_2\text{O}$ . What was found is that the most accurate reproduction of experimental data was achieved by using hybrid functionals as a starting point for GW-based calculations (the so called HSE +  $G_0W_0$  approach). Ruiz and co-workers studied  $\text{Cu}_2\text{O}$  using a Hartree-Fock based calculation with the Lee, Yang, and Parr (LYP) correlation functional [67] obtaining a value of 9.7 eV for the direct band gap, reflecting the well known overestimation of periodic Hartree-Fock calculations.

Isseroff and Carter [68] surveyed common DFT-based approaches and XC functionals to conclude that the HSE06 functional is the most accurate in reproducing a number of experimental observables of  $\text{Cu}_2\text{O}$ . Also, the combined HSE +  $G_0W_0$  approach was established as a sufficiently accurate tool for studying photoemission and inverse-photoemission spectra of  $\text{Cu}_2\text{O}$ . Lany *et al* conducted a GW study to establish trends along the 3d series of TM oxides [69], examining, amongst many other,  $\text{Cu}_2\text{O}$ . It was demonstrated how GW the random phase approximation ( $GW^{\text{RPA}}$ ) underestimates not only the dielectric constant and hence the band gap energies, but also yields wrong band ordering. Improvements upon RPA, taking the LDA derived local-field (LF) effects into account ( $GW^{\text{LF}}$ ), result in a critical underestimation of the  $\text{Cu}_2\text{O}$  gap. Finally, supplying a non-local external potential ( $GW^{\text{LF}} + V_d$ ) to  $\text{Cu}_2\text{O}$  d-orbital energies improves the band gap energy to a value of 2.03 eV. Contrary to results from Ref. [68], findings show how the  $G_0W_0(\text{HSE})$  approach gives a quantitatively good description of the band gap energy itself, yet inverts the conduction band ordering of  $\text{Cu}_2\text{O}$ .

Table 3.4: Summary of calculated values for  $\text{Cu}_2\text{O}$  available in literature.

Reference	Lattice parameter (Å)	Band gap (eV)	Method employed
Ruiz <i>et al</i> [67]	4.435	9.7	CRYSTAL - HF
Martinez-Ruiz <i>et al.</i> [70]	4.300	0.5	Wien97 - GGA
Jiang <i>et al</i> [71]	4.310	-	VASP - GGA
Soon <i>et al</i> [72]	4.340	-	Quantum Espresso - GGA
Soon <i>et al</i> [73]	4.320	0.64	Dmol <sup>3</sup> - GGA
Dash <i>et al</i> [74]	4.260	0.50	ABINIT - LDA
Nolan <i>et al</i> [75]	4.289	0.47	VASP - GGA
Islam <i>et al</i> [76]	4.312	0.70	VASP - GGA
Scanlon <i>et al</i> [77]	4.290	2.12	VASP - HSE
Yan <i>et al</i> [78]	4.352	2.18	VASP - PBE0
Isseroff <i>et al</i> [68]	4.288	2.17	VASP - HSE + $G_0W_0$

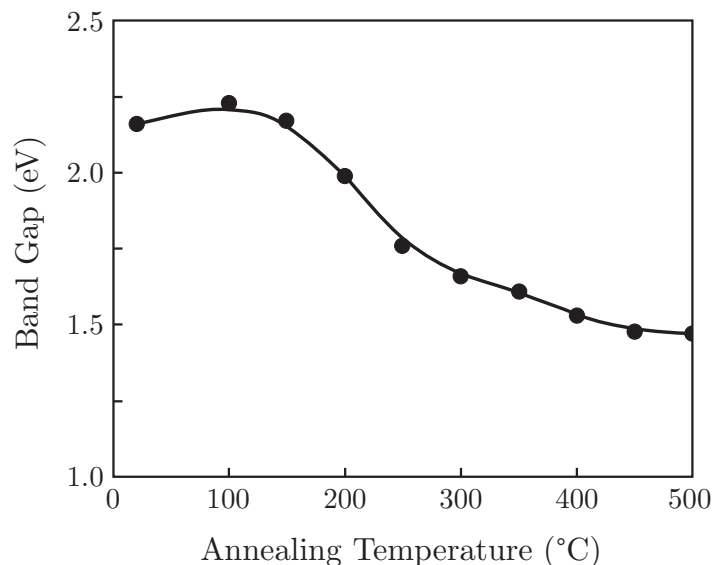


Figure 3.3: Band gap of copper oxide thin films as a function of the annealing temperature. A transformation of  $\text{Cu}_2\text{O}$  into  $\text{CuO}$  at higher temperature can be observed. Adapted from Chatterjee *et al* [43].

### 3.1.2 Cupric oxide – $\text{CuO}$

**Structural properties**  $\text{CuO}$  crystallizes in a lower symmetry monoclinic crystal structure (space group  $C2/c$ , Number 15), compared to  $\text{Cu}_2\text{O}$ . The unit cell consists of eight atoms, four Cu atoms and four O atoms. Each copper atom is coordinated by four oxygen atoms in an approximately square planar configuration, while each oxygen atom is located at the centre of a copper distorted tetrahedron [79], with the following lattice parameters:  $a = 4.6837 \text{ \AA}$ ,  $b = 3.4226 \text{ \AA}$ ,  $c = 5.1288 \text{ \AA}$  [64].  $\text{CuO}$  is usually formed upon annealing of  $\text{Cu}_2\text{O}$  at higher temperatures ( $20 - 500 \text{ }^\circ\text{C}$ ). Chatterjee and co-workers recorded the band gap dependence on temperature upon annealing and observed a full conversion into  $\text{CuO}$  taking place at around  $450 \text{ }^\circ\text{C}$  [43], as shown in Figure 3.3.

**Mechanical properties** High pressure experiments done on high-purity single crystals of  $\text{CuO}$  show no phase transitions up to 70 GPa and 3000 K [83]. Wang *et al* [84] performed high pressure studies up to 47 GPa of nanocrystalline  $\text{CuO}$ , and showed how its compressibility does not change upon particle size reduction. In addition, an anomalous lattice compression with a maximum at 13 GPa has been observed recently, associated with the change of the oxygen coordination around copper atoms from the square fourfold to octahedral sixfold coordination [85].  $\text{CuO}$  has three Raman active modes,  $A_g$  and  $2B_g$  [45].

Table 3.5: Structural and mechanical properties of CuO, as obtained from existing literature.

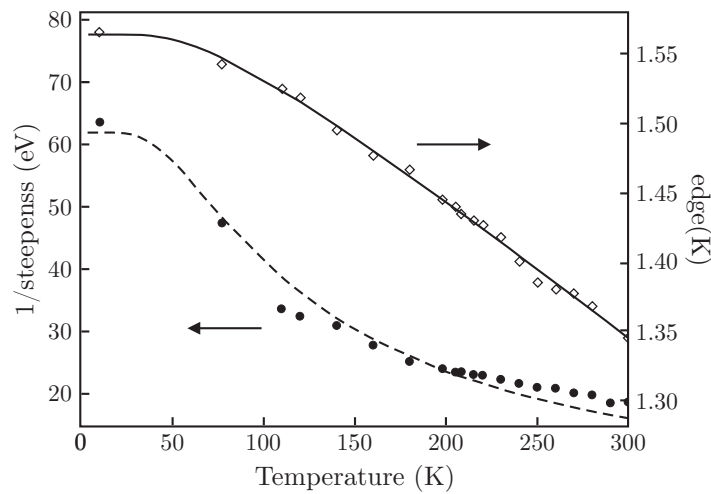
	$a = 4.6845 \text{ \AA}$ [80]
Lattice Constant	$b = 3.4221 \text{ \AA}$ [80]
	$c = 5.1288 \text{ \AA}$ [80]
Space Group	$C2/c - C_{2h}^6$ (15)
Crystal Structure	monoclinic
Cu - O <sub>1</sub>	1.946 \AA [80]
Cu - O <sub>2</sub>	1.964 \AA [80]
Cu - O <sub>3</sub>	2.785 \AA [80]
O - O	2.620 \AA [81]
Cu - Cu	2.900 \AA [81]
Bulk modulus	98 GPa [82]

**Electronic properties** First extensive electronic properties of CuO have been reported by Koffyberg and Benko in 1981 [86]. They performed photo-current measurements of polycrystalline CuO samples and estimated the band gap by plotting the quantum efficiency dependence on the photon energy. An indirect allowed band gap of  $(1.35 \pm 0.02) \text{ eV}$  has been identified, with a further direct allowed transition at  $(3.25 \pm 0.05) \text{ eV}$ . X-ray photoelectron spectroscopy (XPS) measurements done by Tahir *et al* [87] showed an energy gap value of 1.0 eV, while X-ray diffractometric (XRD) studies on CuO thin films obtained 1.9 eV (also stating that the nature of the gap is direct allowed) [88]. This large difference could be explained with the fact that a relatively large change of the band gap occurs with temperature (preceding a large temperature dependence of the absorption edge and Urbach tail), as identified by Marabelli *et al* and shown in Figure 3.4 [89]. The nature of the optical features of CuO implies a strongly localized charge distribution, valid in particular for the  $d$  states responsible for the magnetic properties [90]. Electrochemical data shows that the valence band of cupric oxide consists of Cu  $3d$  states and O  $2p$  states, while the conduction band is mainly determined by Cu  $3d$  states [38].

**Optical properties** Tanaka *et al* [94] determined the optical constants (in particular, reflectivity and absorption coefficient) for a range of polycrystalline oxides, including CuO, for incident light polarized parallel and perpendicular to the plane of incidence in the wavelength region between 350 and 1200 nm. A gradual decrease of the extinction coefficient with increasing wavelength was observed for CuO, as well as a large absorption coefficient and medium reflectivity. Measurements of optical properties, in particular the absorption spectra, depend strongly on the sample preparation and on the measurement technique used. Marabelli *et al* [89] investigated the reflectance and transmittance of CuO at different temperatures. They found that val-

Table 3.6: Electronic properties of CuO.

	1.4 eV [49], 1.9 eV[88]
	1.43 eV [43], 1.21 – 1.5 eV[89]
Electronic band gap (indirect)	1.46 eV, allowed (T = 300 K) [91] 1.54 eV, allowed (T = 80 K) [91]
	2.1 eV [92]
Electronic band gap (direct)	(3.25 ± 0.05) eV, allowed [86]
Effective mass	7.9 m <sub>0</sub> [51]
Optical dielectric constant	6.45 [48]
Refractive index	2.1 – 2.37 [93]

Figure 3.4: CuO electronic band gap value as a function of temperature. Adapted from Marabelli *et al* [89].

ues differ for samples for varying thickness and could determine no correlation between them. A strong temperature dependence of the absorbance was observed as well, with a large blue-shift for decreasing temperatures. The same conclusion was derived by Ito *et al* [48], who performed dielectric function measurements by spectroscopic ellipsometry. Due to the low crystal symmetry of CuO it is difficult to make assignments of the band-to-band transition or define exciton effects. It is also worth mentioning that, like in the case of Cu<sub>2</sub>O, the simple Tauc expression does not adequately describe (fit) the experimental absorbance above the absorption edge [48]. Excitonic structure have been tentatively speculated first by Marabelli *et al* [89].

**Magnetic structure** CuO is one of the few magnetic copper oxides that does not contain other magnetic atoms. Neutron scattering measurements have shown that CuO has anti-ferromagnetic ordering below (225 ± 5) K (Néel temperature), with an intrinsic magnetic moment placed entirely on the Cu atom with a value of (0.68 ± 0.1) μ<sub>B</sub>

(values obtained at 78 K) [95]. The observed doubling of the lattice periodicity along the  $\vec{a}$  and  $\vec{c}$  axes has been shown to appear as a consequence of the antiferromagnetic ordering of the Cu moments. The Cu–O–Cu chains are completely antiferromagnetically arranged along the [010] direction. Forsyth *et al* [96] refined the complete magnetic structure of CuO, identifying two antiferromagnetism orderings: the commensurate phase below 213 K (with a magnetic moment of  $(0.65 \pm 0.03) \mu_B$  and  $(\frac{1}{2} 0 \frac{1}{2})$  propagation) and the incommensurate phase in the range of 213–230 K. Yang *et al* [97] studied the magnetic scattering in single crystal CuO experiments. A low-temperature phase below  $T_{N1} = (212.5 \pm 1.0)$  K and an intermediate phase unto  $T_{N2} = (231 \pm 2)$  K were observed. The low-temperature phase confirmed the  $(\frac{1}{2} 0 \frac{1}{2})$  magnetic propagation. Further experiments confirmed the collinear magnetic ordering in the commensurate phase below  $T_{N1}$  and spiral magnetic ordering in the incommensurate phase between  $T_{N1}$  and  $T_{N2}$  [98]. Above  $T_{N2}$ , CuO becomes paramagnetic. The super-exchange in the Cu–O–Cu chains along the  $[10\bar{1}]$  direction was identified as the principal AFM magnetic interaction, whose large absolute value ( $J \approx 67 - 80$  meV) is responsible for the high magnetic ordering temperature  $T_{N2}$  [85]. The super-exchange along the [101] direction was found to be weakly FM, with a magnetic interaction value of  $J_1 \approx 5$  meV.

High-pressure experiments observed a decrease of the transition temperature from the commensurate into the incommensurate AFM state from 215 K to 190 K in the pressure range between 0 GPa and 11 GPa [85]. The Néel temperature demonstrates a saturation above 20 GPa, reaching a peak value of 260 K at 38 GPa. A peculiarity of CuO is the occurrence of a local magnetic moment not only at the copper atoms, but also at the oxygen atoms. This is a direct consequence of the interplay between the complex magnetic ordering and the crystal structure of CuO. Each oxygen atom is embedded in a tetrahedral environment of four copper atoms whereby one atom exhibits a magnetic moment pointing in the direction opposite to the magnetic moments of the three other copper atoms. This leads to a magnetic polarization of the electrons in the vicinity of the oxygen atom [99]. Experiments find a value of  $0.03 \mu_B - 0.05 \mu_B$  per oxygen atom.

**Transport properties** The relatively small value of mobility of CuO, whose value can be found in Table 3.7, is associated with the fact that the hole phonon coupling is large ( $m^*/m_0 = 7.9$ ) and the valence band is narrow [86]. CuO shows no phase transition (to a conventional metal) up to 700 kBar and 3000 K, but has a thermal activation energy that decreases with pressure and extrapolates to zero at 1 Mbar. This suggest that a change in the electrical behaviour could occur at this pressure [83]. The free-hole concentration showed a three-fold increase with increasing oxygen flux during deposition, associated with the increasing copper deficiency in form of

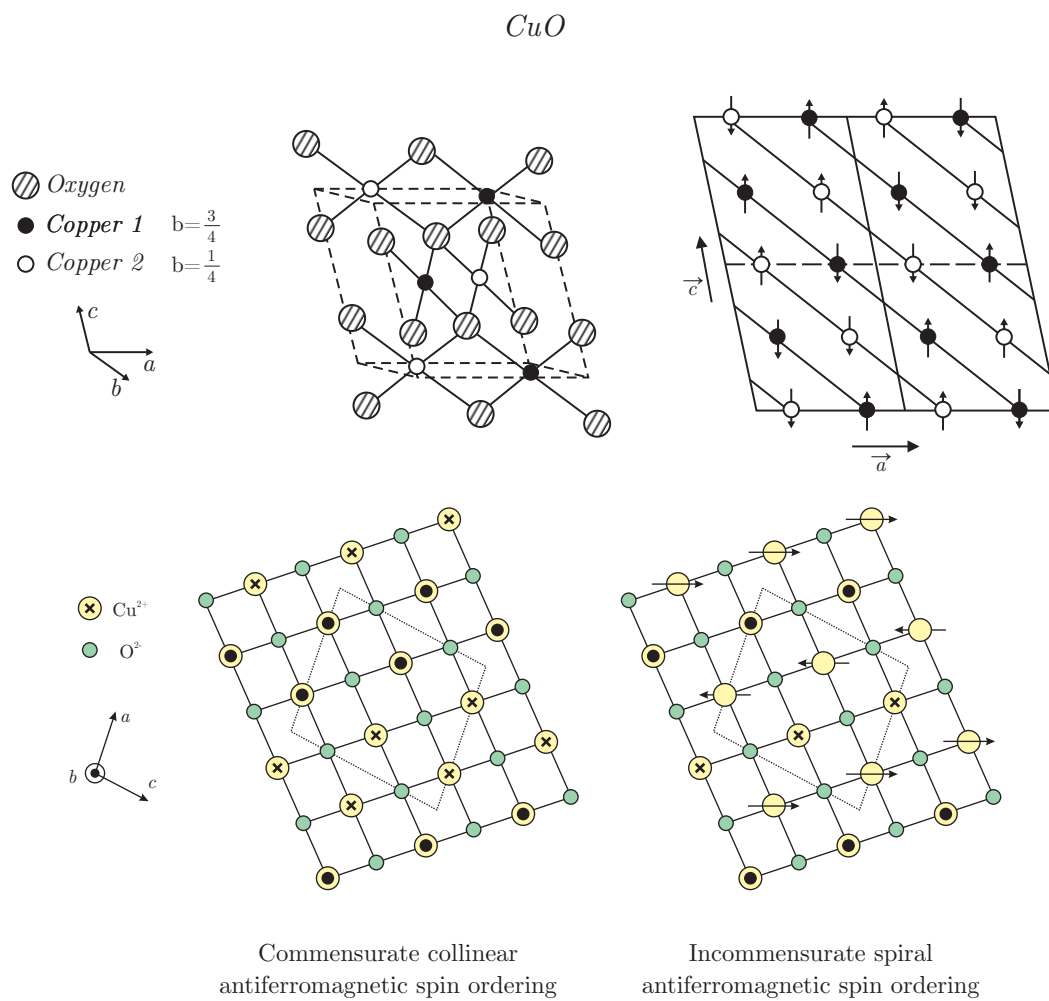


Figure 3.5: Magnetic ordering of CuO. Top figure adapted from Yang *et al* [97] and bottom figure adapted from Kimura *et al* [98].

copper vacancies and/or oxygen interstitial defects [58].

Table 3.7: Transport properties of CuO.

	Temperature	Value
Seebeck coefficient	300 K	$770 (\pm 3\%) \mu\text{V K}^{-1}$ [86]
	room temp.	$150 - 500 \mu\text{V K}^{-1}$ [58]
Resistivity	300 K	$16 (\pm 10\%) \Omega\text{ cm}$ [86]
	290 K	$1.5 \times 10^3 \Omega\text{ cm}$ [100]
Hole mobility	300 K	$0.1 \text{ cm}^2 \text{ V}^{-1} \text{ s}^{-1}$ [86]
Hole concentration	300 K	$4 \times 10^{18} \text{ cm}^{-3}$ [86]
	room temp.	$2 \times 10^{17} - 5 \times 10^{20} \text{ cm}^{-3}$ [58]
Electrical conductivity	room temp.	$0.2 - 100 (\Omega\text{ cm})^{-1}$ [58]
Thermal conductivity	room temp.	$8.6 \text{ W m}^{-1} \text{ K}^{-1}$ [58]

***n*-type CuO** Du *et al* [101] reported single phase *n*-type intrinsic CuO films prepared by magnetron sputtering combined with a high-voltage and low-current technique. Increasing substrate temperature was found to convert CuO from a *p*-type semiconductor at 75° C (348 K) to an *n*-type semiconductor at 500° C (773 K). The *n*-type conductivity was assigned to oxygen vacancies and interstitial copper atoms. Enhanced scattering rates with increasing temperature were identified as the main cause of decreasing overall carrier mobility rates with increasing temperature. Baturay and co-workers [102] observed *p*-type conductivity conversion into *n*-type in CuO thin films when doped with Co. Capacity-voltage measurements verified a change in polarity at 3% doping ratio, with no change in the band gap. Singh *et al* [93] reported successful deposition of *n*-type CuO via spin-coating. *n*-type CuO was created at moderate oxygen partial pressures (metal excess phase), leaving the material oxygen deficient in the form of oxygen vacancies. The annealing time was reported to be a crucial parameter, with CuO changing into Cu<sub>2</sub>O with prolonged time.

**Theoretical studies** CuO has been studied theoretically as well, but not extensively as Cu<sub>2</sub>O. By nature, CuO is a *p*-type semiconductor, like cuprous oxide, with the addition of a magnetic moment on the Cu atom. Standard DFT calculations, using the LDA or GGA approximation for the exchange correlation functional, fail to reproduce the electronic and magnetic structure, giving rise to a conducting and non-magnetic CuO. However, structural values and atomic distances are given highly accurate. First theoretical calculation on CuO date back to 1989, where Ching *et al* [64] calculated the

Table 3.8: Summary of *ab-initio* calculated properties of CuO collected from available literature.

Reference	Lattice parameter (Å)	Band gap (eV)	Magnetic moment	Method employed
Wu <i>et al</i> [103]	4.550, 3.340, 4.990	1.0	0.60	VASP - LSDA+ <i>U</i>
Heinemann <i>et al</i> [81]	4.588, 3.354, 5.035 4.513, 3.612, 5.141	1.39 (i) 2.74 (i)	0.66 0.54	VASP - LDA+ <i>U</i> VASP - HSE06
Ekuma <i>et al</i> [104]	Fixed structure	1.25	0.68	VASP - GGA+ <i>U</i>

band structure and densities of states by means of the first-principles orthogonalized linear combination of atomic orbitals (OLCAO) method. A direct band gap 1.60 eV at the  $\Gamma$  point was identified. Magnetic ordering was neglected in this work, which makes the ground state structure results somehow ambiguous. However, it was already speculated how CuO "may not be in exactly the same category as the transition-metal monoxides collectively known as Mott insulators" [64].

Wu *et al* [103] performed extensive DFT+*U* (precisely, LSDA+*U*) calculations on CuO to investigate its structural, electronic, and magnetic properties. Their analysis confirmed that the top of the valence band and two bottom conduction bands are attributed to Cu 3*d* orbitals. The calculated electron and hole effective masses indicated small carrier mobilities, compared to widely used Si.

Rocquefelte *et al* [105] studied the temperature dependence of magnetic and optical properties of CuO via hybrid DFT calculations. Exploring different magnetic configurations in the magnetic unit cell consisting of eight formula units, the experimentally observed ground state was reproduced with spin moments on the Cu and O atoms of  $0.65 \mu_B$  and  $0.12 \mu_B$ , respectively, and a band gap of 1.42 eV. The calculations showed that at least five magnetic exchange coupling parameters are required to describe the magnetic properties of CuO (four super-exchange and one super-super-exchange interaction parameters), with the strongest interaction in the *z*-direction of the crystal. The high-temperature behaviour of magnetism in CuO was explored via progressive destruction of the AFM spin correlation via the introduction of paramagnetic components. Simulations show a reduction in the band gap by about 0.3 eV when 37.5% of the AFM ordering is destroyed (corresponding to paramagnetic states), evidencing that the temperature dependence of the optical properties of CuO is a consequence of strong coupling between the spin order and electronic properties. Rocquefelte *et al* [106] also studied the possibility of tuning the spin exchange interaction between nearest neighbour Cu–Cu atoms from AFM to FM when the bond angle of the Cu–O–Cu bond changes from  $180^\circ$  to  $90^\circ$ , using PBE0 hybrid DFT calculations. An alternative to that is applying physical pressure which leads to significant bond angle modifications. Calculations show that applying high pressure (up to 8.8 GPa) on CuO induces an

increase in the AFM coupling implying an increased Néel temperature. Also, a larger stability of the incommensurate phase was observed, decreasing the lock-in temperature from 213 K to 207 K. The influence of bond length variation was found to be smaller compared to bond angle variation, yet retaining significance.

Heinemann *et al* [81] calculated the band structure of all three copper oxides using the DFT(LDA)+ $U$  and hybrid DFT (HSE06 with 25% of exact exchange). The DFT+ $U$  approach gives results for lattice parameters closer to experimental values, while bond lengths and the cell volumes are better described by the hybrid functional. The electronic structure was accurately reproduced with DFT+ $U$  calculations, while hybrid calculations overestimate the intrinsic band gap by almost 1 eV. Ekuma *et al* [104] presented a study of optical properties of CuO based on DFT+ $U$  calculations, using a self-consistently determined  $U_{\text{eff}}$  of 7.14 eV. A good agreement was found between the calculated valence and conduction band spectrum and experimental data, as well as electronic structure and optical spectrum, validating the use of DFT+ $U$  to study strongly-correlated systems, such as CuO. Rödl and co-workers [99] employed quasiparticle calculations to study the electronic excitations and the fundamental band gap of the CuO using the GW approximation. For a comparison between different flavours of GW self-consistency applied on the DOS and band gap of CuO, the reader is referred to the full version of the article. It was found that the band gap of CuO is extremely sensitive to the details of the GW iteration scheme employed, overestimating it dramatically (depending on the scheme, the values are overestimated by a few eV).

### 3.1.3 Paramelaconite – $\text{Cu}_4\text{O}_3$

**Structural and mechanical properties** One of the very first reports on the structure of  $\text{Cu}_4\text{O}_3$  dates back to 1941 and the work of Frondel [107], who analysed its chemical composition, density, cell size, and space group. Later on, Datta *et al* [108] postulated how paramelaconite is an oxygen-deficient tetragonal copper oxide, where the omission of oxygen atoms is compensated by the appearance of cuprous ions in place of cupric ones. However, both proposed structures had a unit cell content of  $\text{Cu}_{16}\text{O}_{14}$ , which was later attributed to the presence of admixed CuO in the analysed sample. A refined structure with the unit cell content of  $\text{Cu}_{16}\text{O}_{12}$  (i.e.,  $\text{Cu}_4\text{O}_3$ ) was identified by O’Keeffe and Bovin [109]. The correct chemical formula of paramelaconite is  $\text{Cu}_2^1+\text{Cu}_2^2+\text{O}_3$ , with two distinct copper atoms, Cu(1) and Cu(2). The first one, Cu(1), is cuprous copper and has two nearest neighbour oxygen atoms, O(1), forming collinear bonds of length 1.87 Å as found in  $\text{Cu}_2\text{O}$  (Table 3.9). Similarly, Cu(2) is cupric copper and is surrounded by four oxygen atoms in an almost square

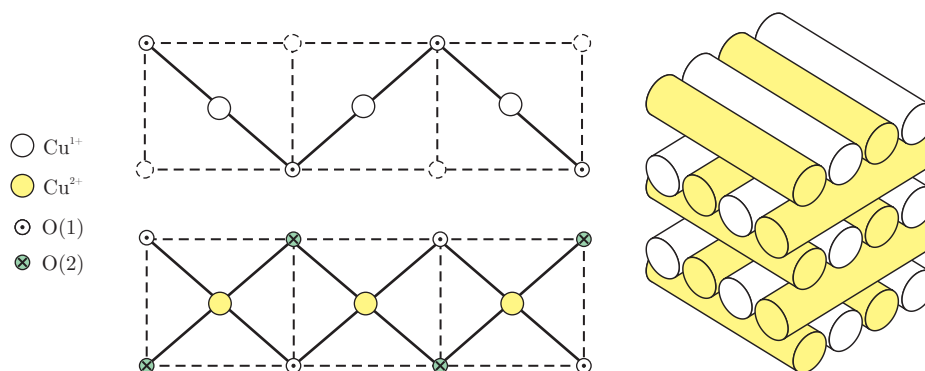


Figure 3.6: Illustration of two types of rods of atoms running through the structure of  $\text{Cu}_4\text{O}_3$ . The top rod is a zig-zag string of  $\text{O-Cu}^+-\text{O-Cu}^+$  atoms, while the bottom one is a string of  $\text{Cu}^{2+}\text{O}_4$  rectangles joined by sharing opposite edges. Adapted from O’Keeffe *et al* [110].

planar configuration with bond lengths varying between  $1.92 \text{ \AA}$  and  $1.97 \text{ \AA}$ , as illustrated in Figure 3.6.

Referring to the top Figure 3.6, it can be noted how an additional oxygen atom at sites indicated by dashed circles converts a rod of  $\text{Cu}^{1+}$  and oxygen into a rod identical to the one of  $\text{Cu}^{2+}$  and oxygen. The structure would then be that of  $\text{CuO}$ . Conversely, removing  $\text{O}(2)$  atoms from the rods on the bottom of Figure 3.6 converts  $\text{Cu}^{2+}\text{-O}$  rods into  $\text{Cu}^+\text{-O}$  ones and the resulting structure would be the same as that of  $\text{Cu}_2\text{O}$ . Hence, the structure of  $\text{Cu}_4\text{O}_3$  can be thought of as derived from  $\text{CuO}$  by ordered removal of oxygen atoms or derived from  $\text{Cu}_2\text{O}$  by ordered insertion of oxygen atoms – an intermediate stoichiometry between cupric and cuprous oxide. The name paramelaconite itself was derived from an old term used to describe the mineral  $\text{CuO}$ , namely melaconite [111]. Interestingly, Morgan *et al* [111] reported an investigation in 1996 of numerous specimen labelled as paramelaconite identifying only tenorite as the constituent phase. At that time, all authentic specimen of paramelaconite originated from the same Copper Queen mine located in Arizona, United States.

Table 3.9: Structural properties of  $\text{Cu}_4\text{O}_3$ .

Lattice Constant	$a = 5.837 \text{ \AA}$ [88] $c = 9.932 \text{ \AA}$ [88]
Space Group	$I4_1/amd$ (141)
Crystal Structure	tetragonal
Cu - O	$1.870 \text{ \AA}$ [88]
O - O	$2.560 \text{ \AA}$ [88]
Cu - Cu	$2.920 \text{ \AA}$ [88]

Pierson *et al* [112] observed the phase composition of the three copper oxides sputtered films depending on the oxygen flow rate. Up to  $3 \text{ sccm}^2$ , the films are biphased between

<sup>2</sup>Sccm – standard cubic centimetre per minute, is a flow measurement term indicating  $\text{cm}^3/\text{min}$

metallic copper and  $\text{Cu}_2\text{O}$ . Upon further increase of the oxygen flow rate, at around 4 sccm only cuprite is formed. When the oxygen flow rate is increased up to 5 sccm, no diffraction peaks of cuprite are observed and only the paramelaconite phase is detected.  $\text{Cu}_4\text{O}_3$  shows a preferred orientation in the (100) direction. When the oxygen flow rate is higher or equal to 6 sccm, only CuO is detected. Paramelaconite was observed to be sensitive to air oxidation due to different valence copper atoms within the structure, hence the observed decomposition into  $\text{Cu}_2\text{O}$  and Cu at 350 °C and into Cu at 500 °C. However, it was observed to be stable in air at 250 °C for 0.55  $\mu\text{m}$  thick samples and 350 °C for 3.2  $\mu\text{m}$  thick films [112]. In other words, the thickness and orientation of the films influence the stability and conversion temperature of  $\text{Cu}_4\text{O}_3$  in air. Furthermore,  $\text{Cu}_4\text{O}_3$  films exhibit different preferred orientations depending on the film thickness and on the sputtering mode [113]. Djurek *et al* [114] were able to prepare  $\text{Cu}_4\text{O}_3$  in the form of nanoparticles with a diameter of 56 nm. High purity paramelaconite was prepared, with two stoichiometric modifications:  $\text{Cu}_4\text{O}_3$  and  $\text{Cu}_4\text{O}_{2.5}$ , where the later one indicates an oxygen defect system. It was also observed how optical irradiation and corresponding local heating converts  $\text{Cu}_4\text{O}_3$  into CuO locally. Hence, caution is required when using excitation laser techniques in any optical probing of multivalent metal oxides [115].  $\text{Cu}_4\text{O}_3$  was observed to be stable up to 250 °C (520 K) when annealed in air [116]. It was also emphasized that upon annealing of  $\text{Cu}_4\text{O}_3$  at 410 °C (683 K) a phase conversion into CuO is observed, as well as a further conversion into  $\text{Cu}_2\text{O}$  at 450 °C (723 K). Similarly, experiments conducted by Wang *et al* [117] observed a decomposition of candy-like  $\text{Cu}_4\text{O}_3$  micro-structures into CuO and  $\text{Cu}_2\text{O}$  at 400 °C (673 K).

Group theory predicts 42 vibrational modes for  $\text{Cu}_4\text{O}_3$ , based on its crystal structure. Three modes are acoustic, while all the others are optical modes. Nine modes are Raman active ( $A_{1g}$ ,  $B_{1g}$ , and  $E_g$ ), 21 are infra-red active, and nine are silent. Low-temperature Raman measurements indicate that within the temperature range of 77 K–300 K no structural phase transitions of strong electron-phonon coupling take place [116].

**Electronic properties** First measurements of the optical band gap determined for single phase oxide films based on UV-vis transmission measurements were undertaken by Pierson *et al* in 2003 [112]. Considering two types of transitions, a direct gap of 2.47 eV and an indirect band gap of 1.34 eV were measured (see Table 3.10).

**Optical properties** The measured absorption coefficient for  $\text{Cu}_4\text{O}_3$  reaches a value of  $1 \times 10^5 \text{ cm}^{-1}$  at a value of 2.4 eV. The rise of absorbance ( $\lambda \leq 500 \text{ nm}$ ) was derived

---

in standard conditions of temperature and pressure

Table 3.10: Electronic properties of  $\text{Cu}_4\text{O}_3$ .

Electronic band gap (indirect)	1.34 eV [112], 1.5 eV [115]
Electronic band gap (direct)	2.47 eV [112], 1.75 eV [118] 2.3 eV [115]

Table 3.11: Summary of transport properties of  $\text{Cu}_4\text{O}_3$  as obtained from available literature.

	Temperature	Value
Seebeck coefficient	room temp.	$110 \mu\text{V K}^{-1}$ [58]
	room temp.	$1 \times 10^{17} \text{cm}^{-3}$ [58]
Hole concentration	N/A	$1 \times 10^{16} - 3 \times 10^{17} \text{cm}^{-3}$ [118]
	room temp.	$2.4 \times 10^{18} \text{cm}^{-3}$ [115]
	190 K	$3.0 \times 10^{16} \text{cm}^{-3}$ [116]
Electrical conductivity	room temp.	$0.1 (\Omega \text{cm})^{-1}$ [58]
	N/A	$5 \times 10^{-4} - 5 \times 10^{-3} \text{Scm}^{-1}$ [118]
Electrical resistivity	room temp.	$6.2 \times 10^8 \mu\Omega \text{cm}$ [112]
	room temp.	$55 \Omega \text{cm}$ [115]
Thermal conductivity	room temp.	$5.6 \text{W m}^{-1} \text{K}^{-1}$ [58]

from the direct band gap of 2.25 eV, while the light absorption corresponding to the indirect band gap (1.5 eV) was found to be relatively less effective [119].

**Magnetic properties** Paramelaconite was measured to order antiferromagnetically below 40 K with a propagation vector  $\vec{k} = (\frac{1}{2}, \frac{1}{2}, \frac{1}{2})$  with respect to the reciprocal basis of the conventional body centred cell [120]. The authors were unable to explain the observed magnetic ordering within models limited to isotropic super-exchange interactions, speculating upon the need to invoke higher order interactions or anisotropic exchange. Djurek *et al* [114] observed an antiferromagnetic ordering of nanoscaled  $\text{Cu}_4\text{O}_3$  at  $T < 55$  K together with an additional transition at  $T = 120$  K, whose ordering was not clarified.

**Transport properties** Hall effect measurements confirm that  $\text{Cu}_4\text{O}_3$  is a *p*-type semiconductor [116]. The reported activation energy, in other words, the thermal energy required for holes to jump into the valence band, is reported as 0.14 eV, which lies between the reported values of CuO (0.12 – 0.16 eV) and  $\text{Cu}_2\text{O}$  (0.20 – 0.24 eV). Further reported values are summarized in Table 3.11.

**Theoretical studies** First theoretical studies of  $\text{Cu}_4\text{O}_3$  date back, to the best knowledge of the author, to 2002 and the hybrid-DFT (B3LYP) study of Tejada-Rosales *et al* [121]. They evaluated the structure and magnetic exchange interactions (between nearest neighbouring Cu atoms) and obtained values of  $J_a = -11.1 \text{ cm}^{-1}$  (for the interaction along of Cu atoms along the chains) and  $J_c = -9.8 \text{ cm}^{-1}$  (for the interaction between neighbouring perpendicular chains). More recently, DFT calculations using the L(S)DA+ $U$  approach were used to study the vibrational properties of both CuO and  $\text{Cu}_4\text{O}_3$ , obtaining good agreement with experimental values [122]. A clear distinction between CuO and  $\text{Cu}_4\text{O}_3$  was observed based on the peak positions in the Raman spectrum, making it a useful probe for phase analysis.

Heinemann *et al* [81] studied the structural stability and electronic structure of all three copper oxides using the LDA+ $U$  and hybrid (HSE06) functional calculations within DFT. The reported electronic energy gaps are in good agreement with experiment for  $\text{Cu}_2\text{O}$ , while CuO and  $\text{Cu}_4\text{O}_3$  showed discrepancies between theory and experiment.

Debbichi *et al* [123] studied the lattice dynamics for paramelaconite using the LDA+ $U$  approximation. From the calculated phonon band structures, a dynamic stability was noted, as no soft modes were detected. Furthermore, the magnetic exchange coupling constants between neighbouring  $\text{Cu}^{2+}$  sites were calculated, yielding values of  $J_1 = -18.2 \text{ meV}$  and  $J_1 = -12.6 \text{ meV}$ , confirming the frustrated antiferromagnetism within  $\text{Cu}_4\text{O}_3$ . By including vibrational energy contributions to the total energy, they demonstrated the influence of the vibrational entropy on the instability of  $\text{Cu}_4\text{O}_3$  at elevated temperatures.

Recently, Wang *et al* [124] performed calculations within the  $GW$  method (highly accurate many-body perturbation technique) of the full optical absorption spectrum (both in the independent particle approximation and including excitonic effects) and quasi-particle densities of state for all three copper oxides. The  $GW$  calculations predict an indirect gap of 0.84 eV and a direct gap of 1.59 eV with an absorption onset of 1.61 eV in the IPA for  $\text{Cu}_4\text{O}_3$ . Excitonic effects were found to cause a redshift in the absorption spectrum of about 150 meV. Despite the different subgap absorption mechanisms proposed, the prediction of an indirect band gap for  $\text{Cu}_4\text{O}_3$  was confirmed through the experimentally and theoretically measured absorption spectrum.

### 3.1.4 Photovoltaic potential of copper oxides

Copper oxides are very good candidate materials for low-cost photovoltaic power generation for multiple reasons, namely [47]:

1. Theoretical solar cell power conversion efficiency.

2. Material's constituent element abundance.
3. Simple process of semiconductor layer formation.
4. Compatibility to use as material for a tandem system.

The theoretical maximum power conversion efficiency of a  $\text{Cu}_2\text{O}$  solar cell is around 20% under AM1 solar illumination. Early development, consisting of mostly Schottky barrier solar cells, yielded efficiencies on the order of 1% [125]. The main reason for this discrepancy has been attributed to the low barrier heights in the contact region between the metal and  $\text{Cu}_2\text{O}$ . Most metals, apart from gold and thallium, reduce  $\text{Cu}_2\text{O}$  to form a copper-rich region thus reducing the barrier. From that moment it was clear that in order to fabricate efficient  $\text{Cu}_2\text{O}$  solar cells, one must utilize a metal-insulator-semiconductor (MIS) structure or a hetero-junction with an  $n$ -type partner. Intrinsic  $n$ -type conductivity within  $\text{Cu}_2\text{O}$  has been speculated in the literature for a long time and is still a matter of debate. Theoretical studies elucidated and ruled out all intrinsic  $n$ -type defects (simple or complex) as the source of  $n$ -type conductivity in  $\text{Cu}_2\text{O}$  due to their high formation energies (higher in comparison to defects leading to  $p$ -type conductivity) [77].  $n$ -type  $\text{Cu}_2\text{O}$  thin films were recently reported, with the  $n$ -type conductivity expected to arise from unintentional H doping during hydrothermal synthesis [126], contradicting theoretical studies claiming that interstitial H kills effectively both  $p$ -type and  $n$ -type conductivity [127]. Despite the mentioned ongoing debate, there are three key issues concerning the employability of  $\text{Cu}_2\text{O}$  as a photovoltaic material: material growth, photocurrent, and junction formation [47].

Contrary to that, undoped  $\text{CuO}$  solar cells have been rarely reported. To make matters worse, pure  $\text{CuO}$  thin film solar cells were observed not to function [45].

Similarly, reports dealing with undoped  $\text{Cu}_4\text{O}_3$  photoabsorbers are scarce. Kim *et al* [128] reported  $\text{NiO}/\text{Cu}_4\text{O}_3/\text{ZnO}/\text{ITO}$  and  $\text{Cu}_4\text{O}_3/\text{ZnO}/\text{ITO}$  photodetectors with high-transmittance and quick photoresponse, which renders  $\text{Cu}_4\text{O}_3$  effective for transparent photoelectric applications. Meyer *et al* [38] deposited  $\text{Cu}_4\text{O}_3$  onto  $n$ -type  $\text{GaN}$  and measured the resulting current-voltage characteristics. An efficiency of 0.009% was measured for the heterojunction, showing inferiority to the already low efficiency of 0.14% for a heterostructure of  $\text{Cu}_2\text{O}/\text{GaN}$ .

### 3.1.5 Concluding remarks on literature review

To summarize the information obtained from extensive literature research, all three copper oxides of interest are  $p$ -type semiconductors with distinct properties governing their physical, electronic, magnetic, and optical behaviour. Regarding theoretical studies, the main issue with simple approximation for the XC functional within DFT

is the failure to accurately describe the electronic and magnetic properties. While the electronic band gap of  $\text{Cu}_2\text{O}$  is underestimated, for  $\text{CuO}$  and  $\text{Cu}_4\text{O}_3$  it is non-existent, if one relies on LDA and GGA approximations. This was attributed to strong hybridization between copper  $d$  and oxygen  $p$  orbitals, which varies from one oxide of copper to another. One way of overcoming those issues is supplementing DFT by an on-site Coulomb correction (DFT+ $U$ ), which allows one to tune the electronic band gap value for  $\text{CuO}$  and  $\text{Cu}_4\text{O}_3$ , yet wrongly addressing the nature of the gap of  $\text{Cu}_4\text{O}_3$  as being direct. Also,  $\text{Cu}_2\text{O}$  remains severely underestimated due to it being a band insulator, whereas  $\text{CuO}$  and  $\text{Cu}_4\text{O}_3$  are Mott/charge-transfer insulators for which the DFT+ $U$  approximation was constructed in the first place [124, 129]. Hybrid functionals give excellent structural results, but yield overestimated electronic band gaps values of strongly correlated materials, in this case  $\text{CuO}$  and  $\text{Cu}_4\text{O}_3$  [81]. More sophisticated methods using Green's functions and the screened Coulomb interaction (so-called  $GW$  methods [130, 131]) yield promising accuracy, but are prohibitively computationally expensive and bring additional parametrizations which are strongly dependent on the system of interest. Also, their validity for doped systems, nanostructures, or junctions of copper oxides is yet to be confirmed and evaluated.

Being aware of the vast and detailed work that has been already carried out on all three copper oxides, the aim of this work is not to duplicate existing data, but rather to define an affordable approach and address missing parts that could help to explain some of the major questions still open in this area. Some of the questions being assessed within this chapter include:

- Can a unique computational (DFT based) framework for all three copper oxides of interest be defined? If so, what is the extent to which it is applicable?
- Can the power conversion efficiencies of copper oxides be calculated accurately within this framework?
- Can calculated values elucidate why copper oxides fail to achieve high-absorbing photovoltaic efficiencies?

In order to do so, first-principle calculations within a set of unique approximation (relying on a minimal number of additional parameters), for the description of three oxides of copper have been performed.

## 3.2 Technical details and computational parameters

Within this part of the work, density functional theory (DFT) calculations of all three copper oxides using the Vienna Ab-Initio Simulation Package (VASP) code [132, 133] with a plane-wave basis set and PAW potentials [134, 135] have been employed. The Perdew–Burke–Ernzerhof (PBE) generalised gradient approximation (GGA) [136] for the exchange-correlation (XC) functional was used for both DFT and DFT+ $U$  [16, 17, 137, 138], while the hybrid-DFT XC functional was used with an additional 25% of the exact Hartree-Fock (HF) exchange (HSE06) [19–21]. The total energy was required to converge to within  $10^{-5}$  eV, and the interatomic forces were minimized to less than  $0.01$  eV/Å for structural relaxations.

For the sampling of the Brillouin-zone, a  $\Gamma$ -centered Monkhorst-Pack k-mesh was used [22]. Long distance dispersion corrections were included using the D3-approach of Grimme *et al* [139]. All calculations have been performed with spin polarization. Convergence of the size of the plane wave basis and the number of k-points employed was tested independently for  $\text{Cu}_2\text{O}$ ,  $\text{CuO}$ , and  $\text{Cu}_4\text{O}_3$ . A cut-off energy of 500 eV together with  $7 \times 7 \times 7$ ,  $5 \times 5 \times 5$ , and  $5 \times 5 \times 3$  meshes, respectively, was sufficient to reach convergence. Electronic band structure and density of states (DOS) calculations were performed along high-symmetry directions obtained from the Bilbao Crystallographic Server [140–142]. The electronic band structures were plotted using the Wannier90 code [143]. Crystal structure drawings were produced with VESTA [144]. Due to the increasing computational cost of the proposed approach, and in order to compare structural and mechanical properties, a simplified arrangement of  $\text{CuO}$  spins was adopted, rather than the fully extended model proposed by Forsyth *et al* [96]. Values for the effective Hubbard parameter  $U_{\text{eff}}$  were applied on the localized  $3d$  electrons of Cu, and systematically varied in intervals of 1 eV from 0 eV up to 9 eV. For each material, the atomic positions and lattice parameters were fully relaxed until the required convergence criterion was satisfied. Calculated values were compared with experimental lattice parameters, magnetic moments, and band gap values. On this basis, a common  $U_{\text{eff}}$  value of 8 eV was determined to give the closest representation of the properties of interest for all three copper oxides (see Figure 3.7). Using the DFT+ $U$  generated wave functions and relaxed geometries as starting points, additional hybrid DFT calculations were performed in two different ways. In the first approach, the geometry was allowed to fully relax, while the second approach included one static self-consistent calculation, which showed no significant differences in band structures, magnetic configurations or lattice parameters.

Frequency dependent dielectric calculations were performed within the independent

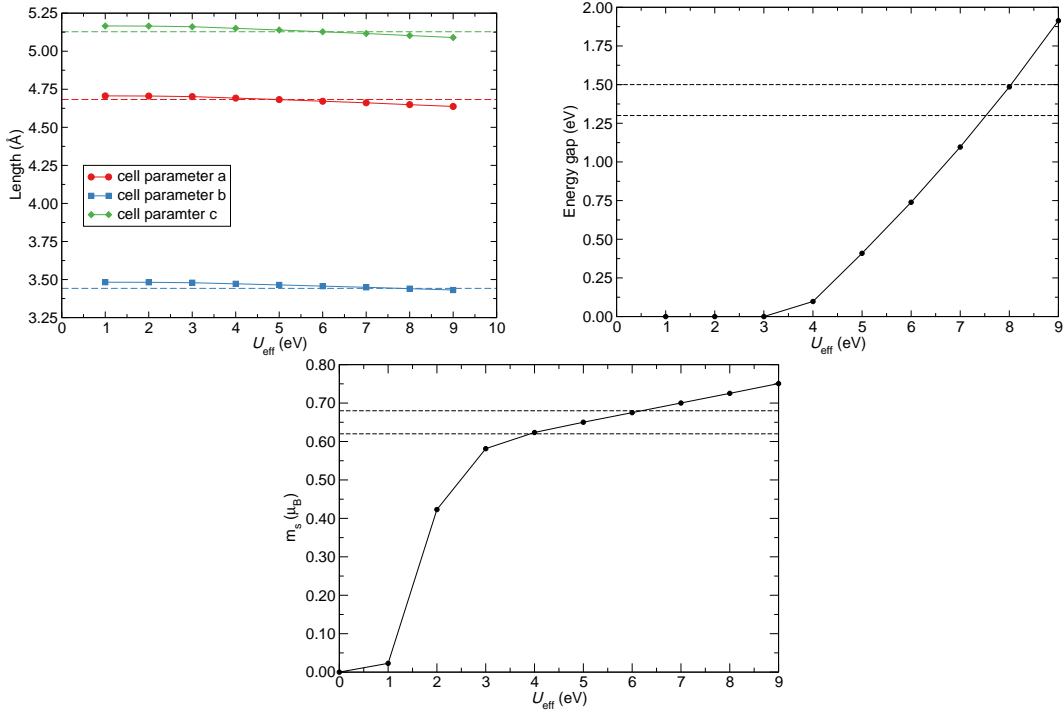


Figure 3.7: Calculated dependence of the lattice parameters (top left), electronic band gap value (top right) and (spin only) magnetic moment (bottom) on the effective  $U_{\text{eff}}$  parameter within DFT+ $U$  for CuO. Dashed lines indicate the range of experimental values used to fit the  $U_{\text{eff}}$ .

particle approximation and electronic allowed or forbidden band gaps were determined from the dipole matrix element square at the  $\Gamma$ -point,  $|M|^2$ .  $|M|$  contains dipole transition matrix elements between valence and conduction states. If  $|M|^2 < 10^{-3} \text{ eV}^2/\text{\AA}^2$ , the transition was considered to be dipole forbidden, otherwise it was viewed as dipole allowed [145]. Local field effects have been neglected. The number of empty conduction states in the calculation were checked for convergence until the same values were obtained as resulted from density functional perturbation theory embedded in VASP. It was also noted that the dipole matrix elements do not depend on the employed XC functional, i.e., they retain the nature of transitions.

For solar cell applications, the most important consideration is how absorption varies over the solar spectrum, so the single value of band gap is of little consequence in practice. To assess the PV absorbing potential of copper oxides, the selection metric of ‘spectroscopic limited maximum efficiency’ (SLME) proposed by Yu and Zunger was followed [145]. This concept allows to evaluate the PV conversion efficiency of copper oxides relying on two calculated values: absorption spectrum (coefficient) and band gap. SLME reproduces the SQ metric in the simple case of direct allowed band gap materials. The elastic tensor was determined by performing finite lattice distortions (which allow the calculation of the Hessian matrix) and elastic constants were derived from the strain-stress relationship [146]. Spin-orbit coupling and excitonic effects were

not included within this part of the work.

**Dielectric function** The dielectric function describes the response of a crystalline material to an incident electromagnetic field, in this case sunlight. It is a complex entity which depends sensitively on the electronic band structure and can be written as the sum of a real and imaginary part  $\varepsilon(\omega) = \varepsilon_r(\omega) + i\varepsilon_i(\omega) \equiv \varepsilon_1(\omega) + i\varepsilon_2(\omega)$ . The real part describes the change in velocity of the incident electromagnetic wave (wave propagation), while the imaginary part characterizes the energy transfer from the wave (and its field) to the solid (wave attenuation). The dielectric function was calculated by activating the LOPTICS tag within VASP, which calculates the frequency dependent dielectric matrix after the electronic ground state has been determined (in the independent particle approximation). The imaginary part is determined by a summation over empty states, as introduced by Gajdoš *et al* [147], and the real part is obtained using Kramers-Kronig relations. Unfortunately, the dielectric function is not directly accessible experimentally from optical measurements, where one often directly measures the reflectance  $R(\omega)$ , refractive index ( $n(\omega)$ ), and the extinction coefficient  $\kappa(\omega)$ . However, once the dielectric function is obtained, the absorption coefficient can be calculated:

$$\alpha = \frac{4\pi\kappa}{\lambda_0} = \frac{4\pi E}{hc_0}\kappa, \quad (3.1)$$

where  $\kappa$  is the extinction coefficient<sup>3</sup> and  $\lambda_0$  the light wave length in vacuum. The extinction coefficient is expressed through the following equation:

$$\kappa = \sqrt{\frac{-\varepsilon_r + |\varepsilon|}{2}}. \quad (3.2)$$

Within these relationships, the absorption coefficient can be further expressed as:

$$\alpha(\omega) = \frac{\omega\varepsilon_i(\omega)}{c_0n(\omega)}, \quad (3.3)$$

where  $\omega$  is the frequency,  $c_0$  the speed of light in vacuum, and  $n(\omega)$  the refractive index.

---

<sup>3</sup>The term extinction coefficient has been declared obsolete, yet it still can be found in both old and new literature. The new term is attenuation coefficient and within this work they are used interchangeably.

**Spectroscopic limited maximum efficiency - SLME** Once the absorption coefficient is calculated, the absorptivity  $a(E)$  is determined through the expression:

$$a(E) = 1 - e^{-2\alpha(E)L}, \quad (3.4)$$

where  $L$  is the thickness of the absorber layer with a reflecting back surface [148]. The theoretical maximum solar cell efficiency is defined as:

$$\eta = \frac{P_m}{P_{in}}, \quad (3.5)$$

where  $P_m$  is the maximum power density and  $P_{in}$  is the total incident power density available from the solar spectrum. Within SLME, the maximum power density is derived using the  $J - V$  characteristic of the solar cell:

$$P = JV = \left( J_{sc} - J_0 \left( e^{\frac{eV}{kT}} - 1 \right) \right) V, \quad (3.6)$$

where  $J$  is the total current density,  $V$  the potential over the absorber layer,  $k$  Boltzmann's constant,  $T$  temperature of the device, and  $e$  the elementary charge. The short circuit current density  $J_{sc}$  and the reverse saturation current density  $J_0$  are calculated from the absorptivity  $a(E)$  of the material, the AM1.5G solar spectrum  $I_{sun}(E)$ , and the black-body spectrum  $I_{bb}(E, T)$ :

$$J_{sc} = e \int_0^\infty a(E) I_{sun}(E) dE, \quad (3.7)$$

$$J_0 = \frac{J_0^r}{f_r} = \frac{e\pi}{f} \int_0^\infty a(E) I_{bb}(E, T) dE, \quad (3.8)$$

where  $J_0^r$  is the radiative recombination current density. The fraction of radiative recombination  $f_r$  is modelled using a Boltzmann factor:

$$f_r = \exp \left( - \frac{E_g^{da} - E_g}{kT} \right), \quad (3.9)$$

where  $E_g$  and  $E_g^{da}$  are respectively the fundamental and direct allowed band gap.

### 3.3 Results and discussion

**Structural and mechanical properties** The calculated lattice parameters for the considered three copper oxides reproduce experimental data very well, as shown at the top of Table 3.12. As demonstrated within earlier studies, the present GGA(+ $U$ ) and hybrid functionals provide good description of the structural properties of stoi-

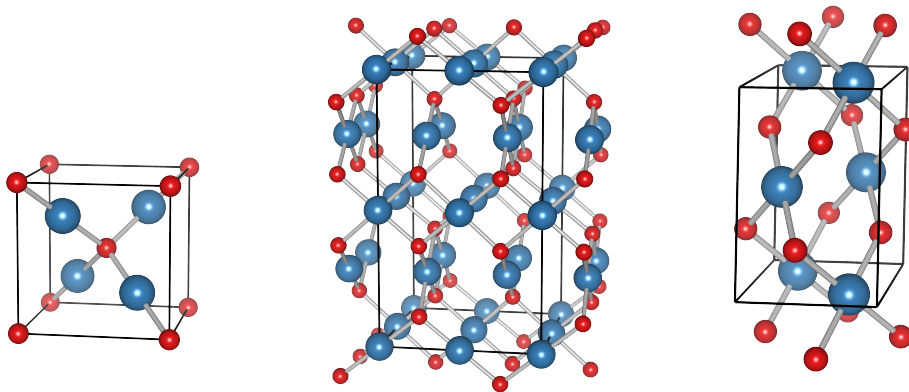


Figure 3.8: Crystal structure of copper oxides:  $\text{Cu}_2\text{O}$  (left),  $\text{Cu}_4\text{O}_3$  (middle), and  $\text{CuO}$  (right). Blue coloured spheres represent copper atoms, while red coloured balls represent oxygen atoms.

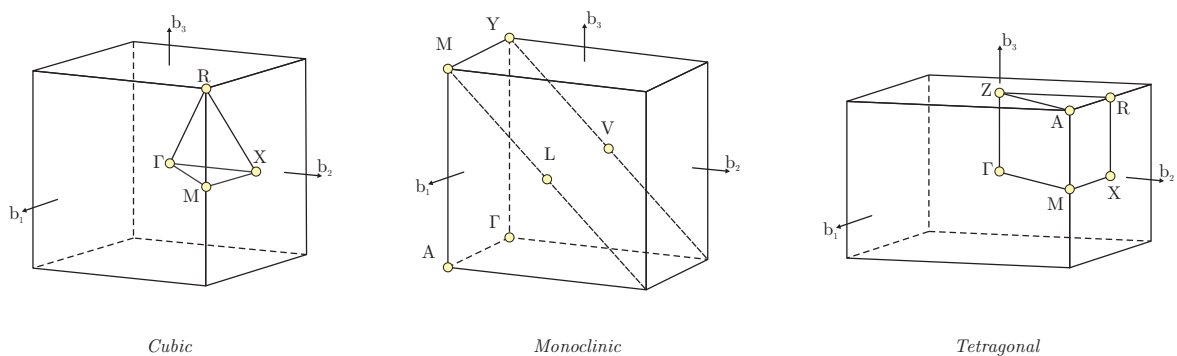


Figure 3.9: Brillouin zone of cubic, monoclinic, and tetragonal crystal lattice, out of which the electronic band structure path was derived for  $\text{Cu}_2\text{O}$ ,  $\text{CuO}$ , and  $\text{Cu}_4\text{O}_3$ , respectively.

stoichiometric copper oxides. The crystal structure of copper oxides is depicted in Figure 3.8.

Elastic constants and elastic moduli are amongst the most fundamental parameters that provide information on the mechanical properties and behaviour of materials. The number of inequivalent elastic coefficients for each oxide of copper depends on the lattice symmetry and respective point group, yielding three for  $\text{Cu}_2\text{O}$ , thirteen for  $\text{CuO}$ , and six for  $\text{Cu}_4\text{O}_3$ . Elastic constants and various elastic properties, e.g., the bulk modulus ( $B$ ), shear modulus ( $G$ ), effective Young's modulus ( $E$ ), and Poisson's ratio ( $\nu$ ), have been calculated for each copper oxide and summarized in Tables 3.12, 3.13, 3.14, and 3.15. To confirm values obtained from elastic constant calculations, the bulk modulus was deduced from a Birch-Murnaghan equation of state (EOS) [153]. Calculated values fall within the experimental range of available data, confirming the high accuracy of the proposed modelling approach. Furthermore, compared to previous theoretical data, the elastic constants do not show negative values, indicating the stability and rigidity of bulk copper oxides.

Furthermore, the stiffness of copper oxides was explored through calculations of the micro-hardness parameter ( $H$ ) [149], which denotes the resistance of a physical

Table 3.12: Calculated values of structural and elastic properties for  $\text{Cu}_2\text{O}$ ,  $\text{Cu}_4\text{O}_3$ , and  $\text{CuO}$  using DFT, DFT+ $U$ , and HSE06. The shear and first bulk modulus (BM) were calculated using the Voigt-Reuss-Hill approximation [149], while an additional bulk modulus was calculated using the Birch-Murnaghan equation of state.

		$\text{Cu}_2\text{O}$	$\text{Cu}_4\text{O}_3$	$\text{CuO}$
Lattice parameter (Å)	DFT	4.271	5.863, 9.939	4.716, 3.439, 5.104
	DFT+ $U$	4.231	5.742, 9.970	4.648, 3.439, 5.031
	HSE06 <sub>relaxed</sub>	4.253	5.773, 9.928	4.670, 3.455, 5.055
	HSE06 <sub>single point</sub>	4.231	5.742, 9.970	4.648, 3.439, 5.031
	Experimental	4.269 [150]	5.837, 9.932 [81]	4.683, 3.422, 5.128 [88]
BM - Hill (GPa)	DFT	114.07	119.26	101.32
	DFT+ $U$	102.60	118.89	99.16
BM - EOS (GPa)	DFT	108.66	127.35	144.25
	DFT+ $U$	94.40	110.10	95.58
	Experimental	112 [64]	-	98[82], 80[84], 72[151]
Shear modulus (GPa)	DFT	7.06	42.96	54.50
	DFT+ $U$	5.06	57.69	78.92
	Experimental	9.1-11.8 [152]	-	-
Young modulus (GPa)	DFT	20.76	115.08	138.65
	DFT+ $U$	14.92	148.99	187.12
	Experimental	25.3-32.3 [152]	-	-
Microhardness parameter (GPa)	DFT	0.142	4.607	8.286
	DFT+ $U$	0.081	8.033	16.547
	Experimental	-	-	-
Isotropic Poisson ratio	DFT	0.469	0.339	0.271
	DFT+ $U$	0.475	0.291	0.185
	Experimental	0.360-0.391 [152]	-	-
Equivalent Zener anisotropy factor	DFT	1.933	4.661	1.217
	DFT+ $U$	1.469	7.262	1.041
	Experimental	-	-	-

Table 3.13: Calculated values of elastic constants for  $\text{Cu}_2\text{O}$  using DFT and DFT+ $U$ . Reported values are listed in GPa.

	$c_{11}$	$c_{12}$	$c_{44}$
Exp.[154]	116-126	105-108	11-13
DFT	121.46	110.39	2.86
DFT+ $U$	106.23	100.79	3.99

Table 3.14: Calculated values of elastic constants for  $\text{Cu}_4\text{O}_3$  using DFT and DFT+ $U$ . No experimental work is, to the best of author's knowledge, available for comparison. Reported values are listed in GPa.

	$c_{11}$	$c_{12}$	$c_{44}$	$c_{13}$	$c_{33}$	$c_{66}$
DFT	156.96	64.14	9.96	113.52	227.51	7.78
DFT+ $U$	186.76	44.01	9.82	101.38	250.07	3.92

Table 3.15: Calculated values of elastic constants for CuO using DFT, DFT+ $U$ . Reported values are listed in GPa.

	$c_{11}$	$c_{12}$	$c_{44}$	$c_{13}$	$c_{33}$	$c_{66}$	
Ref.[154]	196.41	122.63	20.28	114.64	293.70	56.44	
DFT	243.28	132.03	45.70	151.88	277.56	63.50	
DFT+ $U$	258.19	139.52	56.99	118.93	312.80	106.67	
	$c_{22}$	$c_{55}$	$c_{15}$	$c_{23}$	$c_{25}$	$c_{35}$	$c_{46}$
Ref.[154]	125.01	30.07	-26.99	96.89	-27.85	-48.94	-1.15
DFT	96.26	13.59	0.00	87.71	0.00	0.00	0.00
DFT+ $U$	109.83	56.99	0.00	57.26	0.00	0.00	0.00

object against compression of the contacting parts. Based on this characterization, only copper (II) oxide can be regarded as a hard material, with  $\text{Cu}_4\text{O}_3$  falling closely behind (hard materials reach values of  $H > 10$  [155]). In addition, the equivalent Zener anisotropy factor ( $A_z^{eq}$ ) was examined in order to explore the elastic anisotropy characteristics of the crystal. A factor that is close to 1 means that the material is fully elastically isotropic, otherwise it is elastically anisotropic. Interestingly, the value for  $\text{Cu}_2\text{O}$  is higher than the one for CuO, indicating greater elastic isotropy for the monoclinic structure (perhaps due to instability), with  $\text{Cu}_4\text{O}_3$  being highly elastically anisotropic.

**Electronic properties** In contrast to its mechanical properties, the electronic properties of  $\text{Cu}_2\text{O}$  are underestimated within the GGA approximation, giving rise to an electronic band gap value of only 0.5 eV. An additional potential added to GGA ( $+U_{\text{eff}}$ ) increases the value to 0.95 eV, which is still less than half of the experimental value (2.10 – 2.38 eV [50]). The cause of this discrepancy has been explained and reported extensively [57, 156, 157]. The influence of the  $U_{\text{eff}}$  value on the electronic band structure and densities of state is shown in Figure 3.10, where the VB top and CB bottom remain largely unaffected because they arise from Cu  $d$  states – such materials are usually named band insulators, where correlation effects are weak due to either com-

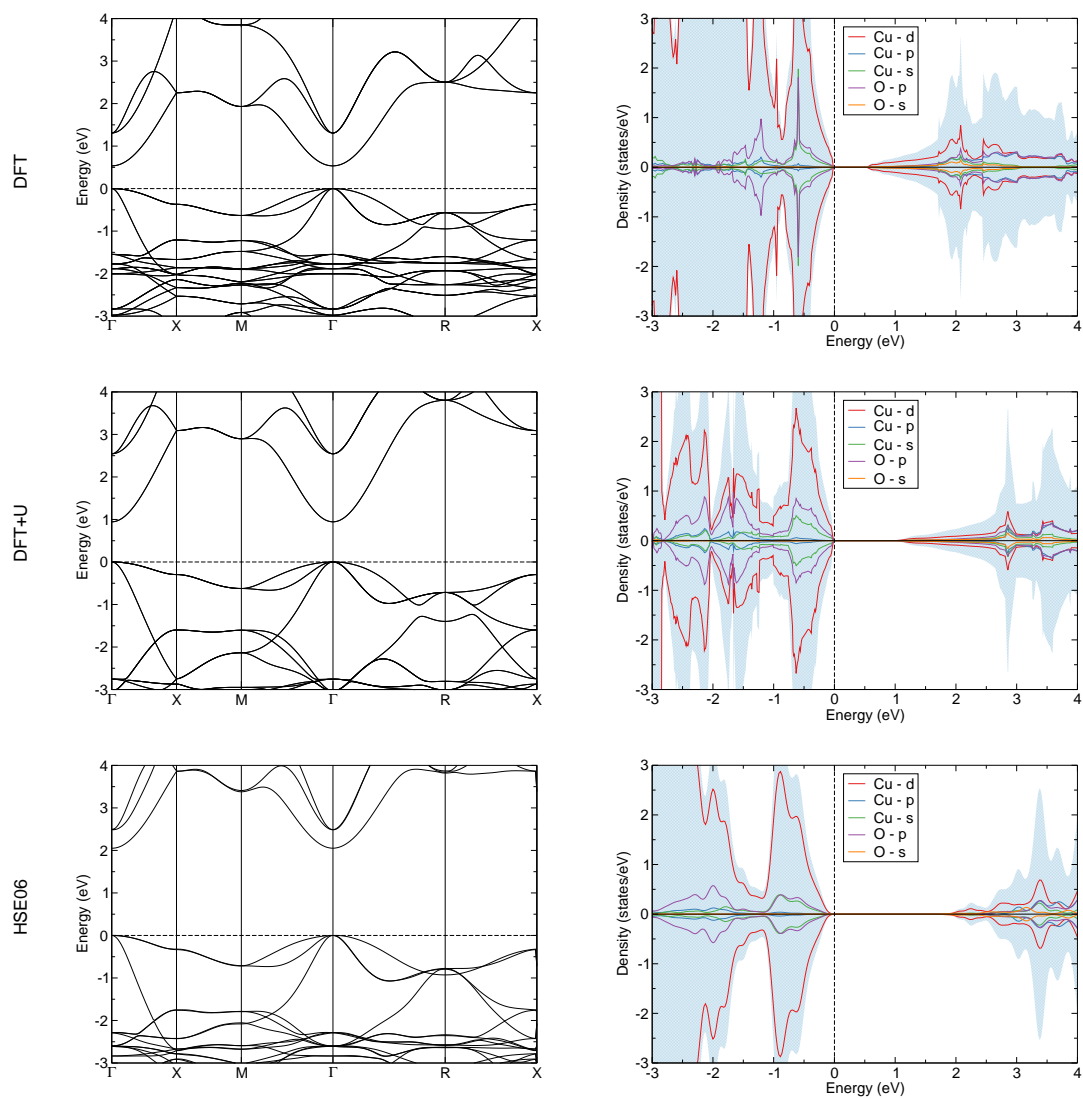


Figure 3.10: Calculated electronic band structure and orbital projected densities of state for  $\text{Cu}_2\text{O}$ . The top two graphs are derived from DFT, middle two graphs from DFT+ $U$ , and the bottom two graphs from HSE06 calculations.

pletely filled or entirely empty bands. A major improvement was obtained using hybrid functionals, which led to the calculated values listed in Table 3.16. Broadly speaking, the electronic structure calculations of bulk  $\text{Cu}_2\text{O}$  show the typical features that have already been described [35, 38].

Calculations of the electronic dipole transition matrix provide insight into the nature of certain band transitions and rationalise the link to absorption properties. For  $\text{Cu}_2\text{O}$ , the first transition between the VB top and the CB bottom is electric dipole forbidden, agreeing with previous experimental and theoretical observations [54, 158, 159]. Nevertheless, this transition is electric quadrupole allowed (and possibly magnetic dipole allowed, which has only been speculated upon so far) so that, linking it to the absorption spectra and dielectric function, it will give rise to a small, almost negligible absorption onset. The first allowed transitions are from the two top valence bands to the second conduction band with calculated energies of 2.478 eV and 2.485 eV, respectively. The nature and values of the transitions correspond very well with experimental data, as shown in Table 3.16. Furthermore, it should also be noted that no spin-orbit interaction was included in the calculations, which is known to affect the top of the valence band by an additional splitting of  $\approx 0.15$  eV [38].

$\text{CuO}$  is a strongly correlated system and standard DFT fails to predict its semi-conducting ground state, obtaining a non-magnetic (zero local magnetic moment) and metallic ground state instead, as shown in Figure 3.11 and reported previously [103, 160, 161]. However, by adding and tuning the  $+U_{\text{eff}}$  value, the electronic and magnetic structure of cupric oxide is simulated accurately [104, 138]. Surprisingly, adding a portion of the exact HF exchange does not seem to systematically improve the electronic structure calculations for  $\text{CuO}$ . Heinemann *et al* [81] performed HSE06 simulations on top of LDA+ $U$  and obtained a value of 2.74 eV with an indirect nature of the band gap and AFM ordering. Calculations employing hybrid functionals on top of GGA+ $U$  give a value of 2.102 eV, with the same indirect nature of the fundamental transition and a magnetic moment placed entirely on copper atoms with an individual value of  $0.70 \mu_{\text{B}}$  (agreeing well with the experimental value of  $0.68 \mu_{\text{B}}$  [143]). In addition, total energies of all three possible unique AFM ground states configurations were calculated and compared within the conventional cell of  $\text{CuO}$ , employing hybrid functionals. Surprisingly, band gap values range from 2.102 eV to 2.718 eV, keeping the nature of the transition intact. This indicates that not all AFM spin configurations are equally favourable and that  $\text{CuO}$  is sensitive to the initial calculation parameters.

Dipole transition matrix element calculations could clarify the picture for  $\text{CuO}$ . These suggest that the nature of the transport gap is not only indirect, but also forbidden on the basis of the electric dipole. Furthermore, the next three transitions between the valence and conduction band (ordered by the lowest possible energy)

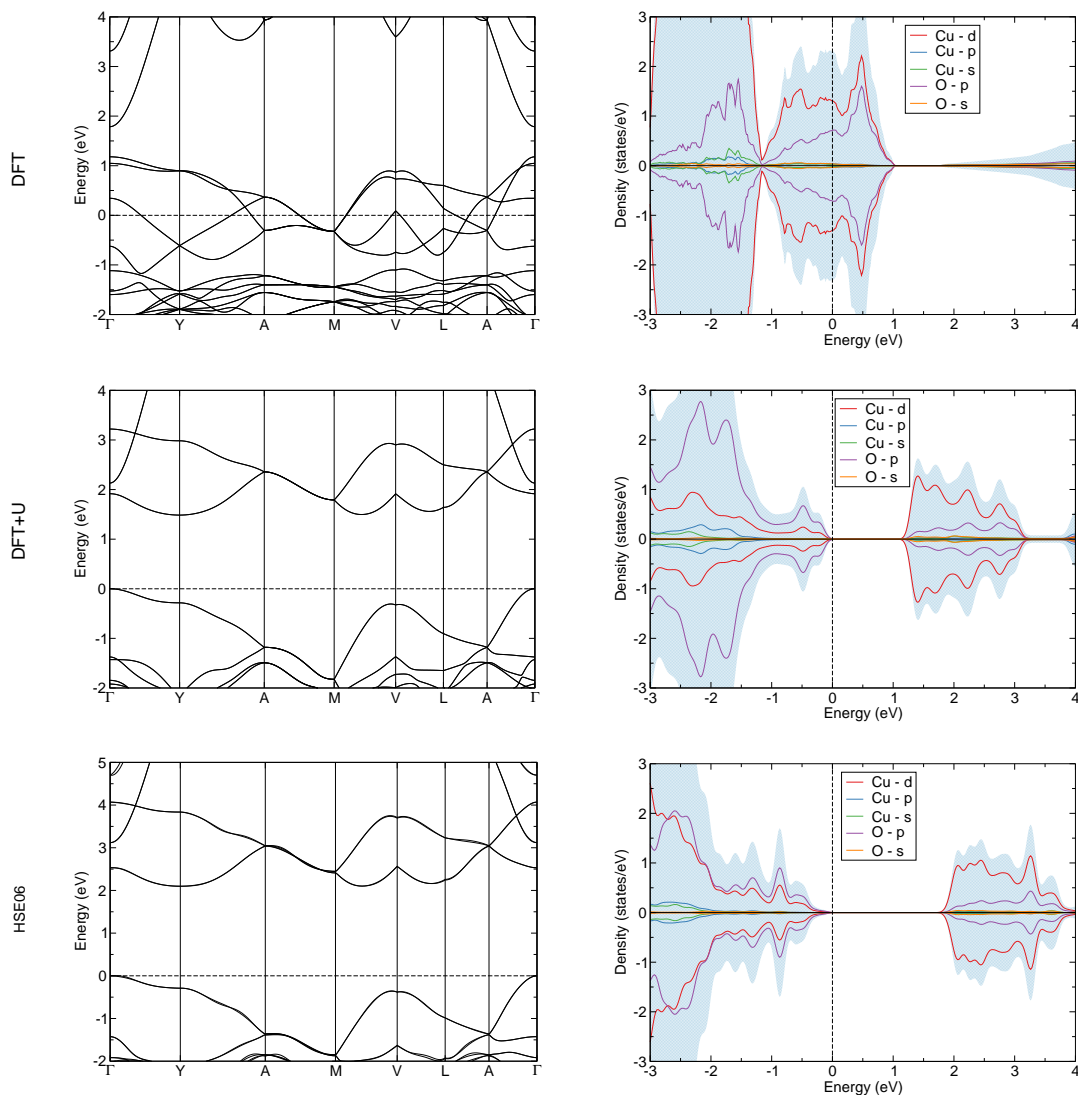


Figure 3.11: Calculated electronic band structure and orbital projected densities of state for CuO. The top two graphs are derived from DFT, middle two graphs from DFT+ $U$ , and the bottom two graphs from HSE06 calculations.

Table 3.16: Calculated electronic band gap energies of  $\text{Cu}_2\text{O}$ ,  $\text{Cu}_4\text{O}_3$ , and CuO, compared to experimental values. Also, the estimated nature of the transition together with the type of the band gap are listed.

Compound	Type of transition	Nature of transition	DFT (eV)	DFT+ $U$ (eV)	HSE06 (eV)	Exp. value (eV)
$\text{Cu}_2\text{O}$	Direct	Dipole forbidden	0.535	0.945	2.052	2.10 – 2.38 [50]
$\text{Cu}_4\text{O}_3$	Indirect	-	-	-	2.370	1.34 – 1.50 [81], 1.75 [128]
	Direct	Dipole forbidden	-	1.558	2.620	
CuO	Indirect	-	-	1.485	2.102	1.0 – 1.9 [38, 87, 88]
	Direct	Dipole forbidden	-	1.916	2.578	

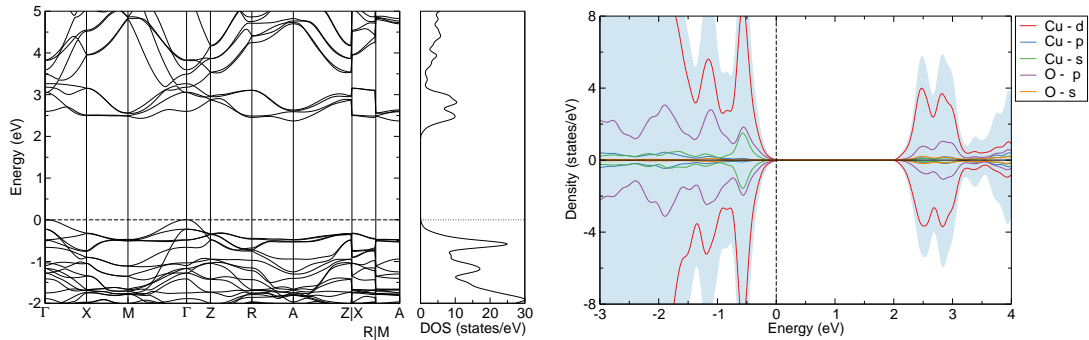


Figure 3.12: Calculated electronic band structure diagrams together with the cumulative densities of state (right) for  $\text{Cu}_4\text{O}_3$ . Also, the orbital projected densities of state have been presented, both calculated with the HSE06 functional. The valence band maximum has been set to zero and indicated with the dashed line.

indicate dipole forbidden character. The first direct allowed transition occurs at an energy difference bigger than 4 eV and only in certain directions within the crystal. This information could serve as a starting point for new and accurate experimental work, but also for theoretical work incorporating spin-orbit coupling effects, which could affect those values and induce possible band splitting. One additional point of awareness regards the modelling of indirect gap semiconductors in general. In order to move away from the Gamma point and obtain matrix elements for indirect transitions, one needs to perform phonon-assisted optical calculations. Those are only recently implemented in literature and, despite showing remarkable accuracies, are available (at the moment) for only a handful of functionals and neglect magnetic features [162–164].

Similar to  $\text{CuO}$ , basic DFT fails to reproduce a band gap value for  $\text{Cu}_4\text{O}_3$  and results in fully non-magnetic behaviour. By employing DFT+ $U$  methodology the value of the electronic band gap opens up to 1.558 eV, together with a recovery of the AFM ordering and magnetic moment of  $0.71 \mu_B$ . Hybrid functional calculations show a dipole forbidden indirect band transition between the valence and conduction band, with a band gap value of 2.370 eV and magnetic moment of  $0.68 \mu_B$ , as is shown in Figure 3.12 (agreeing well with the experimental value of  $0.46 - 0.66 \mu_B$  [81]).

**Optical properties** The calculated real and imaginary part of the dielectric function of  $\text{Cu}_2\text{O}$ ,  $\text{Cu}_4\text{O}_3$ , and  $\text{CuO}$ , together with their corresponding absorption coefficients (obtained using the HSE06 hybrid functional) plotted as a function of the incident wave energy are shown in Figure 3.13 and Figure 3.14. In the calculated absorption spectra of  $\text{Cu}_2\text{O}$ , the two aforementioned allowed transitions can be observed at around  $500 \text{ nm} \approx 2.5 \text{ eV}$ . Hybrid functionals tend to give roughly the right positions of the peaks but slightly underestimate their intensity. The imaginary part of the dielectric function shows similar results for the positions of the transition energies, as expected,

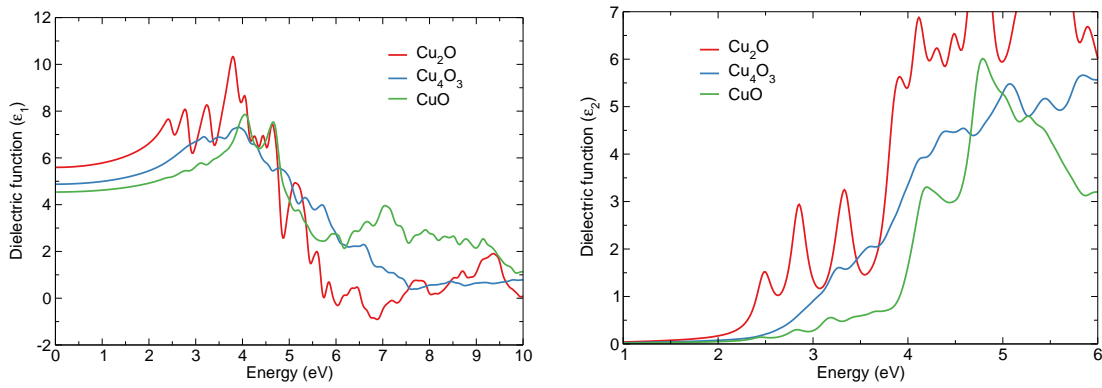


Figure 3.13: Calculated real part of the dielectric function ( $\epsilon_1$ , left) and imaginary part of the dielectric function ( $\epsilon_2$ , right) for  $\text{Cu}_2\text{O}$ ,  $\text{Cu}_4\text{O}_3$ , and  $\text{CuO}$  employing the HSE06 functional.

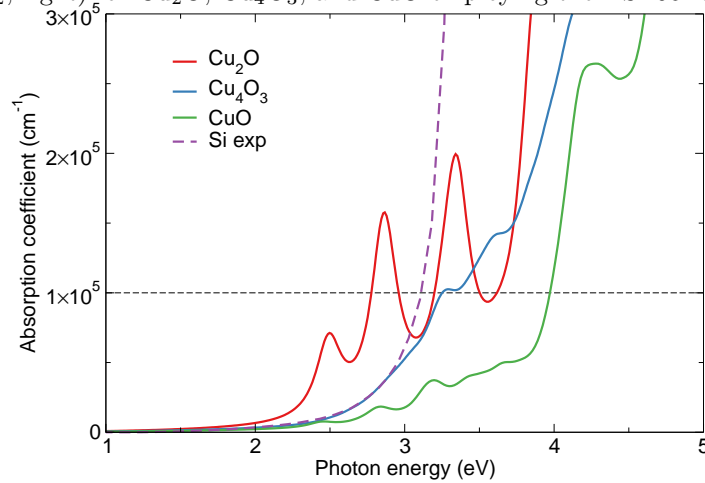


Figure 3.14: Calculated absorption coefficient for  $\text{Cu}_2\text{O}$ ,  $\text{Cu}_4\text{O}_3$ , and  $\text{CuO}$  using the HSE06 functional averaged over cartesian coordinates. For comparison, the silicon experimental value has been shown with the purple dashed line [165].

since they are connected through the formalism outlined earlier.

Within the experimental data of the imaginary part of the dielectric function of  $\text{CuO}$ , Meyer *et al.* [38] were able to identify multiple positions of possible interband transitions. Dipole matrix calculations explain why it is difficult to identify those transitions within the dielectric function or by looking at the shape of the absorption coefficient curve. Unlike in the case of  $\text{Cu}_2\text{O}$ ,  $\text{CuO}$  seems to have a more complex band structure and transition occurrence between certain bands, where a dipole forbidden nature could be responsible for hardly visible interband transitions. Looking closer at the absorption coefficient curve between 2 eV and 3 eV gives an idea when the absorption of photons starts to take place, but the extremely low intensity and smeared peaks are not conclusive about a precise onset of absorption.

Calculations of optical properties for  $\text{Cu}_4\text{O}_3$  suggest low absorption until the energy of the incident photon reaches  $\approx 3.250$  eV (around 380 nm). One additional stronger peak can be observed at around  $\approx 3.600$  eV (around 345 nm) which could be assigned

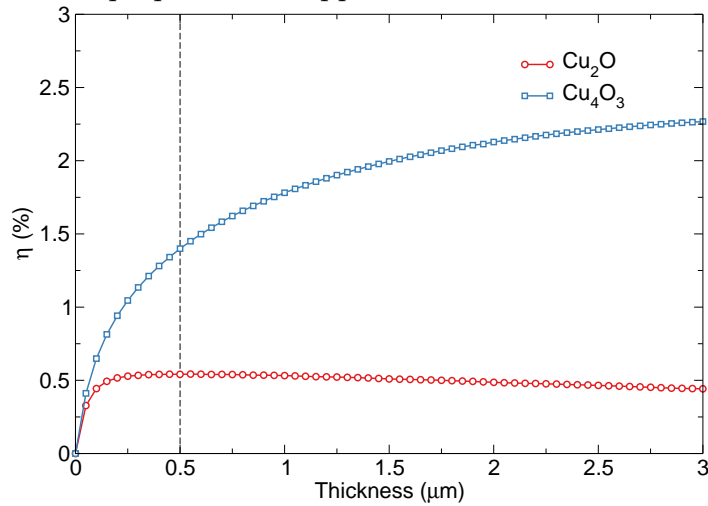


Figure 3.15: Calculated spectroscopic limited maximum efficiency (SLME) plotted as a function of the film thickness.

to a possible interband transition, but to the best of author's knowledge, experimental data are lacking to confirm this suggestion. Other transitions cannot be observed as the absorption curve shows hardly any peaks in the relevant distinguishable visible spectrum.

**Photovoltaic absorber efficiency** By combining the nature of the elementary transitions between the VB and CB with their dipole allowance and accompanying absorption spectra, the classic SQ limit has been extended into the SLME metric for all three copper oxides. This approach classifies copper oxides into different groups of optical materials, according to the order of dipole allowed and forbidden transitions (more details on the division scheme can be found in Yu and Zunger [145]). As mentioned before, the lowest energy transition of  $\text{Cu}_2\text{O}$  is direct dipole forbidden, followed by a direct allowed transition. For  $\text{Cu}_4\text{O}_3$  and  $\text{CuO}$ , the first transitions are indirect dipole forbidden. In the case of  $\text{Cu}_4\text{O}_3$ , the following transition is an indirect, but dipole allowed one, while for  $\text{CuO}$  only forbidden transitions are noted within the visible part of the electromagnetic spectrum. SLME calculations give absorbing efficiencies based upon those considerations.

The calculated dependence of SLME on the film thickness for copper oxides is shown in Figure 3.15. Choosing a reasonable reference thin film thickness of  $0.5 \mu\text{m}$  efficiency values of 0.54 % and 1.40 % for  $\text{Cu}_2\text{O}$  and  $\text{Cu}_4\text{O}_3$  were obtained, respectively. This corresponds well with experimentally observed PCE values, which take values of 1 – 2 % for  $\text{Cu}_2\text{O}$  and  $\text{CuO}$  [35, 38, 125]. For  $\text{Cu}_4\text{O}_3$ , no experimental PCE values have been obtained, to the best of author's knowledge. It is also worth mentioning that increasing the thickness leads to a plateau in efficiency. In other words,  $\text{Cu}_2\text{O}$  single-crystal compounds cannot exceed conversion efficiencies of 1 % without further

modification. For  $\text{Cu}_4\text{O}_3$ , this threshold is slightly higher, reaching 2 – 3%. As noted, CuO does not appear in the analysis due to negligible efficiency values, attributed to low absorption onsets and a clear majority of electrically dipole forbidden transitions that govern weak interactions between the incoming sunlight and valence electrons. In addition, photons that get absorbed by CuO are not efficiently converted due to significant non-radiative recombination processes inside the material. This correlates well with experimentally observed charge recombination processes preventing large-scale application of CuO-based solar cells [86, 166]. This is attributed to the large radiative fraction (order of  $10^{-40}$ ) which is used to calculate the reverse saturation current, imposing a significant influence on the open circuit voltage of the operating device. If we model CuO as a direct gap material, the maximum efficiency obtained does not exceed 2 – 3%. This implies that even if the non-radiative recombination processes are neglected, the absorption of CuO is very low and does not produce favourable output voltages.

These findings suggest that single-crystal copper oxides cannot be efficiently employed as solar-collecting materials. However, modifying the material's inner properties could lead to notable improvements. I.e., introducing extrinsic dopants could allow one to tune the Fermi level and create defect states situated within the band gap. Photon-induced transitions from defect states can lead to enhanced photocurrent generation through sub-bandgap absorption. This has been already demonstrated by electrochemical doping in *n*-type  $\text{Cu}_2\text{O}$  with chlorine [167]. It improved the conductivity of  $\text{Cu}_2\text{O}$  and hence, the overall efficiency of an intrinsic *pn*-junction of  $\text{Cu}_2\text{O}$ . Also, defect states can cause carrier trapping or additional non-radiative recombination, depending on the position of the defect states relative to the VB or CB.

Another possibility is the combination of copper oxides with other materials to create tandem cells. Improvement has been demonstrated, i.e., by creating heterojunction solar cells between AZO,  $\text{Ga}_2\text{O}_3$  and  $\text{Cu}_2\text{O}$ . This has led to an increase in efficiency to almost 5.5% [37]. If we compare this efficiency to the almost negligible conversion as a single cell, it offers suggestions for new designs. However, while forming junctions with copper oxides, the control of the interface properties is crucial in order to avoid mixture phases. Again, first principle calculations can provide useful information which include Schottky barrier heights of interfaces, band offsets or band positioning.

### 3.4 Conclusion

The photovoltaic efficiency of copper oxides has been modelled using density functional theory. Employed DFT+*U* and HSE06 calculations have proven to be a computation-

ally feasible and accurate approach to determine the electronic, magnetic, and optical properties of all three copper oxides considered.  $\text{Cu}_2\text{O}$ ,  $\text{Cu}_4\text{O}_3$ , and  $\text{CuO}$  are shown to be semiconductors with different types of fundamental band gap transition. Moreover, reported dipole transition matrix calculations allowed to characterize certain transitions from the valence to the conduction band and to assign them to peaks in the dielectric function and absorption spectrum. Finally, the usual SQ limit was extended into the SLME metric, which has allowed to explain why bulk single-crystal copper oxides solar cells have low photovoltaic conversion efficiencies, as seen experimentally. Two significant outcomes have arisen from the outlined analysis:

- Copper oxides are intrinsically incapable of reaching the efficiencies proposed by previous theoretical studies (mostly based on the SQ limit), owing to the many dipole-forbidden transition within their electronic band structure. Those prevent effective capture of electromagnetic radiation in the visible part of the spectrum.
- Suggested PCE values, therefore, need revision. Any future studies concerning copper oxides need to be aware of the given limitations in order to avoid searching for behaviour that cannot be achieved.

Future calculations should incorporate phonon-assisted interband transitions and absorption spectra into the SLME metric (or equivalent) in order to obtain even better descriptors and accurate prediction.

## Doping of $\text{Cu}_2\text{O}$ with first row transition metals

*"If you would be a real seeker after truth, it is necessary that at least once in your life you doubt, as far as possible, all things."*

---

René Descartes, *French philosopher*

Since solar energy is an easy to obtain and an inexhaustible source, sunlight converters are increasingly attracting scientific attention. As a result, an intensive search is being carried out for new low-cost materials for the fabrication of solar conversion devices [70]. Despite the apparent efficiency of perovskites in solar cell applications [168–170], the search for oxide absorbers remains highly relevant, mostly due to their stability under atmospheric conditions, abundance, and non-toxicity. Photoactive oxides are environmentally friendly and cost-effective, making them ideal for large-scale photovoltaic deployment [43].

Cuprous oxide is a promising alternative to traditional thin-film photovoltaic materials (CIGS, CdTe,  $\alpha$ -Si, etc.) because of its low materials cost, abundance of its component elements, and uniquely straightforward manufacturing process [171, 172]. It has recently received renewed interest as a photovoltaic and photocatalytic material, mainly due to its favourable band gap energy, high hole mobility, and favourable band edge positions [4, 173–175]. Ideal as it may seem,  $\text{Cu}_2\text{O}$  is not widely employed as a thin-film solar cell, mainly because the foremost optical transitions at the band gap are forbidden by selection rules, leading to weak absorption thus limiting the efficiency substantially [69, 176, 177]. Once high recombination rates and intrinsic trap state are added to the list,  $\text{Cu}_2\text{O}$  becomes rather unusable.

Controlling the presence of dopants in oxides provides an important mechanism to tune and alter the optoelectronic properties of a given compound [178]. Transition metal (TM) impurities, introduced in semiconducting compounds, are able to create a range of energy levels in the band gap [28]. Doping has already been shown to provide a way of improving the photostability of  $\text{Cu}_2\text{O}$ , circumventing complicated fabrication

processes such as coating, integration with other materials and use of co-catalysts [179].

This chapter is organized as follows: in the first section, a brief review of intrinsic and extrinsic defects of  $\text{Cu}_2\text{O}$  from the literature is presented. Some key aspects, like the origin of  $p$ -type conductivity or specific synthesis conditions are identified. In the subsequent section the specific theoretical parameters used in this chapter have been listed, followed by a section of results and discussion, where appropriate. In the last section, answers to some of the questions outlined during the introduction were addressed and the extend of the validity of results outlined.

## 4.1 Summary of available literature

**Experimental evidence of intrinsic defects** Point defects in  $\text{Cu}_2\text{O}$  have been studied extensively since the first utilization of the compound itself. Olsen *et al* [47] were amongst the first to observe an increase of photoconductivity with increasing copper vacancy distribution for  $\text{Cu}_2\text{O}$ . Porat and Riess [180] measured the deviation from stoichiometry in  $\text{Cu}_{2-y}\text{O}$  as a function of the oxygen partial pressure,  $P_{\text{O}_2}$  (in a range of  $10^{-13} \text{ atm} \leq P_{\text{O}_2} \leq 0.1 \text{ atm}$ ). The predicted dominant neutral point defects for  $\text{Cu}_2\text{O}$  at high  $P_{\text{O}_2}$  are neutral copper vacancies,  $V_{\text{Cu}}^\times$ , and copper interstitials,  $\text{Cu}_i^\times$ , at low values of  $P_{\text{O}_2}$  and low temperatures ( $873 \text{ K} < T < 1245 \text{ K}$ ) while at higher temperatures ( $T > 1245 \text{ K}$ ) oxygen vacancies,  $V_{\text{O}}^\times$ , dominate. The enthalpy of formation of  $V_{\text{Cu}}^\times$  varies with temperature, from 0.62 eV at 1200 K to 0.39 eV at 950 K. The formation enthalpy of  $\text{Cu}_i^\times$  temperature independent, with a value of 1.93 eV. The concentration of defects in  $\text{Cu}_2\text{O}$  reaches values as great as  $10^{18} - 10^{19} \text{ cm}^{-3}$  for copper vacancies and  $10^{17} - 10^{18} \text{ cm}^{-3}$  for oxygen vacancies [42].

Porat and Riess [181] performed measurement on electrical conductivity and thermoelectric power as function of temperature and oxygen partial pressure, to determine the nature of charged point defects in  $\text{Cu}_2\text{O}$ . Three types of charged defects were identified at different temperatures. In the range  $1150 \text{ K} \leq T \leq 1300 \text{ K}$  dominant defects are holes,  $h^\cdot$ , and doubly-charged oxygen interstitials,  $\text{O}_i^{\prime\prime}$ . At lower temperatures,  $900 \text{ K} \leq T \leq 950 \text{ K}$  the leading charged defects are holes and singly charged copper vacancies,  $V_{\text{Cu}}'$ . At intermediate temperatures all three charged defects occur and neither of them is dominant. The formation enthalpy for  $\text{O}_i^{\prime\prime}$  is found to be 3.1 eV and for  $V_{\text{Cu}}'$  1.8 eV.

Paul *et al* [182] studied defect energies of thin film polycrystalline  $\text{Cu}_2\text{O}$  solar cells via deep level transient spectroscopy (DLTS) in the temperature range between 100 K and 350 K. A hole trap with the activation energy of 0.45 eV from the valence band edge was confirmed and assigned to Cu vacancies together with a new trap level at

0.25 eV (from VB) tentatively assigned to Cu di-vacancy. Paul and co-workers [61] confirmed the values of 0.5 eV for the Cu vacancy and 0.2 eV for the vacancy-vacancy complex.

**Extrinsic dopants** Nitrogen was found to easily incorporate in  $\text{Cu}_2\text{O}$  in the oxygen lattice, forming an acceptor level positioned at about 0.14 eV above the valence band maximum [183]. Nitrogen cations disrupt the  $3d-3d$  electron interaction between different O-Cu-O networks, hence widening the band gap up to 2.5 eV [60]. In other words, one can alternate the band gap of  $\text{Cu}_2\text{O}$  by fabricating it under N-rich conditions. In contrast, under O-rich conditions copper cations are removed from the copper oxide lattice due to oxidation and the band gap shrinks (also showing small resistivity and large conductivity). Biccari *et al* [184] introduced seven impurities in  $\text{Cu}_2\text{O}$  (chromium, iron, silver, silicon, sodium, sulphur, and phosphorus). However, they did not notice any significant effect neither on the resistivity nor mobility. Doping  $\text{Cu}_2\text{O}$  with magnesium (Mg) does not affect the band gap energy due to similar ionic radii and minimal structural distortion that does not disrupt the Cu-Cu interaction. However, it enhances the photoconductivity by preventing split vacancy formation and thus eliminating trap states and minority carrier diffusion [185].

Kale *et al* [186] reported Co-doped  $\text{Cu}_2\text{O}$  films without and with Al, V, and Zn co-doping. Significant magnetization at room temperature was observed for  $\text{Cu}_2\text{O}:\text{Co}$  co-doped with 0.5% Al content. Chang and co-workers [187] studied the electronic structure of Mn-doped  $\text{Cu}_2\text{O}$  bulk samples with x-ray emission spectroscopy and theoretical linear muffin-tin orbital based calculations. For less than 1% of Mn doping, ferromagnetism arises from substitutional atoms as well as present interstitials in the samples, where the defect configuration depends on the sintering temperature. These defects were identified to exhibit a strong exchange interaction. Brandt *et al* [188] observed FM behaviour in Co doped  $\text{Cu}_2\text{O}$  films, with a magnetization of  $5.6 \mu_B$  per Co atom together with an increase in the point defect concentration (i.e., hole density) around the substitutional Co atom.

**Computational modelling of intrinsic defects of  $\text{Cu}_2\text{O}$**  Nolan and Elliott [57] were amongst the first to study the mechanism of copper vacancies and  $p$ -type conductivity in  $\text{Cu}_2\text{O}$  using a first principles analysis (DFT and DFT+ $U$ ). The results for 3% and 1.5% copper vacancy concentrations are summarized in Table 4.1. The vacancy excess spin density, resulting from the created difference between the majority and minority spin density, was found to delocalise over many Cu atoms extending over a region of  $6 \text{ \AA}$  – a delocalised hole (valid for both concentrations). Also, the report predicts facile simple and split vacancies irrespective of the vacancy structure present,

indicating the likelihood of copper vacancies present in  $\text{Cu}_2\text{O}$ .

Raebiger *et al* [189] performed first principles calculations of equilibrium non-stoichiometry and defect stability of  $\text{Cu}_2\text{O}$ . Results imply cation deficiency accommodated mostly by Cu vacancies rather than oxygen interstitials, due to higher formation energy, thus preventing hole compensation. In addition, a stable concentration of  $V_{\text{Cu}}$  was identified to reach  $10^{20} \text{ cm}^{-3}$ , and  $V_{\text{Cu}}$  to induce acceptor levels naturally making  $\text{Cu}_2\text{O}$  *p*-type. At room temperature, the hole concentration was found to reach only  $\approx 10^{18} \text{ cm}^{-3}$  as not all  $V_{\text{Cu}}$  are ionized to produced holes.

Scanlon *et al* [157] re-examined the defect levels within the band gap of cuprous oxides using periodic plane wave basis set DFT calculations using the GGA and GGA+*U* approximation. It was noted how copper vacancies always remained more stable than oxygen interstitials, regardless of the limiting conditions of the chemical potentials [190]. This clarified previous theoretical considerations which claimed spontaneous formation of simple copper vacancies, which was attributed to neglecting limits of CuO formation in chemical potential space. It was also observed how  $V_{\text{Cu}}$  and  $V_{\text{Cu}}^{\text{split}}$  show no distinct acceptor band (Fermi level crossing appears) giving rise to semi-metallic defect complexes. However, calculated thermodynamic ionization (transition) levels of charged defects were not consistent with experimental reported transition values. The work concluded how neither GGA or GGA+*U* give single particle levels or transition levels that can be regarded in good agreement with experiment, i.e. the polaronic nature of  $\text{Cu}_2\text{O}$  is not well captured.

Furthermore, Scanlon *et al* [156] investigated intrinsic defects of  $\text{Cu}_2\text{O}$  using a hybrid-DFT approach. Using a screened HSE hybrid density functional ( $\alpha=27.5\%$ ) it was possible to report single-particle levels above the valence band maximum (no Fermi crossing) for  $\text{Cu}_2\text{O}$  for the first time. Once more, the most favourable defects were copper vacancies, excluding oxygen interstitials from contributing to the *p*-type conductivity due to high formation energies and transition levels located deep within the band gap. Isseroff and Carter [191] revisited the hybrid-DFT calculations (HSE06) of intrinsic defects in  $\text{Cu}_2\text{O}$  in order to resolve possible accuracy issues due to unconverged formation energies and to understand fully the electronic structure of vacancies. Regardless of the XC functional employed, the difference between the simple and split copper vacancy remains fairly consistent. This indicates a minimal impact of the chosen XC on the relative stability. Identified differences in energies reported in literature can be attributed to differing variables, e.g., supercell size, cell volume and structure, Brillouin zone integration technique, or *k*-point mesh size.

Scanlon *et al* [77] also investigated the possibility of intrinsic *n*-type defects in  $\text{Cu}_2\text{O}$ . The conclusion points out that intrinsic defects are not a source of *n*-type conductivity in undoped  $\text{Cu}_2\text{O}$  films, the later one more likely arising from an inversion

layer that display  $n$ -type conductivity formed during electrodeposition. Isseroff *et al* [191] showed how the usage of a converged  $k$ -point mesh significantly impacts (hybrid) defect calculations, as insufficient sampling leads to localized holes with discrete states in the middle of the band gap, regardless of the type of vacancy.  $\text{Cu}_2\text{O}$  is found to have two types of vacancies: a simple one and a split vacancy, depending on whether a Cu atom is removed or moved towards the vacancy site. The simple vacancy exhibits a delocalized hole with states smeared through the Fermi level, while the split vacancy exhibits a discrete trap state (indicating a localized hole).

**Computational modelling of extrinsic defects of  $\text{Cu}_2\text{O}$**  Several works have been devoted to study the nature of foreign impurities in  $\text{Cu}_2\text{O}$  theoretically. Martinez-Ruiz [70] studied the structural and electronic properties of  $\text{Cu}_2\text{O}$  doped with Ni, Zn, Ag using GGA with the full potential linearised augmented plane wave (FP-LAPW) method and the experimentally observed crystal structure (no relaxation allowed). It was observed how Ni has a negative formation energy under O-rich conditions, indicating readily incorporation into the crystal. Doping with Ag results in a reduction of the band gap, while doping with Zn creates  $n$ -type conductivity where impurity levels are located above the conduction band minimum. Raebiger *et al* [192] studied Co impurities in  $\text{Cu}_2\text{O}$ , showing strong ferromagnetic interaction (magnetization of  $2\mu_B$  per Cu atom) originating from the occupation of previously unoccupied levels within the band gap. Furthermore, the introduction of multiple Co impurity atoms leads to the formation of compact Co clusters, showing favourable ferromagnetism.

Sieberer *et al* [193] explored the possibility of magnetism in Mn, Fe, Co, and Ni doped  $\text{Cu}_2\text{O}$  using GGA and GGA+ $U$ . Results yield a total magnetic moment of  $4.02$  ( $4.34$ )  $\mu_B$ ,  $3.00$  ( $3.07$ )  $\mu_B$ ,  $2.00$  ( $2.00$ )  $\mu_B$ , and  $1.00$  ( $1.00$ )  $\mu_B$  for Mn, Fe, Co, and Ni, respectively (numbers indicate GGA results while GGA+ $U$  results are shown in brackets). The authors also investigated the effective magnetic exchange between two substituent atoms and possible clustering effects. Co and Mn show strong clustering tendency, favouring ferromagnetism and antiferromagnetism, respectively. In addition, single copper, as well as oxygen vacancies, have been added to the system with two substituent atoms (only at GGA level). Both oxygen and copper vacancies strongly seem to enhance the ferromagnetic character of Mn–Mn interactions. For the Co-doped system only copper holes stabilize magnetic interactions, whilst oxygen holes induce oscillations between the two magnetic states.

Nolan and Elliott [194] studied the possibility of tuning transparency of  $\text{Cu}_2\text{O}$  with cation doping, which included Ba, Sn, Ti, Cr, In, and Cd, amongst many others (on a GGA–PBE theoretical level). Despite the underestimation of the band gap with DFT ( $0.47$  eV compared to  $2.17$  eV experimentally observed), authors refer to trends in band

Table 4.1: Summary of defect formation energies, impurity levels, electronic band gap, and effective masses of intrinsically doped  $\text{Cu}_2\text{O}$ .

Defect structure	Defect formation energy (eV)	Impurity level (eV)	Effective mass ( $m_e$ )
$V_{\text{Cu}}$	0.34 – 0.41 (GGA)[57]	$E_V + 0.20$	-0.50
	0.41 (GGA)[157]	$E_F$ crossing	-
	0.73 – 0.92 (GGA+ $U$ )[157]	$E_F$ crossing	-
	1.15 (HSE)[156]	$E_V + 0.52$	-
	1.15 – 1.34 (HSE06)[191]	$E_F$ crossing	-
Exp	0.39 – 0.97[191]	0.55 – 0.61[191]	-
$V_{\text{Cu}}^{\text{split}}$	0.47 (GGA)[57]	$E_V + 0.20$	-0.53
	1.24 (GGA)[157]	$E_F$ crossing	-
	1.47 – 1.66 (GGA+ $U$ )[157]	$E_V + 0.04$	-
	1.14 (HSE)[156]	$E_V + 1.12$	-
	1.36 – 1.58 (HSE06)[191]	$E_V + 0.57$	-
Exp	0.39 – 0.97[191]	0.55 – 0.61[191]	-
$O_i^{\text{oct}}$	1.36 (GGA)[157]	$E_V + 0.25$	-
	1.69 – 2.07 (GGA+ $U$ )[157]	$E_V + 0.29$ , $E_V + 0.62$	-
	1.94 (HSE)[156]	$E_V + 1.14$	-
Exp	-	-	-
$O_i^{\text{tet}}$	1.65 (GGA)[157]	$E_V + 0.29$	-
	1.59 – 1.97 (GGA+ $U$ )[157]	$E_V + 0.18$ , $E_V + 0.50$	-
	1.87 (HSE)[156]	$E_V + 1.05$	-
Exp	-	-	-
$\text{Cu}_i^{\text{oct}}$	1.25 (HSE06)[77]	$E_C - 1.18$	-
Exp	-	-	-
$\text{Cu}_i^{\text{tet}}$	1.40 (HSE06)[77]	$E_C - 1.23$	-
Exp	-	-	-

gap values rather than absolute magnitudes. It was observed how potential  $n$ -type donors, like Zn and Sn, are disfavoured due to the formation of neutral Cu vacancies. The formation of  $p$ -type dopants, on the other side, was found to increase the gap for alkaline earth elements and decrease in the case of transition metals.

Isseroff and Carter studied, amongst other things, the effect of doping  $\text{Cu}_2\text{O}$  with Li, Mg, Mn, and Zn on vacancy formation energies, electronic structure, and photoconductivity [191]. Results demonstrate lower formation energies as the dopant–vacancy distances decrease, indicating a thermodynamic preference for defect pair formation. The dopant stabilization via structural reorganization, to obtain its preferred coordination of four, is the main factor for lowering the formation energy. It was also pointed out how these dopants prevent the formation of a split vacancy, thus preventing creation of midgap states. Adding a second vacancy to the Mg and Mn dopant–vacancy pair system has no clear impact on photoconductivity due to increased formation energy and no preferred clustering, whereas Zn may slightly inhibit the formation of trap states.

Scanlon *et al* [127] also examined the complex behaviour of hydrogen in cuprous oxide. They showed, using hybrid–DFT, that hydrogen preferentially occupies the tetrahedral position in stoichiometric  $\text{Cu}_2\text{O}$  and is not a cause of  $n$ -type conductivity. Also, it was noted how hydrogen will bind into any copper vacancy easily and kill  $p$ -type conductivity. To remove hydrogen from the system, a sufficient annealing temperature of 72 K for  $\text{H}_i$  and 943 K for a  $(\text{H}_i-\text{V}_{\text{Cu}})$  was calculated. Soon *et al* [195] investigated via DFT (PBE) the properties of early transition metal (TM) doped  $\text{Cu}_2\text{O}$  systems, focusing on  $3d$  (Ti, V, and Cr),  $4d$  (Zr, Nb, and Mo), and  $5d$  (Hf, Ta, and W) metals. It was observed how  $3d$  dopants magnetize the system to a larger extent than  $4d$  and  $5d$  TM dopants. Also, a doubly doped  $\text{Cu}_2:\text{Ti}_2$  system was found to be thermodynamically more stable than the singly doped one, showing antiferromagnetic behaviour which decreases as the distance between Ti atoms increases. Similar to the work of Isseroff [191], preferential pairing of Ti atoms was observed over the long dispersed case.

Brandt *et al* [188] employed DFT+ $U$  calculation to study the effect of Co doping on  $\text{Cu}_2\text{O}$ . Substitutional Co (on the copper site) was assumed to have +1 oxidation state, which is not a usual configuration, thus leading to doping instability. Introducing various point defects in the Co doped  $\text{Cu}_2\text{O}$  cell, the possibility of dopant–defect clustering was studied. The  $\text{Co}_{\text{Cu}} + \text{Cu}_{\text{V}}$  complex was found to retain the +1 oxidation state of Co, whilst  $\text{Co}_{\text{Cu}} + 2\text{Cu}_{\text{V}}$ ,  $\text{Co}_{\text{Cu}} + \text{O}_i^{\text{tet}}$ , and  $\text{Co}_{\text{Cu}} + 4\text{O}_i^{\text{tet}} + 4\text{O}_{\text{V}}$  favour a change to the +2 oxidation state of Co. Also, a model for the observed FM was proposed, where a Co dopant concentrates around itself a large number of point defects, acting as a pinning centre and increasing the number of defect clusters. A cluster of at least

Table 4.2: Summary of defect formation energies, impurity levels, electronic band gap, and effective masses of extrinsically doped  $\text{Cu}_2\text{O}$ .

Dopant/complex	Formation energy (eV)	Impurity level/ Band gap (eV)	Effective mass ( $m_e$ )
$\text{Ni}_{\text{Cu}}$	$(-1.76) - (+0.75)$ (GGA)[70]	-	-
$\text{Zn}_{\text{Cu}}$	$+0.27 - (+2.77)$ (GGA)[70]	-	-
$\text{Zn}_{\text{Cu}} + \text{V}_{\text{Cu}}$	$(-1.389) - (-1.573)$ (HSE06)[191] $-0.78$ (GGA)[194]	no defect states no defect states	- -
$\text{Zn}_{\text{Cu}} + 2\text{V}_{\text{Cu}}$	$+1.018 - (+1.161)$ (GGA+ $U$ )[191] $+1.161 - (+1.829)$ (HSE06)[191] $+0.22$ (GGA)[194]	no defect states $E_{\text{F}}$ cross $E_g = 0.49$	- - $-0.93$
$\text{Mn}_{\text{Cu}}$	$+1.30$ (tight binding)[187]	N/A	-
$2\text{Mn}_{\text{Cu}}$	$+2.70$ (tight binding)[187]	-	-
$2\text{Mn}_{\text{Cu}} + \text{Mn}_{\text{i}}$	$+3.00$ (tight binding)[187]	N/A	-
$4\text{Mn}_{\text{Cu}} + \text{Mn}_{\text{i}}$	$+8.40$ (tight binding)[187]	N/A	-
$\text{Mn}_{\text{Cu}} + \text{V}_{\text{Cu}}$	$(-1.341) - (-1.526)$ (HSE06)[191]	no defect states	-
$\text{Mn}_{\text{Cu}} + 2\text{V}_{\text{Cu}}$	$+0.969 - (+1.185)$ (GGA+ $U$ )[191] $+1.149 - (+1.466)$ (HSE06)[191]	N/A $E_{\text{V}} + 0.80$	- -
$\text{Mg}_{\text{Cu}} + \text{V}_{\text{Cu}}$	$(-2.228) - (-2.412)$ (HSE06)[191] $-0.46$ (GGA)[194]	no defect states N/A	- -
$\text{Mg}_{\text{Cu}} + 2\text{V}_{\text{Cu}}$	$+1.010 - (+1.197)$ (GGA+ $U$ )[191] $+1.58 - (+1.761)$ (HSE06) [191] $+0.26$ (GGA)[194]	N/A $E_{\text{F}}$ cross $E_g = 0.56$	- - -
$\text{Li}_{\text{Cu}} + \text{V}_{\text{Cu}}$	$+0.918 - (+1.102)$ (HSE06)[191]	no defect states	-
$\text{Ag}_{\text{Cu}}$	$+1.76 - (+4.27)$ (GGA)[70] N/A (GGA)[75]	- gap unchanged	- $-1.24$
$\text{Ag}_{\text{Cu}}^{\cdot\cdot} + 2\text{V}'_{\text{Cu}}$	N/A (GGA)[75]	$E_g = 0.21$	$-1.00$
$\text{Au}_{\text{Cu}}$	N/A (GGA)[75]	gap unchanged	$-0.31$
$\text{Co}_{\text{Cu}}$	$\approx +0.65$ (GGA)[192]	$E_{\text{V}} + 0.26$	-
$\text{Co}_{\text{Cu}} + \text{Cu}_{\text{V}}$	$(-2.15) - (+0.79)$ (GGA+ $U$ )[188]	N/A	-
$\text{Co}_{\text{Cu}} + 2\text{Cu}_{\text{V}}$	$(-2.47) - (-0.51)$ (GGA+ $U$ )[188]	N/A	-
$\text{Co}_{\text{Cu}} + \text{O}_{\text{i}}^{\text{tet}}$	$(-3.93) - (+1.80)$ (GGA+ $U$ )[188]	N/A	-
$\text{Co}_{\text{Cu}} + 4\text{O}_{\text{i}}^{\text{tet}} + 4\text{O}_{\text{V}}$	$+3.15 - (+5.24)$ (GGA+ $U$ )[188]	N/A	-
$\text{Sn}_{\text{Cu}} + \text{V}_{\text{Cu}}$	$-0.95$ (GGA)[194]	no defect states	$-0.96$
$\text{Sn}_{\text{Cu}} + 2\text{V}_{\text{Cu}}$	$+0.15$ (GGA)[194]	$E_g = 0.63$	$-0.93$
$\text{Ti}_{\text{Cu}} + 3\text{V}_{\text{Cu}}$	$+0.12$ (GGA)[194]	N/A	-
$\text{Ti}_{\text{Cu}} + 4\text{V}_{\text{Cu}}$	$+0.42$ (GGA)[194]	$E_g = 0.27$	-
$\text{Cr}_{\text{Cu}} + 3\text{V}_{\text{Cu}}$	$+0.22$ (GGA)[194]	N/A	-
$\text{Cr}_{\text{Cu}} + 4\text{V}_{\text{Cu}}$	$+0.34$ (GGA)[194]	$E_g = 0.04$	-
$\text{V}_{\text{Cu}} + 3\text{V}_{\text{Cu}}$	$-0.02$ (GGA)[194]	N/A	-
$\text{V}_{\text{Cu}} + 4\text{V}_{\text{Cu}}$	$+0.15$ (GGA)[194]	$E_g = 0.04$	-

16 atoms is proposed to explain the observed experimental magnetization of  $5.6 \mu_{\text{B}}$  per Co atom.

**Photovoltaic potential** Zhu and Panzer [178] prepared Zn doped  $\text{Cu}_2\text{O}$  thin films via single step electrodeposition successfully incorporating Zn cations into the  $\text{Cu}_2\text{O}$  lattice without the formation of local ZnO. A 3-fold improvement in the PCE of the doped sample was noted over the undoped one, attributed to the increase of the Fermi level leading to a conductivity increase and reduced  $p$ -type character of the films. It was observed how the incorporation of Zn at low doping concentrations does not change the morphology of the films. Doping with Zn was found to improve photostability of  $\text{Cu}_2\text{O}$  electrodes, suppressing oxidation of  $\text{Cu}_2\text{O}$  into CuO [179]. Zn doping increases the carrier concentration and improves charge transfer efficiency. However, too high doping concentrations induce charge recombination, counter-balancing the positive effects. Depending on the synthesis technique, Zn doped  $\text{Cu}_2\text{O}$  films often show local ZnO clusters and non-oxidised Cu atoms, lowering the overall transmittance [196]. Fe doped  $\text{Cu}_2\text{O}$  thin films showed improved optical transmittance over the undoped samples [197].

#### 4.1.1 Concluding remarks on literature review

While performing the literature review on  $\text{Cu}_2\text{O}$  defects, a few key points worth summarizing have been found. The  $p$ -type conductivity was found to originate from small amounts of Cu vacancies ( $V_{\text{Cu}}$ ), whose formation energy depends on the oxygen partial pressure and temperature conditions of synthesis [180–182]. Theoretical studies confirmed the most favourable polaronic defects in  $\text{Cu}_2\text{O}$  to be simple ( $V_{\text{Cu}}$ ) and split vacancies ( $V_{\text{Cu}}^{\text{split}}$ ), demonstrating the need to go beyond local and semi-local theoretical approximations to capture the essential nature of those processes accurately [75, 77, 156]. As shown,  $\text{Cu}_2\text{O}$  has been doped experimentally with many extrinsic elements, mostly in the form of thin films and bulk samples. A pronounced difficulty is to achieve effective cation incorporation in the  $\text{Cu}_2\text{O}$  matrix and at the same time avoid the formation of local impurity clusters or dopant-based oxides [179].

Despite the significant effort invested into exploring the conventional properties of doped  $\text{Cu}_2\text{O}$ , relatively less effort has been devoted to study the impact of extrinsic dopants on the photovoltaic properties of  $\text{Cu}_2\text{O}$ . Moreover, theoretical investigations performed at the general gradient approximation level often lack completeness in the description of oxide electronic properties [198].

The aim of this part of the work is to explore the eventual effect that first row transition metals (FRTM) could have on the overall photovoltaic absorption potential

of  $\text{Cu}_2\text{O}$ . The choice of dopants was strongly driven by experimental input. Within this chapter, some of the questions being assessed are:

- How readily are extrinsic FRTM dopants incorporated into the  $\text{Cu}_2\text{O}$  matrix?
- What is the nature of the electronic defect states created via doping? Which valence state do defects take?
- Are clustering effects present?
- Do FRTM extrinsic defect influence the overall photovoltaic potential of  $\text{Cu}_2\text{O}$ ? If so, which hindering processes, identified in the previous chapter, are bypassed?

To attempt in answering some of these questions, a systematic hybrid-DFT study was conducted. The effect of dopants on the electronic structure was examined, together with their formation energies, charge distribution, and influence on the optical response of  $\text{Cu}_2\text{O}$ . In addition, a selection metric is employed to assess the limiting power conversion efficiency of doped  $\text{Cu}_2\text{O}$ .

## 4.2 Technical details and computational parameters

The theoretical results presented in this chapter were based on spin polarized DFT calculations performed with the Vienna Ab-initio Simulation Package [135]. The interactions between core and valence electrons were represented using the projector augmented wave (PAW) method [134].

The general gradient approximation (GGA) [136] exchange–correlation (XC) functional with the Perdew–Burke–Ernzerhof (PBE) parametrization was employed for DFT+ $U$  within the formalism of Dudarev *et al* [16]. The values for the effective Hubbard parameter ( $U_{\text{eff}}$ ) were taken from parameter-free self-consistent calculations, yielding accurate electronic properties for transition metal oxides [199–201]. For the hybrid-DFT calculations, the HSE06 XC functional was used, which incorporates 25% of the non-local exact Hartree–Fock (HF) exchange and a screening parameter of  $0.2 \text{ \AA}^{-1}$  [19–21]. The hybrid functional approach demonstrated accurate descriptions of various oxide semiconductors, including  $\text{Cu}_2\text{O}$  [174, 175]. The method of Gajdoš *et al* [147] was used to obtain the real and imaginary parts of dielectric functions, from which the absorption coefficient was derived. Long distance dispersion corrections were included using the D3 approach of Grimme *et al* [139]. The plane wave expansion cutoff was set to 500 eV and the force convergence criterion to cell relaxation was  $0.01 \text{ eV/\AA}$ .  $\text{Cu}_2\text{O}$  crystallizes in a high symmetry cubic structure containing six

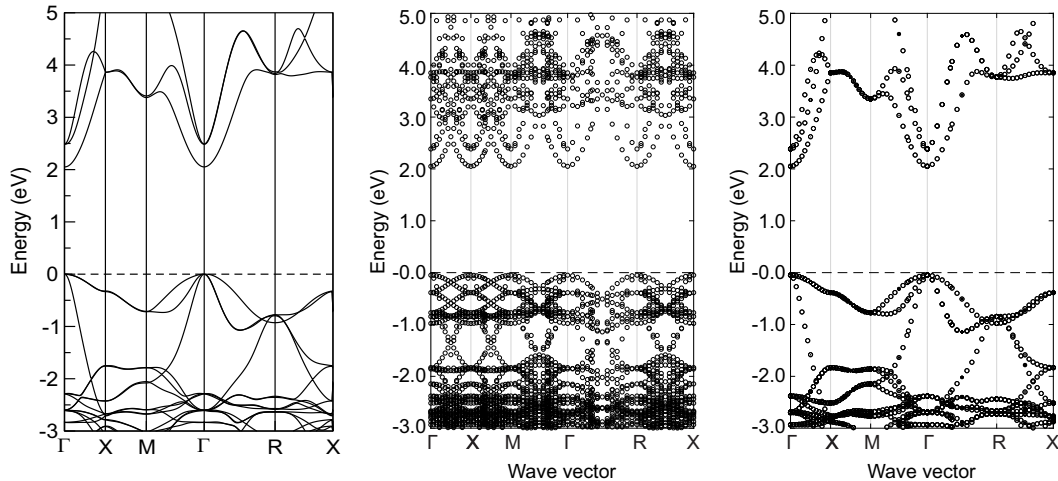


Figure 4.1: Calculated band structure for a  $\text{Cu}_2\text{O}$  unit cell (left) together with the unfolded band structure of a  $\text{Cu}_2\text{O}$   $2 \times 2 \times 2$  supercell (middle). After unfolding has been performed, the effective band structure in a primitive representation has been obtained (right), which matches the initial band structure accurately.

atoms in the unit cell arranged in the cuprite structure. The initial computed Kohn–Sham band gap (with the HSE06 functional) at the  $\Gamma$ -point is 2.052 eV (see Figure 4.1), in good agreement with the experimental value of 2.1 – 2.4 eV [50]. Defects were modelled in a 48-atom ( $2 \times 2 \times 2$ ) supercell where one Cu atom was replaced with a FRTM dopant giving a concentration of 3.125%, which is well accessible within the experimental regime [193, 195]. The starting supercell lattice constant was 8.461 Å, obtained from DFT+ $U$  calculations on the stoichiometric unit cell. A Monkhorst-Pack [22]  $3 \times 3 \times 3$  k-mesh was employed to ensure total energy convergence up to 1 meV/atom.

DFT+ $U$ , which has been shown to accurately reproduce the structural parameters of the stoichiometric unit cell, was used to relax the doped  $\text{Cu}_2\text{O}$  structure (including atomic position and volume optimization), whilst hybrid-DFT permitted an accurate electronic structure at affordable computational cost [157]. Based on the electronic band structure, the optical absorption spectra were obtained by calculations from the real and imaginary parts of the dielectric function within the independent particle approximation. Since DFT and DFT+ $U$  fail to accurately model the formation energies of defects in  $\text{Cu}_2\text{O}$  [156, 157], defect formation energies were calculated using a single point calculation with hybrid-DFT.

The phase stability diagram of  $\text{Cu}_2\text{O}$  for a range of accessible chemical potentials was computed using the Chemical Potential Limits Analysis Program (CPLAP) [202], taking into account its limiting competing phases. All reference enthalpies and elemental energies were calculated keeping the hybrid exchange-correlation functional consistent to ensure transferability of results. The extent of defect charge distribution was studied using the Bader scheme as implemented in the Henkelman code [203–205].

All inequivalent dopant configurations for site substitutions in the supercell approach were generated using the Site–Occupation Disorder package [206]. Graphical drawings were produced using VESTA [144] and band structure unfolding was performed using the `fold2Bloch` software [207, 208]. Excitonic and spin–orbit coupling effects were not taken into account.

**Phase stability** The formation energy of a neutral defect ( $q = 0$ ) is defined through (2.53), which is repeated here for sake of readability:

$$E^f[X^q] = E_{\text{tot}}[X^q] - E_{\text{tot}}[\text{bulk}] - \sum_i n_i \mu_i, \quad (4.1)$$

where  $E_{\text{tot}}[X^q]$  and  $E_{\text{tot}}[\text{bulk}]$  are the total energies of the respective supercell containing the defect and equivalent perfect supercell. The integer  $n_i$  represents the number of atoms of element  $i$  removed or added to the system and  $\mu_i$  is the chemical potential of element  $i$ . The chemical potential is referenced to the chemical potential of element  $i$  in its standard phase ( $\mu_i^\circ$ ), referenced to the total energy of the elementary phases at zero K.

The allowed values of  $\Delta\mu_i$  are determined from a set of thermodynamic limits. The upper limit is given by  $\Delta\mu_i \leq 0$  where element  $i$  precipitates to its standard state, in this case metallic copper and molecular oxygen in the gas phase. Also, to avoid the formation of secondary solids, i.e.  $\text{Cu}_4\text{O}_3$  and  $\text{CuO}$ , the chemical potentials must also be bound by:

$$4\Delta\mu_{\text{Cu}} + 3\Delta\mu_{\text{O}} \leq \Delta H_f(\text{Cu}_4\text{O}_3), \quad (4.2)$$

$$\Delta\mu_{\text{Cu}} + \Delta\mu_{\text{O}} \leq \Delta H_f(\text{CuO}), \quad (4.3)$$

with  $\Delta H_f$  being the standard enthalpy of formation at zero K. The total energies of the phases competing with  $\text{Cu}_2\text{O}$ , i.e.,  $\text{Cu}_4\text{O}_3$  and  $\text{CuO}$ , were calculated using their respective unit cells. For tetragonal  $\text{Cu}_4\text{O}_3$ , a primitive cell containing 14 atoms was used together with the antiferromagnetic spin ordering leading to the observed lowest energy configuration [114, 120, 209]. For monoclinic  $\text{CuO}$ , the experimentally observed antiferromagnetically ordered unit cell with 16 atoms was used [96, 210].

In addition, the solubility of the dopant species are limited by the formation of secondary phases:

$$\Delta\mu_{\text{TM}} + \Delta\mu_{\text{O}} = \Delta H_f(\text{TMO}), \quad (4.4)$$

where TMO denotes the corresponding (dopant) transition metal oxide, namely  $\text{Sc}_2\text{O}_3$ ,  $\text{TiO}$ ,  $\text{VO}$ ,  $\text{CrO}$ ,  $\text{MnO}$ ,  $\text{FeO}$ ,  $\text{CoO}$ ,  $\text{NiO}$ , and  $\text{ZnO}$  (whose enthalpies were calculated using the same parameters outlined earlier).

Table 4.3: Calculated enthalpies of formation (eV/formula unit) for  $\text{Cu}_2\text{O}$ ,  $\text{Cu}_4\text{O}_3$ , and  $\text{CuO}$ .

	$\Delta H_f$ ( $\text{Cu}_2\text{O}$ )	$\Delta H_f$ ( $\text{Cu}_4\text{O}_3$ )	$\Delta H_f$ $\text{CuO}$
DFT+ $U$	-1.72	-4.99	-1.62
HSE06	-1.66	-4.92	-1.57
Experiment	-1.75 [40]	-4.69 (at 427° C) [211] -4.88 (at 25° C) [211] -5.94 $\pm$ 25 (at 25° C) [211]	-1.59 [40]

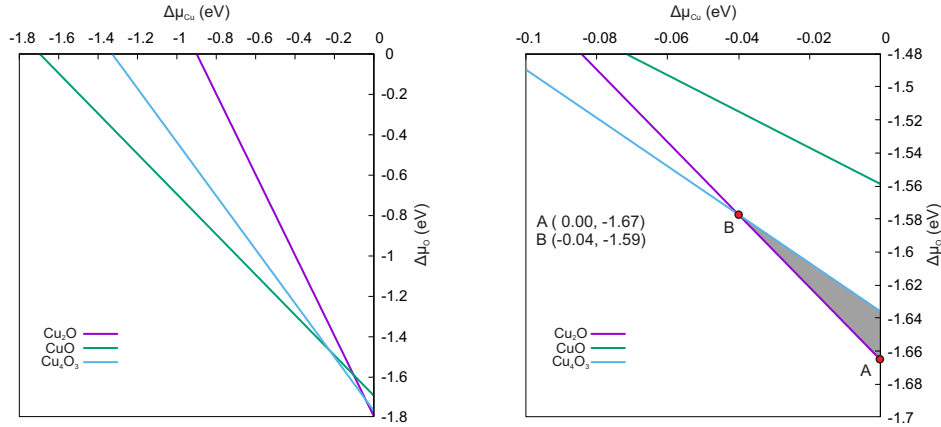


Figure 4.2: Phase stability in the range of accessible chemical potentials for  $\text{Cu}_2\text{O}$  with the figure on the left indicating the whole range and the figure on the right showing a magnification of the region of interest. Limits are imposed by the formation of competing phases.

## 4.3 Results and discussion

### 4.3.1 Formation enthalpies of pristine $\text{Cu}_2\text{O}$

Calculated formation enthalpies of  $\text{Cu}_2\text{O}$ ,  $\text{Cu}_4\text{O}_3$ , and  $\text{CuO}$  are reported in Table 4.3. Qualitatively, both DFT+ $U$  and HSE06 predict  $\text{Cu}_2\text{O}$  to be more stable than  $\text{CuO}$  and give energies very close to experimental trends (differences most likely arise from temperature effects when comparing with tabulated values). From the obtained formation enthalpies and constraints set by equations (4.1)–(4.2), boundaries for the chemical potential can be calculated, which are shown in Figure 4.2. The chemical potentials for Cu (point A and B in Figure 4.2, right), providing boundary values for cation substitution energies, possess values in a very narrow range. Hence, we explicitly consider only point A, with chemical potential values of  $\Delta\mu_{\text{Cu}} = 0$  eV and  $\Delta\mu_{\text{O}} = -1.67$  eV. This approach illustrates the importance of taking competing phases into account, as otherwise calculated defect energetics can end up describing unphysical conditions [87, 212].

Table 4.4: Structural lattice distortion, dopant-anion bond distance, and bond distance distortion (with respect to the pristine Cu–O bond distance of 1.831 Å).

	Sc	Ti	V	Cr	Mn	Fe	Co	Ni	Zn
Lattice distortion (%)	0.731	0.714	0.505	0.363	0.442	0.272	0.155	0.078	0.349
$d(\text{TM-O})$ (Å)	1.981	2.067	1.909	1.987	1.939	1.861	1.832	1.891	1.828
$\Delta d(\text{TM-O})$ (%)	8.158	12.836	4.246	8.452	5.850	1.600	0.034	3.256	-0.184

### 4.3.2 Single substitutional cation-doped $\text{Cu}_2\text{O}$

First row transition metal (FRTM) atoms have been introduced into  $\text{Cu}_2\text{O}$  by substitution of Cu on the copper site. The cubic  $\text{Cu}_2\text{O}$  structure holds only one non-equivalent copper position, resulting in one unique configuration for the position of the dopant in the supercell. The substitution of one Cu atom with a FRTM does not alter the geometry substantially, giving a maximum distortion of only 0.7% in the lattice parameter for Ti and Sc dopants, compared to the undistorted structure. Complete results are presented in Table 4.4. The calculated TM–O bond distances are increased for all dopant atoms, compared to the Cu–O bond length of the pure host, apart from the Zn dopant, where a small bond shortening was observed, most likely due to the fact that the Zn  $d$  orbitals are full. Calculated results compare well with trends observed in previous studies [193, 195].

The oxidation state of the TM atom replacing a copper atom in  $\text{Cu}_2\text{O}$  remains +1, maintaining charge balance (charge neutrality) in the material. The stability of doped systems is determined by their defect formation energies, which are summarized in Table 4.5. The sign convention for the defect formation energy is such that a negative value would lead to spontaneous formation of the defect unless it was kinetically hindered. Two different values have been reported,  $E^{f_0}$  and  $E^f$ , referring to defect formation energies obtained "as is" and with taking into account the competing transition metal oxide phases outlined in equation (4.4), respectively. Without the inclusion of competing phases, almost all of the considered dopants would form spontaneously representing an unphysical situation where only the end-metallic form of the dopant is created. Limiting the range of available chemical potentials by the formation of (respective dopant) transition metal (mono)oxides reflects the physical energy requirements to create defects within the  $\text{Cu}_2\text{O}$  pristine matrix. For the evaluated range of accessible chemical potentials, most of the considered neutral TM defects replacing one copper atom are likely to form, apart from Sc, whose formation energy is found extensively high, reaching 5.5 eV. Most favourable defect formation energies, with values below 1 eV are assigned to Mn and Co, comparable to intrinsic vacancy formation energies in  $\text{Cu}_2\text{O}$  which range from 0.39 eV – 0.97 eV [213].

Table 4.5: Formation energies for substitutional defects on the copper site in  $\text{Cu}_2\text{O}$  together with the accompanying magnetic moment on the transition metal dopant and nearest-neighbouring oxygen. Two types of formation energies are reported,  $E^{f_0}$  calculated "as is" from obtained DFT energies and  $E^f$  calculated taking into account the limiting competing phases of corresponding (dopant) transition metal oxides.

	Sc	Ti	V	Cr	Mn	Fe	Co	Ni	Zn
$E^{f_0}$ (eV)	-1.538	-0.807	-0.657	-0.715	-1.448	-0.261	-0.408	-0.196	0.888
$E^f$ (eV)	5.537	2.065	2.835	1.964	0.296	1.831	0.991	1.350	2.490
$m_{\text{TM}}$ ( $\mu_{\text{B}}$ )	0.000	2.025	2.109	4.259	4.252	3.156	2.058	0.814	0.163
$m_{\text{O}}$ ( $\mu_{\text{B}}$ )	0.000	0.109	0.013	0.074	0.035	0.033	0.023	0.015	0.056

The computed unfolded electronic band structure together with the total and TM dopant-projected densities of state of the doped systems are shown in Figure 4.3 and Figure 4.4. The band structure of pristine  $\text{Cu}_2\text{O}$  is altered by the introduction of a FRTM substitutional dopant. When doped with an impurity having a higher atomic number, i.e. Zn replacing Cu, the system gains an excess electron. The Zn dopant introduces a singly occupied impurity level that lies at about 1.387 eV above the valence band maximum (VBM) and 0.520 eV below the conduction band minimum (CBM) at the  $\Gamma$ -point. Since the impurity level is occupied, the donor atom is neutral. The spin density shows delocalization of the excess electron over the dopant and its neighbouring atoms, as shown in Figure 4.5. A small magnetization of  $0.163 \mu_{\text{B}}$  was found on the Zn atoms, accompanied by  $0.056 \mu_{\text{B}}$  on the nearest O atom (Table 4.5).

In contrast, when doped with an impurity with a lower atomic number, the system gains a spare hole. Substituting Ni for Cu creates an acceptor impurity level in the spin minority channel. This unoccupied level, which consists of hybridizing Cu and Ni  $3d t_{2g}$  states, lies at  $\approx 0.059$  eV below the CBM (or  $\approx 0.456$  eV from the spin minority channel, read from the complementary densities of state), as shown in Figure 4.3. The spin density is localized on the Ni atom, with a magnetic moment of  $0.814 \mu_{\text{B}}$  on the Ni and a negligible moment of  $0.015 \mu_{\text{B}}$  on the O atom (Figure 4.5).

A single Co dopant creates a donor level located at 0.536 eV above the VBM in the minority spin channel at the  $\Gamma$ -point. The unpaired electron is shared between Co and Cu  $3d$  states, whereas the empty Co  $3d$  states are merged with the  $\text{Cu}_2\text{O}$  conduction band. Fe introduces two occupied donor levels in the spin minority channel, located at 0.480 eV and 0.888 eV above the VBM, respectively. One additional acceptor level can be identified at approximately 0.350 eV above the CBM.

A single impurity band is created when Cu is replaced by Mn or Cr. Substitutional Mn creates an intermediate impurity level located at around 1.351 eV above the VBM in the spin minority channel, whereas Cr induces an intermediate level in the spin

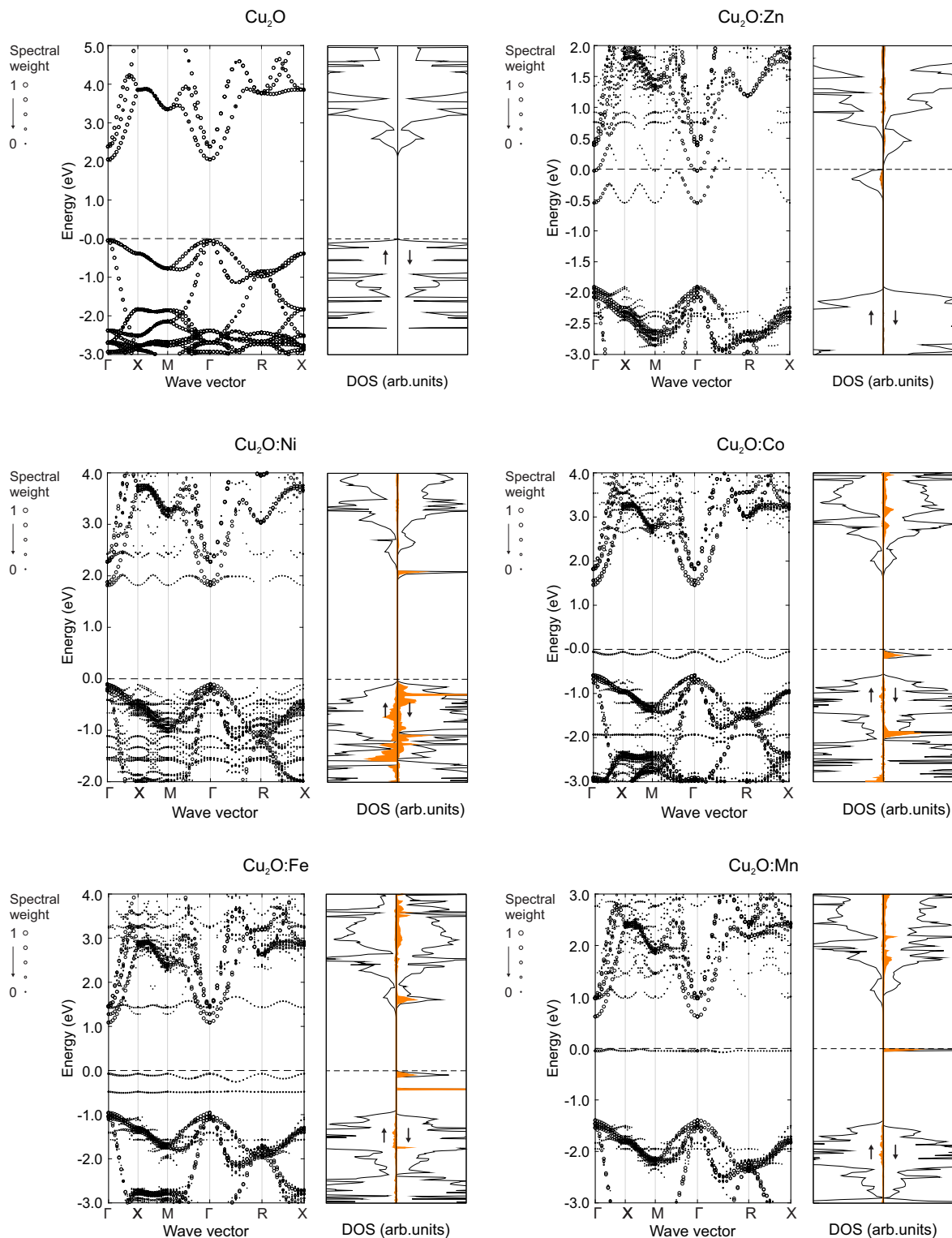


Figure 4.3: Electronic band structures together with total (black line) and TM dopant-projected densities of state (orange line) of clean and doped  $\text{Cu}_2\text{O}$ . Top left figure shows the undoped  $\text{Cu}_2\text{O}$  supercell after performing unfolding of the bands. The dashed line indicates the highest occupied state and arrows represent different spin channels.

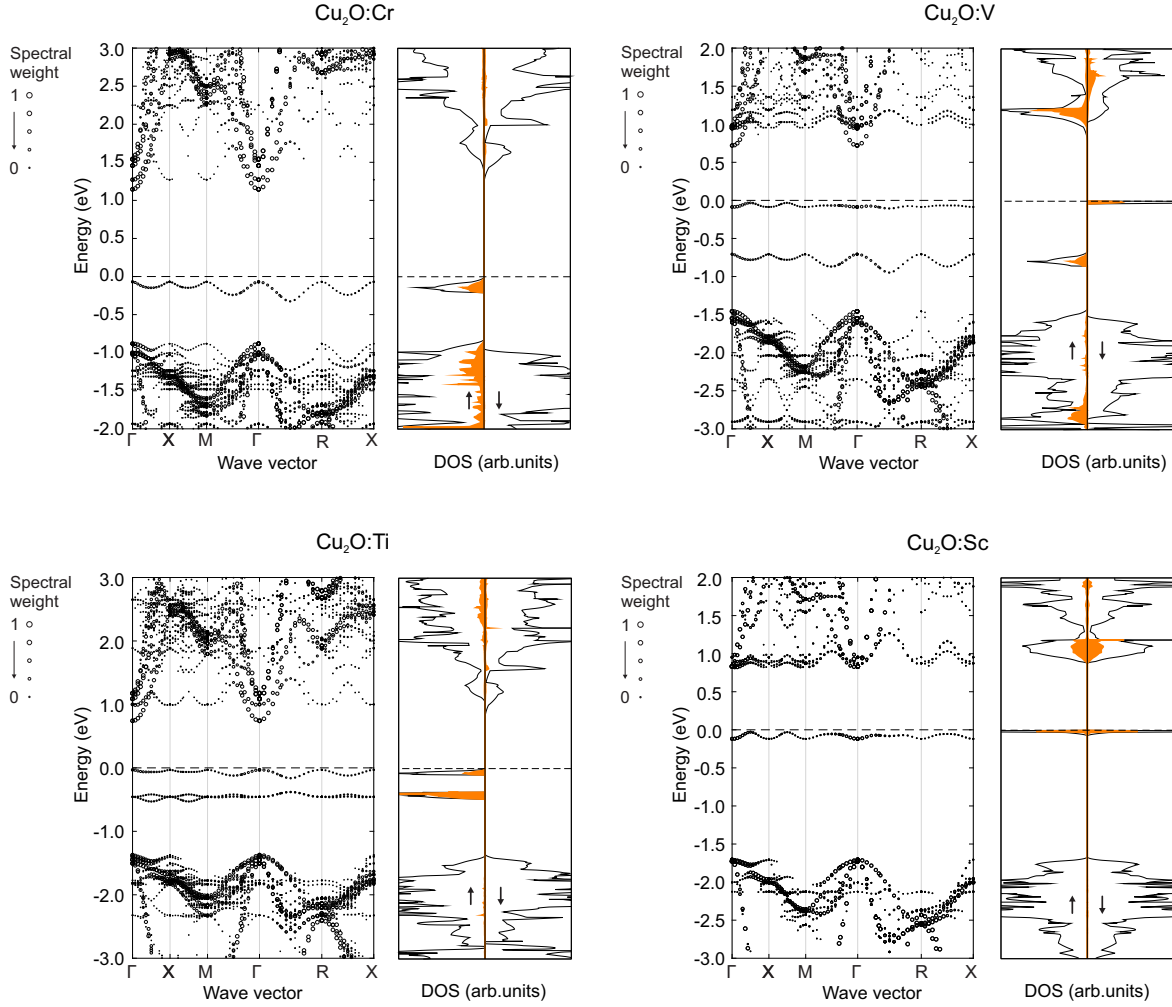


Figure 4.4: Electronic band structures together with total (black line) and TM dopant-projected densities of state (orange line) of doped  $\text{Cu}_2\text{O}$ . The dashed line indicates the highest occupied state and arrows represent different spin channels.

majority channel at around 0.817 eV above the VBM. The empty  $3d$  states are merged with the conduction band for Mn doping, while in the case of Cr doping the filled  $3d$  states are placed slightly below the valence band. Mn and Cr also show strong magnetization of  $4.252 \mu_B$  and  $4.259 \mu_B$ , respectively, on the impurity dopant atom.

A single substitutional V dopant atom creates two donor states within the band gap of  $\text{Cu}_2\text{O}$ . The first one is located at about 0.842 eV above the VBM, whilst the second is found at 1.370 eV above the VBM.

One doubly-occupied donor band at 0.917 eV from the VBM and one single occupied donor impurity band located at 1.342 eV from the VBM can be identified when a single Ti atom replaces Cu in  $\text{Cu}_2\text{O}$ . The introduction of a Sc dopant creates an intermediate band level occupied in both spin channels at around 1.607 eV from the VBM, whose high formation energy reflects the low probability of finding such a defect in any real form of this material.

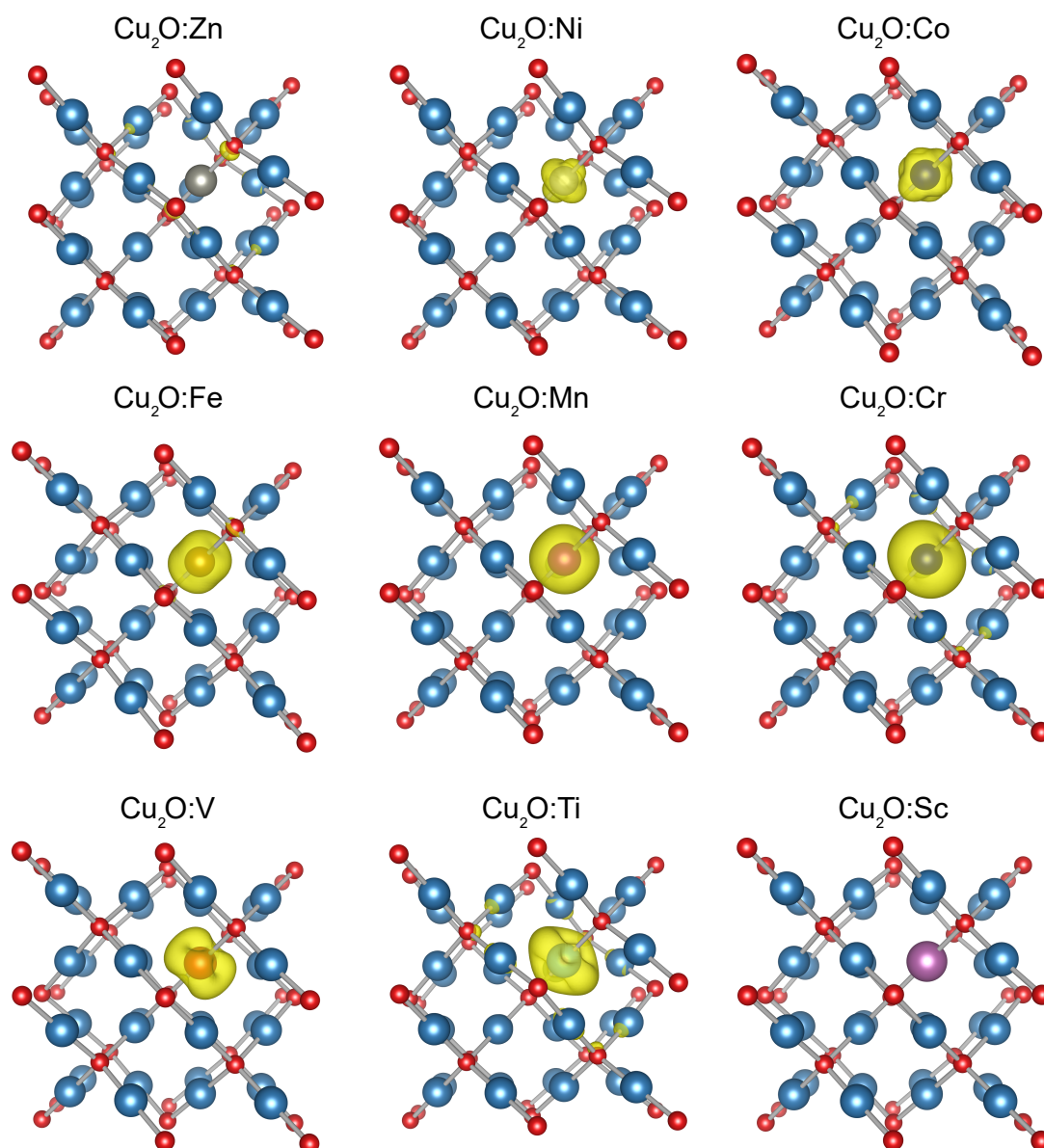


Figure 4.5: Spin density difference (depicted in yellow) for TM doped  $\text{Cu}_2\text{O}$ . Isosurface level set to  $0.011 e/\text{\AA}^2$ . Red and blue spheres represent oxygen and copper atoms, respectively, while the differently coloured atoms represent the transition metal dopant.

Table 4.6: Formation energies for substitutional defects on the copper site with an additional copper vacancy in  $\text{Cu}_2\text{O}$  together with the accompanying magnetic moment on the transition metal dopant and nearest-neighbouring oxygen. Two types of formation energies are reported,  $E^{f_0}$  calculated "as is" from obtained DFT energies and  $E^f$  calculated taking into account the limiting competing phases of corresponding (dopant) transition metal oxides.

	Sc	Ti	V	Cr	Mn	Fe	Co	Ni	Zn
$E^{f_0}$ (eV)	-1.931	0.004	-0.799	-0.139	-1.540	-0.114	0.172	0.750	0.398
$E^f$ (eV)	5.144	2.875	2.692	2.540	0.205	1.456	1.517	2.295	2.000
$m_{\text{TM}}$ ( $\mu_{\text{B}}$ )	0.000	1.768	2.575	3.803	4.546	3.541	2.507	1.502	0.000
$m_{\text{O}}$ ( $\mu_{\text{B}}$ )	0.000	0.017	0.048	0.045	0.034	0.047	0.041	0.039	0.000

### 4.3.3 Copper vacancies in cation-doped $\text{Cu}_2\text{O}$

The situations described above refer to an ideal, perfect crystal where no other defects are present beyond the dopants. In reality, intrinsic Cu vacancies ( $V_{\text{Cu}}$ ) are usually present in  $\text{Cu}_2\text{O}$ , which could alter the charge state of the TM dopant. To explore the stabilization of the electronic structure and simulate conditions closer to experiments, one additional  $V_{\text{Cu}}$  is introduced in the previously doped system. The complementing band structure has been omitted from this analysis due to increased computational cost. Clustering effects were noted when the  $V_{\text{Cu}}$  was introduced in the proximity of the extrinsic dopant, demonstrating lower formation energies (not shown), as has been observed in previous studies [189, 191, 193].

The additional hole generated by the  $V_{\text{Cu}}$  compensates the electron donation effect induced by the single Zn dopant. In the presence of the copper vacancy, the defect formation energy is lowered by 0.490 eV, while the donor level and the magnetisation are fully quenched (values listed in Table 4.6). Empty Zn 4s states are hybridized with the  $\text{Cu}_2\text{O}$  conduction band with an overall band gap calculated from single particle levels to be 1.909 eV, as shown in Figure 4.6. In contrast, the additional  $V_{\text{Cu}}$  together with the Ni dopant increases the defect formation energy by 0.946 eV. The additional hole is now transferred to the Ni impurity, creating two empty states in the minority spin channel, located at 0.866 eV and 1.532 eV above the VBM, respectively. The magnetization on the Ni impurity atom is increased to  $1.502 \mu_{\text{B}}$ , arising from re-arranged unpaired electrons of Ni  $d$  states.

A  $V_{\text{Cu}}$  located near the Co dopant features an increase in the formation energy, creating empty states within the conduction band. One additional singly unoccupied state in the spin minority channel originating from Co  $3d$  and  $4s$  orbitals is located around 1.260 eV above the VBM. For the systems doped with Fe, Mn, Cr, and V, a lowering of the defect formation energy is observed. In contrast to the system without an additional Cu vacancy, empty states within the gap are created. Their positions

Table 4.7: Bader charge analysis of first row transition metal doped  $\text{Cu}_2\text{O}$  without and with an additional copper vacancy in the vicinity of the dopant atom. Values listed are in  $e^-$ . NN represents the nearest-neighbour and NNN the next nearest-neighbour to the dopant atom.

	Sc	Ti	V	Cr	Mn	Fe	Co	Ni	Zn
$\text{TM}_{\text{Cu}}$	+1.585	+1.150	+1.118	+0.887	+0.914	+0.759	+0.633	+0.522	+0.939
$\text{TM}_{\text{Cu}} + \text{V}_{\text{Cu}}$	+1.879	+1.544	+1.223	+1.188	+1.201	+1.090	+0.980	+0.909	+1.084
$\text{O}_{\text{NN}} (\text{TM}_{\text{Cu}})$	-1.232	-1.215	-1.199	-1.232	-1.145	-1.158	-1.134	-1.129	-1.160
$\text{O}_{\text{NN}} (\text{TM}_{\text{Cu}})$ + $\text{V}_{\text{Cu}}$	-1.121	-1.196	-1.108	-1.125	-1.122	-1.120	-1.092	-1.082	-1.110
$\text{Cu}_{\text{NN}}$	+0.532	+0.560	+0.536	+0.570	+0.531	+0.567	+0.563	+0.549	+0.598
$\text{O}_{\text{NN}} + \text{V}_{\text{Cu}}$	+0.568	+0.574	+0.555	+0.555	+0.546	+0.556	+0.588	+0.546	+0.548

relative to the CBM minority spin channel are 0.640 eV and 0.260 eV for Fe and Mn, respectively. The Cr dopant creates two acceptor states within the gap, one positioned at 1.352 eV and the other at 2.245 eV above the VBM. Substitution by V favours an electron transfer from the V 3d band, where the formed acceptor level becomes merged with the bottom of the CBM. The net magnetisation per impurity atom is increased for the Fe-, Mn-, Cr- and V-doped system in the material with the  $\text{V}_{\text{Cu}}$  due to increased number of spin unpaired electrons.

The Ti- and Sc-doped  $\text{Cu}_2\text{O}$  systems undergo substantial lattice distortions. The impurity atoms move into the tetrahedral position, increasing the formation energy by 0.811 eV for Ti and lowering it by 0.393 eV for Sc. The Sc-doped system is found to be metallic in nature, due to hybridised Cu 3d, 4s, and O 2p states crossing the Fermi level. Together with a formation energy of more than 5 eV, this defect is, again, by far the least favourable of all the considered ones.

Results shown in Table 4.7 illustrate the Bader charge distribution analysis undertaken on the extrinsic dopant and its nearest neighbouring atoms. Charge differences confirm the increased loss of negative charge (i.e. positive charge gain – increased hole concentration) on the transition metal dopant between the systems without and with the additional copper vacancy. This hole localization is further highlighted by visualizing the spin density difference, as shown in Figure 4.7. Small charge fluctuations are observed on the nearest neighbouring Cu atoms, surrounding the dopant, with a value between 0.01 and 0.03  $e^-$ . The charges on the nearest neighbouring oxygen atoms in the stoichiometric FRTM-doped systems are distributed symmetrically, in contrast to the FRTM-doped system with the additional copper vacancy. The copper vacancy leads to a distortion of the TM-oxygen distances causing slight increases in the bond lengths and, as a consequence, fluctuation of the charge.

Partial charge densities of the vacant impurity bands, created when  $\text{Cu}_2\text{O}$  was

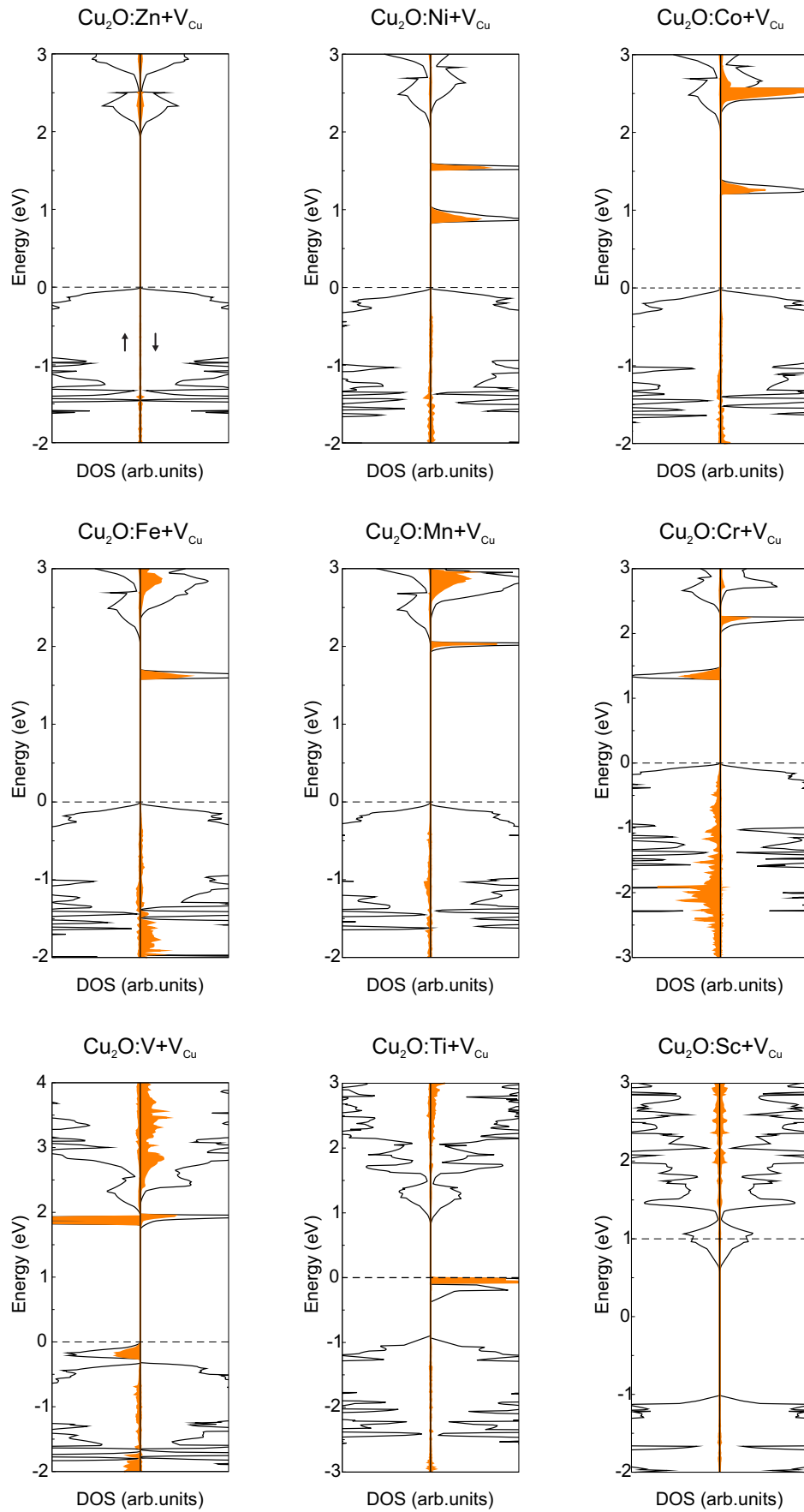


Figure 4.6: Total (black line) and TM dopant-projected (orange line) densities of state of TM doped  $\text{Cu}_2\text{O}$  with one additional Cu vacancy. The dashed line indicated the highest occupied state and arrows represent different spin channels.

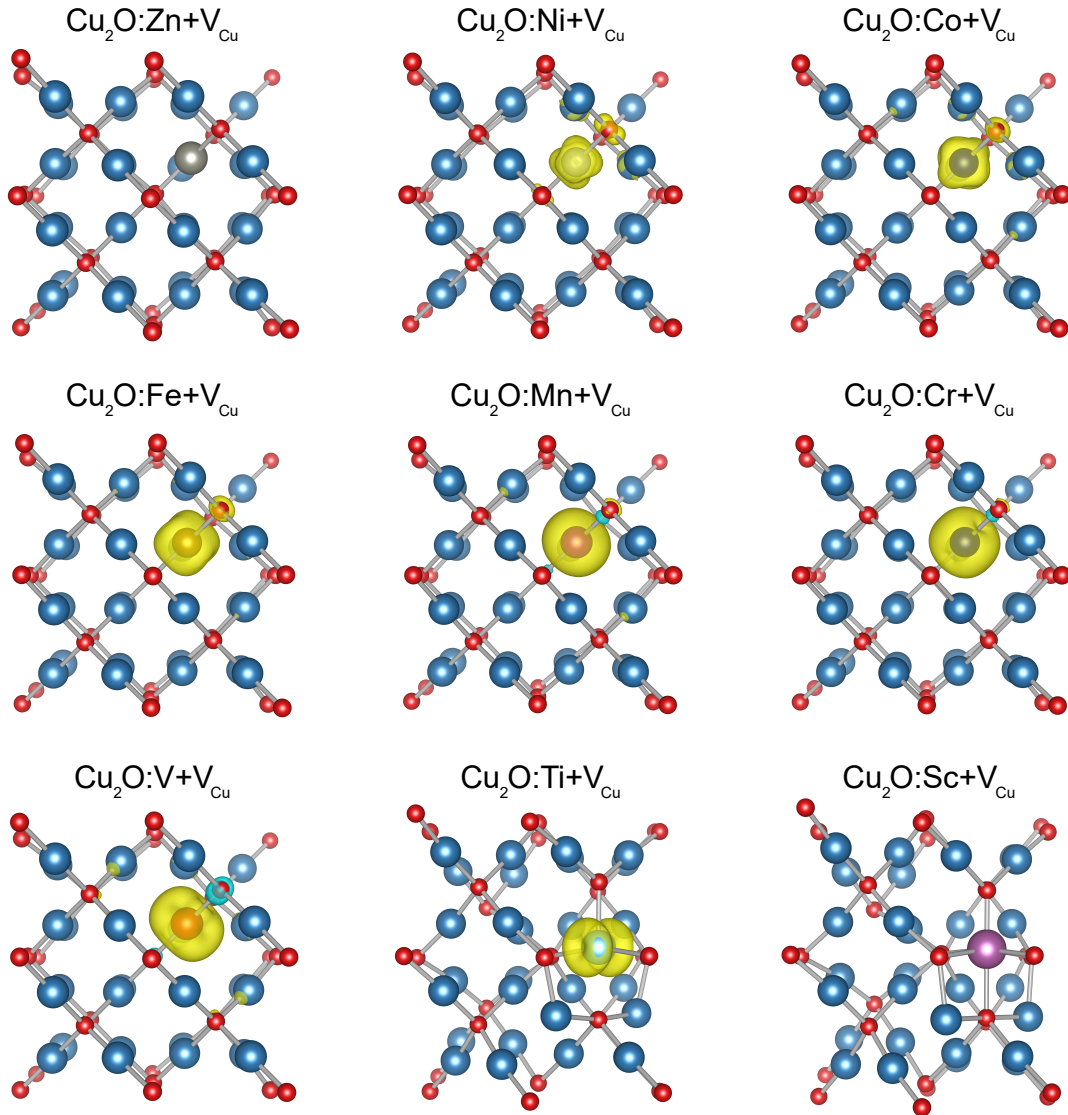


Figure 4.7: Spin density difference (depicted in yellow) for TM doped  $\text{Cu}_2\text{O}$  with an additional  $\text{V}_{\text{Cu}}$ . Isosurface level set to  $0.011 \text{ e}/\text{\AA}^2$ . Red and blue spheres represent oxygen and copper atoms, respectively, while the differently coloured atoms represent the transition metal dopant.

doped with TM and one additional copper vacancy, have been presented in Figure 4.8. Shown are systems where a distinct impurity band was observed, leaving out Zn and Sc due to merging of states with the CBM. Delocalisation of the additionally created states is observed in the case of Ni and Co, whilst the remaining systems demonstrate a high degree of localisation of states on the impurity atom. Delocalised states do not act as hole traps, thus leading to potentially favourable increases in conductivity [28].

Electronic structure calculations provide insight into charge transfer processes, occurrence of additional impurity states within the host's band gap or the degree of localization of excess carriers. However, direct impact on photovoltaic properties of relevance is often difficult to assess. One available metric to do so is the so-called Spectroscopic Maximum Limited Efficiency (SLME) approach, developed by Yu and

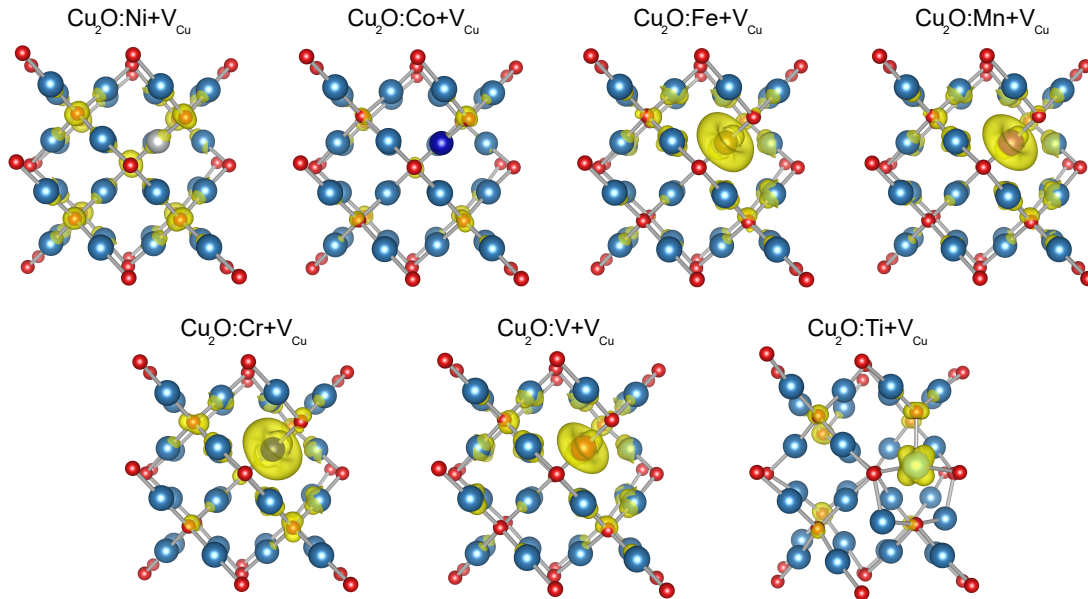


Figure 4.8: Partial charge density (depicted in yellow) representation of vacant impurity band in the electronic structure of TM doped  $\text{Cu}_2\text{O}$  with one additional copper vacancy on the nearest-neighbouring site. Isosurface level set to  $0.03 \text{ e}/\text{\AA}^2$ . Red and blue spheres represent oxygen and copper atoms, respectively, while the differently coloured atoms represent the transition metal dopant. The represented densities were chosen from the respective densities of state to match the vacant impurity bands discussed in the main text.

Zunger [145]. It extends beyond the commonly used Shockley–Queisser criterion to incorporate a fraction of non-radiative recombination, whilst approximating the power conversion efficiency (PCE) of a material employed as a thin film absorber.

The calculated SLME for substitutionally doped  $\text{Cu}_2\text{O}$  without and with an additional copper vacancy are shown in Figure 4.9 and Figure 4.10, respectively. The most prominent enhanced effect is observed for Zn and Ni, when considering single substitutional defects on the copper site in  $\text{Cu}_2\text{O}$ , whereas Mn, V, and Ti impaired the already low efficiency of pure  $\text{Cu}_2\text{O}$  (efficiencies lowering those of pristine  $\text{Cu}_2\text{O}$  were omitted from the graph). The introduction of an additional copper vacancy stabilizes the system energetically, in addition to favouring higher light absorption. The main cause of the significant increase in SLME is attributed to the nature of inter-band transitions between the VBM and CBM. Pure  $\text{Cu}_2\text{O}$  exhibits a parity forbidden lowest fundamental absorption transition (neglecting excitons), hindering immediate light capturing until  $\approx 2.6 \text{ eV}$ . In the case of doped  $\text{Cu}_2\text{O}$ , defects create band levels within the band gap, allowing an earlier absorption onset. This can be observed in the calculated absorption coefficients (right hand side of Figure 4.9 and Figure 4.10), which indicate the absorption probability of incident photons of different energies. In both types of studied defect systems, a shift of the absorption onset towards lower energies is observed, approaching the ideal band gap value for photovoltaic materials which lies around  $1.3\text{--}1.5 \text{ eV}$  [8, 214]. Since SLME incorporates the difference between

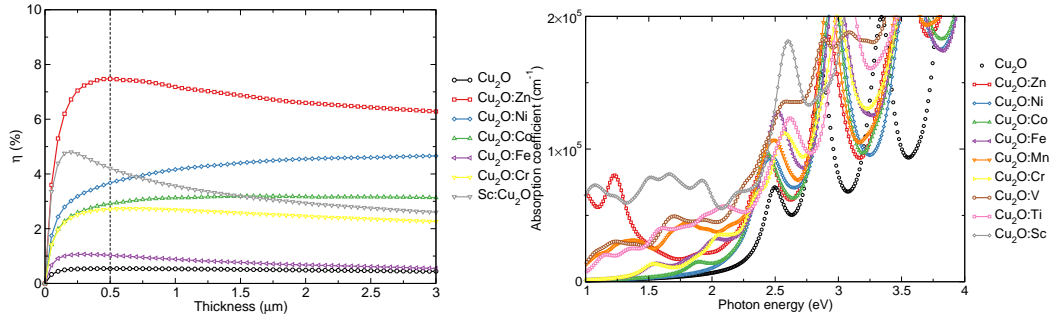


Figure 4.9: Calculated SLME (left) together with the absorption coefficient (right) for FRTM substitutional dopants in  $\text{Cu}_2\text{O}$ . SLME values lower than the initial  $\text{Cu}_2\text{O}$  (denoted with the black line) were omitted from the graph.

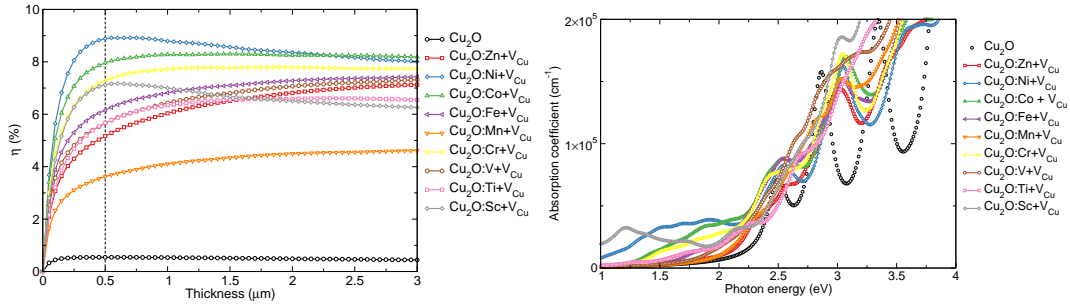


Figure 4.10: Calculated SLME (right) together with the absorption coefficient (left) for FRTM substitutional dopants in  $\text{Cu}_2\text{O}$  with an additional copper vacancy. Values for SLME lower than the one for pristine  $\text{Cu}_2\text{O}$  (denoted with the black line) were omitted from the graph.

the first direct allowed interband transition and the fundamental band gap to estimate non-radiative recombination processes, the resulting efficiencies are observed to have increased.

While interpreting these results, one has to keep in mind the theoretical limitations of the employed methodology. Spin-orbit coupling and excitonic effects, which could influence the calculated electronic structure, were omitted from this study due to their significant increased computational cost. Furthermore, defect properties (i.e. mobility, arrangement, migration) are significantly influenced by temperature fluctuations, which are not accessible within the methodological framework used here. In addition, values illustrated within this work are valid for a single-crystal material, where band alignment or interface barrier effects, though valid in real-time applications, are not present. Despite those limitations and their most likely negative effect on the calculated absorption efficiencies, the results discussed here match experimentally observed phenomena. A 3-fold improvement was shown in the overall PCE of  $\text{Cu}_2\text{O}$  thin films doped with Zn compared to clean  $p$ -type  $\text{Cu}_2\text{O}$  ones [178], confirming the theoretical calculated values. In addition, Fe-doped  $\text{Cu}_2\text{O}$  films have shown significant improvement of optical transmittance over undoped samples [197].

## 4.4 Conclusion

A systematic computational study within a hybrid DFT formalism of the electronic and optical properties of transition metal-doped  $\text{Cu}_2\text{O}$  was carried out. Additional copper vacancies, observed intrinsically in  $\text{Cu}_2\text{O}$ , were also considered and found to have a stabilizing effect on the defect formation energies. To assess the overall absorption potential of doped compounds, the SLME metric was calculated. Two significant outcomes have resulted from the aforementioned analysis:

- First row transition metal dopants, once incorporated into the  $\text{Cu}_2\text{O}$  matrix, allow band gap tunability by creating a range of defect levels in the pristine electronic structure, which range from shallow levels (e.g. for dopants Zn or Ni) to deep levels (e.g. for dopants Mn or Cr).
- Extrinsic transition metal dopants increase substantially the capacity of  $\text{Cu}_2\text{O}$  to absorb light, reaching PCE values close to 10%, attributed to the bypassing effect of impurity levels on the optical transition selection rules. Most promising dopants were found to be Ni, Fe, and Zn.

Results presented in this chapter indicate the potential of first row transition metals as favourable dopants for improved absorption properties and overall photovoltaic performance of  $\text{Cu}_2\text{O}$ .

## Altering between intrinsic *p*-type and *n*-type defects of CuO

*"I know you think you understand what you thought I said but I'm not sure you realize that what you heard is not what I meant"*

---

Alan Greenspan, *American economist*

As pointed out in the previous chapter, CuO is a strongly correlated transition metal oxide which shows strong coupling between spin, charge, orbital, and vibrational degrees of freedom. It was studied heavily since the discovery of cuprate high-temperature superconductors due to its close resemblance of structural, electronic, and magnetic properties [105]. In CuO, low-energy physics gives rise to antiferromagnetism with two distinct Néel temperatures and multiferroicity, reflecting the presence of competing equilibrium phases that are close in energy [215].

Despite the ideal value of the electronic band gap of CuO, which measures around 1.4 eV, reports of maximum efficiencies for single junction solar cells are rare. As it was demonstrated in the previous chapter, one single ideal value does not guarantee good applicability for solar harvesting, as a multitude of factors (recombination, strong absorption onset, charge carrier lifetimes, etc.) is being neglected that way.

The chapter is organized as follows: in the first section, a brief review of works considering the doping of CuO, both intrinsic and extrinsic, is presented. In the subsequent section the theoretical parameters have been listed, followed by a section of results and discussion, where appropriate. In the last section, answers to some of the questions outlined within the chapter were discussed and the extent of the validity of results being addressed.

## 5.1 Summary of available literature

**Experimental evidence of intrinsic defects** Shah *et al* [216] studied CuO doped with 0.5 % Fe. Fe was observed to weaken the antiferromagnetic interaction between Cu spins, causing a decrease in the Néel temperature. Borzi *et al* [217] explored CuO doped with 0.5 % Fe and 1.2 % Zn, respectively, focusing on the possible magnetization effects in the temperature range between 4.2 K and 300 K. Fe<sup>3+</sup> doping was observed to create point defects in order to keep charge balance, while Zn doped CuO samples exhibited properties close to the undoped compound. Further studies observed a decrease in Néel temperature for Zn doped CuO with a 5 % doping ratio to  $\approx 200$  K and  $\approx 170$  K for  $T_{N1}$  and  $T_{N2}$ , respectively [218].

Yang and co-workers [219] doped CuO with 3.5 – 15 % of Mn and measured their magnetoresistance for temperatures as low as 5 K. Two phase transitions were observed, one at about  $T_{N\acute{e}el} = 30$  K and another at  $T_{Curie} = 80$  K. Ohashi *et al* [151] examined the effects of pressure on the magnetic phase transition of single crystalline CuO up to 1.3 GPa and compared it to Li doped CuO. A comparison between pressure increased carrier concentration and extrinsic hole doping was undertaken to clarify the observed suppression of AFM coupling. Results indicate a hole hopping mechanism between Cu atoms being enhanced when external pressure is applied or holes are doped by substitutional Li.

Zhu *et al* [220] fabricated CuO highly (111) oriented thin films doped with 6.6 – 29.8 % of Mn. Results indicate that both Cu and Mn atoms are in the +2 valence state. Ferromagnetism of the sample was observed for Mn doping concentration above 13 %, while below 10 % a paramagnetic behaviour was measured. In the low doping regime, Mn ions are separated far apart and they behave like isolated ions, where a magnetic moment of  $4.5 \mu_B$  was evaluated per Mn ion. The small lattice variation observed in the doped samples, compared to the original structure, hints toward successful Mn incorporation via substitution of Cu in the CuO lattice [221]. Additional 5 % of copper vacancies was observed in the doped samples, responsible for the *p*-type conductivity. Ferromagnetism for highly Mn doped CuO samples was observed in following studies as well [222].

Gao and co-workers [223] doped CuO with small Mn concentrations (0.2 %, 0.4 %, 0.75 %, 1.25 %, 3 % and 5 %). By analysing the expansion of the doped lattice volume, a doping limit for Mn in CuO was reached at 1.5 %, followed by the appearance of secondary phases, in this case Mn<sub>2</sub>O<sub>3</sub>. Samples with lower doping concentrations retain Mn dopants predominantly in the +2 valence state, while higher doping concentrations show a mixture of +2 and +3 states. Comparing different sizes of CuO nanocrystals, a threshold of 10 nm was shown to reproduce the magnetic properties of the bulk. In

other words, samples with grain size larger than 10 nm retain the antiferromagnetic properties of the bulk CuO ground state. For samples doped with less than 4% Mn, only antiferromagnetism was detected, while for samples doped with  $\geq 4\%$  Mn a ferromagnetic to paramagnetic transition was observed with a Curie temperature of 45 K–79 K, depending on the doping concentration. This has been attributed to the formation of a bound magnetic polaron (BMP), which consists of a localized electron and many  $\text{Mn}^{2+}$  ions around the localization centre. Neighbouring BMPs are able to produce long-range ferromagnetic coupling, depending on the concentration of Mn doping. Li *et al* [222] synthesised CuO films doped with 30% Mn annealed in three different environments ( $\text{O}_2$ , air, and  $\text{N}_2$ ). Samples annealed in  $\text{O}_2$  exhibited ferromagnetic characteristics together with the formation of a secondary phase  $\text{CuMn}_2\text{O}_4$ , while the ones annealed in  $\text{N}_2$  showed pure CuO phases.

Room temperature ferromagnetism was observed for CuO powder samples doped with 2% Fe [224], retaining antiferromagnetism below the Néel temperature. A super-exchange mechanism of  $\text{Cu}(\text{Fe})\text{-O-Cu}(\text{Fe})$  was identified to be responsible for the observed magnetic structure. Further measurements indicated that Fe ions substitute Cu ones with a valence state of +3 coupled to localized oxygen vacancies. Similar to the case of CuO:Mn, ferromagnetic thin films doped with 10% Fe were found to contain  $\text{Fe}^{2+}$  and  $\text{Fe}^{3+}$  valence states, indicating the formation of secondary spinel ferrite phases in the film [225]. A decrease of the indirect band gap from 1.037 eV to 1.015 eV was observed in the same work, with a simultaneous increase of the direct band gap from 1.66 eV to 1.96 eV.

Ti doped CuO (0.1% concentration) was found to decrease the resistivity of the thin films, while leaving the optical band gap, transmittance, and reflectance unaltered [226]. CuO thin films doped with N showed properties heavily dependent on the dopant concentration and annealing temperature [227] (*no specification of dopant site*). CuO is the dominant phase formed for concentrations up to 1.5%, while higher concentrations have  $\text{Cu}_2\text{O}$  phases present in the samples. The films have higher transmittance and reflectance compared to CuO, with an increasing indirect (direct) band gap from 1.1 eV to 1.83 – 2.06 eV (2.45 – 2.92 eV), for concentrations from 1.5% to 4.1%.

CuO doped with Ni does not undergo significant crystal structure changes for doping up to 10% [228]. A decrease of the band gap was measured, from 2.03 eV for the undoped sample to 2.01 eV, 1.96 eV for 2% and 4% doping, respectively. An enhancement of the magnetization properties was noticed when CuO is doped with Co (1, 3, and 5%) [229]. Co doping induces a change in the antiferromagnetic transition temperatures in CuO, increasing  $T_{\text{N}_2}$  for about 2 K and decreasing  $T_{\text{N}_2}$  up to 180 K (compared to the initial 213 K). Furthermore, the 5% doped sample showed presence of mixed +2 and +3 valence states of both Cu and Co ions.

An incorporation of 5% Zn into the CuO matrix does not lead to creation of secondary phases, as experiments conducted by Jones *et al* [230]. However, a small change in the lattice parameters is observed, with an increase in *a*, decrease in *b*, and almost no change in the *c* lattice vector.

Nasir *et al* [231] observed stronger ferromagnetism in Fe doped CuO samples (up to 12.5% doping), with mixed valence state of majority Fe +3 and minority +2 ions. The measured magnetism was attributed to the incorporation of Fe<sup>3+</sup> ions leading to a reduction of oxygen vacancies. Hence, cation vacancies are generated to maintain charge neutrality thereby increasing the sample's magnetic properties. Also, metallic Fe clusters and Fe<sub>2</sub>O<sub>3</sub> impurity phases have been ruled out, pointing towards proper substitution in the samples.

Das *et al* [232] reported successful incorporation of Ni dopants up to 8% into CuO thin films (thickness of  $\approx$  300 nm). An increase of the band gap was found with increasing dopant concentration up to 6%, followed by decrease for further doping. Enhanced conductivity and dielectric constant were observed up to that particular level of Ni, indicating increased charge carrier density. Doping of CuO thin films with Cr showed successful incorporation of the dopant into the lattice with a +3 charge state [233]. Furthermore, performing surface sensitive measurements did not reveal any signal from Cr, indicating dopant location further away from the surface.

Chtouki *et al* [234] observed a reduction of CuO's direct band gap from 1.67 eV to 1.56 eV while increasing the number of deposited layers (from 5 to 7) on CuO thin films. At the same time, an upsurge of the absorption coefficient was noted with the increase of the deposited layers. This was attributed to the crystallinity development (improvement of structural and morphological properties, i.e. grain size increase, lowering of porosity). However, introducing 2% of dopants (Sn, In, Fe, and Mn) has a negative effect on the overall crystal structure thereby reducing the absorbance of the doped thin films.

### Modelling results on intrinsic defects of CuO as obtained from literature

CuO was computationally confirmed as a *p*-type semiconductor, as reported by Wu *et al* [103]. Within the same work, LSDA+*U* has been proven to be sufficiently accurate for intrinsic defect studies, indicating that the V<sub>Cu</sub><sup>2-</sup> defect always has the lowest formation energy. Nolan *et al* [57] studied copper vacancy formation in CuO. Employing a DFT+*U* methodology, a similar behaviour was found to that of Cu<sub>2</sub>O, indicating a delocalised hole originating from the difference between majority and minority spin states. The hole delocalises over few vacancy neighbouring copper atoms, according to their conclusions.

Filippetti and Fiorentini [235] explored the ferromagnetic phase of Mn doped CuO

Table 5.1: Summary of defect formation energies, impurity levels, electronic band gap, and effective masses of intrinsically doped CuO, as available in existing literature.

Structure	Formation energy (eV)	Impurity level (eV)	Effective mass ( $m_e$ )
$V_{Cu}$	1.17 (DFT+ $U$ )[57]	$E_V + 0.20$	-0.65
$V_{Cu^{2-}}$	$\approx 0.50$ (DFT+ $U$ )[103]	-	-
$V_O$	$\approx 3.50$ (DFT+ $U$ )[103]	-	-
$V_{Cu}^{Split}$	1.70 (DFT+ $U$ )	$E_V + 0.20$	-0.79
$Cu_i$	$\approx 3.60$ (DFT+ $U$ )[103]	-	-
$O_i$	$\approx 3.40$ (DFT+ $U$ )[103]	-	-
$Cu_O^{2+}$	$\approx 6.20$ (DFT+ $U$ )[103]	-	-
$O_{Cu}^{2-}$	$\approx 2.80$ (DFT+ $U$ )[103]	-	-

via self-interaction-corrected LSDA calculations (between 3.1% and 12.5% doping). Substitutional Mn in CuO induces shallow donors with ionization energies between 0.05 eV and 0.25 eV, depending on spin ordering. A double-exchange hopping mechanism mediated through Mn–O–Cu–O spin alignment was observed to provide long-range conductivity, even at low doping concentrations. On the other hand, spin misalignment generates a depletion of the Mn- $d_{z^2}$  states creating a barrier for electron mobility – the system behaves insulating.

Peng *et al* [34] undertook a first-principle analysis of possible  $p$ - (Li and Na) and  $n$ -type (Al, Ga, In, Ti, Zr, and Hf) dopants for CuO using the LSDA+ $U$  method. Calculations confirm copper vacancies as the lead contributor to  $p$ -type conductivity, with oxygen vacancies showing high formation energies under O-rich conditions. Under O-poor conditions, the formation energy of  $V_{Cu}$  surpasses that of  $V_O$ , yet the created transition levels are located deep in the band gap, thus not being able to convert the conductivity to  $n$ -type. The investigation revealed only 2 possible  $n$ -type dopants, Zr and Hf, although with high formation energies which make the doping process challenging.

Yang *et al* [236] considered the doping of CuO with Fe, using the antiferromagnetic unit cell with a single (6.25%) and double (12.5%) dopant concentration, employing a DFT+ $U$  model. The doped atom was considered having the same magnetic moment orientation as the substituted Cu atom. The system with a single dopant exhibited ferrimagnetic properties due to Fe replacing Cu with a different magnetic moment, while the double-doped system showed a ferromagnetic ground state with lower energy than the antiferromagnetic one.

Ganga *et al* [237] analysed the effect of impurity spins on the magnetic chains within

CuO, using the GGA+ $U$  ( $U = 5$  eV) on a magnetic unit cell. Exploring the stability of CuO<sub>4</sub> square planar complexes it was shown how a perfectly planar complex (in theory) would have led to a non-magnetic metallic CuO. However, the destabilization of those planar complexes leads to an opening of the gap and favours the antiferromagnetism observed experimentally. Furthermore, by varying the Hubbard  $U$  value, the effect of impurities (Cr, Fe, Mn, Co, and Ni) on the spin arrangement of CuO was studied. The spin states of Cr and Mn show to be independent of the  $U$  value, always taking the high spin state with 4 and 5 unpaired electrons, respectively. DFT calculations indicate retained spin orientation for Mn, Fe, Co, and Ni (in the high-spin state), and a reverse spin orientation for Cr (high spin,  $S = 2$ ), Fe (intermediate spin,  $S = 1$ ), and Co (low spin,  $S = 0$ ) impurities.

### 5.1.1 Concluding remarks on literature review

From the undertaken literature examination presented within the current chapter and Chapter 3, several conclusions regarding the physics and chemistry underpinning CuO can be summarized. The conductivity of CuO, created without significant structural/composition modifications, is prevalingly *p*-type. In other words, there is a certain amount of missing Cu atoms in the crystal structure of CuO that induce hole states, whose number is sufficient to become the main current carriers. Also, CuO is an antiferromagnetic insulator, known for its high Néel temperature as well as strong magnetic coupling within. Upon doping with Fe or Mn, long lasting ferromagnetism extending into the range of room temperature was observed. Theoretical studies identified simple Cu vacancies as the dominant defects appearing in CuO.

However, majority of works deals with either magnetic features of CuO or the influence of extrinsic dopants onto the magnetic transition temperatures. Theoretically, the use of the correct ground state magnetic configuration was elucidated but its incorporation was found in only a handful of studies [105, 106, 238]. Furthermore, several computational frameworks were found capable of modelling various aspects of CuO, yet their extent to account for defects was not examined.

In this part, a comparative study between two different theoretical approximations modelling CuO was undertaken. Based upon that, a systematic study of simple defects and their energetic cost of formation in CuO were studied. Some of the questions being assessed within this chapter include:

- Which computational framework describes the ground state properties of CuO accurately? Can the different parameters found within the literature be explained?
- Which model describes the intrinsic defect properties of CuO?

- Can CuO be created intrinsically *n*-type? If so, under which conditions?
- What role do defects play in the experimentally measured low photovoltaic efficiency of CuO?

In order to do so, first-principle calculations using GGA+ $U$  and hybrid approximations for CuO have been performed in order to elucidate some of the questions outlined above.

## 5.2 Technical details and computational parameters

Results computed and presented in this chapter were based on spin polarized DFT-based calculations performed with the Vienna Ab-initio Simulation Package [135]. The interactions between core and valence electrons were represented using the projector augmented wave (PAW) method [134]. The general gradient approximation (GGA) [136] exchange-correlation (XC) functional with the Perdew–Burke–Ernzerhof (PBE) parametrization was employed for DFT+ $U$  within the formalism of Dudarev *et al* [16]. For the hybrid-DFT calculations, the HSE XC functional was used [19–21], with a screening parameter of  $0.2 \text{ \AA}^{-1}$ . Long distance dispersion corrections were included using the D3 approach of Grimme *et al* [139]. The plane wave expansion cutoff was set to 450 eV and the force convergence criterion to cell relaxation was  $0.01 \text{ eV/\AA}$ .  $\Gamma$ -centred Monkhorst-Pack [22] meshes ( $7 \times 7 \times 7$  for the primitive unit cell,  $5 \times 5 \times 3$  for conventional unit cell,  $3 \times 5 \times 3$  for magnetic unit cell and a single  $\Gamma$ -point for the  $2 \times 3 \times 2$  supercell) were employed to sample the Brillouin zone in reciprocal space. Band structure and density of state (DOS) calculations were performed at the optimized structure along high-symmetry directions obtained from the Bilbao Crystallographic Server [140–142]. Band structures were plotted using the `Wannier90` code [239, 240]. The phase stability diagram of CuO for a range of accessible chemical potentials was computed using CPLAP (Chemical Potential Limits Analysis Program) [202], taking into account its limiting competing phases. The extent of defect charge distribution was studied using the Bader scheme as implemented in the Henkelman code [203–205]. Graphical drawings were produced using `VESTA` [144].

The values for the effective Hubbard parameter ( $U_{\text{eff}}$ ) and the amount of the non-local exact Hartree-Fock exchange used within the HSE XC functional were tuned according to the value of the ground state electronic band gap and (spin only) magnetic moment of the respective Cu atoms. Excitonic and spin-orbit coupling effects were not taken into account.

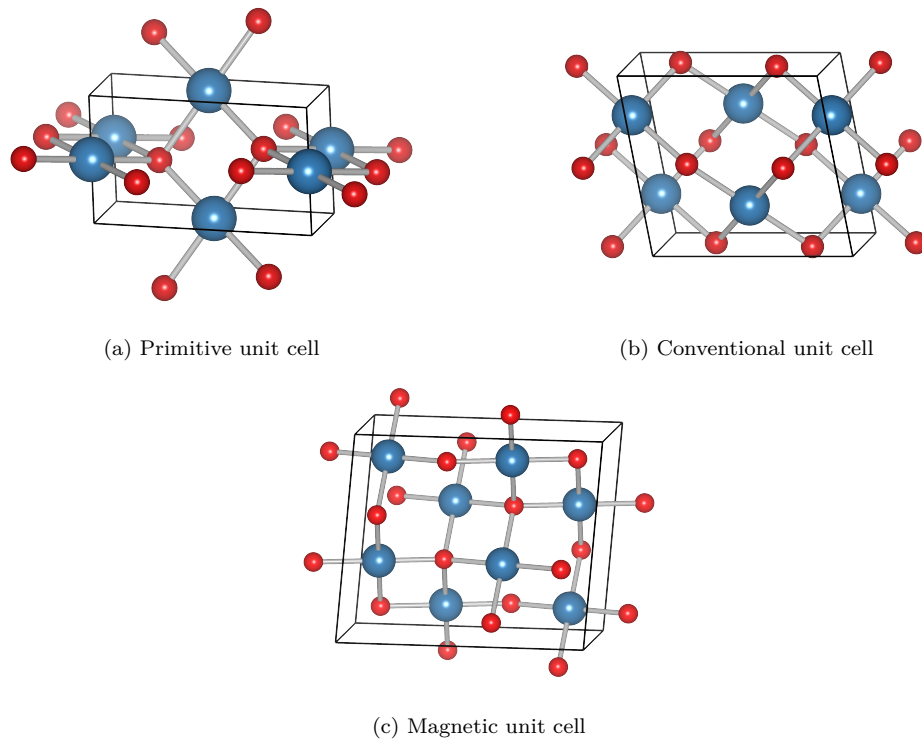


Figure 5.1: Different ways of defining the modelling unit cell of CuO. The emphasis on choosing the model lies within the correct antiferromagnetic ground state ordering.

Table 5.2: Lattice parameters for different simulation cells of CuO. Values were obtained by matrix transformations of the experimentally observed conventional unit cell of CuO from Årsbrink *et al* [82].

	Primitive cell	Conventional cell	Magnetic cell
a (Å)	2.9005	4.6837	6.3466
b (Å)	2.9005	3.4226	3.4226
c (Å)	5.1288	5.1288	7.4968
$\alpha$ (°)	82.3099	90.0000	90.0000
$\beta$ (°)	97.6901	99.5400	84.7332
$\gamma$ (°)	107.6853	90.0000	90.0000
Volume (Å <sup>3</sup> )	40.5399	81.0798	162.1597

### 5.3 Results and discussion

Firstly, the ground state properties of CuO are being discussed, focusing on the different definitions of the simulation cells. After that, the cell with the correct antiferromagnetic ordering is taken in order to assess the validity of various computational parameters.

**Modelling of CuO with different simulation cells** The smallest building unit, defined through the minimal volume required to fill space by repetition of its elements and the requirement to contain one lattice point, is the primitive cell. The primitive cell of CuO contains two Cu and two O atoms, with lattice parameters listed in Table 5.2. In order to transform between the primitive, conventional, and magnetic unit cell of CuO, the following transformations apply:

$$\begin{array}{cc}
 P \rightarrow C & C \rightarrow P \\
 \begin{pmatrix} 1 & 1 & 0 \\ -1 & 1 & 0 \\ 0 & 0 & 1 \end{pmatrix} & \begin{pmatrix} \frac{1}{2} & -\frac{1}{2} & 0 \\ \frac{1}{2} & \frac{1}{2} & 0 \\ 0 & 0 & 1 \end{pmatrix} \\
 & (5.1)
 \end{array}$$

$$\begin{array}{cc}
 C \rightarrow M & M \rightarrow C \\
 \begin{pmatrix} 1 & 0 & -1 \\ 0 & 1 & 0 \\ 1 & 0 & 1 \end{pmatrix} & \begin{pmatrix} \frac{1}{2} & 0 & \frac{1}{2} \\ 0 & 1 & 0 \\ -\frac{1}{2} & 0 & \frac{1}{2} \end{pmatrix}
 \end{array}$$

where *P*, *C*, *M*, stand for primitive, conventional, and magnetic cell, respectively <sup>1</sup>. Those transformations do not alter the physical properties of CuO, rather they allow for the right magnetic properties to be reproduced. However, significant band folding might occur when the electronic band structure is calculated because the conventional and magnetic unit cell are effectively supercells from the perspective of the primitive cell. This does not affect the value of the electronic band gap itself, but can cause misinterpretation of the nature of the gap due to the overlap of electronic bands. The calculated electronic band structure of CuO in the primitive unit cell is shown in Figure 5.2. The GGA approximation yields a metallic phase, as already reported for the conventional cell in the previous chapters, while DFT+*U* ( $U_{\text{eff}} = 8 \text{ eV}$ ) HSE06

<sup>1</sup>This can be done in a software like VESTA, where one specifies a transformation to the cell of choice by selecting *Edit data* → *Unit cell* → *Transform*. The software applies then the necessary symmetry operations and generates the new atomic positions accordingly.

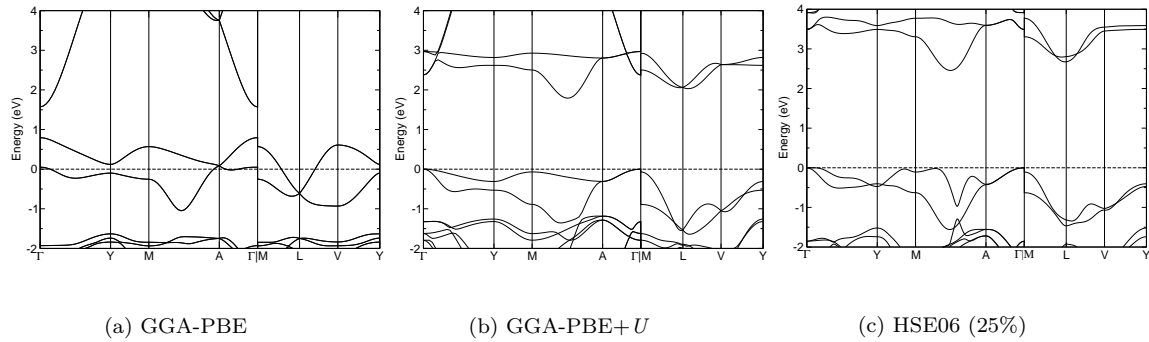


Figure 5.2: Calculated electronic band structure of CuO in the primitive simulation cell.

Table 5.3: Calculated values of the electronic band gap and (spin only) magnetic moment per copper atom for CuO. For the DFT+ $U$  calculations, the value of 8 eV for  $U_{\text{eff}}$  determined in the previous chapter was used and the default value of 25% exact exchange was used for the HSE06 functional.

		Primitive cell	Conventional cell	Magnetic cell
Electronic band gap (eV)	GGA-PBE	Metal	Metal	Metal
	GGA-PBE+ $U$	1.82 (i)	1.49 (i)	1.90 (i)
	HSE06	2.46 (i)	2.07 (i)	2.51 (i)
Magnetic moment ( $\mu_B$ )	GGA-PBE	0.00	0.00	0.00
	GGA-PBE+ $U$	0.70	0.73	0.70
	HSE06	0.65	0.71	0.65

functional (default 25% exact exchange) reproduces the semiconducting nature of CuO with an indirect band gap (between the  $\Gamma$  point and the path between the  $M$  and  $A$  points in the reciprocal space) with value of 1.82 eV and 2.46 eV. The calculated values for all three employed simulation cells can be found in Table 5.3. Two mini-conclusions can be drawn from these results:

- The nature of the electronic band gap is predicted to be indirect, regardless of the employed modelling scheme.
- In order to properly describe the electronic and, hence, magnetic properties of CuO, a tuning of used calculation parameters is required. This proceeds either via the effective on-site interaction within DFT+ $U$  or the exact exchange parameter entering the hybrid-DFT scheme.

**Modelling magnetic CuO** As pointed out in preceding chapters, CuO has a peculiar ground state magnetic arrangement valid below 230 K. This antiferromagnetic ordering is described within an eight-formula magnetic unit cell whose lattice vectors are related by the matrix transformation outlined in Eq. (5.1) to the four-formula unit conventional face-centred monoclinic chemical unit cell of CuO. Within the magnetic

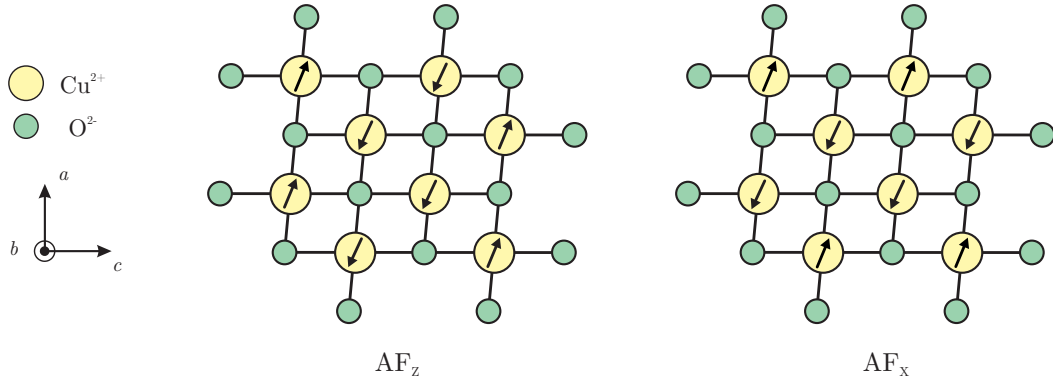


Figure 5.3: Two different spin arrangements considered within this work, depicted parallel to the  $ac$  plane. Arrows pointing upwards and downwards represent spin up and spin down electrons, respectively. The nomenclature was adapted from Rocquefelte *et al* [105] in order to allow direct comparison with literature.

cell, each oxygen atom binds to three copper atoms of parallel spin orientation and one copper atom of anti-parallel spin.

As it was already demonstrated by Rödl *et al* [99], the local magnetic moments that occur both on the Cu and O atoms, as well as the electronic band gap, can be tuned depending on the screened exchange parameter ( $\alpha$ ) in hybrid (HSE), or as a function of the on-site interaction  $U$  in PBE+ $U$  calculations. Moreover, a majority of works available in literature employ experimental lattice parameters within their simulations. This ensures consistency between calculated and experimental crystal structures. However, experimental geometries are (usually) not identical to minimum-energy geometries obtained by structural relaxations within a given functional. This issue is particularly pronounced when hybrid density functionals are employed [241], where calculation time increases dramatically (in the range of a thousand-fold) and system size is limited to a few dozen of atoms.

In order to examine the underlying effects of strain remnants within the magnetic CuO simulation cell, various pre-relaxed, atomically-relaxed, and fully-relaxed geometries were tested and their validity assessed. Two different spin arrangements were considered, one along the  $z$  axis and one along the  $x$  axis, as shown in Figure 5.3. The AF<sub>z</sub> magnetic arrangement is the most stable magnetic state, which corresponds well with observed experimental measurements [105].

First, the influence of the  $U_{\text{eff}}$  parameter within DFT+ $U$  and the exact exchange  $\alpha$  within hybrid DFT on the electronic (Kohn-Sham) band gap were assessed. Results for the two distinct magnetic arrangements are summarized in Figure 5.4. What is noticed are the different values of  $U_{\text{eff}}$  and  $\alpha$  when a fitting to the electronic band gap is undertaken. For a fit to the low temperature band gap value of 1.3 – 1.5 eV [89], a value of  $U_{\text{eff}} = 5$  eV and  $U_{\text{eff}} = 7$  eV can be read for the AF<sub>z</sub> and AF<sub>x</sub> magnetic ordering, respectively. Similarly, for hybrid DFT calculations, values of  $\alpha \approx 0.125$  and

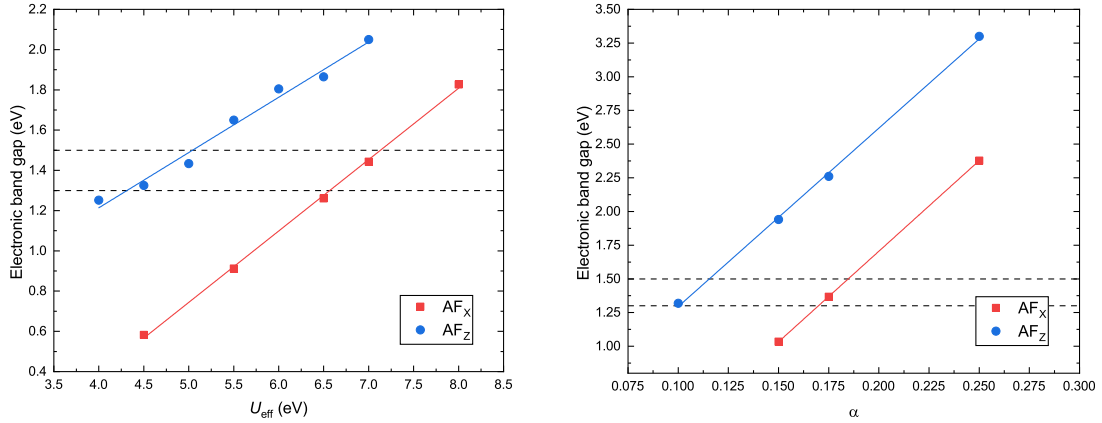


Figure 5.4: The electronic band gap dependence on the effective  $U$  parameter within DFT+ $U$  (left) and the exact exchange amount  $\alpha$  used for hybrid DFT calculations (right). The red filled squares refer to the  $\text{AF}_X$  magnetic arrangement, while the blue filled dots represent the  $\text{AF}_Z$  magnetic configuration. The linear fit is merely an eye-guide for easier data readout. The dashes black lines indicate the range of experimentally available low-temperature values.

$\alpha \approx 0.175$  used within HSE are read for  $\text{AF}_Z$  and  $\text{AF}_X$ . This explains the variety of  $U_{\text{eff}}$  and  $\alpha$  values in existing literature that were used for bulk CuO calculations. Together with the choice of an appropriate simulation cell and magnetic arrangement, the quest of defining a unique simulation setup becomes a question of the physical properties under examination.

Furthermore, so far the simulation included relaxation effects only up to the atomic position level, i.e., lattice parameters and the cell volume were kept fixed. Starting from the experimental lattice parameters of the CuO magnetic unit cell with two different magnetic arrangements, calculations allowing for lattice cell shape relaxation were performed. This was undertaken in order to circumvent the observed internal pressure left within the geometry of the system after only atomic relaxation was performed. The pressure was in certain cases as high as  $\pm 2$  GPa (20 kBar), depending on the system under study. Such values are large enough to drive lattice instabilities and subsequent structural phase transitions [242]. Thus, care must be taken in order to avoid and minimize internal lattice stress when dealing with CuO. Results of those simulations are illustrated in Figure 5.5. Based on those results and discussion outlined above, values of  $U_{\text{eff}} = 5.5$  eV for DFT+ $U$  and  $\alpha = 0.125$  for HSE were chosen for upcoming studies, as those reproduce the electronic band gap and magnetic moments values accurately, minimizing the internal pressure simultaneously. Surprisingly, allowing for the lattice parameters to change during the relaxation run of  $\text{AF}_X$ , the calculations proceed in such way that it converges to the  $\text{AF}_Z$  geometry, indirectly confirming the most stable magnetic configuration.

The results of a fully relaxed  $\text{AF}_Z$  structure are shown in Figure 5.6. The most notable changes develop along the  $b$  axis, with a 10 – 13% increase of the lattice

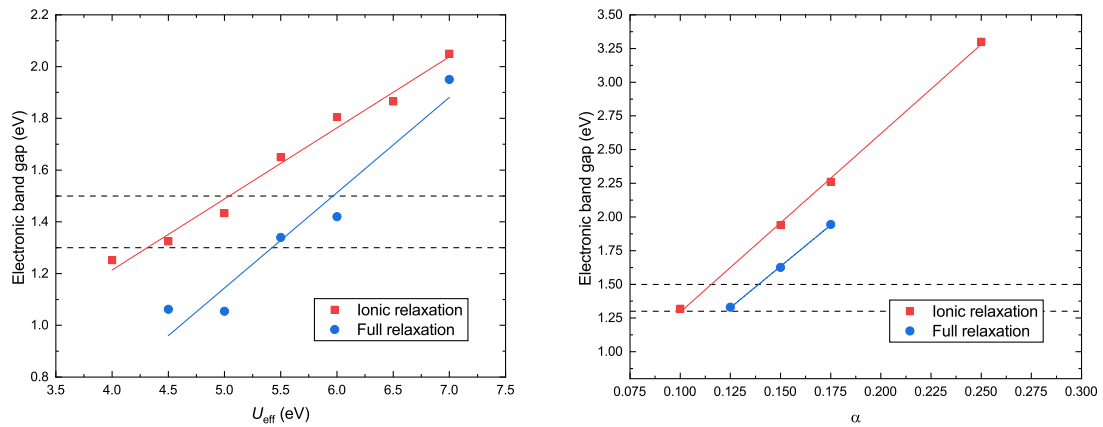


Figure 5.5: The electronic band gap dependence on the effective  $U$  parameter (left) and the exact exchange amount  $\alpha$  (right) for the AF<sub>Z</sub> configuration. The red filled squares refer to the atomically relaxed geometry, while the blue filled dots represent the fully relaxed geometry (incorporating atomic, cell, and volume relaxation). The linear fit is merely an eye-guide for easier data readout. The dashes black lines indicate the range of experimentally available low-temperature values.

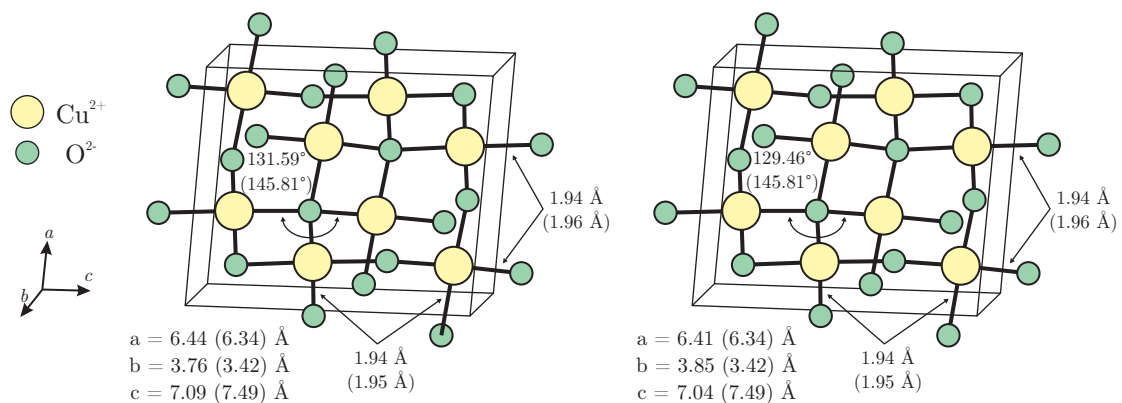


Figure 5.6: Fully relaxed (atomic+cell+volume) ground state geometry of CuO in the AF<sub>Z</sub> magnetic configuration using DFT+ $U$  (left) and HSE (right). The arrows indicate bond lengths and bond angles before (number in brackets) and after the relaxation. Also, the unit cell parameters are listed below the graphic representation. The biggest change, of around 10%, is observed for the  $b$  lattice direction.

parameter, depending on the used functional. The Cu–O bond lengths do not alter significantly (at most 0.01 Å), while the Cu–O–Cu bond angle decreases for 9 – 11%, based on the chosen functional approximation. These effects are driven via the release of internal pressure which is present in the system once the experimentally observed lattice parameters are coupled with an XC functional approximation. Atomic relaxations proceed down a potential energy curve of the un-relaxed system, not taking the additional geometric relaxation effects into account. These effects depend on the system’s symmetry and composition, making general conclusions quite vague. Performing individual tests and assessing the origin of eventual lattice or bond strain proves to be a crucial step.

### 5.3.1 Intrinsic defects of CuO

Despite a substantial number of publications studying the ground state properties of CuO, the intrinsic defects still remain largely unexplored. Nolan et al [57] and Wu et al [103] studied the native defects within CuO using LSDA+*U*. However, defects were studied in the monoclinic conventional cell and simple antiferromagnetic configuration, not necessarily corresponding to the experimentally observed ground state.

To explore the native defects in CuO, an antiferromagnetic  $2 \times 3 \times 2$  supercell was created. This ensures a minimal interaction between introduced defects, located at least 10 Å apart in each crystallographic direction. A single defect corresponds to 1% defect concentration within the cell, which is well accessible in the experimental range. Furthermore, two types of relaxations were analysed, the first taking into account atomic relaxation only and the second employing full volume and atomic relaxation. In addition, the differences between DFT+*U* and HSE values of defect energies and impurity band positions within the electronic structure are examined.

Following the formalism outlined in equations (4.1)–(4.2), the boundaries for chemical potentials were calculated and shown in Figure 5.7. To analyse the effect of experimental growth conditions on undoped CuO samples, two chemical potential limits were chosen: one with O-rich/Cu-poor and other with Cu-rich/O-poor conditions. The selected values read:

- O-rich/Cu-poor (*p*-type):  $\Delta\mu(\text{Cu}) = -1.594$ ,  $\Delta\mu(\text{O}) = 0.000$ .
- Cu-rich/O-poor (*n*-type):  $\Delta\mu(\text{Cu}) = -0.157$ ,  $\Delta\mu(\text{O}) = -1.437$ .

Simple native defects were introduced into the CuO magnetic supercell, including simple vacancies (labelled  $V_{\text{Cu}}$  and  $V_{\text{O}}$ ), antisites ( $\text{Cu}_{\text{O}}$  and  $\text{O}_{\text{Cu}}$ ), and interstitials in various positions within the cell ( $\text{Cu}_i$  and  $\text{O}_i$ ).

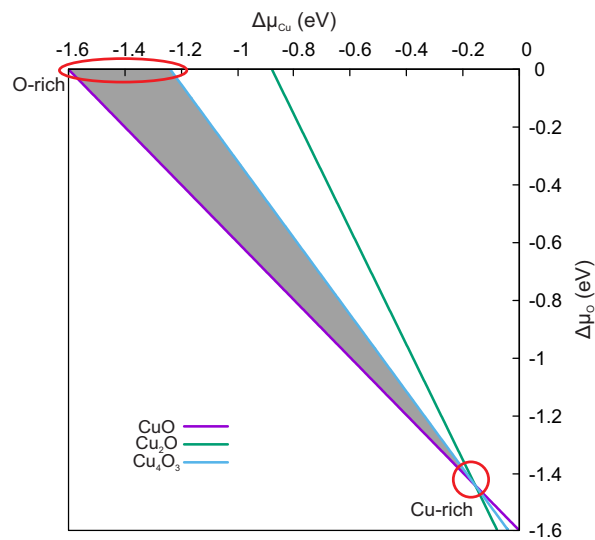


Figure 5.7: Phase stability of CuO in the range of accessible chemical potentials, emphasized within the grey-shaded area. The regions highlighted with red circles/ellipse indicate the representative chemical potential limits, i.e., O-rich and Cu-rich conditions corresponding to  $p$ -type and  $n$ -type CuO, respectively. Values were calculated from experimental formation enthalpies in order to assure transferability of results.

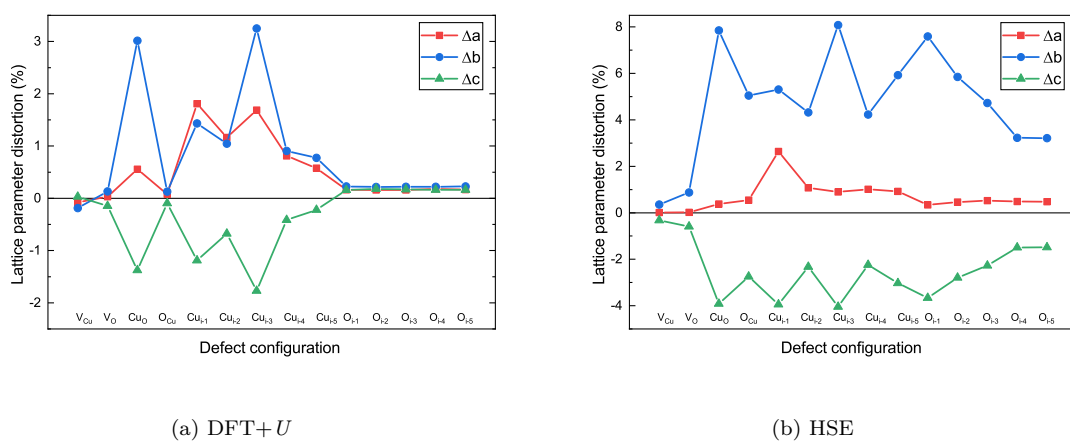
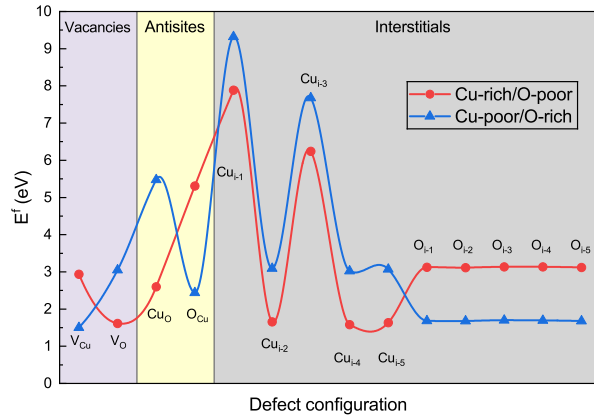
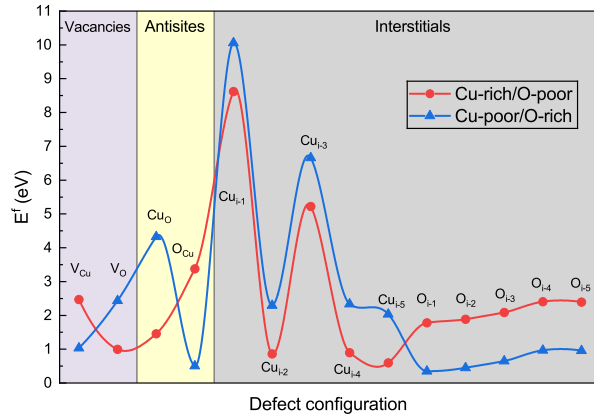


Figure 5.8: Lattice distortions of CuO with intrinsic defects. Positive values indicate lattice expansion while negative values illustrate lattice shrinkage.

(a) DFT+*U*

(b) HSE

Figure 5.9: Calculated (simple native) defect formation energies of CuO under different chemical potential limits, using two types of approximation for the XC functional.

The influence of the individual defect on the overall lattice parameters of the simulation cell is depicted in Figure 5.8. Simple vacancies show the smallest influence on the overall lattice parameters for both DFT+*U* and HSE, causing a distortion of less than 0.2%. Further defects exhibit different distortions, depending on whether DFT+*U* or HSE is used. For DFT+*U*, the largest expansion in the *b*, and lattice contraction in the *c* direction is observed for Cu<sub>0</sub> antisite and interstitial Cu defects, while a small amount of 0.5% increase is found for interstitial O defects. For hybrid-DFT, a lattice expansion in the *b* direction is observed for all antisite and interstitial defects, with a simultaneous expansion in the *c* direction. The *a* lattice vector has undergone the smallest change for all defects, with a maximum of  $\approx 2\%$  lattice expansion.

The calculated defect formation energies, determining the overall stability of the system with induced defects present, are summarized in Figure 5.9. It is observed that the formation energy of defects varies depending on growth environments, while

it retains overall similar trends for DFT+*U* and HSE. In the Cu-rich/O-poor environment, the most favourable defects are  $V_O$  and  $Cu_i$ , with the hindmost depending on the position of the defect within the cell. On the other hand, under O-rich/Cu-poor conditions, the most stable defects are  $V_{Cu}$ ,  $O_{Cu}$ , and  $O_i$ , which, unlike their Cu counterparts, do not depend on the positioning within the cell. This reproduces accurately the experimentally observed *n*-type conductivity assigned to O vacancies and interstitial Cu atoms [93, 101] as well as *p*-type conductivity assigned to Cu vacancies [102, 243]. This confirms that, depending on the growth conditions, CuO can be created intrinsically both *n*-type (Cu-rich/O-poor environment) or *p*-type in nature (O-rich/Cu-poor environment).

To study the influence of native point defects on the pristine band structure of CuO, electronic densities of state have been calculated and illustrated in Figures 5.10, 5.16, and 5.20.

**Vacancies** Cu is surrounded by four almost equidistant O atoms, organized in a square planar arrangement. Removing one Cu atom leaves four dangling bonds from the neighbouring O atoms, creating four distinct acceptor states located about 0.5 eV above the top of the VB. The formation of a neutral Cu defect causes neighbouring O atoms to relax away from the site in order to minimize the overlap with the surrounding O atoms in the lattice. The hole states delocalize along the *c* axis over the nearest neighbouring O atoms and next-nearest neighbouring Cu and O atoms, with little effect on the atoms along the *a* and *b* axis, as shown in Figure 5.11. Surprisingly, despite the delocalized nature of the  $V_{Cu}$  hole states and the negligible strain introduced in the lattice, defect levels lie close to the middle of the (otherwise empty) band gap region, which classifies them as deep levels.

O is tetrahedrally coordinated to four Cu atoms, with two equidistant pairs of bonds differing by 0.01 Å. In CuO, O exists in the  $-2$  oxidation state in the pristine material. When a  $V_O$  is created, the electrons from the surrounding Cu atoms are left with highly energetic Cu bonding states to move into. The removal of an O atom creates four different defect states – two donor states located at 0.20 eV (0.35 eV) and 0.80 eV (0.40 eV) above the VB maximum and two acceptor states at 0.30 eV (0.20 eV) and 0.40 eV (0.25 eV) below the CB minimum, calculated for DFT+*U* (HSE). In other words, a neutral  $V_O$  in CuO is an amphoteric defect. Both defect states are delocalized in real space, with the donor density spreading out asymmetrically most along the *c* axis and the acceptor states in the opposite direction. The defect densities are depicted in Figure 5.12. Subsequently, due to the large delocalization of states, the lattice undergoes minimal relaxation towards the empty O site, with the deviation more pronounced for the HSE functional, as already noted in Figure 5.8.

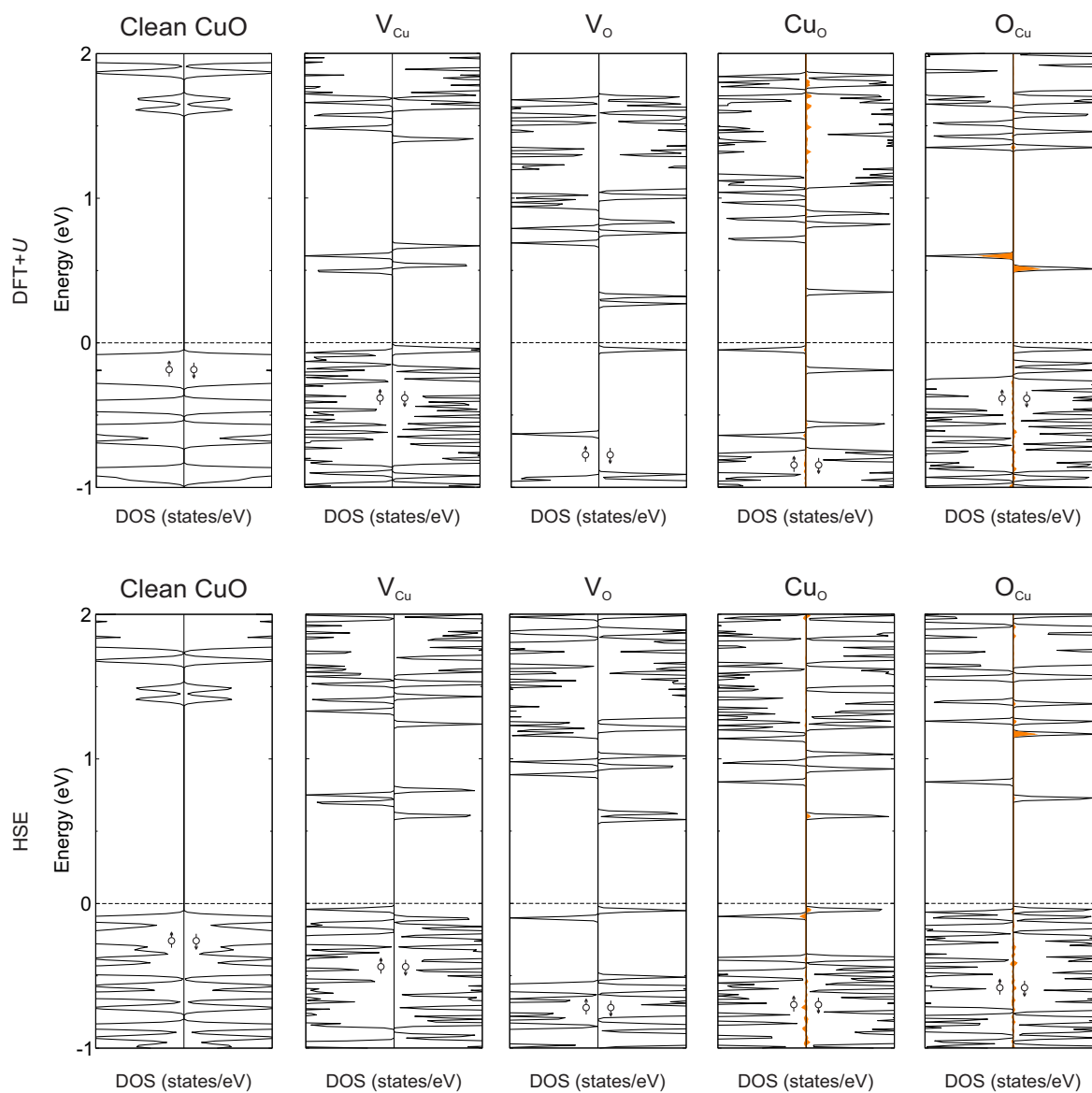


Figure 5.10: Total (black line) and defect-projected (orange line) electronic densities of state (DOS) of clean and defective CuO. A comparison between DFT+ $U$  and HSE calculated values is illustrated in the top and bottom row. The dashed line indicates the highest occupied band and up/down arrows represent different spin channels.

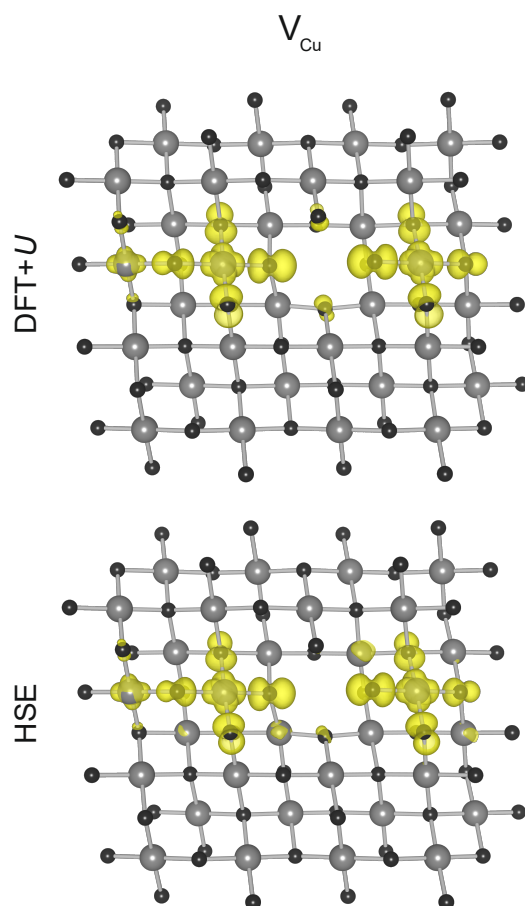


Figure 5.11: Partial charge densities of neutral  $V_{\text{Cu}}$  defect within CuO, along the  $b$  axis. Selected bands correspond to the four acceptor states presented in Figure 5.10. Large grey and small black spheres represent copper and oxygen atoms. A comparison between DFT+ $U$  and HSE values is shown on the top and bottom illustration, respectively. The yellow isosurface is shown at  $0.005 \text{ e}/\text{\AA}^3$ .

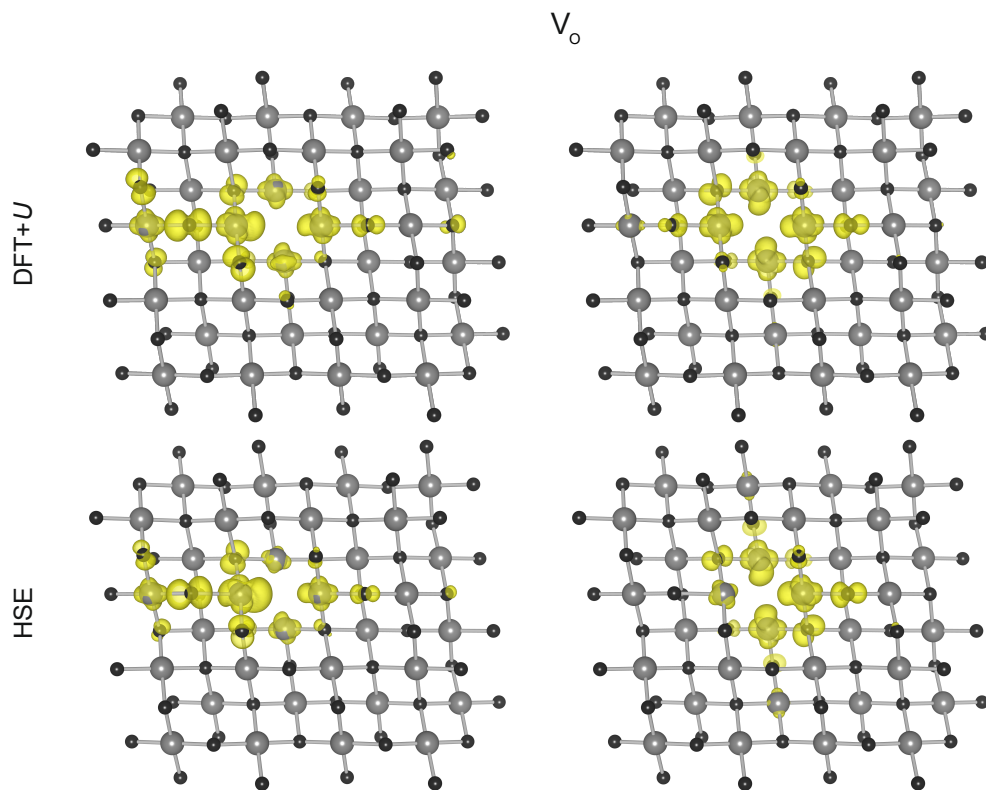


Figure 5.12: Partial charge densities of neutral  $V_O$  defect within CuO, with the occupied states shown in the right and empty states in the left column, along the  $b$  axis. Selected states correspond to the two donor and two acceptor states presented in Figure 5.10. Large grey spheres and small black spheres represent copper and oxygen atoms. A comparison between DFT+ $U$  and HSE values is shown on the top and bottom illustration, respectively. The yellow isosurface is shown at  $0.003 e/\text{\AA}^3$ .

**Antisites** Antisite defects show the largest defect formation energy differences when considered under different growth environments, changing by  $\approx 3$  eV when going from Cu-rich/O-poor to Cu-poor/O-rich conditions. When Cu is incorporated onto the O lattice site, a local relaxation is observed arising from the artificially induced Cu–Cu bonds. The  $\text{Cu}_\text{O}$  displaces towards the nearest neighbouring Cu atom, causing it to relax further away due to Coulomb repulsion between the electrons. This is counterbalanced by the attractive force of the nearest O atoms, forming the structure shown in Figure 5.13, for both DFT+*U* and HSE. It is also noted, from the Bader charge as well as bond distance analysis, that no interaction is present between the  $\text{Cu}_\text{O}$  and neighbouring O atoms (no charge transfer and bond distance larger than 2.33 Å). However, there is significant charge accumulation on the neighbouring Cu atoms, forming weakly bound donor states depicted in Figure 5.10. The donor states are spread across the band gap, with the HSE calculations delocalizing them less compared to DFT+*U* values. The acceptor states situated at 0.35 eV below the CB minimum are localized on the nearest neighbouring copper atoms, which alter depending on the functional approximation employed.

When O is incorporated on the Cu site, a minimal lattice deformation is observed. This is due to the relaxation of three O atoms away from the defect site, while the  $\text{O}_\text{Cu}$  defect itself goes towards the fourth O atom ending up at a distance of 1.41 Å or 1.39 Å depending on the employed functional (DFT+*U* and HSE, respectively).  $\text{O}_\text{Cu}$  alters the initial band structure of pure CuO as shown on the right hand side of Figure 5.10, directly creating acceptor states in the middle of the gap, with additional donor states originating from the altered CuO framework itself. Calculated Bader charges for the defect structure yield values of  $-0.07 e^-$  ( $-0.20 e^-$ ) for  $\text{O}_\text{Cu}$ ,  $-0.51 e^-$  ( $-0.57 e^-$ ) for the nearest "binding" O, (an average value of)  $-0.74 e^-$  ( $-0.94 e^-$ ) for the three nearest neighbouring O atoms, and  $-0.93 e^-$  ( $-1.05 e^-$ ) for an O atom far away from the defect site, using DFT+*U* (HSE). These values indicate very little charge transfer between the  $\text{O}_\text{Cu}$  impurity and its nearest O atom, followed by a weak bond formation between them. The remaining three O atoms show lack of charge according to the Bader analysis, which can be attributed to the missing Cu atom and delocalization of created holes.

**Interstitials** For both Cu and O interstitials, a systematic search for appropriate sites was employed based on coordination patterns that resemble basic motifs (e.g., tetrahedral, octahedral, bcc-like environments, etc.), as implemented in the PyCDT code [244]. Five suitable positions were identified, labelled i-1 ... i-5, and depicted in Figure 5.15.

The incorporation of Cu interstitial atoms in position i-1 creates a structural de-

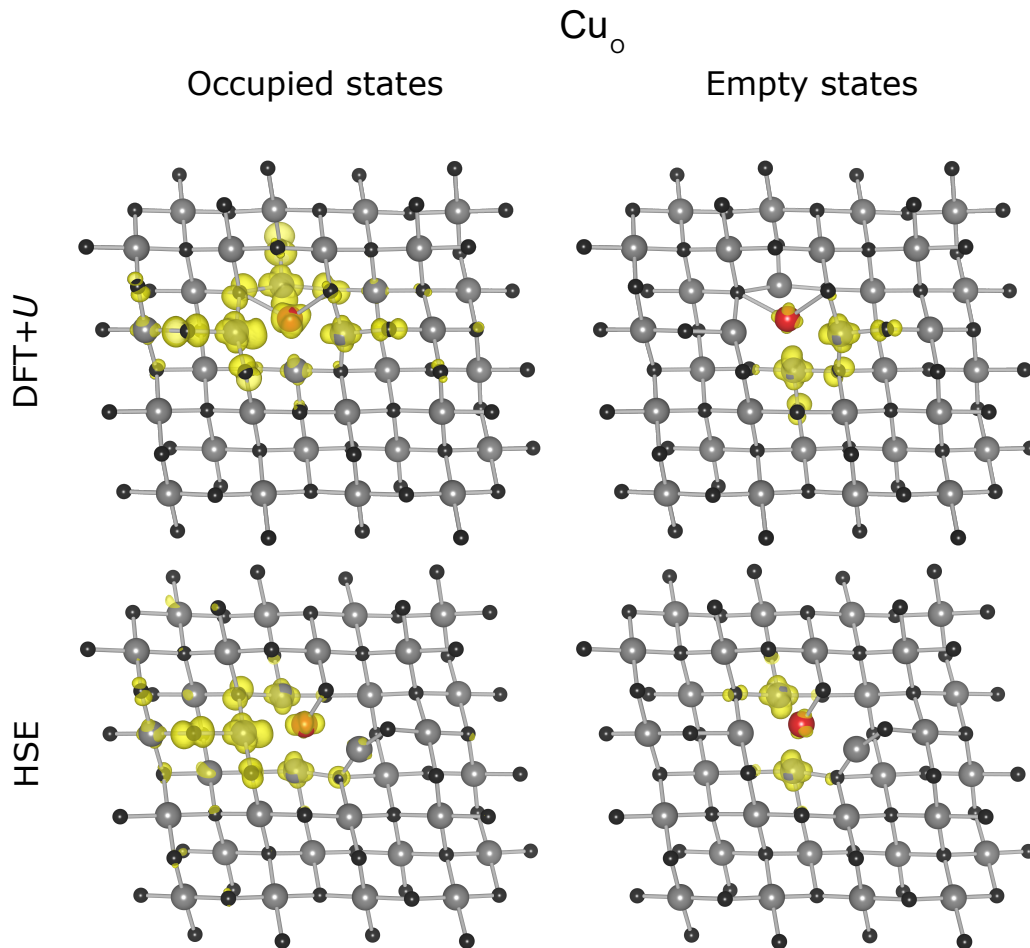


Figure 5.13: Partial charge densities of neutral  $\text{Cu}_\circ$  defect within CuO, with the occupied states shown in the right and empty states in the left column, along the *b* axis. Selected states correspond to the four donor and one acceptor states presented in Figure 5.10. Large grey spheres and small black spheres represent copper and oxygen atoms, while the red sphere distinguishes the  $\text{Cu}_\circ$ . A comparison between DFT+*U* and HSE values is shown on the top and bottom illustration, respectively. The yellow isosurface is shown at  $0.005 e/\text{\AA}^3$ .

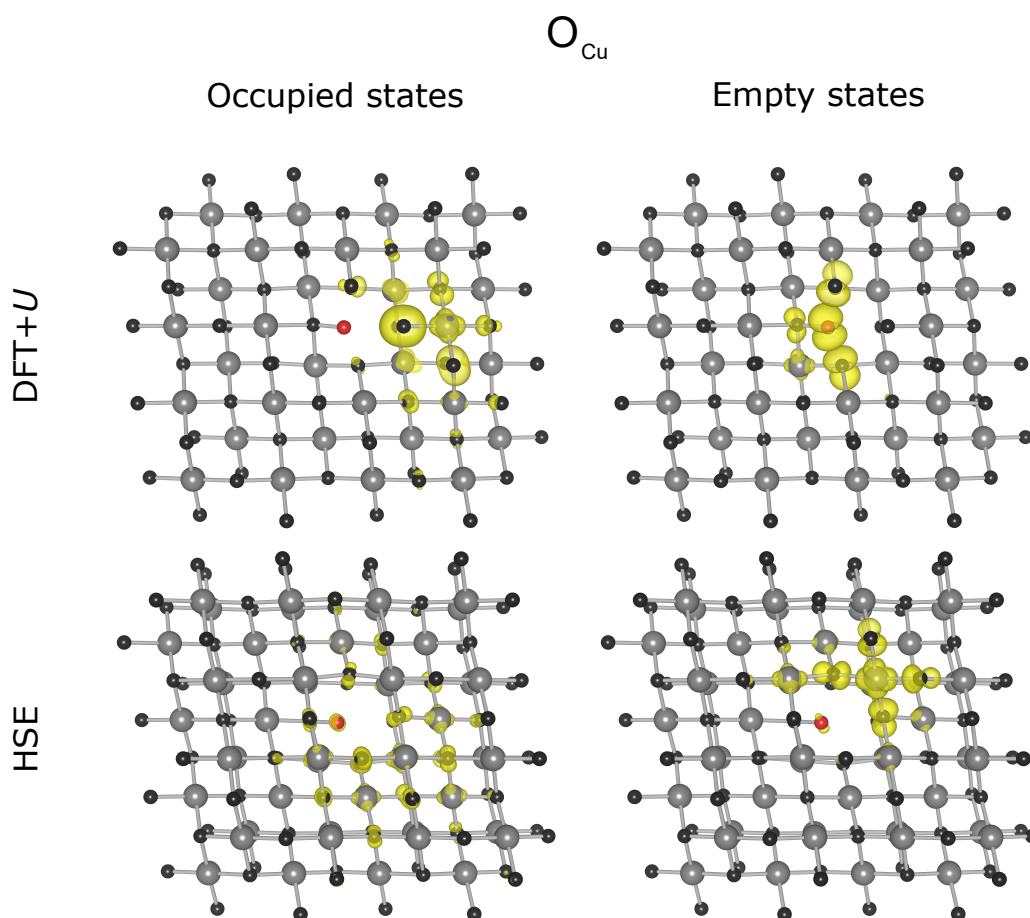


Figure 5.14: Partial charge densities of neutral  $O_{Cu}$  defect within CuO, with the occupied states shown in the right and empty states in the left column, along the  $b$  axis. Selected states correspond to the donor and acceptor states presented in Figure 5.10. Large grey spheres and small black spheres represent copper and oxygen atoms, while the red sphere distinguishes the  $O_{Cu}$ . A comparison between DFT+ $U$  and HSE values is shown on the top and bottom illustration, respectively. The yellow isosurface is shown at  $0.005 e/\text{\AA}^3$ .

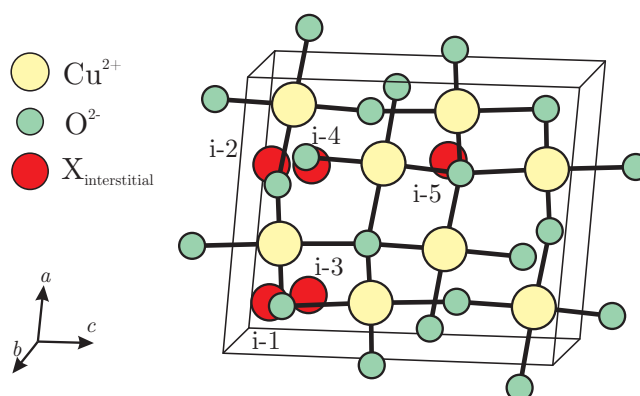


Figure 5.15: Schematic representation of the five identified suitable positions for interstitial atoms in CuO. Yellow, green, and red spheres represent the positions of copper, oxygen, and interstitial atoms in the magnetic unit cell.

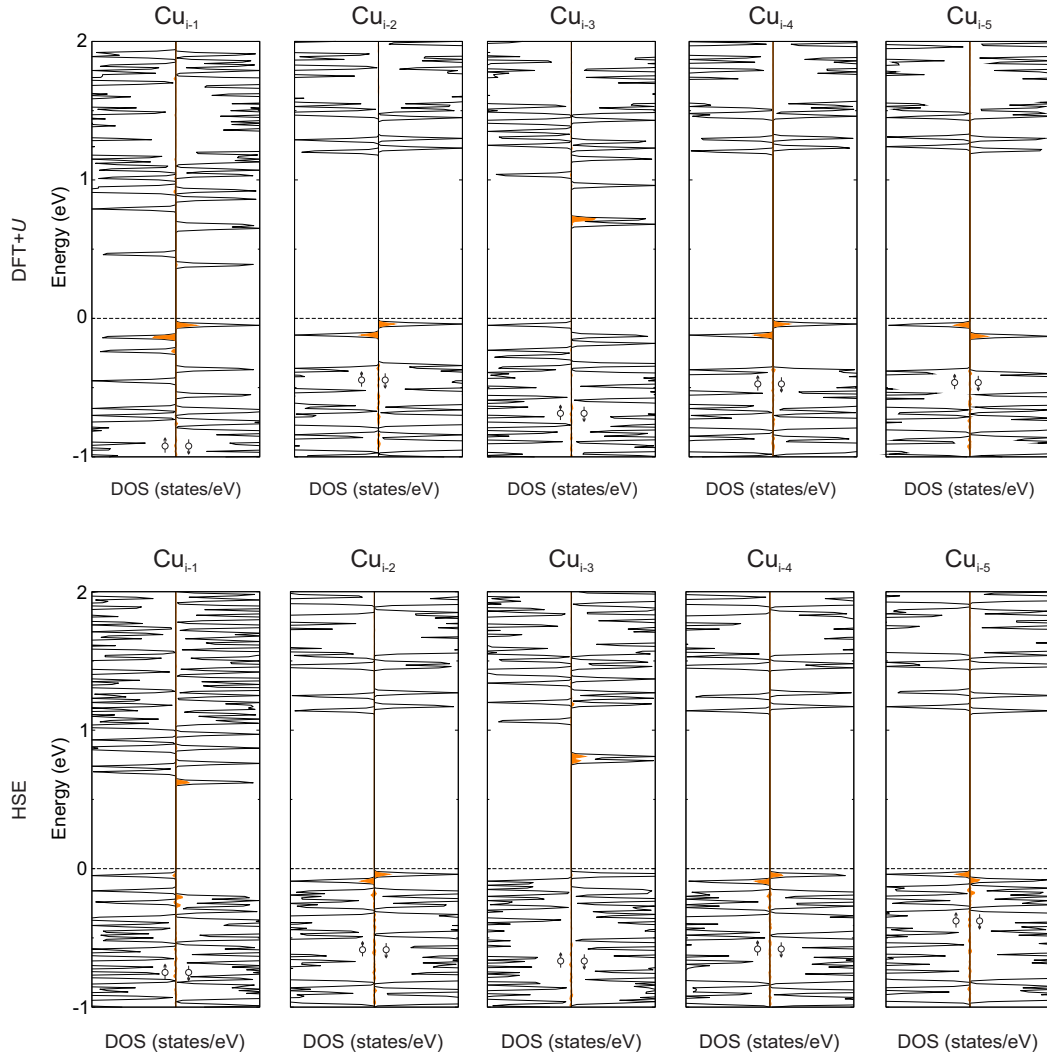


Figure 5.16: Total (black line) and defect-projected (orange line) electronic densities of state (DOS) of clean and defective CuO. A comparison between DFT+ $U$  and HSE calculated values is illustrated in the top and bottom row. The dashed line indicates the highest occupied band and up/down arrows represent different spin channels.

formation driven by substantial atomic rearrangement. The  $\text{Cu}_{i-1}$  atom moves into the nearest Cu site, displacing the already present Cu atom further along the  $-c$  axis into the subsequent chain of Cu atoms. The initial O atom nearest to  $\text{Cu}_{i-1}$  relaxes into the consecutive chain of O atoms along the  $c$  axis (opposite the displaced Cu atom), effectively creating an O vacancy. The valence state of the  $\text{Cu}_{i-1}$  atom is +1 (Bader charge of  $0.54 e^-$  ( $0.76 e^-$ )) compared to the value of  $1.00 e^-$  ( $1.06 e^-$ ) of a non-displaced Cu atom far away from the defect site, for DFT+ $U$  (HSE) calculations, confirming the lack of O atoms in the near proximity along the  $c$  axis. Consequently, the original  $\text{AF}_Z$  magnetic arrangement is distorted as well. A qualitatively similar trend in the structural properties is noted between DFT+ $U$  and HSE values, while the defect positions differ quite substantially. What are described as  $\text{Cu}_{i-1}$  donor states within DFT+ $U$ , turn into acceptor states below the CB minimum within HSE.

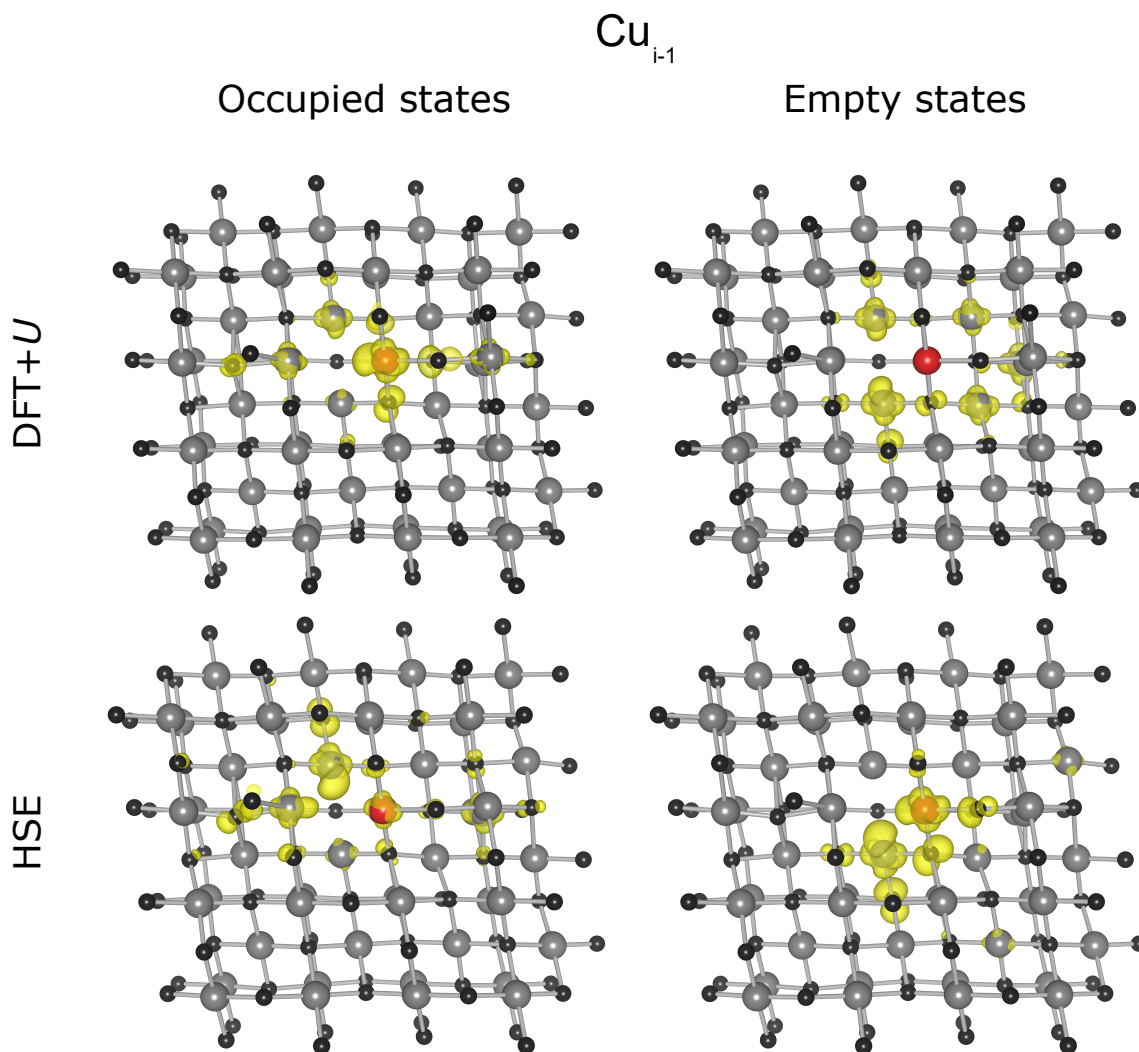


Figure 5.17: Partial charge densities of neutral  $\text{Cu}_{i-1}$  defect within CuO, with the occupied states shown in the right and empty states in the left column, along the  $b$  axis. Selected states correspond to the donor and acceptor states presented in Figure 5.16. Large grey spheres and small black spheres represent copper and oxygen atoms, while the red sphere distinguishes the  $\text{Cu}_{i-1}$ . A comparison between DFT+ $U$  and HSE values is shown on the top and bottom illustration, respectively. The yellow isosurface is shown at  $0.005 \text{ e}/\text{\AA}^3$ .

Accordingly, the partial charges noted in Figure 5.17 show localization of electrons on the  $\text{Cu}_{i-1}$  atom in DFT+ $U$  and localization of holes within HSE.

The  $\text{Cu}_{i-2}$  defect causes lattice relaxation similar to  $\text{Cu}_{i-1}$ , with a much lesser reorganization of the atomic structure. The nearest neighbouring Cu atom relaxes away from its site, which causes two bonds with the nearest O atoms to break and change its oxidation state to +1. In order to retain their 4-fold coordination, the  $\text{Cu}_{i-2}$  atom moves towards the displaced Cu atom due to increased Coulomb attraction and forms two new bonds (see Figure 5.18). This way all of the O atoms retain their +2 valence state, while the  $\text{Cu}_{i-2}$  and displaced Cu atom end up in a +1 state, losing their magnetic properties. Due to the small influence on the overall atomic parameters,

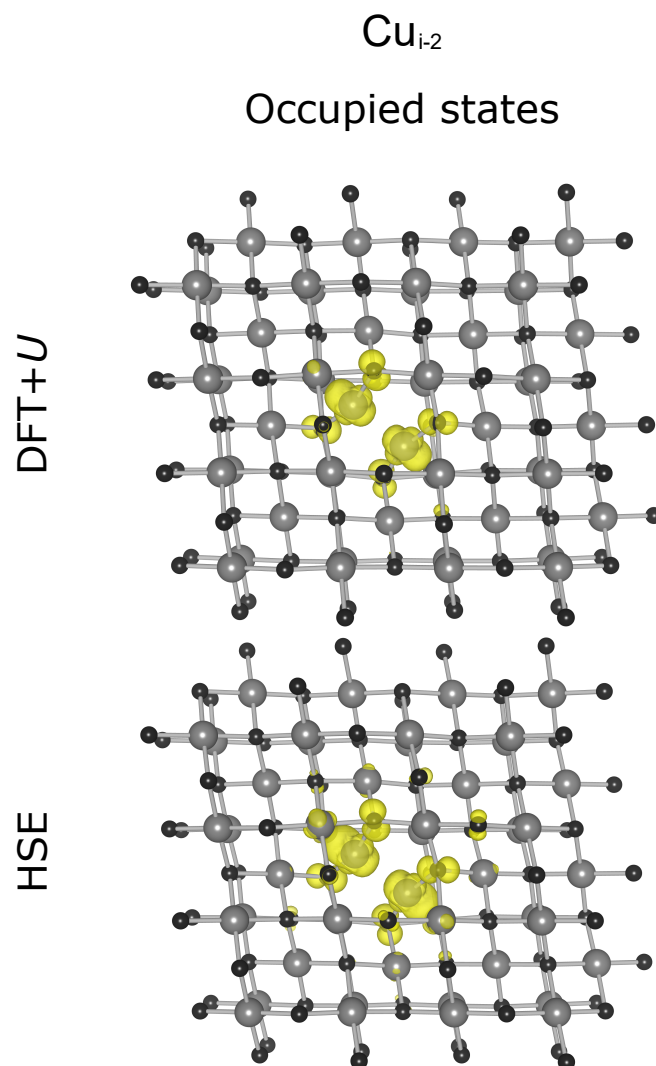


Figure 5.18: Partial charge densities of donor state for the neutral  $\text{Cu}_{i-2}$  defect within CuO, along the  $b$  axis. Selected states correspond to the donor and acceptor states presented in Figure 5.16. Large grey spheres and small black spheres represent copper and oxygen atoms, while the red sphere distinguishes the  $\text{Cu}_{i-1}$ . A comparison between DFT+ $U$  and HSE values is shown on the top and bottom illustration, respectively. The yellow isosurface is shown at  $0.003 e/\text{\AA}^3$ .

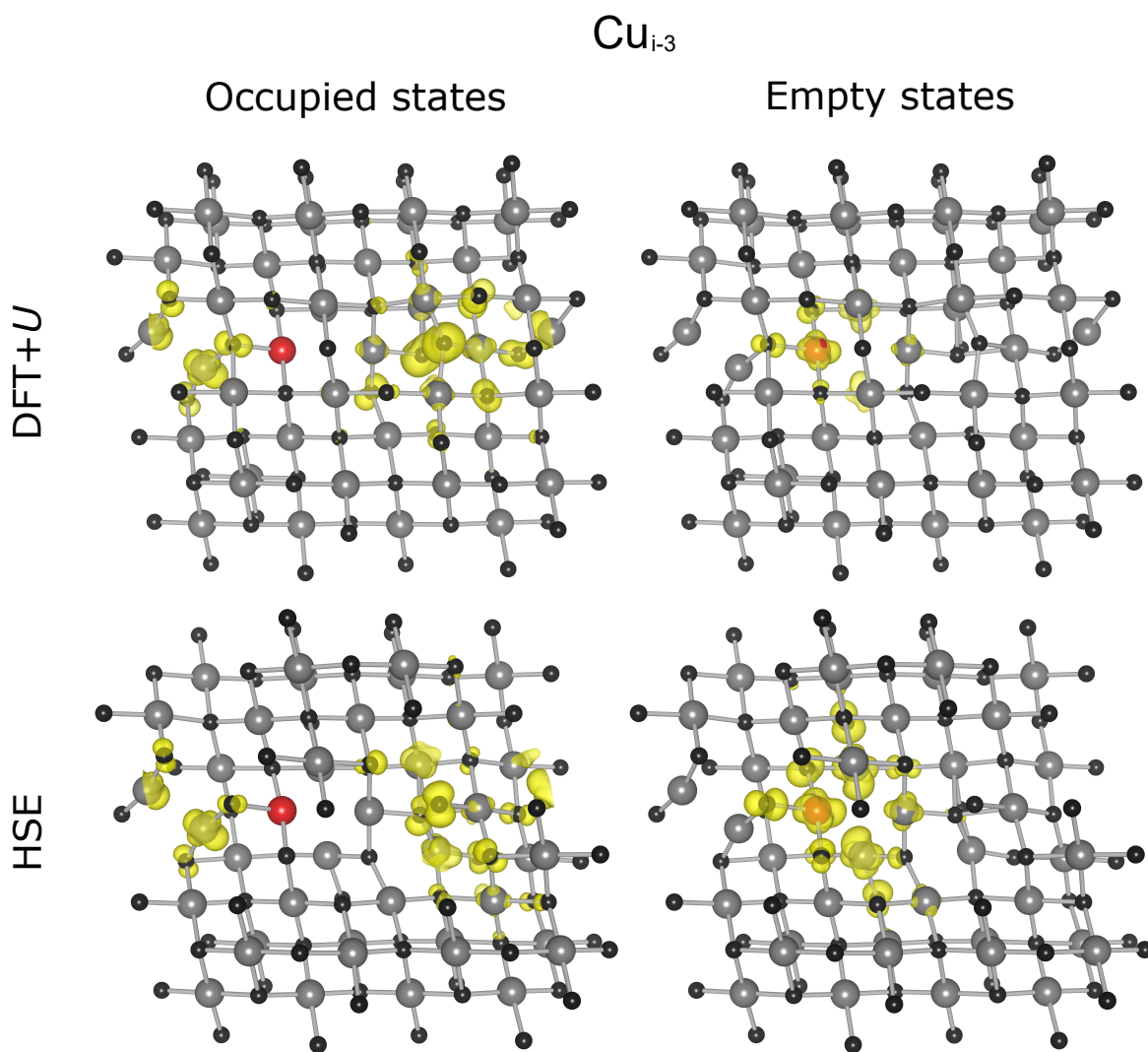


Figure 5.19: Partial charge densities of neutral  $\text{Cu}_{i-3}$  defect within CuO, with the occupied states shown in the right and empty states in the left column, along the  $b$  axis. Selected states correspond to the donor and acceptor states presented in Figure 5.16. Large grey spheres and small black spheres represent copper and oxygen atoms, while the red sphere distinguishes the  $\text{Cu}_{i-1}$ . A comparison between DFT+ $U$  and HSE values is shown on the top and bottom illustration, respectively. The yellow isosurface is shown at  $0.003 e/\text{\AA}^3$ .

the initial antiferromagnetism is retained, with an isolated "island" of non-magnetic Cu atoms. In terms of electronic properties, neutral  $\text{Cu}_{i-2}$  creates a shallow doubly-occupied donor state located  $\approx 0.30$  eV ( $\approx 0.15$  eV) above the CB maximum, modelled accurately and complementary with both DFT+ $U$  and HSE. No acceptor states were observed.

Interstitial Cu in position  $i-3$  behaves somehow similar to the defect in position  $i-1$ . Namely, a strong structural relaxation occurs where the  $\text{Cu}_{i-3}$  atom displaces the nearest Cu atom, occupying its site and causing a migration of the displaced atom into the next channel of Cu atoms. However, the displaced atom now displaces one additional Cu atom forming a structure analogous to the one observed in the  $\text{Cu}_{i-2}$  defect arrangement. Also, the O atom closest to  $\text{Cu}_{i-3}$  is relaxed further away from the defect leaving a vacancy behind and effectively forming an interstitial O defect in the nearest chain of O atoms. Because this structure is more stable compared to the one on  $\text{Cu}_{i-1}$ , the created donor states at the top of the VB are more shallow than the analogues and the magnetic structure retains most of its initial arrangement. The localization of created acceptor states on the defect site, found 0.24 eV (0.45 eV) below the CB minimum, is depicted in Figure 5.19. In this case, both DFT+ $U$  and HSE give qualitatively agreeing results regarding the positioning of the defect bands, with a double acceptor level located around 0.20 eV below the CB maximum, see Figure 5.16.

$\text{Cu}_{i-4}$  and  $\text{Cu}_{i-5}$  defect calculations yield structural, energetic, and electronic results that are identical to those of the  $\text{Cu}_{i-2}$  configuration, confirming their equivalence as defects within CuO. As such, further discussion about  $\text{Cu}_{i-4}$  and  $\text{Cu}_{i-5}$  is omitted.

When O is introduced interstitially into the CuO matrix, all five positions are of equal probability to be formed, according to the calculated defect formation energies, Figure 5.9. Depending on the growth conditions, formation energies can go low as  $\approx 1.70$  eV ( $\approx 0.65$  eV) for *p*-type CuO or up to  $\approx 3.10$  eV ( $\approx 2.00$  eV) for *n*-type CuO, for DFT+ $U$  (HSE).

Structurally, all five modelled  $\text{O}_i$  defects relax into a similar geometry, with the differences observed in the lattice parameter arising mostly from the different structural optimization and orbital treatment within DFT+ $U$  and HSE.  $\text{O}_i$  causes a slight displacement of the surrounding Cu atoms, as well as the nearest neighbouring O atom. The  $\text{O}_i$  and the displaced O atom both reveal a loss of electronic charge compared to an O atom located far away from the defect site, with values of  $-0.21 e^-$  ( $-0.59 e^-$ ),  $-0.34 e^-$  ( $-0.61 e^-$ ) compared to  $-0.92 e^-$  ( $-1.05 e^-$ ) for  $\text{O}_i$ , displaced O, and pristine O from DFT+ $U$  (HSE) calculations. Depending on the chosen functional approximation, the level of charge localization on the  $\text{O}_i$  differs, yet the overall trends remain intact, as noted from the calculated densities of state presented in Figure 5.20

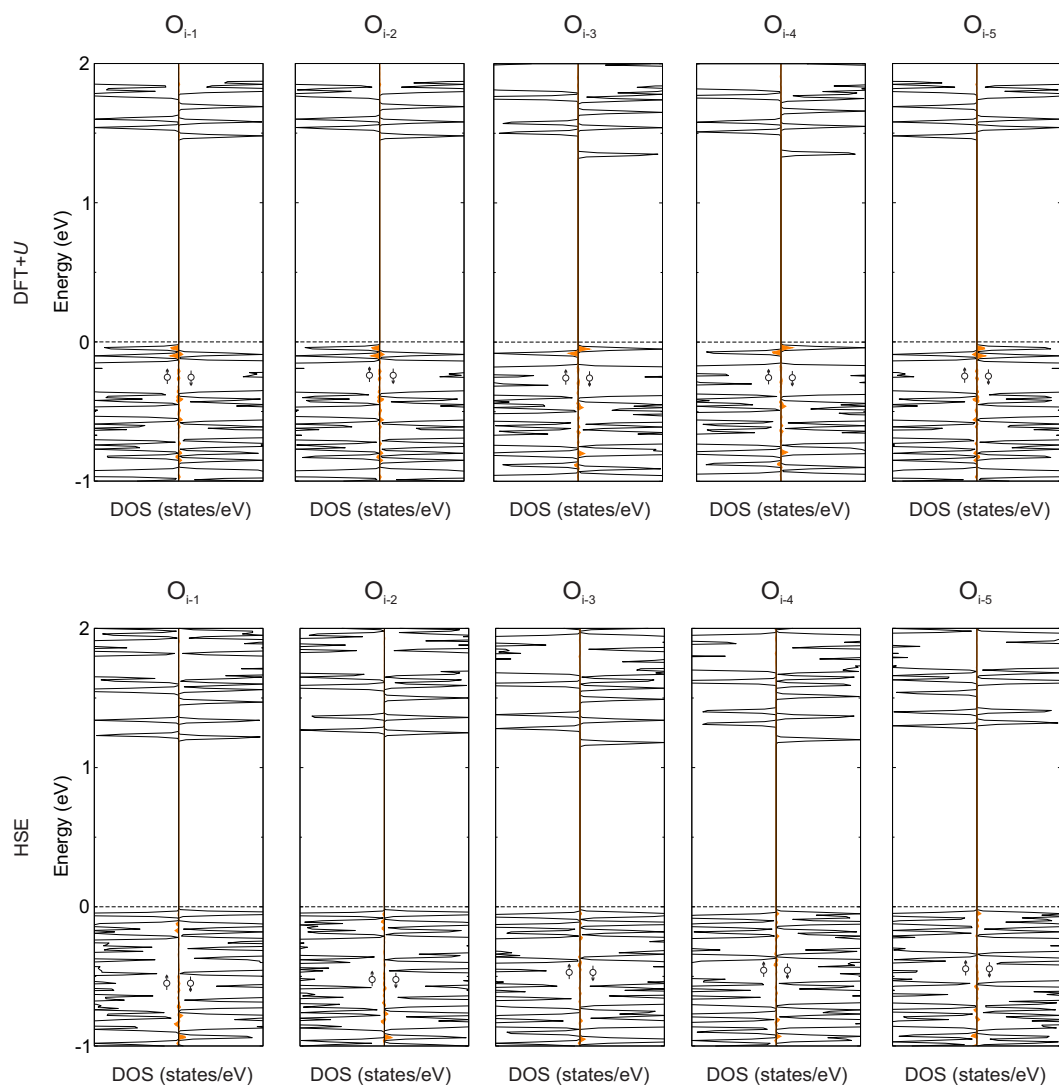


Figure 5.20: Total (black line) and defect-projected (orange line) electronic densities of state (DOS) of clean and defective CuO. A comparison between DFT+ $U$  and HSE calculated values is illustrated in the top and bottom row. The dashed line indicates the highest occupied band and up/down arrows represent different spin channels.

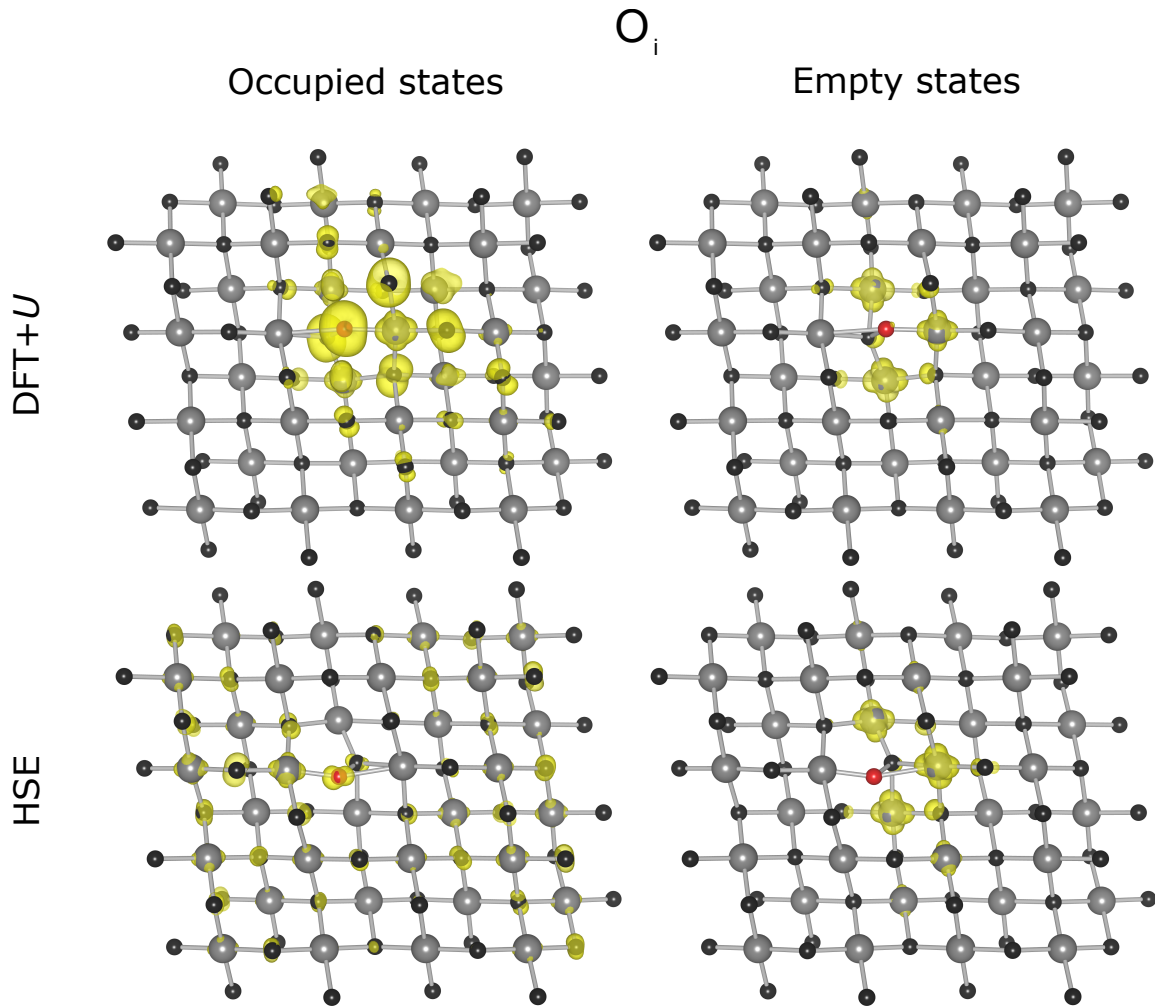


Figure 5.21: Partial charge densities of neutral  $O_{i-1}$  defect within CuO, with the occupied states shown in the right and empty states in the left column, along the  $b$  axis. Selected states correspond to the donor and acceptor states presented in Figure 5.20. Large grey spheres and small black spheres represent copper and oxygen atoms, while the red sphere distinguishes the  $Cu_{i-1}$ . A comparison between DFT+ $U$  and HSE values is shown on the top and bottom illustration, respectively. The yellow isosurface is shown at  $0.003 e/\text{\AA}^3$ .

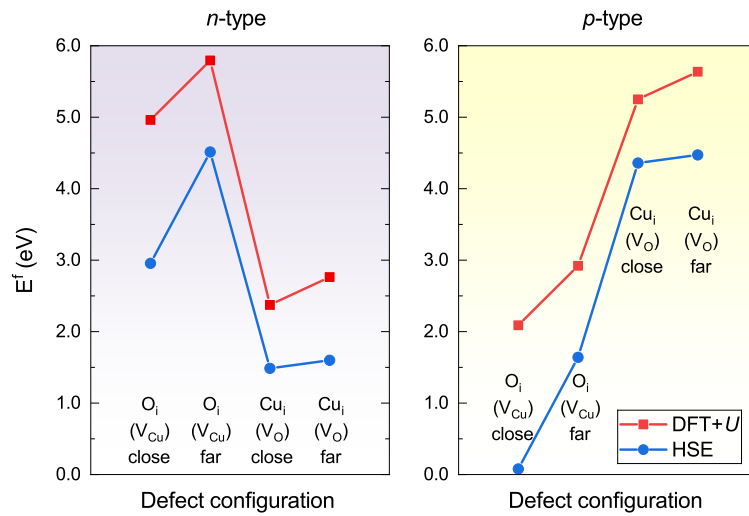


Figure 5.22: Defect formation energies for pairs of defects within CuO, under different growth conditions. The used notation specifies a newly induced defect into a cell where the one enclosed in brackets is already present. The pairs were chosen according to the lowest formation energies of individual defects illustrated earlier. A trend of small cluster can be observed both under Cu-rich ( $n$ -type) and O-rich ( $p$ -type) conditions.

and partial charges in Figure 5.21.

### 5.3.2 The formation of defect pairs

Since a clear occurrence trend of distinct defects is observed,  $V_{Cu}$  or  $O_i$  under O-rich and  $V_O$  or  $Cu_i$  under Cu-rich conditions, the question whether these defects would appear simultaneously arises naturally. In order to verify this suggestion, defect pairs were introduced into the simulation cell. Pairs were chosen according to the lowest formation energies for their individual appearance under specific growth conditions. The possibility of clustering effects was analysed in addition by introducing defects in close proximity of each other and as far as possible across the simulation cell.

The calculated formation energies for pairs of defects in CuO is shown in Figure 5.22. From these results, a clear trend of defect clustering over their dispersed counterpart is noticed, regardless of the defect nature itself or employed functional approximation. Furthermore, particular defect formation in close proximity demonstrates a lowering of the formation energy compared to the sum of individual energies. For example, under Cu-rich conditions, to create a Cu interstitial next to an already present O vacancy one needs to invest 2.38 eV (1.49 eV) worth of energy, which is lower compared to the sum of individual defect formation energies  $E^f(Cu_i) + E^f(V_O) = 1.58$  (0.99) eV + 1.61 (0.89) eV = 3.19 (1.88) eV, calculated using DFT+ $U$  (HSE).

First, the case where defects are maximally dispersed through the cell is analysed. The two defects were placed at a minimum distance of 8.32 Å in the case of  $O_i(V_{Cu})$

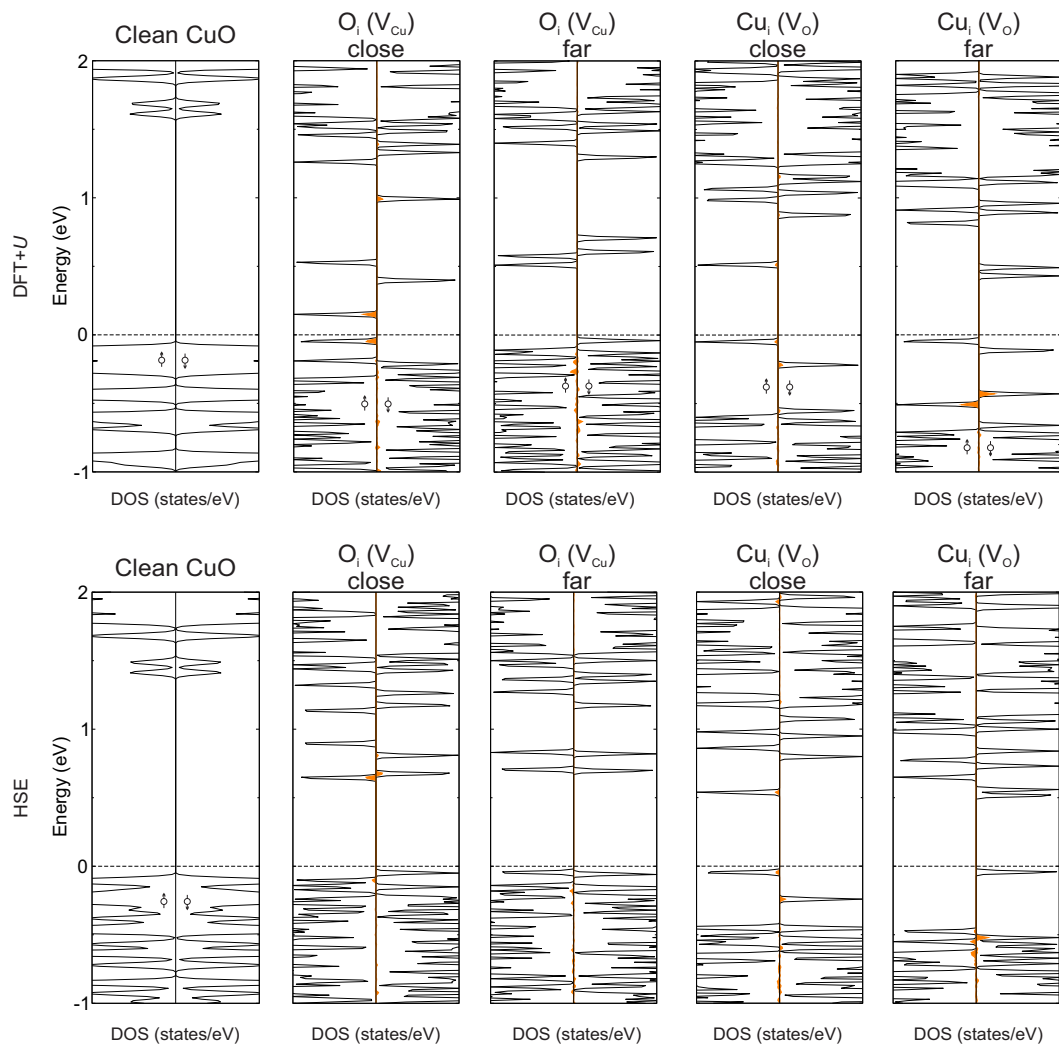


Figure 5.23: Calculated total (black line) and defect-projected (orange line) electronic densities of state (DOS) of clean and pairwise defective CuO. A comparison between DFT+ $U$  and HSE calculated values is illustrated in the top and bottom row. The dashed line indicates the highest occupied band and up/down arrows represent different spin channels.

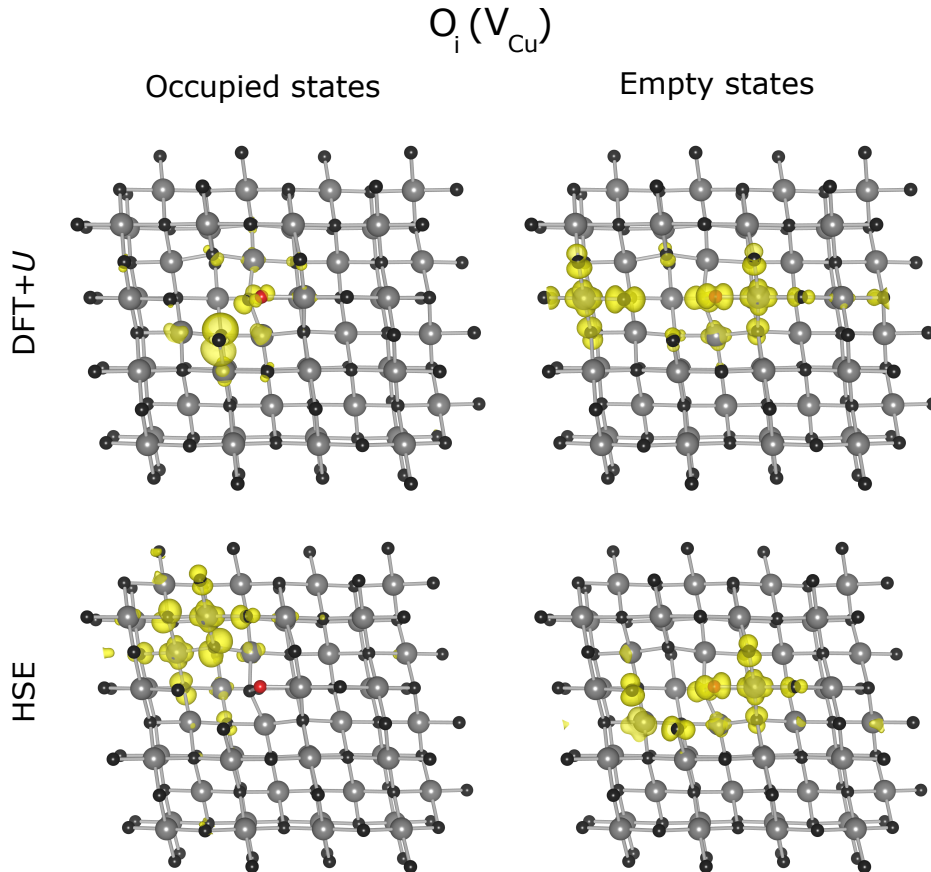


Figure 5.24: Partial charge densities of neutral  $O_i(V_{Cu})$  defect complex within CuO, along the  $b$  axis. Selected states correspond to the donor and acceptor states presented in Figure 5.23. Large grey spheres and small black spheres represent copper and oxygen atoms, while the red sphere distinguishes the  $O_i$ . A comparison between DFT+ $U$  and HSE values is shown on the top and bottom illustration, respectively. The yellow isosurface is shown at  $0.002 e/\text{\AA}^3$ .

and  $8.44 \text{\AA}$  for  $Cu_i(V_O)$ . This ensures that the overlap of respective wave functions is minimized as far as possible within the supercell. The notation implies a defect introduced in the host cell where the defect written in brackets was already present. As expected, defects introduced far away across the cell do not interact significantly with each other. They localize around the defect site, creating individual local distortions discussed in earlier paragraphs for single impurities. This is confirmed through electronic structure calculations for the considered pairs of defects, where the resulting densities of state correspond to an overlap of individual densities of state shown earlier, depicted in Figure 5.23.

Defects occurring in close proximity of each other show different properties compared to their dispersed analogues, due to strong overlap of interacting impurity wave functions. For  $O_i(V_{Cu})$ , the newly introduced O interstitial atom distorts the structure around the defect site negligibly. The three O atoms around the  $V_{Cu}$  remain relaxed away from the site, while the fourth O atom migrates towards the empty site due to strong Coulomb repulsion of the  $O_i$ . The distortion does not go beyond the nearest

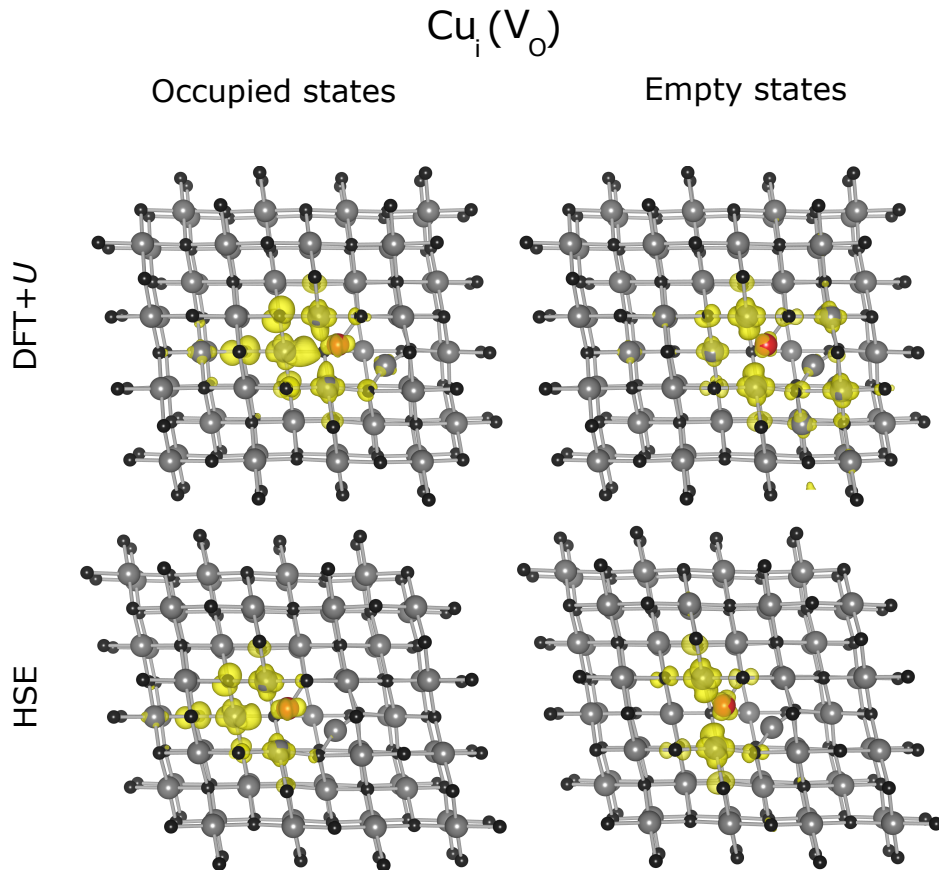


Figure 5.25: Partial charge densities of neutral  $\text{Cu}_i(\text{V}_\text{O})$  defect complex within CuO, along the  $b$  axis. Selected states correspond to the donor and acceptor states presented in Figure 5.23. Large grey spheres and small black spheres represent copper and oxygen atoms, while the red sphere distinguishes the  $\text{Cu}_i$ . A comparison between DFT+ $U$  and HSE values is shown on the top and bottom illustration, respectively. The yellow isosurface is shown at  $0.003 e/\text{\AA}^3$ .

neighbours, as the  $\text{O}_i$  quickly stabilizes within the lattice, forming weak bonds with three Cu atoms at distances of  $1.84 \text{ \AA}$  ( $1.81 \text{ \AA}$ ) –  $2.30 \text{ \AA}$  ( $2.50 \text{ \AA}$ ) and the nearest O atom at  $1.37 \text{ \AA}$  ( $1.38 \text{ \AA}$ ), which is comparable to the separation length of the  $\text{O}_2$  molecule of  $1.208 \text{ \AA}$  [245], as calculated using DFT+ $U$  (HSE). The  $\text{O}_i$  and its nearest O atom have charges of  $-0.46 e^-$  ( $-0.43 e^-$ ) and  $-0.42 e^-$  ( $-0.46 e^-$ ), which compared to a value of  $-0.96 e^-$  ( $-1.05 e^-$ ) on O atoms away from the defect, implies strong hole localization around the impurity atom, as calculated with DFT+ $U$  (HSE) and visualized in Figure 5.24. As a result of this structural rearrangement, the hole states are being spread across the band gap, compared to the case where the defects are placed further apart, as indicated in Figure 5.23. Slight differences are observed between the two utilized approaches, where DFT+ $U$  yields acceptor states spread out further compared to the more conglomerated ones from HSE calculations. These differences arise mostly from the way the different approximations treat structural parameters and bond angles, as pointed out earlier.

On the other hand, the addition of  $\text{Cu}_i$  around an existing  $\text{V}_\text{O}$  defect does not

distort the structure significantly. The Cu<sub>i</sub> relaxes into the void left behind the vacancy, easing the bond stress induced by the interstitial on the nearest O and Cu atoms. This allows the structure to relax into a more ordered one, hence lowering the formation energy of the defect complex by almost 0.80 eV (0.40 eV), as indicated before, obtained for DFT+*U* (HSE). The migration of the interstitial Cu proceeds until a position where the Coulomb repulsion of the surrounding electrons (left behind in the created O vacancy) is minimal. This is visualized with the two uppermost donor states in Figure 5.25, indicating a delicate charge balance in the void left behind when the vacancy was created. The two acceptor states are shown as well, placed at 0.10 eV and 0.46 eV below the CB minimum and localized around the defect site, not extending further than the nearest neighbouring Cu atoms.

Following this discussion, a general tendency of defect clustering in CuO is observed. More importantly, defects tend to create states located in the middle of the band gap, which is detrimental for any application requiring effective charge capture and separation processes. Deep states favour recombination of created carriers, impairing the overall conductivity, regardless of it being *n*-type or *p*-type.

### 5.3.3 Intentional passivation

A further question emerging is whether the mid-gap states created by intrinsic impurities can be removed whilst maintaining the desired conductivity type? One mechanism through which one could influence the character of an impurity is called *passivation*. It explains the often observed compensating nature of defects when donor dopants attract impurities of the opposite kind – acceptors, and vice versa. The resulting complex is often charge neutral and electrically inactive.

In order to test the system for eventual passivation effects, hydrogen was incorporated interstitially into the CuO matrix with the most stable defects present, as identified earlier. Hydrogen was chosen as the simplest possible impurity in order to track the changes that a single electron/hole induce onto the defect complex. Furthermore, the ambiguity when modelling hydrogen is drastically reduced compared to transition metal atoms or complex molecules, which often rely on additional  $U_{\text{eff}}$  parametrization or exact exchange tuning.

In the initial setup, one H atom is placed into the vacancy site of the O<sub>i</sub>(V<sub>Cu</sub>) defect complex (favouring *p*-type conductivity). After structural relaxation, the (effectively interstitial) H atom migrates towards the nearest neighbouring O closest to the vacancy site. The H atom binds onto one of the three dangling O bonds left after the O<sub>i</sub>(V<sub>Cu</sub>) defect complex was formed. This removes the strain present in the cell along the *c* direction and the nearest atoms surrounding the H site relax into their original

Table 5.4: Calculated defect formation energies for passivated CuO with intrinsic defects present.

	<i>n</i> -type		<i>p</i> -type	
	DFT+ <i>U</i>	HSE	DFT+ <i>U</i>	HSE
O <sub>i</sub> (V <sub>Cu</sub> )	4.963	2.954	2.089	0.080
O <sub>i</sub> (V <sub>Cu</sub> ) + H	3.722	2.430	1.566	0.274
O <sub>i</sub> (V <sub>Cu</sub> ) + 2H	2.759	1.468	1.322	0.031
Cu <sub>i</sub> (V <sub>O</sub> )	2.374	1.485	5.248	4.359
Cu <sub>i</sub> (V <sub>O</sub> ) + H	3.008	2.345	6.600	5.937
Cu <sub>i</sub> (V <sub>O</sub> ) + 2H	3.504	2.183	7.481	6.493

crystallographic positions in a cell without defects. However, two O dangling bonds along the *a*-axis remain present, with reduced repulsion effects due to their missing analogues in the perpendicular direction. More importantly, two acceptor states were removed from the electronic structure when compared to the case without interstitial H (see Figure 5.26). Qualitatively similar results are obtained using DFT+*U* and HSE, with differences occurring only in the relative positioning of the two remaining acceptor states within the gap. A notable disparity is observed in the calculated Bader charge values for the interstitial H and its nearest neighbouring O atom, with DFT+*U* yielding values of  $-0.55 e^-$  on H and  $+0.73 e^-$  on O, while HSE reads  $+0.69 e^-$  on H and  $-0.27 e^-$  on O. The later one is in good agreement with the calculated electronic structure as well as anticipated bonding behaviour based on tabulated electronegativity values [246], whereas the Bader partitioned values obtained using DFT+*U* are inaccurate for CuO.

Adding a further H atom into the vacancy site of the (O<sub>i</sub>(V<sub>Cu</sub>) + H) complex generates defect behaviour similar to the case of a single interstitial H. The newly added H binds onto its nearest neighbouring O atom left unpaired after the Cu vacancy was created. The surrounding structure remains largely unaffected, with the two interstitial H atoms relaxing away from each other due to active repulsion between identical charges. More importantly, this defect complex configuration leads to removal of the impurity states previously present in the middle of the band gap, leaving an electronic structure similar to that of simple interstitial O atoms, as observed from Figure 5.26. Effectively, interstitial H passivates the *p*-type effect of Cu vacancies, leaving O interstitial atoms intact. Despite the fact that neutral O interstitials do not create defect states in the vicinity of the band gap, Bader charge values of  $-0.43 e^-$  ( $-0.62 e^-$ ) and  $-0.48 e^-$  ( $-0.55 e^-$ ) on O<sub>i</sub> and its nearest neighbour indicate lowered bond strength, obtained for DFT+*U* (HSE). This could serve as a source of holes once

the defect changes charge state or the material is exposed to incoming radiation.

The formation energies of the H doped complexes are found to vary depending on the growth conditions. For *p*-type CuO, i.e., grown under O-rich conditions, the values read 1.566 eV (0.274 eV) for  $(\text{O}_i(\text{V}_{\text{Cu}}) + \text{H})$  and 1.322 eV (0.031 eV) for  $(\text{O}_i(\text{V}_{\text{Cu}}) + 2\text{H})$ , obtained with DFT+*U* (HSE) (full results available in Table 5.4). These results for CuO indicate similar behaviour to Cu<sub>2</sub>O, where a  $(\text{H}-\text{V}_{\text{Cu}})$  complex was found to be the most stable defect with a formation energy of only 0.17 eV (results obtained using a HSE functional with 27.5% of exact exchange) [127]. Furthermore, H<sub>*i*</sub> in Cu<sub>2</sub>O was found to be an amphoteric impurity under both sets of conditions, effectively killing both *p*-type and *n*-type conductivity.

In contrast, under Cu-rich conditions, interstitial H is placed into the O vacancy site of the Cu<sub>*i*</sub>(V<sub>O</sub>) complex. This causes the nearest neighbouring Cu atoms to relax away from the interstitial site, at distances of 1.59 Å (1.59 Å) and 1.68 Å (1.67 Å), calculated using DFT+*U* (HSE). The resulting electronic band structure remains largely unaltered, as observed from the calculated densities of state in Figure 5.27.

Inserting an additional H into the vacancy site results in a stronger relaxation of surrounding atoms, compared to the case of a single H interstitial. The added H migrates into the layer beneath the O vacancy (along the *-a* crystallographic axis) binding onto an O atom, causing the nearest neighbouring Cu to relax towards the vacant O site. More importantly, the initial electronic structure of the Cu<sub>*i*</sub>(V<sub>O</sub>) complex remains unaffected, from both DFT+*U* and HSE calculations (see right hand side of Figure 5.27). Two donor states remain present in the band gap, being elevated in energy as a result of the new structural distortion, with one donor state exhibiting notable H *s*-state contributions. However, no passivation effects were noted, as a consequence of the inability of H to counterbalance the large structural distortion originating from the interstitial Cu atom introduced in the first place. This behaviour demonstrates the difficulty of realizing un-doped *n*-type CuO. Unlike the case of *p*-type CuO, where O interstitials and Cu vacancies are easily incorporated into the lattice, without significantly affecting the surrounding, *n*-type CuO suffers large atomic rearrangements to accommodate interstitial Cu atoms – the most effective intrinsic donor defects.

In *n*-type CuO, grown under the Cu-rich regime, the formation energy of the  $(\text{Cu}_i(\text{V}_\text{O}) + \text{H})$  and  $(\text{Cu}_i(\text{V}_\text{O}) + 2\text{H})$  complexes are found to be 3.008 eV (2.345 eV) and 3.504 eV (2.183 eV), obtained using DFT+*U* (HSE), respectively. These formation energies are substantially higher compared to the initial Cu<sub>*i*</sub>(V<sub>O</sub>) defect complex, suppressing effective incorporation of H in CuO. Furthermore, a competitive interplay between the Cu<sub>*i*</sub>(V<sub>O</sub>) and O<sub>*i*</sub>(V<sub>Cu</sub>) is noted when considering the Cu-rich regime. For single H incorporation, the  $(\text{Cu}_i(\text{V}_\text{O}) + \text{H})$  defect complex is still found to be the most stable, while in the case when two H atoms are incorporated, the  $(\text{O}_i(\text{V}_{\text{Cu}}) + 2\text{H})$

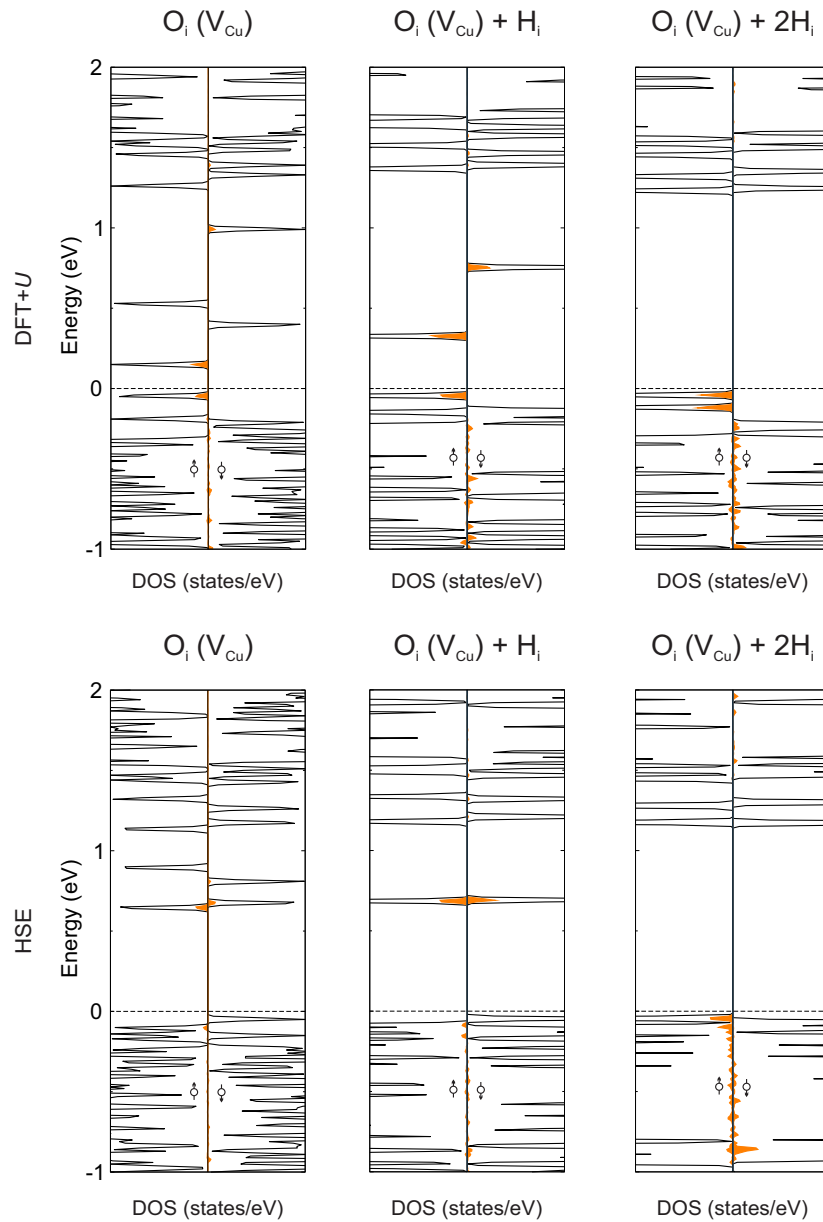


Figure 5.26: Calculated total (black line) and defect-projected (orange line) electronic densities of state (DOS) of clean and pairwise defective CuO with interstitial hydrogen. A comparison between DFT+*U* and HSE calculated values is illustrated in the top and bottom row. The dashed line indicates the highest occupied band and up/down arrows represent different spin channels.

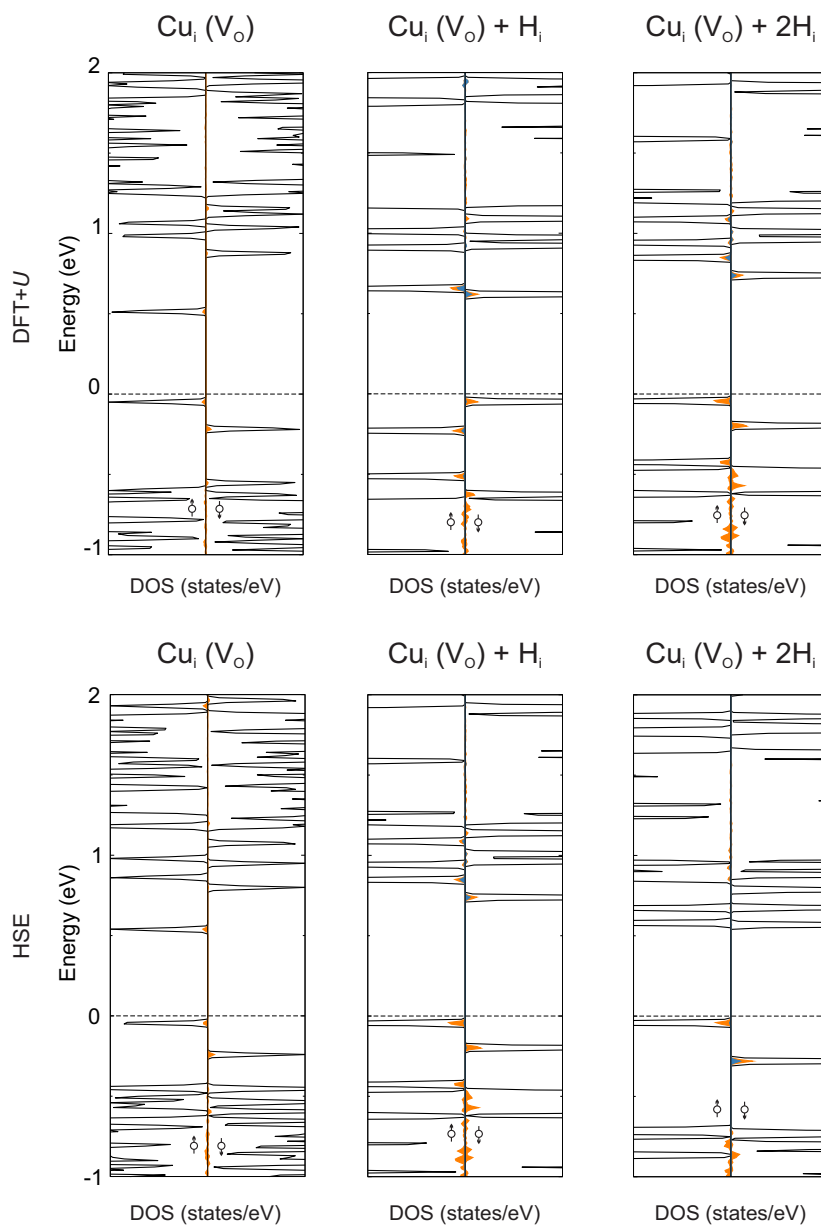


Figure 5.27: Calculated total (black line) and defect-projected (orange line) electronic densities of state (DOS) of clean and pairwise defective CuO with interstitial hydrogen. A comparison between DFT+ $U$  and HSE calculated values is illustrated in the top and bottom row. The dashed line indicates the highest occupied band and up/down arrows represent different spin channels.

complex is obtained as more favourable compared to the  $(\text{Cu}_i(\text{V}_\text{O}) + 2\text{H})$  one. This further indicates the difficulty of integrating H into *n*-type grown CuO, as an interplay between intrinsic donor and intrinsic acceptor impurities starts to take place.

## 5.4 Conclusion

A systematic comparative theoretical study of the DFT+ $U$  and hybrid-DFT formalism on the electronic and magnetic properties of CuO was undertaken. Various modelling parameters, such as the simulation cell, relaxation type, and magnetic configuration were optimized before the introduction of native point defects, both simple and complex, within the magnetic unit cell of CuO, followed by the evaluation of formation energies, as well as the effect on the overall electronic band structure. Following the presented analysis, several significant conclusions can be drawn:

- Both DFT+ $U$  and HSE are able to describe the ground state of CuO accurately. However, care is required when tuning either the  $U$  parameter in DFT+ $U$  or  $\alpha$  in HSE accordingly to the type of simulation that is being undertaken.
- Furthermore, both DFT+ $U$  and HSE approximation yield similar trends in the formation energies of simple defect that are accessible for CuO.
- Intrinsically, CuO can be created either *p*-type or *n*-type, depending on the synthesis conditions employed. However, both conductivity types suffer from states embedded deep in the band gap, hindering effective photo-response utilization, as noted experimentally.
- While deep states in *p*-type CuO can be removed easily with incorporating H as a passivation promoter, the same does not hold for *n*-type CuO.
- Clustering of defects is observed in CuO, lowering the defect formation energies compared to their dispersed analogues. The clustering features depend on the imposed conditions.

One of the main drawbacks while assessing the validity of the results outlined in this chapter is the lack of experimental evidence. Unlike  $\text{Cu}_2\text{O}$ , for which various spectroscopic measurements of intrinsic defects are available, literature for CuO is scarce. Nevertheless, calculations reproduce well the observed conductivity types and the intrinsic defects underpinning them. Furthermore, limitations regarding chemical potentials are outlined, which could serve as a base towards successful fabrication of *pn*-homo as well as heterojunctions based on CuO.

## The role of native point defects in $\text{Cu}_4\text{O}_3$

*"It is by logic that we prove, but by intuition that we discover.  
To know how to criticize is good, to know how to create is better."*

---

J. Henri Poincare, *French mathematician*

Paramelaconite is the least explored oxide of copper. Due to its unique stoichiometry, it is very difficult to synthesize  $\text{Cu}_4\text{O}_3$  and particularly stabilize the mixed  $\text{Cu}^{1+}$  and  $\text{Cu}^{2+}$  valence ions [247]. As it was demonstrated recently,  $\text{Cu}_4\text{O}_3$  is readily converted into  $\text{Cu}_2\text{O}$  and  $\text{CuO}$  by applying laser irradiation or thermal annealing processes [116].

Needless to say, literature about paramelaconite is scarce, with the majority of works dealing with the determination of structural parameters and composition (experimentally), or electronic structure and absorption spectra (theoretically). However, little is known about intrinsic defects present in  $\text{Cu}_4\text{O}_3$ , apart from its  $p$ -type conductivity stemming from Hall measurement and thermal hole activation energy [116]. The question of creating  $n$ -type  $\text{Cu}_4\text{O}_3$  has been neglected as well.

Within this chapter,  $\text{Cu}_4\text{O}_3$  is modelled theoretically in-depth by first obtaining the right set of computational parameters required to reproduce the structural, electronic and magnetic properties of  $\text{Cu}_4\text{O}_3$  as accurately as possible. Based on that, some of the questions being targeted within this chapter include:

- Can the indirect and direct electronic band gap of  $\text{Cu}_4\text{O}_3$  be modelled accurately within DFT? Which approximation for the XC functional yields the most accurate results?
- Which intrinsic defects occur in  $\text{Cu}_4\text{O}_3$ ? Is it possible to create intrinsic  $n$ -type  $\text{Cu}_4\text{O}_3$ ?
- What role do defects play in the stability of  $\text{Cu}_4\text{O}_3$ ?

The chapter is organized as follows: in the first section, theoretical parameters used for modelling and testing various properties of  $\text{Cu}_4\text{O}_3$  were listed. The subsequent section deals with the results and discussion of observed phenomena (where appropriate), followed by answers to some of the questions outlined above as well as the limitations of the given framework. No literature review is present within this chapter, which is based on two reasons: not to duplicate the data on bulk paramelaconite shown in Chapter 1 and simply because data on defects of  $\text{Cu}_4\text{O}_3$  is non-existing.

## 6.1 Technical details and computational parameters

Results shown in this chapter are based (once again) on spin polarized DFT-based calculations performed with the Vienna Ab-initio Simulation Package [135]. The interactions between core and valence electrons were represented using the projector augmented wave (PAW) method [134]. Calculations were carried out in the general gradient approximation (GGA) [136] using the Perdew–Burke–Ernzerhof (PBE) parametrization for DFT+ $U$  within the formalism of Dudarev *et al* [16]. For hybrid-DFT calculations, the HSE06 XC functional was used [19–21], with a screening parameter of  $0.2 \text{ \AA}^{-1}$ . Long distance dispersion corrections were included using the D3 approach of Grimme *et al* [139]. The plane wave expansion cutoff was set to 500 eV and the force convergence criterion to cell relaxation was  $0.01 \text{ eV/\AA}$ .  $\Gamma$ -centred Monkhorst-Pack [22] meshes ( $5 \times 5 \times 5$  for the primitive unit cell,  $5 \times 5 \times 3$  for conventional unit cell, and a single  $\Gamma$ -point for the supercell) were employed to sample the Brillouin zone in reciprocal space. Band structure and density of state (DOS) calculations were performed at the optimized structure along high-symmetry directions obtained from the Bilbao Crystallographic Server [140–142]. Band structures were plotted using the `Wannier90` code [239, 240]. The phase stability diagram of  $\text{Cu}_4\text{O}_3$  for a range of accessible chemical potentials was computed using the CPLAP (Chemical Potential Limits Analysis Program) [202], taking into account its limiting competing phases. The extent of defect charge distribution was studied using the Bader scheme as implemented in the Henkelman code [203–205]. Graphical drawings were produced using `VESTA` [144]. Excitonic and spin-orbit coupling effects were not taken into account.

The amount of non-local exact Hartree-Fock exchange used within the HSE06 XC functional was tuned manually, according to the computed electronic (Kohn-Sham) band gap and (spin only on the Cu atom) magnetic moment to match experimental values. B3LYP calculations were first performed using the all-electron `CRYSTAL17` code [248, 249]. In `CRYSTAL`, the convergence of the real-space summation of the Coulomb

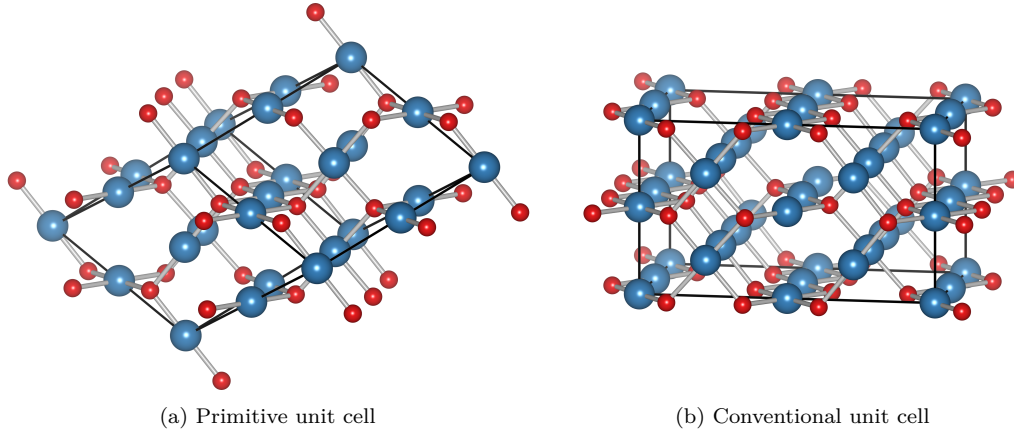


Figure 6.1: Schematic representation of different ways to define the modelling unit cell of  $\text{Cu}_4\text{O}_3$ . Blue and red sphere represent copper and oxygen atoms, respectively.

and exchange contributions to the Hamiltonian matrix is controlled by five overlap criteria. The values used in this study were  $10^{-7}$ ,  $10^{-7}$ ,  $10^{-7}$ ,  $10^{-7}$ , and  $10^{-14}$ . A Monkhorst-Pack shrinking factor of 8 was used to sample the first Brillouin zone and a denser Gilat net consisting of 16 points was used in the evaluation of the Fermi energy and density matrix [248]. The tuning of the exact exchange fraction used in B3LYP was done according to the self-consistent scheme proposed by Skone *et al* [250] and implemented by Erba *et al* [251]. Following that procedure, the system-specific exact exchange fraction, defined as inversely proportional to the static electronic dielectric constant  $\epsilon_\infty$ , is calculated iteratively until it changes by less than 0.1% between two subsequent iterations. CRYSTAL17 uses a fully-automated, computationally-efficient implementation of the self-consistent (global) hybrid functional, where the dielectric functional is computed adopting a Coupled-Perturbed-Hartree-Fock/Kohn-Sham (CPHF/KS) approach [248].

Similarly to  $\text{CuO}$ , the conventional and primitive unit cell of  $\text{Cu}_4\text{O}_3$  (illustrated in Figure 6.1) exhibit different geometries. In order to transform from the primitive to the conventional modelling cell, the following transformations were applied:

$$\begin{array}{cc}
 P \rightarrow C & C \rightarrow P \\
 \begin{pmatrix} -\frac{1}{2} & \frac{1}{2} & \frac{1}{2} \\ \frac{1}{2} & -\frac{1}{2} & \frac{1}{2} \\ \frac{1}{2} & \frac{1}{2} & -\frac{1}{2} \end{pmatrix} & \begin{pmatrix} 0 & 1 & 1 \\ 1 & 0 & 1 \\ 1 & 1 & 0 \end{pmatrix} \\
 & (6.1)
 \end{array}$$

where  $P$  and  $C$  stand for primitive and conventional, respectively. The choice of cell is dictated by the appropriate magnetic propagation vector, which is even experimentally

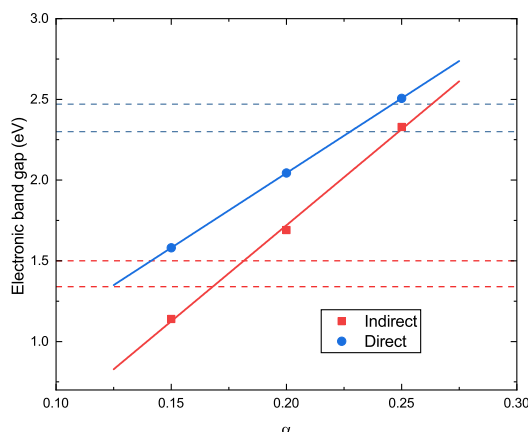


Figure 6.2: The calculated electronic (Kohn-Sham eigenvalue) band gap dependence on the exact exchange amount  $\alpha$  used within HSE06. The filled red squares denote the indirect, while the filled blue circles indicate the values of the direct band gap (at the  $\Gamma$  point). The linear fit is merely an eye-guide for easier data readout. The red and blue dashes lines correspond to the experimentally measured values of the indirect and direct electronic band gap, respectively.

still a matter of debate. The equivalence between the two modelling cells was confirmed and the primitive cell was chosen to study defect formation, in order to reduce the computational cost.

## 6.2 Results and discussion

### 6.2.1 Ground state electronic structure

Following on the results shown in Chapter 2 regarding the modelling of bulk  $\text{Cu}_4\text{O}_3$ , local and semi-local DFT was found unsatisfactory for the description of electronic properties. Hybrid DFT, in the form of HSE06, is able to capture the correct nature of the first band-to-band transition as indirect, but yields too small a difference between the indirect and direct band gaps. The same difference, depending on the exact exchange amount  $\alpha$  used in HSE06, was calculated and is plotted in Figure 6.2. Observed values (from the graph) lead to the conclusion that for no value of  $\alpha$  used in HSE06, the difference between the indirect and direct band gap will be matched accurately. Tuning the exact exchange influences the electronic structure mostly by lowering the position of the conduction band relative to the valence band, thereby decreasing the band gap value without significantly altering its structure.

Since HSE06 is only one of many available hybrid functionals, the questions arises if any other functional can accurately reproduce the electronic properties of  $\text{Cu}_4\text{O}_3$ ? Historically, one of the earliest developed hybrid XC functionals is B3LYP. It is often regarded as the starting point for the development of many other hybrid functionals and has been benchmarked for many systems (especially molecular cases) over the last

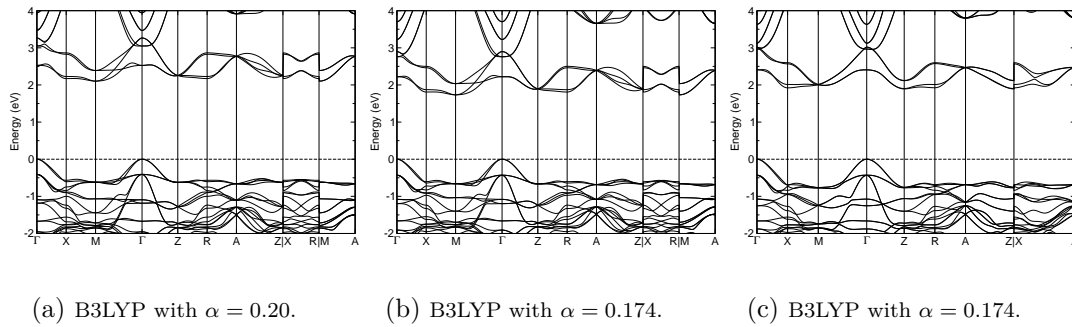
(a) B3LYP with  $\alpha = 0.20$ .(b) B3LYP with  $\alpha = 0.174$ .(c) B3LYP with  $\alpha = 0.174$ .

Figure 6.3: Computed electronic band structure of  $\text{Cu}_4\text{O}_3$  using different approximations for the XC functional. The figures on the left and in the middle were calculated using the all-electron code CRYSTAL17, the figure on the right was obtained using the plane-wave code VASP.

decades. Unlike HSE06, it is a global functional, where the amount of HF exchange included does not depend on the distance between electrons. In order to test the accuracy of a different hybrid functional, B3LYP was used to calculate the electronic properties and optical spectra of  $\text{Cu}_4\text{O}_3$ .

**Self-consistent B3LYP** Default B3LYP is characterized by 20% ( $\alpha = 0.2$ ) of exact HF exchange. Performing calculations with default B3LYP yields electronic band gap values of 2.10 eV and 2.53 eV for the indirect and direct gap, respectively. Despite the overestimation of the indirect gap, the difference between the direct and indirect gap gives a larger value compared to those obtained using HSE06. The calculated electronic band structure calculated with B3LYP is shown in Figure 6.3. Following the improved trend of B3LYP over HSE06, a tuning of the exact exchange fraction was undertaken and its value computed self-consistently using the internal routines of CRYSTAL17. An average electronic static dielectric constant of 5.75 was obtained, followed by the optimal exchange fraction of 17.407%. The calculated electronic structure using the self-consistently determined optimal fraction for B3LYP (SC-B3LYP) is shown in Figure 6.3. The measured SC-B3LYP indirect and direct band gap read 1.73 eV and 2.22 eV, which resembles the experimentally observed gaps very closely.

Since the amount of exact exchange used with B3LYP is determined self-consistently, is it transferable between different codes? In order to verify this statement, a SC-B3LYP calculation was performed using the plane-wave code VASP with the amount of exact exchange determined through the procedure outlined earlier. The resulting band structure is shown on the right hand side in Figure 6.3. Despite the slightly altered values of 1.89 eV and 2.41 eV for the indirect and direct gap respectively (most likely attributable to different implementations between codes), the overall trend remains preserved which hints towards the uniqueness and transferability of the obtained value for the exact exchange parameter used within B3LYP, at least for  $\text{Cu}_4\text{O}_3$ .

Table 6.1: Calculated enthalpies of formation (eV/formula unit) for  $\text{Cu}_4\text{O}_3$ . Values for  $\text{Cu}_2\text{O}$  and  $\text{CuO}$  are shown for validation of values within a used functional.

	$\Delta H_f$ ( $\text{Cu}_2\text{O}$ )	$\Delta H_f$ ( $\text{Cu}_4\text{O}_3$ )	$\Delta H_f$ $\text{CuO}$
HSE06	−1.66	−4.92	−1.57
SC-B3LYP	−2.21	−5.32	−1.69
	−1.75 [40]	−4.69 (at 427° C) [211]	−1.59 [40]
Experiment		−4.88 (at 25° C) [211]	
		−5.94 ± 0.26 (at 25° C) [211]	

**Phase stability** Calculated formation enthalpies of  $\text{Cu}_4\text{O}_3$  are reported in Table 6.1. Both HSE06 (with standard 20% exact exchange) and SC-B3LYP show similar trends with results being reasonably close to experimental values. The slight overestimation of SC-B3LYP values is not necessarily a surprise, since it is known that the B3LYP functional does not provide accurate total energies for metallic Cu, as demonstrated in earlier work [252]. Limits for the chemical potential range valid for pristine  $\text{Cu}_4\text{O}_3$  were calculated from available formation enthalpies and constraints set by the evolution of competing phases, in this case  $\text{Cu}_2\text{O}$  and  $\text{CuO}$ .

In order to bypass stability issues originating from the use of different functionals, values for formation enthalpies entering the stability range calculation were taken from available experimental data. The calculated phase stability region for  $\text{Cu}_4\text{O}_3$  is shown in Figure 6.4. The thermodynamic stability window of  $\text{Cu}_4\text{O}_3$  is narrow, reproducing the observed difficulty of synthesizing pure samples without  $\text{Cu}_2\text{O}$  or  $\text{CuO}$  being present. Effectively,  $\text{Cu}_4\text{O}_3$  can only be created under Cu-rich/O-poor conditions, with the chemical potential values reading  $\Delta\mu_{\text{Cu}} = -0.157$  eV and  $\Delta\mu_{\text{O}} = -1.437$  eV. Furthermore, the observed narrowness of the available stability region for  $\text{Cu}_4\text{O}_3$  indicates that the choice of functional would not alter the calculated defect formation energies substantially.

### 6.2.2 Intrinsic defects

Studied native defects within  $\text{Cu}_4\text{O}_3$  include simple vacancies ( $V_{\text{Cu}}$  and  $V_{\text{O}}$ ), antisites ( $\text{Cu}_{\text{O}}$  and  $\text{O}_{\text{Cu}}$ ), and interstitials in three different positions within the simulation cell ( $\text{Cu}_{i-n}$  and  $\text{O}_{i-n}$ , with  $n = 1, 2, 3$ ). Each defect is modelled in a  $2 \times 2 \times 2$  supercell, obtained by expanding the primitive unit cell, with a corresponding defect concentration of 1.56% and 2.08% for impurities occurring on the Cu site and O site, respectively (as a results of the unequal number of Cu and O atoms in the unit cell).

As outlined in Chapter 1,  $\text{Cu}_4\text{O}_3$  contains two distinct Cu and O atoms. They can

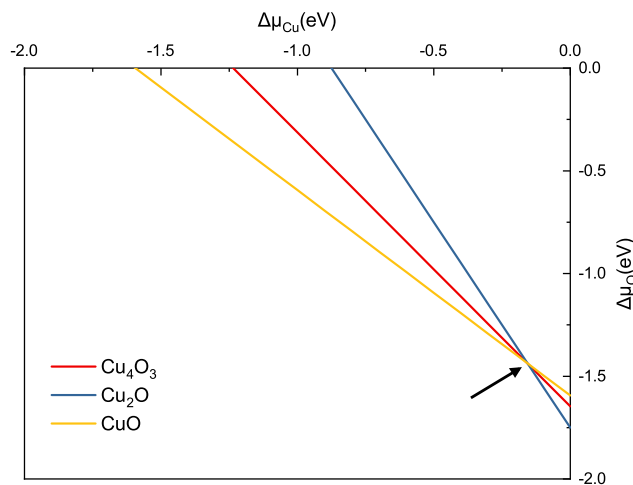


Figure 6.4: Phase stability in the range of accessible chemical potentials for  $\text{Cu}_4\text{O}_3$ . Limits are imposed by the formation of competing phases, in this case  $\text{Cu}_2\text{O}$  and  $\text{CuO}$ . The black arrow denotes the narrow stability point of  $\text{Cu}_4\text{O}_3$ .

Table 6.2: Bader charge analysis of  $\text{Cu}_4\text{O}_3$  using three different approximations for the XC functional. Values reported in  $e^-$ .

	$\text{Cu}^{1+}$	$\text{Cu}^{2+}$	O-1	O-2
DFT+ $U$	+0.534	+0.913	-0.959	-0.936
HSE06	+0.563	+1.122	-1.130	-1.112
SC-B3LYP	+0.545	+1.070	-1.089	-1.065

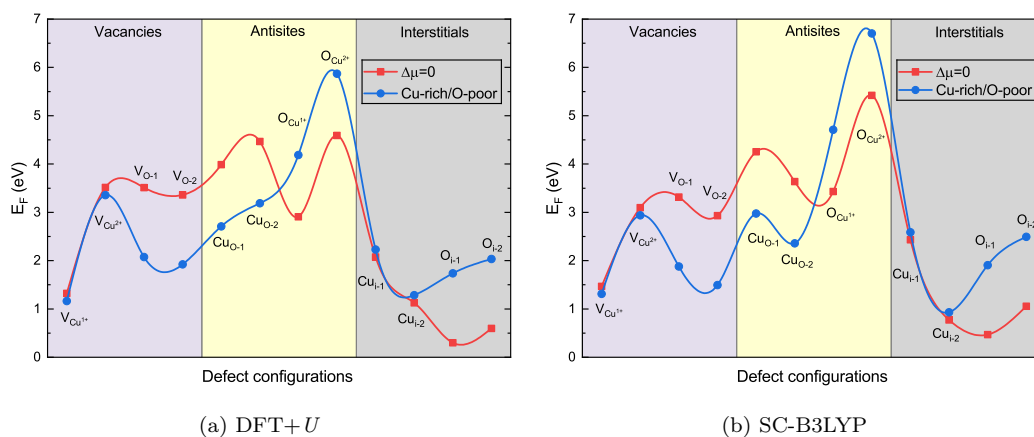


Figure 6.5: Calculated formation energies of native defect occurring in  $\text{Cu}_4\text{O}_3$ . Results are presented for two different approximation for the XC functional as well as two distinct values of chemical potentials. The red line illustrates the maximally Cu- and O-rich conditions, while the blue line represents the only stability point of  $\text{Cu}_4\text{O}_3$  discussed earlier.

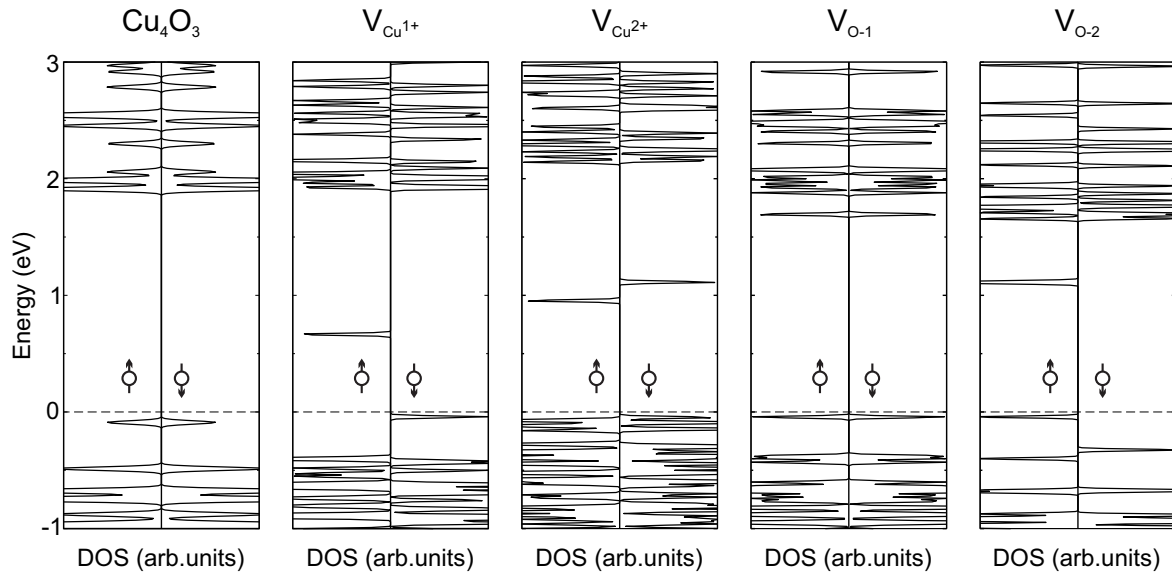


Figure 6.6: Calculated total (black) and defect-projected (orange) electronic densities of states of pure and defective  $\text{Cu}_4\text{O}_3$  with single vacancies. The dashed line indicates the highest occupied band and up/down arrows represent different spin channels.

be distinguished through their coordination number or oxidation (valence) state. The first one ( $\text{Cu}^{1+}$ ) is a cuprous Cu binding two nearest neighbouring O atoms (labelled O-1) in a linear arrangement, while the other ( $\text{Cu}^{2+}$ ) is a cupric Cu surrounded by four O atoms in an almost square planar configuration. Each O atom, on the other hand, binds four Cu atoms, with the difference that the first (O-1) binds four  $\text{Cu}^{2+}$  atoms while the second (O-2) binds two  $\text{Cu}^{1+}$  and two  $\text{Cu}^{2+}$  atoms. The Bader charge analysis provides a useful way of determining those differences in order to detect distinct impurity sites within the cell. Results for clean  $\text{Cu}_4\text{O}_3$  have been presented in Table 6.2. Despite the nominal charge state of  $-2$ , the two O atoms show small differences in accumulated charge of  $\Delta = 0.02 e^-$ , regardless of the chosen functional approximation. Interestingly, DFT+ $U$  results follow the same trend as HSE06 and SC-B3LYP ones, with absolute values being considerably reduced. However, results presented in the following paragraphs consider mostly SC-B3LYP results, due to the accurate description of the initial electronic structure. Comparison with DFT+ $U$  or HSE06 results is drawn where appropriate. Following this small discussion, a conclusion can be drawn that vacancy and antisite defects modelled in  $\text{Cu}_4\text{O}_3$  will include two distinct configurations in order to capture all possible sites.

**Vacancies** The calculated formation energies of simple defects in  $\text{Cu}_4\text{O}_3$  are presented in Figure 6.5, with vacancies shown on the left hand side. The two Cu vacancies, corresponding to the removal of one  $\text{Cu}^{1+}$  or  $\text{Cu}^{2+}$  atom are labelled as  $V_{\text{Cu}^{1+}}$  and  $V_{\text{Cu}^{2+}}$ , respectively, while the two O vacancies are named  $V_{\text{O-1}}$  and  $V_{\text{O-2}}$  to distinguish between the sites identified earlier.

Removing a  $\text{Cu}^{1+}$  atom from the crystal lattice results in two dangling bonds from the neighbouring O atoms with mostly  $p$  character. The formation of a neutral  $V_{\text{Cu}^{1+}}$  defect causes the two closest O atoms to relax away from the site, yet the overall influence on the lattice parameters is below 0.8% expansion. A neutral  $V_{\text{Cu}^{1+}}$  defect creates one empty state in the otherwise pristine electronic band structure (Figure 6.6). The unoccupied acceptor level is located around 0.66 eV above the VB maximum in the spin majority channel, originating mainly from Cu  $d$  and O  $p$  states. The created hole is highly delocalized in real space, as shown at the top of Figure 6.7. The removal of a  $\text{Cu}^{2+}$  atom leads to a relaxation of the nearest O atoms away from the defect site, similar to the  $V_{\text{Cu}^{1+}}$  defect. The neighbouring O atoms also relax towards each other, alternating the O–O distance for 0.02–0.05 Å, in order to maximize their bond overlap. Since the removed Cu atom was initially in a +2 charge state, the  $V_{\text{Cu}^{2+}}$  defect creates two empty states in the otherwise clean band gap of  $\text{Cu}_4\text{O}_3$ . The two acceptor levels are located around 0.95 eV and 1.15 eV above the top of the VB. Compared to  $V_{\text{Cu}^{1+}}$ , the  $V_{\text{Cu}^{2+}}$  induced hole states are more localized around the vacancy site, as expected since they are embedded quite deep in the band gap.

Removing one O–1 atom leaves the two electrons from the surrounding Cu atoms weakly bond to their respective hosts. The  $V_{\text{O}-1}$  causes the nearest neighbouring Cu atoms to relax towards each other in order to lower the energy of the defect state. It adopts the  $-2$  charge state from the missing atom, with Bader values reading a surplus of  $\Delta = +0.23 e^-$  and  $\Delta = +0.34 e^-$  on the pairs of nearest  $\text{Cu}^{1+}$  and  $\text{Cu}^{2+}$  atoms (compared to the values without the defect), respectively. This indicates strong localization of electrons around the defect site. The created acceptor state is doubly unoccupied and located 0.15 eV below the CB minimum. A visual inspection of the empty states reveals their strong localization around the defect site, with minor delocalization on the surrounding atoms (see Figure 6.7).

A similar structural relaxation is observed when the O–2 atom is removed from the  $\text{Cu}_4\text{O}_3$  matrix, where the neighbouring Cu atoms shift towards the empty site in order to minimize the Coulomb repulsion from surrounding electrons. Furthermore,  $V_{\text{O}-2}$  creates two acceptor states in the band gap, both lying very close to each other in energy. They are placed roughly 0.51 eV below the CB, in the spin up channel only. The charge remaining after the induced vacancy is asymmetrically distributed amongst the surrounding Cu atoms, with two distinct pairs reading Bader values of  $+0.75 e^-$  and  $+0.81 e^-$ . This is a surplus of  $\Delta = +0.26 e^-$  and  $\Delta = +0.32 e^-$  compared to the starting value of the  $\text{Cu}^{2+}$  atom. Also, the acceptor levels show strong localization on the Cu atoms surrounding the defect site. The neighbouring O atoms show no change in the accumulated charge, for both O vacancies (see Figure 6.7).

Looking at the formation energies, a clear distinction between the  $V_{\text{Cu}^{1+}}$  and  $V_{\text{Cu}^{2+}}$

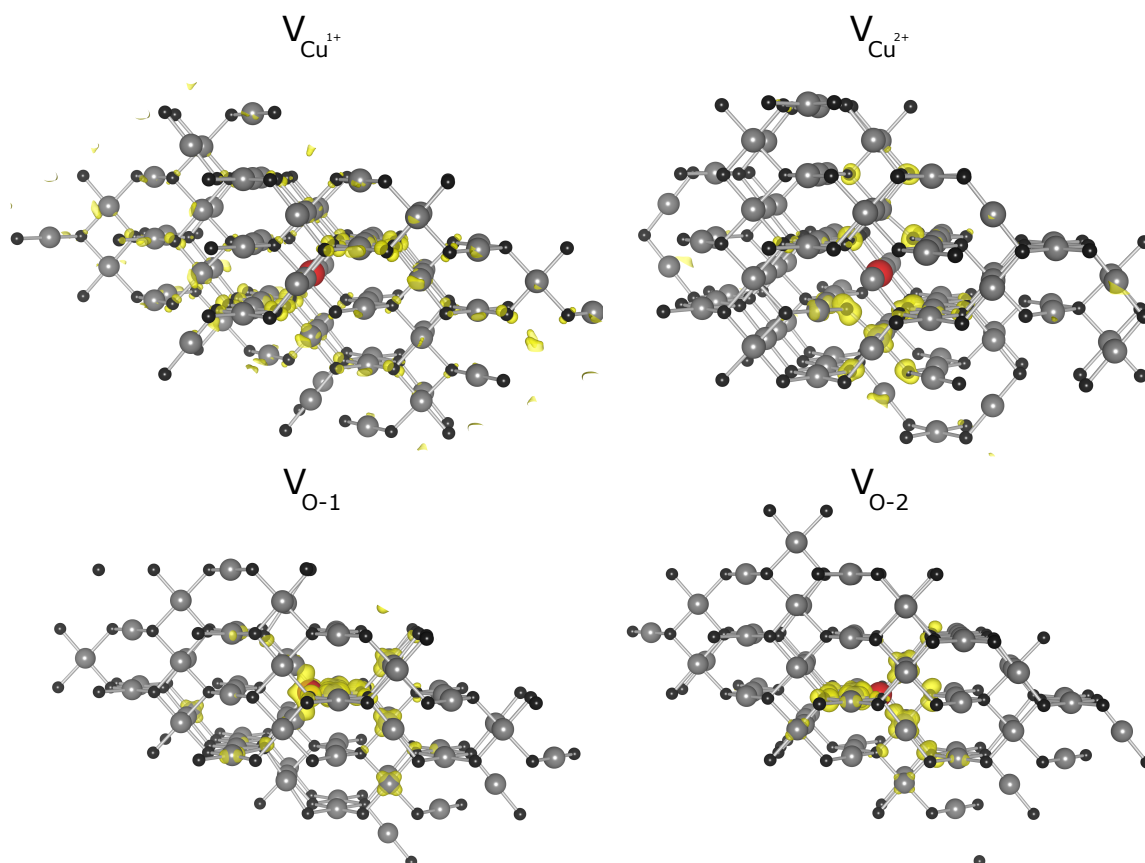


Figure 6.7: Partial charge densities of neutral vacancy defects within  $\text{Cu}_4\text{O}_3$ . Selected states correspond to the acceptor states presented in Figure 6.6. Large grey spheres and small black spheres represent copper and oxygen atoms, while the red sphere distinguishes vacancies. The yellow isosurface is shown at  $0.003 \text{ e}/\text{\AA}^3$ .

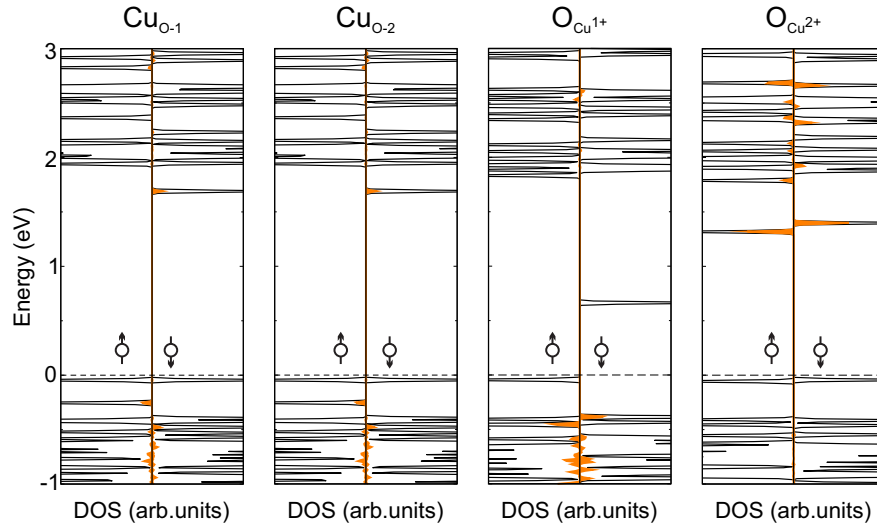


Figure 6.8: Calculated total (black) and defect-projected (orange) electronic densities of states of pure and defective  $\text{Cu}_4\text{O}_3$  with single antisite defects. The dashed line indicates the highest occupied band and up/down arrows represent different spin channels.

defect can be observed. While the  $V_{\text{Cu}^{1+}}$  can be created for less than 1.39 eV (1.27 eV), the cost for inducing  $V_{\text{Cu}^{2+}}$  defect doubles, with formation energies higher than 3.31 eV (2.82 eV), calculated for DFT+ $U$  and SC-B3LYP, respectively. This is somehow anticipated, as it essentially describes the energy required to break existing Cu-O bonds, which for  $V_{\text{Cu}^{2+}}$  count four and for  $V_{\text{Cu}^{1+}}$  only two.

Note how the calculated defect formation energies do not depend greatly on the functional approximation, retaining the overall trends. For O vacancies, an energy difference of 0.30 eV between  $V_{\text{O}-1}$  and  $V_{\text{O}-2}$  with the B3LYP is calculated, compared to 0.02 eV obtained with DFT+ $U$ . This hints towards the usability of DFT+ $U$  calculations as an affordable approach for a pre-screening of defects, while the finer energy distribution should be done with a hybrid functional.

**Antisites** Both Cu and O antisite defects lie much higher in energy, compared to simple vacancies (see Figure 6.5), yet their influence on the overall electronic properties was assessed for completeness. A single Cu antisite defect on the O-1 site requires almost 3 eV of energy to occur in the pristine  $\text{Cu}_4\text{O}_3$  structure. It causes the four neighbouring Cu atoms to relax away from the defect site in order to minimize the Coulomb repulsion effects induced with the extra electrons added to the system. The two  $\text{Cu}^{1+}$  atoms experience a large displacement due to the weaker interaction with the lattice, compared to the  $\text{Cu}^{2+}$  atoms whose rearrangement is counterbalanced by the remaining three bonds with neighbouring O atoms. The charge analysis (values not listed) reads weak electron transfer between the antisite defect and its nearest neighbours, indicating very weak bond formation. The  $\text{Cu}_{\text{O}-1}$  defect creates one acceptor level located 0.20 eV below the CB in the spin minority channel, as shown in

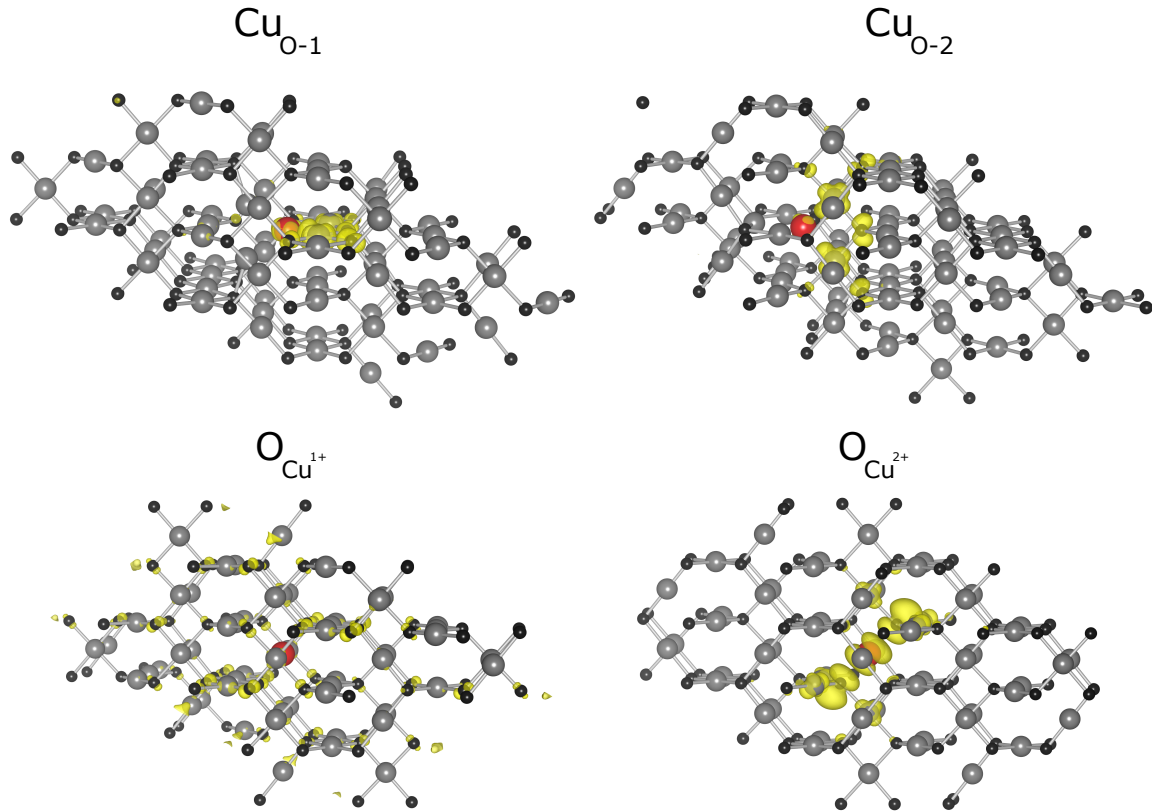


Figure 6.9: Partial charge densities of neutral antisite defects within  $\text{Cu}_4\text{O}_3$ . Selected states correspond to the acceptor states presented in Figure 6.8. Large grey spheres and small black spheres represent copper and oxygen atoms, while the red sphere distinguishes vacancies. The yellow isosurface is shown at  $0.003 e/\text{\AA}^3$  (top row) and  $0.002 e/\text{\AA}^3$  (bottom row), respectively.

Figure 6.8. The remaining  $\text{Cu}_\text{O}$  states are placed below the VB, confirming charge localization on the defect site.

A single  $\text{Cu}_{\text{O}-2}$  defect induces a displacement of the nearest neighbouring Cu towards its two closest O atoms, leaving the remaining three Cu atoms almost intact. This causes the formation energy of  $\text{Cu}_{\text{O}-2}$  to increase compared to the  $\text{Cu}_{\text{O}-1}$  defect. In terms of electronic structure, an acceptor level at the same position as for the  $\text{Cu}_{\text{O}-1}$  defect is created. However, a difference in the spatial localization of the acceptor states is observed, as shown in Figure 6.9.

O antisite defects occurring on the  $\text{Cu}^{1+}$  site exhibit very weak structural relaxation effects, as the impurity radius is not large enough to distort the lattice. Furthermore, the available bonding sites are nearest neighbouring O atoms, which exert active Coulomb repulsion towards the defect. The  $\text{O}_{\text{Cu}^{1+}}$  defect induces a hole state in the pristine electronic band structure, located  $\approx 0.66$  eV on top of the VB. The state manifests itself in the spin minority channel and is fully delocalized across the lattice, as observed in Figure 6.9. According to the calculated Bader charge values,  $-0.53 e^-$  are found on the  $\text{O}_{\text{Cu}^{1+}}$  site (compared to a value of  $-1.08 e^-$  for an O atom located far from the defect), which implies charge accumulation originating from the surrounding

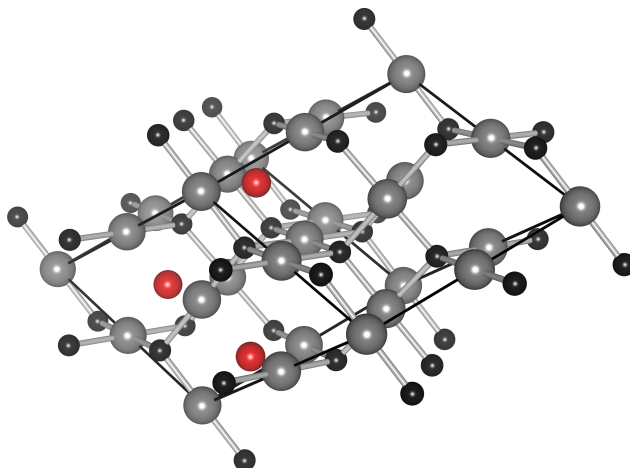


Figure 6.10: Schematic representation of identified suitable interstitial position within the primitive crystal lattice of  $\text{Cu}_4\text{O}_3$ . Interstitial positions are labelled with red letters from  $i-1$  to  $i-3$ .

Cu atoms as they demonstrate a loss of  $\Delta = -0.19 e^-$ , each.

By contrast, the O antisite appearing on the  $\text{Cu}^{2+}$  site counts a Bader value of  $-0.05 e^-$ , indicating negligible charge accumulation. This is not necessarily a surprise, since the defect is embedded in a surrounding of four O atoms in a square linear arrangement. The defect is trapped due to strong Coulomb repulsion, hence the high calculated formation energy of more than 5 eV (for the SC-B3LYP functional). The observed acceptor state lies around 0.4 eV below the CB minimum, originates almost entirely from  $\text{O}_{\text{Cu}^{2+}}$   $p$  states, and is highly localized around the defect site (see bottom right of Figure 6.9).

**Interstitials** Three suitable positions for interstitial atoms were identified in the  $\text{Cu}_4\text{O}_3$  crystal structure and shown in Figure 6.10. Interstitial Cu incorporated in position 1,  $\text{Cu}_{i-1}$ , forms in the plane of zig-zag  $\text{Cu}^{1+}$  atoms. It affects the nearest neighbouring Cu atom as it relaxes away from the similarly charged interstitial site. There is also partial charge transfer from the  $\text{Cu}_{i-1}$  atom onto its nearest neighbouring O atom, in order to compensate for the lack of electrons induced by the displacement of Cu atoms. Incorporating the extra Cu atom into the  $\text{Cu}_4\text{O}_3$  lattice forms a delocalized donor state 0.63 eV below the CB minimum (see Figures 6.11 and 6.12).

Cu interstitial placed in position 2,  $\text{Cu}_{i-2}$ , are predicted to relax, starting from the void, into the plane of  $\text{Cu}^{2+}$  atoms, each bound in a square planar arrangement to four O atoms. The nearest neighbouring Cu atom is affected the most, as two of its four O bonds break and the atom is displaced away from the similarly charged interstitial. The  $\text{Cu}_{i-2}$  atom binds then onto the two remaining O atoms in an almost linear arrangement. Both the  $\text{Cu}_{i-2}$  and the displaced Cu atoms are found in the +1 state, as their Bader charge values read  $+0.51 e^-$  and  $+0.50 e^-$ , derived from SC-B3LYP

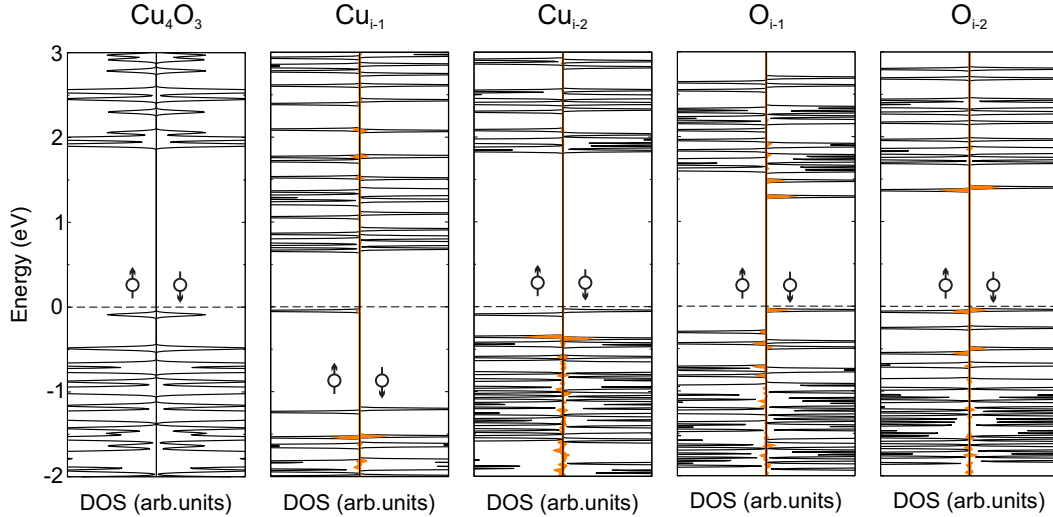


Figure 6.11: Calculated total (black) and defect-projected (orange) electronic densities of states of pure and defective  $\text{Cu}_4\text{O}_3$  with single interstitial Cu (top row) and O (bottom row) defects. The dashed line indicates the highest occupied band and up/down arrows represent different spin channels.

calculations (starting from a value of  $+1.07 e^-$  for the displaced Cu). A complete loss of magnetization on the displaced Cu atom further confirms those results. No defect states between the VB top and CB bottom were observed as a result of incorporating a single  $\text{Cu}_{i-2}$  defect, see Figure 6.11.

Energetically, the cost of forming  $\text{Cu}_{i-2}$  yields 1.74 eV (1.35 eV), which is almost half the value needed to create  $\text{Cu}_{i-1}$ , which reads 2.78 eV (2.17 eV), as obtained from SC-B3LYP (DFT+ $U$ ) calculations. This is attributed to the ability of the lattice to accommodate the interstitial Cu atom. For  $\text{Cu}_{i-2}$ , a simple rearrangement allows the interstitial to fully bind onto its neighbouring O atoms, while for  $\text{Cu}_{i-1}$  there is an over-saturation of paired bonds which do not accept additional electrons.

$\text{Cu}_{i-3}$  yield behaviour identical to that of  $\text{Cu}_{i-2}$ , due to the symmetry of the lattice site where the defect is incorporated. Hence, further analysis of the interstitial defect  $\text{Cu}_{i-3}$  is omitted.

Interstitial O incorporated in position 1,  $\text{O}_{i-1}$ , causes negligible ionic relaxation of surrounding sites (see Figure 6.13). It binds actively to nearest neighbouring Cu atoms, inducing a charge transfer process. A Bader charge value of  $-0.96 e^-$  is identified on the  $\text{O}_{i-1}$  atom, which lies very close to  $-1.08 e^-$  on an O atom in the  $-2$  charge state located further away from the defect site. The surrounding  $\text{Cu}^{1+}$  atoms undergo an oxidation state change into  $\text{Cu}^{2+}$  atoms, with the following calculated variations of the Bader charge:  $\Delta = +0.29 e^-$ ,  $\Delta = +0.28 e^-$ ,  $\Delta = +0.07 e^-$ , and  $\Delta = +0.21 e^-$ . As the defect captures electrons from the surrounding, two depopulated acceptor states are created, found 0.10 eV and 0.28 eV below the CB bottom. Those states localize closely around the defect site. An additional donor state is created at about 0.25 eV above the VB maximum (spin minority channel), originating mostly from Cu  $d$  and  $\text{O}_{i-1}$   $p$  states.

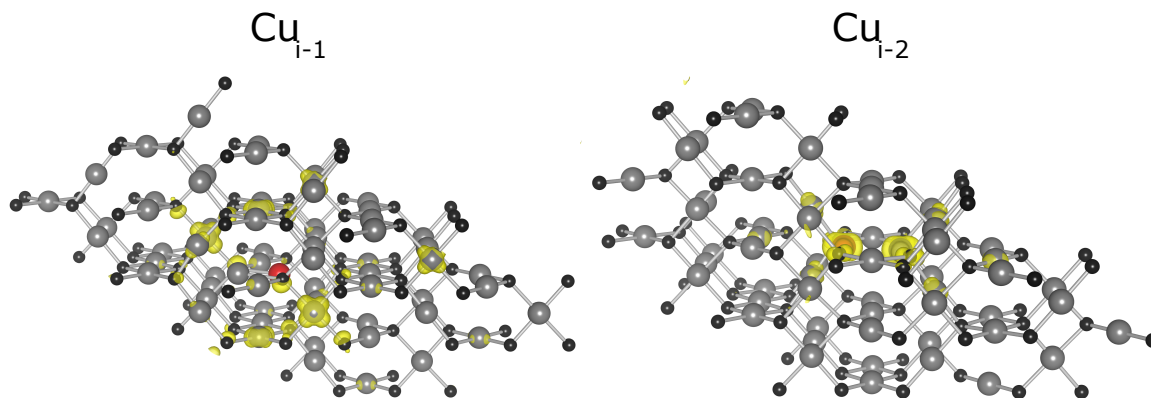


Figure 6.12: Partial charge densities of neutral interstitial Cu defects within  $\text{Cu}_4\text{O}_3$ . Selected states correspond to the donor states presented in Figure 6.11. Large grey spheres and small black spheres represent copper and oxygen atoms, while the red sphere distinguishes interstitial atoms. The yellow isosurface is shown at  $0.002 e/\text{\AA}^3$ .

In addition, a large magnetic moment of  $0.50 \mu_B$  is observed on the  $\text{O}_{i-1}$ , arising from the increased number of unpaired states in the electronic structure. Similarly, the Cu atoms closest to the defect site yield magnetic moments of  $0.28 \mu_B$ ,  $0.41 \mu_B$ ,  $0.05 \mu_B$ , and  $0.40 \mu_B$ , with respect to the charge values listed above.

Single interstitial O defects in configurations 2 and 3,  $\text{O}_{i-2}$  and  $\text{O}_{i-3}$ , relax in a way similar to that of  $\text{O}_{i-1}$ . However, a difference in the calculated formation energies is present, with values of 1.91 eV for  $\text{O}_{i-1}$  and 2.49 eV for  $\text{O}_{i-2}$  and  $\text{O}_{i-3}$ . These differences arise from distinct initial positions of the interstitial atoms in the simulation cell. Whilst  $\text{O}_{i-1}$  is already positioned closely to the final relaxed geometry,  $\text{O}_{i-2}$  and  $\text{O}_{i-3}$  are placed into the void where they have to follow a longer migration path to relax. Despite the symmetrical identical final location of the interstitial atom within the cell,  $\text{O}_{i-2}$  and  $\text{O}_{i-3}$  require more energy to form in order to overcome repulsion effects of the surrounding atoms.

**Trends in formation energies** Altogether, there is a peculiar interplay between the formation of defects and the conditions under which they are formed. In the narrow span of available synthesis conditions for  $\text{Cu}_4\text{O}_3$  (Cu-rich/O-poor as identified from the stability range), defects with the lowest formation energies are Cu interstitials (0.93 eV). Those defects, if found alone, would render the material intrinsically  $n$ -type. However, this is not observed experimentally, as  $\text{Cu}_4\text{O}_3$  is measured to have  $p$ -type conductivity. Does that imply that the theoretically obtained results are faulty? By looking at the rest of the available defects, the given statement can be revised as misleading. Namely, there are at least two other defects that can occur in  $\text{Cu}_4\text{O}_3$ , together with interstitial Cu. These are Cu and O vacancies. Their respective formation energies of 1.31 eV and 1.49 eV hint towards a competitive manifestation within the

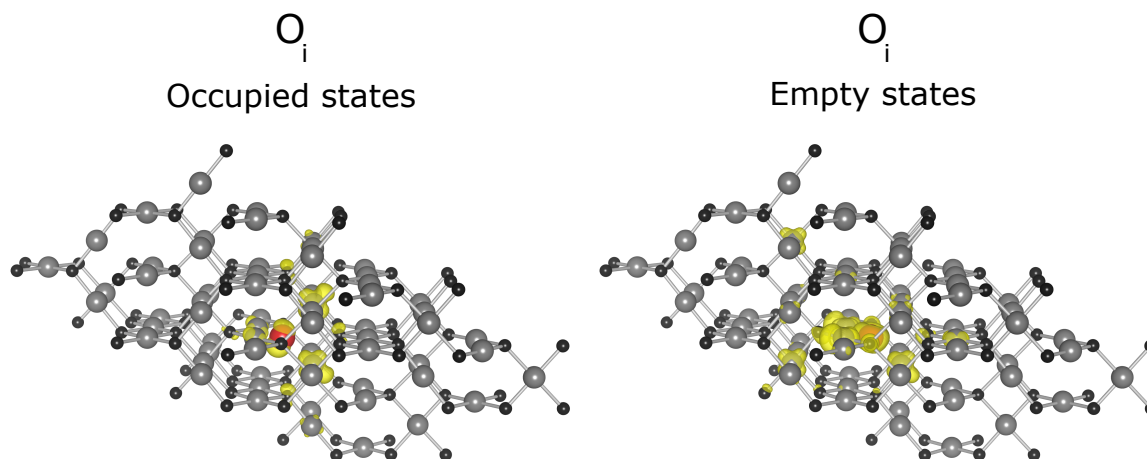


Figure 6.13: Partial charge densities of neutral interstitial O defects within  $\text{Cu}_4\text{O}_3$ . Selected states correspond to the donor states presented in Figure 6.11. Large grey spheres and small black spheres represent copper and oxygen atoms, while the red sphere distinguishes interstitial atoms. The yellow isosurface is shown at  $0.002 e/\text{\AA}^3$ .

crystal.

Furthermore, once the formation conditions are altered from the pinpointed Cu-rich/O-poor one, defect formation energies change drastically. To confirm this, defect formation energies were calculated at  $\Delta\mu_{\text{Cu}} = 0$ ,  $\Delta\mu_{\text{O}} = 0$ , and they are plotted in Figure 6.5. For this case, the dominant defects are O interstitials, with a formation energy below 0.47 eV, followed by Cu interstitials with 0.77 eV. This implies readily formation of intrinsic impurities within  $\text{Cu}_4\text{O}_3$ , converting the material effectively towards  $\text{Cu}_2\text{O}$  or  $\text{CuO}$ , corresponding to experimentally observed mixed phased paramelaconite. Calculated available interstitial defect sites within the cell correlate to those discussed earlier, with  $\text{CuO}$  deriving from  $\text{Cu}_4\text{O}_3$  by ordered insertion of O atoms and  $\text{Cu}_2\text{O}$  by controlled addition of O atoms. Also, the interstitial O defect contributes additional holes (acceptor states) to the system, resulting in it being *p*-type doped – intrinsic conductivity of both  $\text{Cu}_2\text{O}$  and  $\text{CuO}$ .

## 6.3 Conclusion

The ground state properties and native point impurities of  $\text{Cu}_4\text{O}_3$  were modelled using density functional theory calculations. A comparison of multiple approximations of the exchange correlation functional was carried out, based on determined electronic and optical properties. The stability region of  $\text{Cu}_4\text{O}_3$  was assessed, as a function of the chemical potentials of the constituent species. Based on the analysis outlined, several significant findings were concluded:

- Global range hybrid functionals outperform their range-separated analogues in the case of  $\text{Cu}_4\text{O}_3$ , where results close to experimental ones were obtained using

B3LYP-based calculations with a self-consistently determined amount of exact exchange within.

- $\text{Cu}_4\text{O}_3$  is found thermodynamically stable in a very narrow range of accessible chemical potentials. This corroborates the experimentally noted sensitivity upon synthesis conditions.
- Intrinsic impurities form easily in  $\text{Cu}_4\text{O}_3$ , even under applied stability boundaries. Stepping away from those conditions, secondary phases start occurring, in this case  $\text{Cu}_2\text{O}$  and  $\text{CuO}$ .
- Pure  $\text{Cu}_4\text{O}_3$  is postulated to be intrinsically  $n$ -type, based on formation energies of the lowest accessible impurities (Cu interstitials). However, several other defects are identified having comparatively close energies, creating a competitive interplay amongst them.

However, whilst interpreting results outlined in this Chapter, several limitations apply. Thermodynamic stability conditions as well as defect related properties (formation energies, migration barriers, etc.) depend on temperature effects, whose extent is inaccessible within the given theoretical framework. Despite those obvious constraints, the values obtained give valuable insights into difficulties related to obtaining pure  $\text{Cu}_4\text{O}_3$  and maintaining it stable over longer periods of time.



## Summary and future work

*"The time is gone, the song is over,  
Thought I'd something more to say."*

---

Pink Floyd - Time,  
*The Dark Side of the Moon* (1973)

Using quantum mechanical theoretical calculations based on density functional theory, three copper oxides were studied in order to gain insight into their electronic structure and potential photovoltaic usability. First, the search for a set of unique parameters that would describe  $\text{Cu}_2\text{O}$ ,  $\text{Cu}_4\text{O}_3$ , and  $\text{CuO}$  simultaneously at a desired accuracy was undertaken. This has proven to be a *"wild goose chase"*, as those three materials show properties mutually excluding any common set of parameters in use. For  $\text{Cu}_2\text{O}$ , DFT and DFT+ $U$  (in any fashion) fail to give satisfactory results for the electronic band structure. Hybrid-DFT, as used here in the form of HSE06 (default 25 % of exact exchange), is able to yield results in good agreement with experimentally available low temperature data. For  $\text{Cu}_4\text{O}_3$ , DFT gives fully metallic, while DFT+ $U$  captures the true semiconducting nature, yet underestimating the indirect value of the electronic band gap (which is also a matter of debate). Surprisingly, in the case of  $\text{Cu}_4\text{O}_3$ , a global hybrid functional (with a tuned exact exchange value – not default one) seems to outperform range-separated ones when reproducing the electronic band gap. DFT gives similar unsatisfactory metallic behaviour for  $\text{CuO}$ , while DFT+ $U$  and HSE are able to capture the correct magnetic and electronic behaviour at the ground state level. Up to now, there is little evidence of DFT+ $U$  outperforming HSE or vice-versa, however careful tuning is needed according to the type of simulation one is setting up.

Despite the outlined difficulties, using HSE06 as a common functional leads to results in fair agreement for the optical properties of  $\text{Cu}_2\text{O}$ ,  $\text{Cu}_4\text{O}_3$ , and  $\text{CuO}$ . The

simulated absorption spectra as well as calculated selection rules were used successfully in the spectroscopic maximum limited efficiency metric, upon which suitable photovoltaic materials can be identified, to obtain the conversion efficiency of copper oxides when utilized as thin film absorbers. The results were found in good agreement with available literature data, namely low efficiency (1 – 2 %) for  $\text{Cu}_2\text{O}$ , somehow increased efficiency (2 – 3 %) for  $\text{Cu}_4\text{O}_3$ , and hardly any efficiency for  $\text{CuO}$ . These revised maximum conversion values bridge the gap between the previously proposed efficiencies of 20 % for  $\text{Cu}_2\text{O}$  and 30 % for  $\text{CuO}$ , based on the standard Shockley-Queisser predictor, and the low experimentally measured output values. Without denying the negativeness connected with those results, one can rather think of it as solid platform for improvement, as the efficiency values have simply "no where to go but up."

One approved method for boosting the performance of thin film absorbers is via the introduction of extrinsic impurities into the pristine material's matrix. A systematic computational study within a hybrid DFT formalism of the electronic and optical properties of transition metal-doped  $\text{Cu}_2\text{O}$  was carried out. Additional copper vacancies, responsible for the  $p$ -type conductivity of  $\text{Cu}_2\text{O}$ , were also considered in order to mimic conditions closer to experimental ones. Extrinsic transition metal dopants were found to increase substantially the capacity of  $\text{Cu}_2\text{O}$  to absorb light, reaching photovoltaic conversion efficiency values close to 10 %, attributed to the bypassing effect of impurity levels on the optical transition selection rules. Outlined results, despite obvious limitations such as lack of temperature or interface effects, correspond well to experimentally observed phenomena where for instance Zn- or Fe-doped  $\text{Cu}_2\text{O}$  films have already shown considerable improvement in conversion efficiency or optical transmittance.

Similar studies for  $\text{Cu}_4\text{O}_3$  and  $\text{CuO}$  could not have been performed due to the increased complexity/inaccuracy associated with the modelling of indirect electronic band gap absorption spectra. Instead, the focus was shifted to establish a model that is as accurate as possible for the ground state, in the first place, and then to probe the intrinsic defect properties of the material at hand. For  $\text{CuO}$ , a comparative study between a DFT+ $U$  and HSE model was undertaken and both were found to reproduce the ground state properties satisfactory. Compared to  $\text{Cu}_2\text{O}$ , who shows only  $p$ -type,  $\text{CuO}$  was confirmed to support  $p$ -type as well as  $n$ -type conductivity originating from opposite intrinsic defects, depending on the growth conditions enforced. The source of  $p$ -type conductivity was assigned (earlier) to Cu vacancies present, while the source of  $n$ -type was linked to O vacancies as well as interstitial Cu atoms, matching well experimentally observed behaviour. The issue regarding photovoltaic employment of  $\text{CuO}$  as an effective absorber was elucidated through electronic structure calculations, as all of the defects, responsible for the associated intrinsic behaviour, were found to

lie deep in the electronic gap (deep states), acting as radiative and non-radiative recombination centres. Defects were also found to prefer clustering over their dispersed analogues and hydrogen was tested as an eventual passivation promoter. In  $p$ -type, incorporating H is energetically extremely favourable and its effect is to remove the deep states present in the electronic band diagram. On the other hand, in  $n$ -type, incorporating H leads to a competitive interplay between intrinsic defects, compensating hence the rendered conductivity.

And finally, in the case of  $\text{Cu}_4\text{O}_3$  an additional difficulty experienced has been the lack of reliable experimental data. Nevertheless, working with the current state of literature lead to the use of a global hybrid DFT model (B3LYP in the particular case, amount of exchange determined self-consistently) to represent the magnetic ground state properties accurately.  $\text{Cu}_4\text{O}_3$  is found thermodynamically stable within in a very narrow range of accessible chemical potentials with Cu vacancies, O vacancies, as well as Cu interstitials having the lowest defect formation energies and manifesting themselves competitively. This corroborates the experimentally noted sensitivity upon synthesis conditions.

**Future work** *Where to go from here?* Results outlined within this work are by far not perfect or flawless. Apart from seeking for future experimental verification or routing, there are a few theoretical techniques that can bring the results further and can give additional insights into the likely performance of copper oxides as solar cell materials. In order to understand the driving force behind ionic and electronic charge carriers, a fundamental band alignment is desired. A band alignment will always take place at the boundary conditions imposed on a particular interface and will dominate the photoactive or photocatalytic activity. Such alignments can be done computationally from the electronic structure of bulk crystals, electrostatic analysis of the corresponding environments, or absolute vacuum alignments from embedded crystals.

Further, in semiconductors or insulators, defects mostly appear in charged states, which play an important role in the carrier generation and compensation. Such calculations can be undertaken from the respective total DFT energies of defects in different charge states to evaluate either thermodynamic or optic transition levels. Those can help clarify the charge conversion issue, in particular for CuO and  $\text{Cu}_4\text{O}_3$ . Effective electron and hole masses could be added on top of that, as they are decisive factors affecting carrier mobilities – some of the crucial concepts in the background of successful photovoltaic applications. Further, it would be advisable to include phonon-assisted effect into the calculations, especially for indirect electronic band gap materials, as they accurately determine the onset of absorption and indirect absorption coefficients.

Hopefully this work shall stimulate further interest, discussion, research through both experimental work as well as theoretical investigation to indeed exhaust the full spectrum of possibilities copper oxides have to offer as potential photovoltaic absorbing materials.

## Bibliography

- [1] P. Würfel, U. Würfel, *Physics of solar cells : from basic principles to advanced concepts*, Wiley-VCH, Weinheim, **2009**.
- [2] C. Honsberg, S. Bowden, Photovoltaic Education Website, **2019**.
- [3] H. Ritchie, M. Roser, *Our World Data* **2019**.
- [4] R. Wick, S. D. Tilley, *J. Phys. Chem. C* **2015**, *119*, 26243–26257.
- [5] R. Singh, G. F. Alapatt, A. Lakhtakia, *IEEE J. Electron Devices Soc.* **2013**, *1*, 129–144.
- [6] S. Rühle, A. Y. Anderson, H.-N. Barad, B. Kupfer, Y. Bouhadana, E. Rosh-Hodesh, A. Zaban, *J. Phys. Chem. Lett.* **2012**, *3*, 3755–3764.
- [7] C. Jayathilaka, V. Kapaklis, W. Siripala, S. Jayanetti, *Appl. Phys. Express* **2015**, *8*, 065503.
- [8] W. Shockley, H. J. Queisser, *J. Appl. Phys.* **1961**, *32*, 510–519.
- [9] *Fundamentals of Time-Dependent Density Functional Theory*, (Eds.: M. A. Marques, N. T. Maitra, F. M. Nogueira, E. Gross, A. Rubio), Springer Berlin Heidelberg, Berlin, Heidelberg, **2012**.
- [10] F. Jensen, *Introduction to Computational Chemistry*, **2007**, p. 624.
- [11] W. Koch, M. C. Holthausen, *A Chemist's Guide to Density Functional Theory*, Vol. 3, **2001**, p. 294.
- [12] P. Hohenberg, W. Kohn, *Phys. Rev.* **1964**, *136*, B864–B871.
- [13] W. Kohn, L. J. Sham, *Phys. Rev.* **1965**, *140*, DOI 10.1103/PhysRev.140.A1133.
- [14] R. M. Martin, *Electronic Structure: Basic Theory and Practical Methods*, Cambridge University Press, Cambridge, **2004**, p. 648.

- [15] C. G. Van de Walle, A. Janotti, *Advances in Electronic Structure Methods for Defects and Impurities in Solids*, **2011**.
- [16] S. L. Dudarev, G. A. Botton, S. Y. Savrasov, C. J. Humphreys, a. P. Sutton, *Phys. Rev. B* **1998**, *57*, 1505–1509.
- [17] V. I. Anisimov, I. V. Solovyev, M. A. Korotin, M. T. Czyżyk, G. A. Sawatzky, *Phys. Rev. B* **1993**, *48*, 16929–16934.
- [18] A. I. Liechtenstein, V. I. Anisimov, J. Zaanen, *Phys. Rev. B* **1995**, *52*, R5467–R5470.
- [19] J. Heyd, G. E. Scuseria, M. Ernzerhof, *J. Chem. Phys.* **2003**, *118*, 8207–8215.
- [20] J. Heyd, G. E. Scuseria, *J. Chem. Phys.* **2004**, *121*, 1187–1192.
- [21] J. Heyd, G. E. Scuseria, M. Ernzerhof, *J. Chem. Phys.* **2006**, *124*, 219906.
- [22] H. J. Monkhorst, J. D. Pack, *Phys. Rev. B* **1976**, *13*, 5188–5192.
- [23] J.-L. Bredas, *Mater. Horiz.* **2014**, *1*, 17–19.
- [24] P. Muller, *Pure Appl. Chem.* **1994**, *66*, (Eds.: M. Nič, J. Jiráť, B. Košata, A. Jenkins, A. McNaught), 1077–1184.
- [25] A. Kahn, *Mater. Horizons* **2016**, *3*, 7–10.
- [26] E. J. Baerends, *J. Chem. Phys.* **2018**, *149*, 054105.
- [27] J. P. Perdew, W. Yang, K. Burke, Z. Yang, E. K. U. Gross, M. Scheffler, G. E. Scuseria, T. M. Henderson, I. Y. Zhang, A. Ruzsinszky, H. Peng, J. Sun, E. Trushin, A. Görling, *Proc. Natl. Acad. Sci.* **2017**, *114*, 2801–2806.
- [28] M. D. McCluskey, E. E. Haller, *Dopants and Defects in Semiconductors*, First Edit, (Eds.: L. Han, L. Leggio), CRC Press, Boca Raton, **2012**, p. 349.
- [29] C. Freysoldt, B. Grabowski, T. Hickel, J. Neugebauer, G. Kresse, A. Janotti, C. G. Van De Walle, *Rev. Mod. Phys.* **2014**, *86*, 253–305.
- [30] S. B. Zhang, J. E. Northrup, *Phys. Rev. Lett.* **1991**, *67*, 2339–2342.
- [31] C. G. Van De Walle, J. Neugebauer, *J. Appl. Phys.* **2004**, *95*, 3851–3879.
- [32] L.-s. Wang, H. Wu, S. R. Desai, L. Lou, *Phys. Rev. B* **1996**, *53*, 8028–8031.
- [33] K. H. L. Zhang, K. Xi, M. G. Blamire, R. G. Egdell, *J. Phys. Condens. Matter* **2016**, *28*, 383002.
- [34] Y. Peng, Z. Zhang, T. Viet Pham, Y. Zhao, P. Wu, J. Wang, *J. Appl. Phys.* **2012**, *111*, 103708.
- [35] T. Wong, S. Zhuk, S. Masudy-Panah, G. Dalapati, *Materials (Basel)*. **2016**, *9*, 271.

- [36] A. Y. Anderson, Y. Bouhadana, H. N. Barad, B. Kupfer, E. Rosh-Hodesh, H. Aviv, Y. R. Tischler, S. Rühle, A. Zaban, *ACS Comb. Sci.* **2014**, *16*, 53–65.
- [37] T. Minami, Y. Nishi, T. Miyata, *Appl. Phys. Express* **2013**, *6*, 044101.
- [38] B. K. Meyer, A. Polity, D. Reppin, M. Becker, P. Hering, P. J. Klar, T. Sander, C. Reindl, J. Benz, M. Eickhoff, C. Heiliger, M. Heinemann, J. Bläsing, A. Krost, S. Shokovets, C. Müller, C. Ronning, *Phys. Status Solidi* **2012**, *249*, 1487–1509.
- [39] L. O. Grondahl, *Rev. Mod. Phys.* **1933**, *5*, 141–168.
- [40] D. R. Lide, *CRC Handbook of Chemistry and Physics, Internet Version 2005*, CRC Press, Boca Raton, Fl, **2005**.
- [41] J. S. Anderson, N. N. Greenwood, *Proc. R. Soc. London. Ser. A. Math. Phys. Sci.* **1952**, *215*, 353–370.
- [42] T. Ito, H. Yamaguchi, K. Okabe, T. Masumi, *J. Mater. Sci.* **1998**, *33*, 3555–3566.
- [43] S. Chatterjee, S. K. Saha, A. J. Pal, *Sol. Energy Mater. Sol. Cells* **2016**, *147*, 17–26.
- [44] A. Werner, H. D. Hochheimer, *Phys. Rev. B* **1982**, *25*, 5929–5934.
- [45] D.-D. Wang, F.-Z. Zhou, J.-X. Cao, L.-B. Li, G.-L. Li, *Curr. Appl. Phys.* **2017**, *17*, 781–784.
- [46] R. J. Elliott, *Phys. Rev.* **1961**, *124*, 340–345.
- [47] L. Olsen, F. Addis, W. Miller, *Sol. Cells* **1982**, *7*, 247–279.
- [48] T. Ito, H. Yamaguchi, T. Masumi, S. Adachi, Optical Properties of CuO Studied by Spectroscopic Ellipsometry, **1998**.
- [49] J. Ghijsen, L. Tjeng, J. van Elp, H. Eskes, J. Westerink, G. Sawatzky, M. Czyzyk, *Phys. Rev. B* **1988**, *38*, 11322–11330.
- [50] Y. Wang, P. Miska, D. Pilloud, D. Horwat, F. Mücklich, J. F. Pierson, *J. Appl. Phys.* **2014**, *115*, 073505.
- [51] D. S. Murali, S. Kumar, R. J. Choudhary, A. D. Wadikar, M. K. Jain, A. Subrahmanyam, *AIP Adv.* **2015**, *5*, 047143.
- [52] R. J. Elliott, *Phys. Rev.* **1957**, *108*, 1384–1389.
- [53] J. W. Hodby, T. E. Jenkins, C. Schwab, H. Tamura, D. Trivich, *J. Phys. C Solid State Phys.* **1976**, *9*, 1429–1439.
- [54] F. Biccari, PhD thesis, PhD Thesis, Sapienza - University of Rome, **2009**, p. 262.

- [55] C. Malerba, F. Biccari, C. Leonor Azanza Ricardo, M. D’Incau, P. Scardi, A. Mittiga, *Sol. Energy Mater. Sol. Cells* **2011**, *95*, 2848–2854.
- [56] Y. Zhuze, B. Kurchatov, *Phys. Z. Sowjetunion* **1932**, *2*, 453–467.
- [57] M. Nolan, S. D. Elliott, *Phys. Chem. Chem. Phys.* **2006**, *8*, 5350–5358.
- [58] D. Hartung, F. Gather, P. Hering, C. Kandzia, D. Reppin, A. Polity, B. K. Meyer, P. J. Klar, *Appl. Phys. Lett.* **2015**, *106*, 253901.
- [59] A. Musa, T. Akomolafe, M. Carter, *Sol. Energy Mater. Sol. Cells* **1998**, *51*, 305–316.
- [60] L. Zhang, L. McMillon, J. McNatt, *Sol. Energy Mater. Sol. Cells* **2013**, *108*, 230–234.
- [61] G. Paul, R. Ghosh, S. Bera, S. Bandyopadhyay, T. Sakurai, K. Akimoto, *Chem. Phys. Lett.* **2008**, *463*, 117–120.
- [62] J. Dahl, A. Switendick, *J. Phys. Chem. Solids* **1966**, *27*, 931–942.
- [63] L. Kleinman, K. Mednick, *Phys. Rev. B* **1980**, *21*, 1549–1553.
- [64] W. Y. Ching, Y. N. Xu, K. W. Wong, *Phys. Rev. B* **1989**, *40*, 7684–7695.
- [65] J. Robertson, *Phys. Rev. B* **1983**, *28*, 3378–3385.
- [66] P. Marksteiner, P. Blaha, K. Schwarz, *Zeitschrift fur Phys. B Condens. Matter* **1986**, *64*, 119–127.
- [67] E. Ruiz, S. Alvarez, P. Alemany, R. a. Evarestov, *Phys. Rev. B* **1997**, *56*, 7189–7196.
- [68] L. Y. Isseroff, E. A. Carter, *Phys. Rev. B* **2012**, *85*, 235142.
- [69] S. Lany, *Phys. Rev. B* **2013**, *87*, 085112.
- [70] A. Martinez-Ruiz, M. Moreno, N. Takeuchi, *Solid State Sci.* **2003**, *5*, 291–295.
- [71] Y. Jiang, J. B. Adams, D. Sun, *J. Phys. Chem. B* **2004**, *108*, 12851–12857.
- [72] A. Soon, T. Söhnel, H. Idriss, *Surf. Sci.* **2005**, *579*, 131–140.
- [73] A. Soon, M. Todorova, B. Delley, C. Stampfl, *Phys. Rev. B - Condens. Matter Mater. Phys.* **2006**, *73*, 1–12.
- [74] L. K. Dash, F. Bruneval, V. Trinité, N. Vast, L. Reining, *Comput. Mater. Sci.* **2007**, *38*, 482–493.
- [75] M. Nolan, S. D. Elliott, *Thin Solid Films* **2008**, *516*, 1468–1472.
- [76] M. M. Islam, B. Diawara, V. Maurice, P. Marcus, *J. Mol. Struct. THEOCHEM* **2009**, *903*, 41–48.

- [77] D. O. Scanlon, G. W. Watson, *J. Phys. Chem. Lett.* **2010**, *1*, 2582–2585.
- [78] X.-G. G. Yan, L. Xu, W.-Q. Q. Huang, G.-F. F. Huang, Z.-M. M. Yang, S.-Q. Q. Zhan, J.-P. P. Long, *Mater. Sci. Semicond. Process.* **2014**, *23*, 34–41.
- [79] J. B. Forsyth, S. Hull, *J. Phys. Condens. Matter* **1991**, *3*, 5257–5261.
- [80] H. Yamada, X.-G. Zheng, Y. Soejima, M. Kawaminami, *Phys. Rev. B* **2004**, *69*, 104104.
- [81] M. Heinemann, B. Eifert, C. Heiliger, *Phys. Rev. B* **2013**, *87*, 115111.
- [82] S. [Adot]rsbrink, L. Gerward, J. S. Olsen, S. Steenstrup, *High Press. Res.* **1992**, *10*, 515–521.
- [83] L. C. Bourne, P. Y. Yu, A. Zettl, M. L. Cohen, *Phys. Rev. B* **1989**, *40*, 10973–10976.
- [84] Z. Wang, V. Pishedda, S. Saxena, P. Lazor, *Solid State Commun.* **2002**, *121*, 275–279.
- [85] D. P. Kozlenko, K. Drużbicki, S. E. Kichanov, E. V. Lukin, H.-P. Liermann, K. V. Glazyrin, B. N. Savenko, *Phys. Rev. B* **2017**, *95*, 054115.
- [86] F. P. Koffyberg, F. A. Benko, *J. Appl. Phys.* **1982**, *53*, 1173–1177.
- [87] D. Tahir, S. Tougaard, *J. Phys. Condens. Matter* **2012**, *24*, 175002.
- [88] S. C. Ray, *Sol. Energy Mater. Sol. Cells* **2001**, *68*, 307–312.
- [89] F. Marabelli, G. B. Parravicini, F. Salghetti-Drioli, *Phys. Rev. B* **1995**, *52*, 1433–1436.
- [90] F. Marabelli, G. B. Parravicini, *Phys. B Condens. Matter* **1994**, *199-20*, 255–256.
- [91] Y. Sukhorukov, N. Loshkareva, A. Moskvin, V. Arbutov, S. Naumov, *Tech. Phys. Lett.* **1998**, *24*, 5–7.
- [92] H. Q. Nguyen, D. Van Nguyen, A. Fujiwara, B. N. Q. Trinh, *Thin Solid Films* **2018**, *660*, 819–823.
- [93] R. Singh, L. Yadav, Shrey, T. Shweta, *Thin Solid Films* **2019**, *685*, 195–203.
- [94] T. Tanaka, *Jpn. J. Appl. Phys.* **1979**, *18*, 1043–1047.
- [95] B. X. Yang, J. M. Tranquada, G. Shirane, *Phys. Rev. B* **1988**, *38*, 174–178.
- [96] J. B. Forsyth, P. J. Brown, B. M. Wanklyn, *J. Phys. C Solid State Phys.* **1988**, *21*, 2917–2929.
- [97] B. X. Yang, T. R. Thurston, J. M. Tranquada, G. Shirane, *Phys. Rev. B* **1989**, *39*, 4343–4349.

- [98] T. Kimura, Y. Sekio, H. Nakamura, T. Siegrist, A. P. Ramirez, *Nat. Mater.* **2008**, *7*, 291–294.
- [99] C. Rödl, F. Sottile, L. Reining, *Phys. Rev. B* **2015**, *91*, 045102.
- [100] P. Isherwood, J. Walls, *Energy Procedia* **2014**, *60*, 129–134.
- [101] Y. Du, X. Gao, X. Meng, *Phys. B Condens. Matter* **2019**, *560*, 37–40.
- [102] Ş. Baturay, A. Tombak, D. Batibay, Y. S. Ocak, *Appl. Surf. Sci.* **2019**, *477*, 91–95.
- [103] D. Wu, Q. Zhang, M. Tao, *Phys. Rev. B* **2006**, *73*, 235206.
- [104] C. Ekuma, V. Anisimov, J. Moreno, M. Jarrell, *Eur. Phys. J. B* **2014**, *87*, 23.
- [105] X. Rocquefelte, M.-H. Whangbo, A. Villesuzanne, S. Jobic, F. Tran, K. Schwarz, P. Blaha, *J. Phys. Condens. Matter* **2010**, *22*, 045502.
- [106] X. Rocquefelte, K. Schwarz, P. Blaha, *Sci. Rep.* **2012**, *2*, 759.
- [107] C. Frondel, *Am. Mineral.* **1941**, *26*, 657–672.
- [108] N. Datta, J. W. Jeffery, *Acta Crystallogr. Sect. B* **1978**, *34*, 22–26.
- [109] M. O’keeffe, J.-O. Bovin, *Am. Mineral.* **1978**, *63*, 180–185.
- [110] M. O’keeffe, F. Stone, *J. Phys. Chem. Solids* **1962**, *23*, 261–266.
- [111] P. E. Morgan, D. E. Partin, B. L. Chamberland, M. O’Keeffe, *J. Solid State Chem.* **1996**, *121*, 33–37.
- [112] J. F. Pierson, A. Thobor-Keck, A. Billard, *Appl. Surf. Sci.* **2003**, *210*, 359–367.
- [113] A. Thobor, J. Pierson, *Mater. Lett.* **2003**, *57*, 3676–3680.
- [114] D. Djurek, M. Prester, D. Drobac, M. Ivanda, D. Vojta, *J. Magn. Magn. Mater.* **2015**, *373*, 183–187.
- [115] D. S. Murali, A. Subrahmanyam, *J. Phys. D. Appl. Phys.* **2016**, *49*, 375102.
- [116] D. S. Murali, S. Aryasomayajula, *Appl. Phys. A* **2018**, *124*, 279.
- [117] W. Wang, L. Zhu, P. Lv, G. Liu, Y. Yu, J. Li, *ACS Appl. Mater. Interfaces* **2018**, *10*, 37287–37297.
- [118] D. Reppin, A. Polity, B. Meyer, S. Shokovets, *Mater. Res. Soc. Symp. Proc. Vol.* **2012**, *1494*, 25–31.
- [119] H. S. Kim, P. Yadav, M. Patel, J. Kim, K. Pandey, D. Lim, C. Jeong, *Superlattices Microstruct.* **2017**, *112*, 262–268.
- [120] L. Pinsard-Gaudart, J. Rodríguez-Carvajal, A. Gukasov, P. Monod, *Phys. Rev. B* **2004**, *69*, 104408.

- [121] E. M. Tejada-Rosales, J. Rodríguez-Carvajal, N. Casañ-Pastor, P. Alemany, E. Ruiz, M. S. El-Fallah, S. Alvarez, P. Gómez-Romero, *Inorg. Chem.* **2002**, *41*, 6604–6613.
- [122] L. Debbichi, M. C. Marco de Lucas, J. F. Pierson, P. Kruger, *J. Phys. Chem. C* **2012**, *116*, 10232–10237.
- [123] L. Debbichi, M. C. Marco de Lucas, P. Krüger, *Mater. Chem. Phys.* **2014**, *148*, 293–298.
- [124] Y. Wang, S. Lany, J. Ghanbaja, Y. Fagot-Revurat, Y. P. Chen, F. Soldera, D. Horwat, F. Mücklich, J. F. Pierson, *Phys. Rev. B* **2016**, *94*, 245418.
- [125] L. C. Olsen, R. C. Bohara, M. W. Urie, *Appl. Phys. Lett.* **1979**, *34*, 47–49.
- [126] D. Ursu, N. Miclau, M. Miclau, *Electron. Mater. Lett.* **2018**, *14*, 405–412.
- [127] D. O. Scanlon, G. W. Watson, *Phys. Rev. Lett.* **2011**, *106*, 186403.
- [128] H.-s. Kim, M. David, W.-h. Park, M. Patel, J. Kim, *Sensors Actuators A Phys.* **2016**, *253*, 35–40.
- [129] B. J. Morgan, D. O. Scanlon, G. W. Watson, *e-Journal Surf. Sci. Nanotechnol.* **2009**, *7*, 389–394.
- [130] L. Hedin, *Phys. Rev.* **1965**, *139*, A796–A823.
- [131] L. Hedin, S. Lundqvist in *Solid State Phys. Vol. 23*, Academic Press, **1970**, pp. 1–181.
- [132] G. Kresse, J. Furthmüller, *Comput. Mater. Sci.* **1996**, *6*, 15–50.
- [133] G. Kresse, J. Furthmüller, *Phys. Rev. B* **1996**, *54*, 11169–11186.
- [134] P. E. Blöchl, *Phys. Rev. B* **1994**, *50*, 17953–17979.
- [135] G. Kresse, D. Joubert, *Phys. Rev. B* **1999**, *59*, 1758–1775.
- [136] J. P. Perdew, K. Burke, M. Ernzerhof, *Phys. Rev. Lett.* **1996**, *77*, 3865–3868.
- [137] V. I. Anisimov, J. Zaanen, O. K. Andersen, *Phys. Rev. B* **1991**, *44*, 943–954.
- [138] V. I. Anisimov, F. Aryasetiawan, A. I. Lichtenstein, *J. Phys. Condens. Matter* **1997**, *9*, 767–808.
- [139] S. Grimme, J. Antony, S. Ehrlich, H. Krieg, *J. Chem. Phys.* **2010**, *132*, 154104.
- [140] M. I. Aroyo, J. M. Perez-Mato, C. Capillas, E. Kroumova, S. Ivantchev, G. Madariaga, A. Kirov, H. Wondratschek, *Zeitschrift für Krist. - Cryst. Mater.* **2006**, *221*, DOI 10.1524/zkri.2006.221.1.15.
- [141] M. I. Aroyo, A. Kirov, C. Capillas, J. M. Perez-Mato, H. Wondratschek, *Acta Crystallogr. Sect. A Found. Crystallogr.* **2006**, *62*, 115–128.

- [142] M. I. Aroyo, J. M. Perez-Mato, D. Orobengoa, E. Tasci, G. De La Flor, A. Kirov, *Bulg. Chem. Commun.* **2011**, *43*, 183–197.
- [143] A. A. Mostofi, J. R. Yates, G. Pizzi, Y.-S. Lee, I. Souza, D. Vanderbilt, N. Marzari, *Comput. Phys. Commun.* **2014**, *185*, 2309–2310.
- [144] K. Momma, F. Izumi, *J. Appl. Crystallogr.* **2011**, *44*, 1272–1276.
- [145] L. Yu, A. Zunger, *Phys. Rev. Lett.* **2012**, *108*, 068701.
- [146] Y. Le Page, P. Saxe, *Phys. Rev. B* **2001**, *63*, 174103.
- [147] M. Gajdoš, K. Hummer, G. Kresse, J. Furthmüller, F. Bechstedt, *Phys. Rev. B* **2006**, *73*, 045112.
- [148] M. Green, *Third Generation Photovoltaics*, Springer Berlin Heidelberg, **2003**.
- [149] Y.-Y. Yu, W.-C. Chien, Y.-J. Wang, *Thin Solid Films* **2016**, *618*, 134–140.
- [150] N. N. Greenwood, A. Earnshaw in *Chem. Elem.* Elsevier, **1997**, pp. 1173–1200.
- [151] M. Ohashi, A. Tashiro, G. Oomi, E. Maeda, X.-G. Zheng, *Phys. Rev. B* **2006**, *73*, 134421.
- [152] V. Belomestnykh, E. Soboleva, *Appl. Mech. Mater.* **2014**, *682*, 170–173.
- [153] F. Birch, *Phys. Rev.* **1947**, *71*, 809–824.
- [154] N. N. Liu, J. L. Sun, D. Wu, *Adv. Mater. Res.* **2011**, *335-336*, 328–332.
- [155] M. Yovanovich in 44th AIAA Aerosp. Sci. Meet. Exhib. American Institute of Aeronautics and Astronautics, Reston, Virginia, **2006**, pp. 1–28.
- [156] D. O. Scanlon, B. J. Morgan, G. W. Watson, A. Walsh, *Phys. Rev. Lett.* **2009**, *103*, 096405.
- [157] D. O. Scanlon, B. J. Morgan, G. W. Watson, *J. Chem. Phys.* **2009**, *131*, 124703.
- [158] F. Schweiner, J. Main, G. Wunner, C. Uihlein, *Phys. Rev. B* **2017**, *95*, 195201.
- [159] J. Thewes, J. Heckötter, T. Kazimierczuk, M. Aßmann, D. Fröhlich, M. Bayer, M. A. Semina, M. M. Glazov, *Phys. Rev. Lett.* **2015**, *115*, 027402.
- [160] H. Fan, B. Zou, Y. Liu, S. Xie, *Nanotechnology* **2006**, *17*, 1099–1103.
- [161] U. Köbler, T. Chattopadhyay, *Zeitschrift für Phys. B Condens. Matter* **1991**, *82*, 383–386.
- [162] J. Noffsinger, E. Kioupakis, C. G. Van De Walle, S. G. Louie, M. L. Cohen, *Phys. Rev. Lett.* **2012**, *108*, 20–24.
- [163] F. Giustino, *Rev. Mod. Phys.* **2017**, *89*, 015003.
- [164] S. Poncé, E. Margine, C. Verdi, F. Giustino, *Comput. Phys. Commun.* **2016**, *209*, 116–133.

- [165] M. A. Green, *Sol. Energy Mater. Sol. Cells* **2008**, *92*, 1305–1310.
- [166] S. Masudy-Panah, G. K. Dalapati, K. Radhakrishnan, A. Kumar, H. R. Tan, E. Naveen Kumar, C. Vijila, C. C. Tan, D. Chi, *Prog. Photovoltaics Res. Appl.* **2015**, *23*, 637–645.
- [167] Q. Bai, W. Wang, Q. Zhang, M. Tao, *J. Appl. Phys.* **2012**, *111*, 023709.
- [168] S. K. Wallace, D. B. Mitzi, A. Walsh, *ACS Energy Lett.* **2017**, *2*, 776–779.
- [169] R. E. Brandt, J. R. Poindexter, P. Gorai, R. C. Kurchin, R. L. Z. Hoye, L. Nienhaus, M. W. B. Wilson, J. A. Polizzotti, R. Sereika, R. Žaltauskas, L. C. Lee, J. L. MacManus-Driscoll, M. Bawendi, V. Stevanović, T. Buonassisi, *Chem. Mater.* **2017**, *29*, 4667–4674.
- [170] A. Jain, Y. Shin, K. A. Persson, *Nat. Rev. Mater.* **2016**, *1*, 15004.
- [171] Q. Huang, J. Li, X. Bi, *J. Alloys Compd.* **2015**, *647*, 585–589.
- [172] S. S. Wilson, J. P. Bosco, Y. Tolstova, D. O. Scanlon, G. W. Watson, H. A. Atwater, *Energy Environ. Sci.* **2014**, *7*, 3606–3610.
- [173] N. Zhang, J. Sun, H. Gong, *Coatings* **2019**, *9*, 137.
- [174] J. Linnera, A. J. Karttunen, *Phys. Rev. B* **2017**, *96*, 014304.
- [175] M. Giar, M. Heinemann, C. Heiliger, *Phys. Rev. B* **2017**, *96*, 075202.
- [176] T. Ha, I. Park, K. I. Sim, H. Lee, J.-S. Bae, S. J. Kim, J. P. Kim, T.-T. Kim, J. H. Kim, J. I. Jang, S.-Y. Jeong, *APL Mater.* **2019**, *7*, 031115.
- [177] A. Živković, A. Roldan, N. H. de Leeuw, *Phys. Rev. B* **2019**, *99*, 035154.
- [178] C. Zhu, M. J. Panzer, *ACS Appl. Mater. Interfaces* **2015**, *7*, 5624–5628.
- [179] F. Hu, Y. Zou, L. Wang, Y. Wen, Y. Xiong, *Int. J. Hydrogen Energy* **2016**, *41*, 15172–15180.
- [180] O. Porat, I. Riess, *Solid State Ionics* **1994**, *74*, 229–238.
- [181] O. Porat, I. Riess, *Solid State Ionics* **1995**, *81*, 29–41.
- [182] G. K. Paul, Y. Nawa, H. Sato, T. Sakurai, K. Akimoto, *Appl. Phys. Lett.* **2006**, *88*, 141901.
- [183] K. Akimoto, S. Ishizuka, M. Yanagita, Y. Nawa, G. K. Paul, T. Sakurai, *Sol. Energy* **2006**, *80*, 715–722.
- [184] F. Biccari, C. Malerba, A. Mittiga, **2013**.
- [185] K. Kardarian, D. Nunes, P. Maria Sberna, A. Ginsburg, D. A. Keller, J. Vaz Pinto, J. Deuermeier, A. Y. Anderson, A. Zaban, R. Martins, E. Fortunato, *Sol. Energy Mater. Sol. Cells* **2016**, *147*, 27–36.

- [186] S. N. Kale, S. B. Ogale, S. R. Shinde, M. Sahasrabuddhe, V. N. Kulkarni, R. L. Greens, T. Venkatesan, *Appl. Phys. Lett.* **2003**, *82*, 2100–2102.
- [187] G. S. Chang, E. Z. Kurmaev, D. W. Boukhvalov, A. Moewes, L. D. Finkelstein, M. Wei, J. L. MacManus-Driscoll, *J. Phys. Condens. Matter* **2008**, *20*, 215216.
- [188] I. S. Brandt, M. A. Tumelero, E. Lima, D. L. da Silva, R. D. Zysler, R. Faccio, A. A. Pasa, *J. Magn. Magn. Mater.* **2017**, *441*, 374–386.
- [189] H. Raebiger, S. Lany, A. Zunger, *Phys. Rev. B - Condens. Matter Mater. Phys.* **2007**, *76*, 1–5.
- [190] A. Soon, X. Y. Cui, B. Delley, S. H. Wei, C. Stampfl, *Phys. Rev. B - Condens. Matter Mater. Phys.* **2009**, *79*, 1–15.
- [191] L. Y. Isseroff, E. A. Carter, *Chem. Mater.* **2013**, *25*, 253–265.
- [192] H. Raebiger, S. Lany, A. Zunger, *Phys. Rev. Lett.* **2007**, *99*, 167203.
- [193] M. Sieberer, J. Redinger, P. Mohn, *Phys. Rev. B* **2007**, *75*, 035203.
- [194] M. Nolan, S. D. Elliott, *Chem. Mater.* **2008**, *20*, 5522–5531.
- [195] A. Soon, J. Wallman, B. Delley, C. Stampfl, *Curr. Appl. Phys.* **2013**, *13*, 1707–1712.
- [196] F. Ye, X. Q. Su, X. M. Cai, Z. H. Zheng, G. X. Liang, D. P. Zhang, J. T. Luo, P. Fan, *Thin Solid Films* **2016**, *603*, 395–399.
- [197] S. Satheeskumar, S. Vadivel, K. Dhanabalan, A. Vasuhi, A. T. Ravichandran, K. Ravichandran, *J. Mater. Sci. Mater. Electron.* **2018**, *29*, 9354–9360.
- [198] E. Albanese, M. Leccese, C. Di Valentin, G. Pacchioni, *Sci. Rep.* **2016**, *6*, 31435.
- [199] E. Assmann, P. Blaha, R. Laskowski, K. Held, S. Okamoto, G. Sangiovanni, *Phys. Rev. Lett.* **2013**, *110*, 078701.
- [200] C. H. Chien, S. H. Chiou, G. Y. Guo, Y. D. Yao, *J. Magn. Magn. Mater.* **2004**, *282*, 275–278.
- [201] T. Hu, J. Dong, *Nanotechnology* **2015**, *26*, DOI 10.1088/0957-4484/26/6/065705.
- [202] J. Buckeridge, D. Scanlon, A. Walsh, C. Catlow, *Comput. Phys. Commun.* **2014**, *185*, 330–338.
- [203] M. Yu, D. R. Trinkle, *J. Chem. Phys.* **2011**, *134*, 064111.
- [204] W. Tang, E. Sanville, G. Henkelman, *J. Phys. Condens. Matter* **2009**, *21*, 084204.

- [205] E. Sanville, S. D. Kenny, R. Smith, G. Henkelman, *J. Comput. Chem.* **2007**, *28*, 899–908.
- [206] R. Grau-Crespo, S. Hamad, C. R. A. Catlow, N. H. de Leeuw, *J. Phys. Condens. Matter* **2007**, *19*, 256201.
- [207] O. Rubel, A. Bokhanchuk, S. J. Ahmed, E. Assmann, *Phys. Rev. B* **2014**, *90*, 115202.
- [208] V. Popescu, A. Zunger, *Phys. Rev. Lett.* **2010**, *104*, 236403.
- [209] J. Pierson, E. Duverger, O. Banakh, *J. Solid State Chem.* **2007**, *180*, 968–973.
- [210] T. J. Smart, A. C. Cardiel, F. Wu, K.-S. Choi, Y. Ping, *npj Comput. Mater.* **2018**, *4*, 61.
- [211] K. J. Blobaum, D. Van Heerden, A. J. Wagner, D. H. Fairbrother, T. P. Weihs, *J. Mater. Res.* **2003**, *18*, 1535–1542.
- [212] D. O. Scanlon, J. Buckeridge, C. R. A. Catlow, G. W. Watson, *J. Mater. Chem. C* **2014**, *2*, 3429–3438.
- [213] L. Bendavid, E. Carter, *J. Phys. Chem. C* **2013**, *117*, 26048–26059.
- [214] F. H. Alharbi, S. Kais, *Renew. Sustain. Energy Rev.* **2015**, *43*, 1073–1089.
- [215] C. Rödl, K. O. Ruotsalainen, F. Sottile, A.-P. Honkanen, J. M. Ablett, J.-P. Rueff, F. Sirotti, R. Verbeni, A. Al-Zein, L. Reining, S. Huotari, *Phys. Rev. B* **2017**, *95*, 195142.
- [216] P. Shah, A. Gupta, *Phys. Rev. B* **1992**, *45*, 483–485.
- [217] R. A. Borzi, S. J. Stewart, G. Punte, R. C. Mercader, G. A. Curutchet, R. D. Zysler, M. Tovar, *J. Appl. Phys.* **2000**, *87*, 4870–4872.
- [218] D. Prabhakaran, A. T. Boothroyd, *J. Cryst. Growth* **2003**, *250*, 77–82.
- [219] S. G. Yang, T. Li, B. X. Gu, Y. W. Du, H. Y. Sung, S. T. Hung, C. Y. Wong, A. B. Pakhomov, *Appl. Phys. Lett.* **2003**, *83*, 3746–3748.
- [220] H. Zhu, F. Zhao, L. Pan, Y. Zhang, C. Fan, Y. Zhang, J. Q. Xiao, *J. Appl. Phys.* **2007**, *101*, 107–110.
- [221] F. Zhao, H. M. Qiu, L. Q. Pan, H. Zhu, Y. P. Zhang, Z. G. Guo, J. H. Yin, X. D. Zhao, J. Q. Xiao, *J. Phys. Condens. Matter* **2008**, *20*, DOI 10.1088/0953-8984/20/42/425208.
- [222] L. Li, B. Lv, S. Wang, J. Z. Cai, W. Q. Zou, X. S. Wu, F. M. Zhang, *J. Korean Phys. Soc.* **2013**, *62*, 1530–1533.
- [223] K. H. Gao, Z. Q. Li, T. Du, E. Y. Jiang, Y. X. Li, *Phys. Rev. B* **2007**, *75*, 174444.

- [224] Y. R. Park, K. J. Kim, S.-I. Choi, J. H. Lee, H. J. Lee, C. S. Kim, J. Y. Park, *Phys. status solidi* **2007**, *244*, 4578–4581.
- [225] D. Paul Joseph, C. Venkateswaran, S. Sambasivam, B. C. Choi, *J. Korean Phys. Soc.* **2012**, *61*, 449–454.
- [226] S. Masudy-Panah, K. Radhakrishnan, H. R. Tan, R. Yi, T. I. Wong, G. K. Dalapati, *Sol. Energy Mater. Sol. Cells* **2015**, *140*, 266–274.
- [227] S. Masudy-Panah, K. Radhakrishnan, A. Kumar, T. I. Wong, R. Yi, G. K. Dalapati, *J. Appl. Phys.* **2015**, *118*, 225301.
- [228] S. Baturay, A. Tombak, D. Kaya, Y. S. Ocak, M. Tokus, M. Aydemir, T. Kilicoglu, *J. Sol-Gel Sci. Technol.* **2016**, *78*, 422–429.
- [229] N. V. P. Chaudhary, J. K. Murthy, A. Venimadhav, *Solid State Commun.* **2016**, *247*, 36–39.
- [230] S. P. Jones, N. C. Wurz, M. Failla, D. Prabhakaran, C. F. McConville, J. Lloyd-Hughes, *Phys. Rev. B - Condens. Matter Mater. Phys.* **2014**, *90*, 1–10.
- [231] M. Nasir, R. Islam, M. A. Ahmed, S. Ayaz, G. Kumar, S. Kumar, C. L. Prajapat, F. Roussel, S. Biring, S. Sen, *R. Soc. Open Sci.* **2017**, *4*, 170339.
- [232] M. R. Das, P. Mitra, *J. Sol-Gel Sci. Technol.* **2018**, *87*, 59–73.
- [233] A. Szkudlarek, K. Kollbek, S. Klejna, A. Rydosz, *Mater. Res. Express* **2018**, *5*, 126406.
- [234] T. Chtouki, S. Taboukhat, H. Kavak, A. Zawadzka, H. Erguig, B. Elidrissi, B. Sahraoui, *J. Phys. Chem. Solids* **2019**, *124*, 60–66.
- [235] A. Filippetti, V. Fiorentini, *Phys. Rev. B - Condens. Matter Mater. Phys.* **2006**, *74*, 1–4.
- [236] H. Yang, Y. Cheng, G. Chen, W. Mi, H. Bai, *RSC Adv.* **2013**, *3*, 4447.
- [237] B. G. Ganga, P. N. Santhosh, B. R. Nanda, *J. Phys. Condens. Matter* **2017**, *29*, DOI 10.1088/1361-648X/aa58c2.
- [238] X. Rocquefelte, K. Schwarz, P. Blaha, S. Kumar, J. van den Brink, *Nat. Commun.* **2013**, *4*, 1–7.
- [239] G. Pizzi, D. Volja, B. Kozinsky, M. Fornari, N. Marzari, *Comput. Phys. Commun.* **2014**, *185*, 422–429.

- [240] G. Pizzi, V. Vitale, R. Arita, S. Bluegel, F. Freimuth, G. Géranton, M. Gibertini, D. Gresch, C. Johnson, T. Koretsune, J. Ibanez, H. Lee, J.-M. Lihm, D. Marchand, A. Marrazzo, Y. Mokrousov, J. I. Mustafa, Y. Nohara, Y. Nomura, L. Paulatto, S. Ponce, T. Ponweiser, J. Qiao, F. Thöle, S. S. Tsirkin, M. Wierzbowska, N. Marzari, D. Vanderbilt, I. Souza, A. A. Mostofi, J. R. Yates, *J. Phys. Condens. Matter* **2019**, DOI 10.1088/1361-648X/ab51ff.
- [241] J. D. Gouveia, J. Coutinho, *Electron. Struct.* **2019**, *1*, 015008.
- [242] C.-M. Hao, Y. Li, Q. Zhu, X.-Y. Chen, Z.-X. Wang, Y.-L. Li, *CrystEngComm* **2018**, *20*, 5949–5954.
- [243] Z. Wang, L. Zhang, T. U. Schüllli, Y. Bai, S. A. Monny, A. Du, L. Wang, *Angew. Chemie Int. Ed.* **2019**, *58*, 17604–17609.
- [244] D. Broberg, B. Medasani, N. E. Zimmermann, G. Yu, A. Canning, M. Haranczyk, M. Asta, G. Hautier, *Comput. Phys. Commun.* **2018**, *226*, 165–179.
- [245] H. Dietrich, *Angew. Chemie* **1961**, *73*, 511–512.
- [246] L. Pauling, *The Nature of the Chemical Bond: An Introduction to Modern Structural Chemistry*, 3rd, Cornell University Press, Ithaca, New York, **1960**, p. 664.
- [247] L. Zhao, H. Chen, Y. Wang, H. Che, P. Gunawan, Z. Zhong, H. Li, F. Su, *Chem. Mater.* **2012**, *24*, 1136–1142.
- [248] R. Dovesi, V. R. Saunders, C. Roetti, R. Orlando, C. M. Zicovich-Wilson, F. Pascale, B. Civalleri, K. Doll, N. M. Harrison, I. J. Bush, P. D’Arco, M. Llunell, M. Causà, Y. Noël, L. Maschio, A. Erba, M. Rerat, S. Casassa, CRYSTAL17 User’s Manual, Torino, **2017**.
- [249] R. Dovesi, A. Erba, R. Orlando, C. M. Zicovich-Wilson, B. Civalleri, L. Maschio, M. Rerat, S. Casassa, J. Baima, S. Salustro, B. Kirtman, *Wiley Interdiscip. Rev. Comput. Mol. Sci.* **2018**, *8*, 1–36.
- [250] J. H. Skone, M. Govoni, G. Galli, *Phys. Rev. B* **2014**, *89*, 195112.
- [251] A. Erba, *J. Phys. Condens. Matter* **2017**, *29*, 314001.
- [252] C. L. Bailey, L. Liborio, G. Mallia, S. Tomić, N. M. Harrison, *Phys. Rev. B* **2010**, *81*, 205214.